

High-repetition-rate Femtosecond Optical Parametric Oscillators Based on KTP and PPLN



DISSERTATION

zur
Erlangung des Doktorgrades
der Naturwissenschaften
(Dr. rer. nat)

dem
Fachbereich Physik
der
Philipps-Universität Marburg

vorgelegt von
Xinping Zhang
aus der V. R. China

Marburg/Lahn, Germany 2002

Vom Fachbereich Physik der Philipps-Universität Marburg
als Dissertation angenommen am: 02. 10. 2002

Erstgutachter: Prof. Dr. Harald Giessen

Zweitgutachter: Prof. Dr. Wolfgang W. Rühle

Tag der mündliche Prüfung: 22. 10. 2002

Zusammenfassung

In dieser Dissertation werden optische parametrische Oszillatoren (OPO) basierend auf KTP und PPLN mit Femtosekunden-Pulsdauer und hoher Wiederholrate untersucht.

Zu Beginn werden die Grundlagen von OPOs, Methoden der Phasen-anpassung und Dispersionskompensationstechniken beschrieben.

Durch spezielle Spiegel zur Dispersionskompensation (chirped mirrors) erreichten wir Pulsdauern von 32 fs für einen KTP OPO. Dies ist die derzeit kürzeste Pulsdauer für einen OPO.

Die zur Zeit höchste Wiederholrate von einem Gigahertz wurde durch höhere Ordnungen von synchronem Pumpen eines PPLN OPOs mit einer Pulsdauer von 60 fs erreicht.

Wir entdeckten erstmals, daß ein asymmetrisches Polungsverhältnis effiziente nichtlineare Prozesse in einem OPO wie SHG und SFG in Quasiphasen-anpassung gerader Ordnung gleichzeitig mit Quasiphasen-anpassung erster Ordnung erreicht werden kann. Dies ermöglicht es, mehrere Prozesse quasiphasenangepasst in unterschiedlichen Ordnungen gleichzeitig und effektiv in einem OPO durchzuführen. Dadurch wurde effizient Weißlicht erzeugt. Diese Methode zur Erzeugung von Femtosekunden-Pulsen im sichtbaren Spektralbereich ist allen klassischen Methoden überlegen.

Wir entwickelten ein theoretisches Modell, um das Verhalten aller wechselwirkenden Wellen innerhalb eines PPLN OPOs zu simulieren. Dieses Modell enthält sowohl quasiphasengepasste Prozesse erste Ordnung (im OPO) als auch Prozesse höherer Ordnungen (SHG und SFG). Dies ermöglicht es, unser Modell auf alle Untersuchungen anzuwenden, die mehrere gekoppelte nichtlineare Prozesse enthalten.

Abstract

High-repetition-rate femtosecond optical parametric oscillators based on KTP and PPLN are described comprehensively in this dissertation work.

First, in the theory part the basic principles of OPOs and related devices, phase-matching methods, and dispersion compensation and extracavity pulse compression techniques are described systematically.

We achieved 32-fs operation of a KTP OPO using chirped mirrors for intracavity GVD compensation, which is presently the shortest pulse duration in the world for the signal pulses generated directly from an OPO.

We achieved 1 GHz operation of a 60-fs PPLN OPO making use of higher-order synchronous pumping, which is the highest repetition rate of any femtosecond OPOs reported so far.

We discovered for the first time that a non-50% poling duty cycle enables efficient even-order QPM SHG and SFG processes simultaneously in a first-order QPM PPLN OPO. As a result, multiples higher-order QPM processes (odd- and even-order) can operate simultaneously and efficiently in the same OPO device with small reduction in the first-order QPM OPO process. This technique is advantageous over the classical methods to generate visible femtosecond pulses from an IR OPO.

We developed a theoretical model to simulate the behaviour of all of the interacting waves in a PPLN OPO, involving the first-order QPM OPO process and multiple higher-order QPM frequency conversion processes (SHG and SFG). This theoretical model included a variable poling duty cycle of PPLN to investigate in a sophisticated manner the influence of the poling duty cycle on the even- and odd-order QPM processes, and it can be applied to any studies with multiple frequency processes coupled with one another simultaneously.

List of Publications:

Scientific Journals

1. J. Hebling, X. P. Zhang, H. Giessen, J. Kuhl, J. Seres
Pulse characteristics of an optical parametric oscillator pumped by sub-30-fs light pulses.
Opt. Lett. **25**, 1055-1057 (2000)
2. X. P. Zhang, J. Hebling, J. Kuhl, W. W. Rühle, H. Giessen
Efficient intracavity generation of visible pulses in a femtosecond near-infrared optical parametric oscillator.
Opt. Lett. **26**, 2005-2007 (2001)
3. X. P. Zhang, J. Hebling, A. Bartels, D. Nau, J. Kuhl, W. W. Rühle, H. Giessen
1-GHz-repetition-rate femtosecond optical parametric oscillator.
Appl. Phys. Lett. **80**, 1873-1875 (2002)
4. X. P. Zhang, J. Hebling, J. Kuhl, W. W. Rühle, L. Palfalvi, H. Giessen
Femtosecond near-IR optical parametric oscillator with efficient intracavity generation of visible light.
J. Opt. Soc. Am. B **19**, 2479-2488 (2002)
5. X. P. Zhang, J. Kuhl, J. Hebling, A. Bartels, D. Nau, W. W. Rühle, H. Giessen
1-GHz repetition-rate femtosecond optical parametric oscillator.
Proceedings Article in Ultrafast Phenomena XIII, ed. Miller, Springer-Verlag (2003)

Conferences

1. X.P. Zhang, H. Giessen, J. Hebling, W. Rühle, and J. Kuhl
32 fs KTP Optical Parametric Oscillator with Chirped Mirrors
Advanced Solid State Lasers Conference 2000 (PD7), Davos, Switzerland.
2. H. Giessen, X.P. Zhang, J. Hebling, W. Rühle, and J. Kuhl
32 fs KTP Optical Parametric Oscillator with Chirped Mirrors
CLEO 2000, San Francisco, USA (May 2000) [talk CWH6]
3. X. P. Zhang, J. Hebling, J. Kuhl, W. W. Rühle and H. Giessen
Efficient visible light generation in a femtosecond PPLN optical parametric oscillator using an uneven poling duty cycle.
CLEO 2002, Baltimore, USA (May 2002) [talk CWL3].
4. X. P. Zhang, J. Hebling, A. Bartels, D. Nau, J. Kuhl, W. Rühle and H. Giessen
1-GHz repetition-rate femtosecond optical parametric oscillator.
CLEO 2002, Baltimore, USA (May 2002) [talk CML1].
5. J. Kuhl, X. P. Zhang, J. Hebling, A. Bartels, D. Nau, W. W. Rühle, H. Giessen
1-GHz repetition-rate femtosecond optical parametric oscillator.
13th International Conference on Ultrafast Phenomena, Vancouver, Canada (May, 2002) [talk]

Contents

Section I Introduction

1.1 Overview	1
1.2 Motivations and methods	5

Section II Theory

2.1 Basic principles of optical parametric oscillators (OPOs)

2.1.1 Basics of nonlinear optics	7
2.1.2 Optical parametric processes and devices	9
2.1.3 Solutions to the coupled equations for optical parametric processes	13
2.1.4 Tuning methods of OPOs	17

2.2 Birefringent phase matching (BPM) and tuning characteristics of BPM OPO

2.2.1 Birefringent phase matching methods	21
2.2.2 Phase matching bandwidth for OPO processes	27
2.2.3 KTP (K ₂ TiOPO ₄) crystal	29
2.2.4 Noncritical phase matching (NCPM) of a KTP OPO	31
2.2.5 Tuning characteristics of a noncritically phase-matched KTP OPO	33
2.2.6 Temperature phase matching: LBO OPO	34

2.3 Quasi-phase matching(QPM) and tuning characteristics of QPM OPO

2.3.1 Quasi-phase matching	37
2.3.2 LiNbO ₃ and PPLN	42
2.3.3 Tuning characteristics of the PPLN OPO	46
2.3.4 Design of a PPLN crystal	53
2.3.5 PPKTP and PPKTP OPO	55

2.4 Dispersion characteristics of OPO crystals and optical glasses; pulse broadening effects

2.4.1 GVD and GVM	59
2.4.2 Dispersion characteristics of some typical OPO crystals.....	60
2.4.3 Pulse broadening effects induced by GVM	63
2.4.4 Dispersion characteristics of some optical glasses and pulse broadening effects	68

2.5 GVD compensation and pulse compression methods

2.5.1 Prism pair	73
2.5.2 Grating pair	80
2.5.3 Chirped mirrors	82
2.5.4 Glass slabs	83

Section III Experiments

3.1 32-fs KTP OPO

3.1.1 Introduction	87
3.1.2 Experimental setup and pump characteristics	88
3.1.3 Pulse characteristics of the KTP OPO	90
3.1.4 Cavity length detuning effects	92
3.1.5 Pump wavelength tuning effects	94
3.1.6 Pump threshold	95

3.2 Generation of femtosecond visible pulses from an OPO

3.2.1 Introduction	97
3.2.2 Some typical methods for intracavity SHG and SFG	100
3.2.3 Example: Intracavity and extracavity SHG and SFG in a KTP OPO using a BBO crystal	102
3.2.4 Efficient SHG and SFG processes in a PPLN OPO: experiments and results	107
3.2.5 Mechanisms for the efficient visible light generation	110
3.2.6 Temporal characteristics of the generated waves	115
3.2.7 Operation characteristics of the PPLN OPO	117
3.2.8 Conclusions	126

3.3 Coupling among multiple higher-order QPM processes in a PPLN OPO

3.3.1 Higher-order processes in a PPLN OPO	127
3.3.2 “Degenerate” higher-order QPM processes	129
3.3.3 Simulation model: The modified coupling equations	132
3.3.4 Simulation results and discussion	135
3.3.5 Synchronous operation between “ $\omega_p + \omega_s$ ” and “ $2\omega_s$ ”	144

3.4 Lower-order synchronous pumping of PPLN OPO	
3.4.1 Methods to achieve high-repetition-rate operation of a synchronously pumped OPO	147
3.4.2 Lower-order synchronous pumping	149
3.4.3 Experimental setup	150
3.4.4 Experimental results and discussions	151
3.5 Femtosecond 1-GHz PPLN OPO based on higher-order synchronous pumping	
3.5.1 Introduction	157
3.5.2 Experimental setup	158
3.5.3 Mode matching and higher-order synchronous pumping	159
3.5.4 1-GHz-repetition-rate operation of the PPLN OPO	162
3.5.5 Intracavity GDD compensation by a chirped mirror.....	165
3.5.6 Optimization of the output coupling rate	167
3.5.7 Summary	168
Section IV Summary and outlook	
4.1 Summary	171
4.2 Outlook	173
Appendix A. Sellmeier equations of OPO crystals and common glasses	
Appendix B. Abbreviations	
Literature	
Acknowledgement	

Section I Introduction

1.1 Overview

In some research areas, such as spectroscopy, semiconductor analysis, photochemistry and remote sensing, tunable coherent sources of high power or high energy are needed. Dye lasers have been the best solutions in the past decades because of their large tuning ranges and high efficiencies. But the handling of toxic materials and the requirement of changing the dyes due to their continuous photo-degradation make the dye laser disadvantageous. [1]

With the rapid progress in new and better nonlinear materials and laser technology, especially in solid state lasers and semiconductor lasers, other coherent radiation sources are desired to replace tunable dye lasers. In addition, for some applications large bandwidth and wider tuning range (even into near and far infrared) are required simultaneously. In telecommunication, broadband sources within the telecommunication window (1.3 μm to 1.55 μm) are needed. For the studies of time-resolved spectroscopy of semiconductor heterostructures, femtosecond laser pulses at about 1.2 μm are needed for Transient Four-Wave-Mixing (TFWM) [2]. High repetition rate operation enables large signal-to-noise ratio (SNR), which is very important in spectroscopy and pump-probe measurement. High repetition rate also means high data rate in telecommunication applications.

Synchronously pumped optical parametric oscillators (SPOPO) held the promise of providing above qualities. [1] Large tuning range and large bandwidth in the near- and mid-IR regions, which are based on the large phase-matching bandwidth of the nonlinear crystal for optical parametric process, are the most important and attractive characteristics of optical parametric oscillators (OPOs). Sub-picosecond or femtosecond operation of the OPOs makes them suitable for the study of nonlinear spectroscopy (i.e., quantum beat spectroscopy) and applicable in studying ultrafast carrier dynamics in semiconductors (spectral-hole burning), exciton bleaching, the light-induced shift of the exciton resonance, the optical Stark effect, and the time-resolved photon echo, etc..[3] Invention of high repetition rate pump sources (e.g. >1 GHz Kerr Lens Mode-locked or KLM Ti:sapphire lasers [4]) makes it possible to operate a SPOPO at equally high or even higher repetition rate. Owing to this breakthrough, OPOs can potentially improve their characteristics when applied to

femtosecond spectroscopy and pump-probe measurements (with large SNR), telecommunication systems (with high data rates), frequency combs in the near infrared and in the visible (with large frequency span), and high-repetition-frequency optical clock.

The first tunable OPO was built by Giordmaine and Miller [5] in 1965, which was based on lithium niobate. Rapid progress in this field then followed in the 1960s [1]. With the development in the new materials and devices, optical parametric generation devices have found their ways into new research and applications markets.

The nonlinear medium of the OPOs covers KTiOPO_4 (KTP), LiNbO_3 , LiB_3O_5 (LBO), $\beta\text{-BaB}_2\text{O}_4$ (BBO), LiTiO_3 , KtIOAsO_4 (KTA), RbTiOAsO_4 (RTA), CsTiOAsO_3 (CTA), etc. for birefringent phase-matching (BPM), and periodically poled LiNbO_3 , $\text{MgO}:\text{LiNbO}_3$, KTP, KTA, RTA, etc. for quasi-phase-matching (QPM).

Before early 1990s, research areas are mainly on birefringently phase-matched OPOs, e.g., noncritically phase-matched KTP OPO, some main subjects include analysis of phase-matching, generation of the ultrashort signal pulses from OPOs. Methods to compress the signal pulse duration were mostly interested and greatly improved.

From early 1990s, because of the advances in fabrication technologies, quasi-phase-matching materials renewed interests in this approach [6], though it was put forth even earlier than the birefringent phase-matching method [7]. Because of the large effective nonlinear coefficient, the periodically poled lithium niobate (PPLN) makes it possible for the OPO to have much higher efficiency and lower threshold. The research emphasis was not only on the signal pulses, but also on the tuning range and pulse compression of the idler, since PPLN has a large transparency range (0.4 to 5.4 μm) [8]. With aid of temperature tuning, phase matching can be achieved in almost the whole transparency range. A large tuning range of the idler from 1.7 μm to 5.4 μm has been achieved [9]. Since LiNbO_3 has another transmission window extending from 6 to 7 μm , a continuous tuning range of the idler from 2.8 to 6.8 μm was also reported [10]. The more important reason why the studies of the idlers drew more interest is that the tunable high-repetition-rate picosecond and femtosecond pulses in the mid-infrared is of interest for a variety of applications including time-resolved spectroscopy of semiconductors. A partially useful spectral range is from 4 to 6 μm , where intersubband transitions, scattering mechanisms, or Auger recombination and

suppression in narrow-bandgap semiconductors such as InSb, InAlAs, and InAsSb can be studied [11].

More accurate descriptions of the dispersion characteristics of PPLN [8] make it possible to predict and improve the tuning effects of the OPO. MgO doping in LiNbO₃ was found to greatly reduce the photorefractive damage [12].

KTP has a much higher photorefractive damage threshold than lithium niobate, permitting room temperature operation without temperature control. On the other hand, KTP needs a much lower coercive field of 2 kV/mm than lithium niobate to get successful electric-field poling [13]. Therefore PPKTP OPOs are also attractive to generate picosecond or femtosecond pulses in near and mid IR, although the effective nonlinear coefficient of PPKTP is smaller than that of PPLN.

Broadly tunable infrared femtosecond OPO based on periodically poled RbTiOAsO₄ [14] and intracavity second-harmonic generation with periodically poled LiTaO₃ [10] were also reported.

As mentioned above, high repetition rate, large tuning range, large bandwidth or short pulse duration, and low pump threshold have always been the aim of the research work on the OPOs.

A repetition rate of about 80 MHz is typical for a mode-locked Ti:sapphire laser synchronously pumped OPO, and 2.5 GHz repetition rate has already been reached for a picosecond OPO synchronously pumped by a mode-locked diode oscillator amplifier system [15]. Using lower-order synchronous pumping (defined in Chapter 3.3), repetition rate as high as 1.33 GHz has been achieved by B. Ruffing et al. [16] for a picosecond KTA OPO pumped by a mode-locked Nd:YVO₄ laser operating at 83.4 MHz.

Using chirped mirrors as cavity mirrors of a KTP OPO cavity, the duration of the signal pulses was reduced to being much shorter than that of the pump pulses [17]. By use of an intracavity prism pair, signal pulses of 60 fs at 1.27 μm [18] were generated from a PPLN OPO.

In recent years, pulses in the mid-IR region generated from OPOs have been shortened even to a few optical cycles [19][20], and optical parametric amplifiers have generated sub-3-cycle pulses in the visible [21] and near IR [22].

Visible light generation through intracavity and extracavity SHG and SFG between the interaction waves largely extend the tuning range of the OPOs. The generated

ultrashort pulsed green and blue light pulses can be used in femtosecond spectroscopy and other practical applications.

Large phase matching bandwidth of OPOs, especially those based on periodically poled crystals, enables even 300~700 nm of tuning range of the signal wavelength.

Larger effective nonlinear coefficient allows the femtosecond PPLN OPO to run at much lower pump threshold when compared with its birefringently phase-matched counterparts, such as KTP OPOs. The pump threshold of a Ti:sapphire laser pumped PPLN OPO has reached 17 mW by using a semimonolithic cavity and hemispherical focusing [11]. Low-pump threshold allows much higher repetition-rate operation of the corresponding OPOs.

The use of quasi-phase-matched crystals with a linearly varying grating period is another method to generate compressed pulses from an OPO, which was first discussed theoretically for second-harmonic generation and compression [23]. This method was used experimentally first with an aperiodically poled KTP crystal to compress the second harmonic generation of the signal pulses from a RTA OPO [24]. By using aperiodically poled lithium niobate, the pulse duration of the idler of the OPO has been shortened to 53 fs at 3 μm [20], which corresponds to only 5 optical cycles.

But pulse compression by using aperiodically poled lithium niobate or KTP has so far been demonstrated only for SHG and for the idler pulses from an OPO, since this compression method needs the input pulses to be intentionally chirped in advance and to pass through the nonlinear crystal only once. No reports about the compression of the oscillating signal pulses by this method have been found yet.

1.2 Motivation and methods

Our work on the OPOs aims to obtain femtosecond laser sources that can be extensively applied to femtosecond spectroscopic research and are potentially of great importance for telecommunication applications.

Achieving high-repetition-rate, large-tuning-range, large-bandwidth and ultrashort-pulsed operation of SPOPOs is the main task of our research work on the OPOs.

In the theoretical section, we tried to prepare as complete as possible the basis for understanding, analyzing, and designing OPOs based on different crystals for different application purposes.

We begin with the basic principles of OPOs in Chapter 2.1 by explaining various parametric processes and solving the coupled equations.

In Chapter 2.2, we introduce the birefringent phase matching methods. Using KTP and LBO crystals as examples, we explain how to achieve different types of phase matching and present the corresponding tuning characteristics of the OPOs, which is the first step to design a birefringently phase-matched OPO.

In Chapter 2.3, we interpret the principles of QPM and the technology of how to realize QPM in practical devices. Different tuning methods and the corresponding tuning characteristics of PPLN OPOs are described in connection with the experiment. Methods to design the grating periods of PPLN and PPKTP crystal for QPM OPOs with different tuning ranges are formalized. Some practical design curves are presented for direct applications.

In Chapter 2.4, we analyze dispersion characteristics of some typical OPO crystals and some commonly used glasses, as well as the corresponding pulse expansion effects, which is very important and must be considered in femtosecond OPOs.

Then, we demonstrate the GVD compensation and pulse-compression methods in Chapter 2.5, which were used to achieve ultrashort-pulsed and large-bandwidth operation of our OPOs.

In the experimental section, we demonstrate comprehensively our experiments that fulfilled our planned tasks.

Using chirped mirrors for intracavity GVD compensation, we achieved 32 fs operation of a KTP OPO at 80 MHz (Chapter 3.1). This is the shortest pulse duration reported so far for signal pulses centered at about 1200 nm and directly generated from a KTP OPO.

In Chapter 3.2, we describe efficient visible light generation from a femtosecond PPLN OPO that operates at a pulse duration of 65 fs and a repetition rate of about 80 MHz. Making use of a ~56% poling duty cycle of PPLN, we successfully extended the tuning range of the OPO from near IR to the visible spectral region. The wavelength of the generated femtosecond visible pulses covers almost the whole visible spectral range with the considerably efficient generation ranging from 460 nm to 630 nm. Meanwhile, based on the large spectral bandwidth of the pump pulses and large tuning rate of QPM of PPLN, we achieved over 300 nm (1040 nm ~ 1350 nm) tuning range of the signal wave of the OPO.

Based on the experimental work described in Chapter 3.2, we introduce a theoretical model in Chapter 3.3 to investigate the mechanisms for the observed efficient higher-order QPM processes, which applies to any complex processes with multiple parametric interactions which are coupled with each other. We discuss sophisticatedly how the variation of the poling duty influences the efficiencies of both odd- and even-order QPM processes, as well as the behaviors of the OPO signal, and how to optimize the duty cycle to generate the desired wavelengths efficiently.

Chapter 3.4 and Chapter 3.5 describe our methods to achieve high-repetition-rate operation of a femtosecond PPLN OPO. In Chapter 3.4, we illustrate the so-called lower-order synchronous pumping of an OPO. By this method, we achieved as high as 560 MHz operation of a PPLN OPO pumped by a 80 MHz Ti:sapphire laser. The signal pulses are as short as 65 fs. In Chapter 3.5, we demonstrate how the so-called higher-order synchronous pumping methods improve the mode matching between the pump and OPO signal beams for 1 GHz pumping and how we achieved 1 GHz operation of a 65-fs PPLN OPO.

Section II Theory

2.1

Basic principles of optical parametric oscillators (OPOs)

2.1.1 Basics of nonlinear optics

Light is an electromagnetic wave consisting of electric and magnetic fields. For most of optics, the optical wave may be characterized by defining its electric field $E^{(\sim)}$, where the superscript (\sim) implies rapidly varying fields. [1]

For a laser propagating along z -axis, the electric field can be given by

$$E^{(\sim)}(r, t) = E_0(r, t) \exp[i(kz - \omega t)] + c.c.$$

where k is the wave vector, ω is the circular frequency of the rapidly oscillating wave, and $E_0(r, t)$ is the space and time dependent amplitude.

In most cases, the laser beam can be defined as the TEM_{00} mode of a circular Gaussian beam with the form

$$E^{(\sim)}(r, t) = E_0(z, t) \frac{w_0}{w(z)} \exp\left\{i\left[\frac{kr^2}{2q(z)} + kz - \tan^{-1}\left(\frac{z}{z_R}\right) - \omega t\right]\right\} + c.c.$$

where w_0 is radius of the beam waist at $z=0$, $w(z)$ is the radius of the beam at z with

$$w(z) = w_0 \left[1 + \left(\frac{z}{z_R}\right)^2\right]^{1/2}, \quad z_R = \frac{n\pi w_0^2}{\lambda}$$
 is the Rayleigh range (n is the refractive index

of the medium at wavelength λ), and $q(z) = z - iz_R$ is the complex radius of curvature.

When an electric field is applied to a dielectric medium (of neutral electric charge), a separation of bound charges is induced, resulting in a collection of induced dipole moments. The electric polarization ($P^{(\sim)}$) is defined as the net average dipole moment per unit volume, and $P^{(\sim)} = P_L^{(\sim)} + P_{NL}^{(\sim)}$, where $P_L^{(\sim)} = \epsilon_0 \chi^{(1)} \cdot E^{(\sim)}$ is the linear polarization and $P_{NL}^{(\sim)}$ is the nonlinear polarization induced by sufficiently intense light field. $\epsilon_0 = 8.85 \times 10^{-12}$ F/m is the electric permittivity in free space. $\chi^{(l)}$ is the linear dielectric response tensor and becomes a scalar quantity in an isotropic medium.

In linear optics of isotropic media, $\chi^{(l)}$ is a complex function of frequency and can be written as

$$\chi^{(1)} = \chi_R^{(1)} + i\chi_I^{(1)}$$

where the subscripts R and I signify the real and the imaginary parts, respectively.

The refractive index of the medium can be expressed as

$$n(\omega) = \sqrt{1 + \chi_R^{(1)}(\omega)}$$

and the intensity absorption coefficient in the medium is

$$\alpha(\omega) = \frac{\omega\chi_I^{(1)}(\omega)}{n(\omega)c}.$$

Then the electric field can be written as

$$E^{(-)}(z, t) = E_0 \exp\left(-\frac{\alpha z}{2}\right) \exp[i(kz - \omega t)] + c.c.$$

In nonlinear optics, the nonlinear polarization can be written as:

$$P_{NL}^{(-)} = P^{(-)(2)} + P^{(-)(3)} + \dots$$

where

$$P^{(-)(i)} = \varepsilon_0 \chi^{(i)} : \underbrace{E^{(-)} E^{(-)} \dots E^{(-)}}_i$$

with $i=2, 3, \dots$, and $\chi^{(i)}$ is the i th order dielectric response and is a tensor of rank $i+1$.

Here we only care about the frequency conversion processes based on the second order nonlinearity of the media. For a second order polarization oscillating at ω_3 due to the presence of fields oscillating at frequencies ω_1 and ω_2 , with $\omega_3 = \omega_1 + \omega_2$. The i th Cartesian component of the amplitude of the Fourier-transformed nonlinear polarization is expressed as

$$P_i^{(2)}(\omega_3) = 2\varepsilon_0 \sum_{jk} \chi_{ijk}^{(2)}(-\omega_3; \omega_1, \omega_2) E_j(\omega_1) E_k(\omega_2)$$

where $\chi_{ijk}^{(2)}(-\omega_3; \omega_1, \omega_2)$ is called the second order (complex) Fourier transformed dielectric response or the second-order susceptibility.

More commonly, the susceptibility is represented by the so-called d -coefficients, where d is a tensor given by

$$d_{ijk} = \frac{1}{2} \chi_{ijk}^{(2)}$$

Due to the intrinsic permutation symmetry, the last two subscripts of d tensor can be contracted, namely $d_{ijk} \rightarrow d_{lm}$. Then the subscripts can be simplified using the following scheme:

$i:$	$jk:$
$x \rightarrow l=1$	$xx \rightarrow m=1$
$y \rightarrow l=2$	$yy \rightarrow m=2$
$z \rightarrow l=3$	$zz \rightarrow m=3$
	$yz=zy \rightarrow m=4$
	$xz=zx \rightarrow m=5$
	$xy=yx \rightarrow m=6$

Using the above notation, the d -coefficients can be expressed as elements of a 3×6 matrix rather than a $3 \times 3 \times 3$ tensor, which is called the d -matrix.

The forms of the d -matrix for two kinds of crystals are listed in the following table.

Symmetry class	General conditions	Kleinman symmetry
mm2 (KTP)	$\begin{bmatrix} 0 & 0 & 0 & 0 & d_{15} & 0 \\ 0 & 0 & 0 & d_{24} & 0 & 0 \\ d_{31} & d_{32} & d_{33} & 0 & 0 & 0 \end{bmatrix}$	$\begin{bmatrix} 0 & 0 & 0 & 0 & d_{15} & 0 \\ 0 & 0 & 0 & d_{24} & 0 & 0 \\ d_{15} & d_{24} & d_{33} & 0 & 0 & 0 \end{bmatrix}$
3m (LiNbO ₃)	$\begin{bmatrix} 0 & 0 & 0 & 0 & d_{15} & -d_{22} \\ -d_{22} & d_{22} & 0 & d_{15} & 0 & 0 \\ d_{31} & d_{31} & d_{33} & 0 & 0 & 0 \end{bmatrix}$	$\begin{bmatrix} 0 & 0 & 0 & 0 & d_{15} & -d_{22} \\ -d_{22} & d_{22} & 0 & d_{15} & 0 & 0 \\ d_{15} & d_{15} & d_{33} & 0 & 0 & 0 \end{bmatrix}$

In practice, the so-called effective d -coefficient (d_{eff}) is used to analyze the nonlinear interactions, which can be obtained using the d -matrix, the direction of propagation, and the polarizations of the interaction waves defined relative to the laboratory axis (x, y, z) and the crystal principal axes (X, Y, Z). Please refer to Ref. [1] for calculation formulas and measurement methods of d_{eff} .

2.1.2 Optical parametric processes and devices

Optical parametric processes of three interacting beams generally refer to the following frequency mixing processes: second-harmonic generation (SHG), sum-frequency generation (SFG), difference-frequency generation (DFG), optical parametric generation and amplification (OPG and OPA), and optical parametric oscillation (OPO). The SHG may be considered as a special case of SFG. OPG, OPA, and OPO are based on the inverse process of SFG.

When intense fields at frequencies ω_1 and ω_2 are incident on a nonlinear medium, each atom develops an oscillating dipole moment that may contain a component at frequency $\omega_1 + \omega_2$ (SFG) or $\omega_1 - \omega_2$ (DFG) due to nonlinearities in the atomic

response. An isolated atom would radiate at this frequency in the form of a dipole radiation pattern and with a phase that is determined by the phases of the incident fields. If the relative phasing of the dipoles of an enormous number N of atoms is correct, the field radiated by each dipole will add constructively in the forward direction, leading to the radiation of a well-defined beam. The system will act as a phased array of dipoles when the so-called phase-matching condition is satisfied. The electric strength of the radiation will be N times multiplied, and consequently the intensity will be N^2 times as large. [25] The above process constitutes the basis of optical parametric interactions.

In the process of OPG, an input pump photon of higher frequency ω_p is split into two photons of lower frequencies through a down-conversion process in the nonlinear crystal, generating two new waves: one is called the signal (ω_s), the other is called the idler (ω_i), as shown in Fig. 2.1.1.

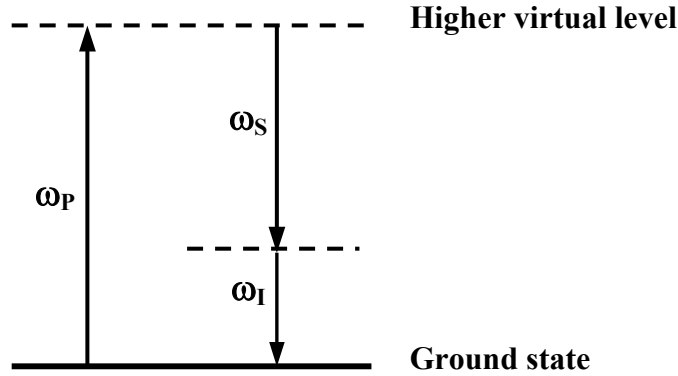


Fig. 2.1.1 Energy level scheme of the OPG process.

In this process, both energy and momentum need to be conserved. The energy conservation condition can be written as:

$$\omega_p = \omega_s + \omega_i \quad \text{or} \quad \frac{1}{\lambda_p} = \frac{1}{\lambda_s} + \frac{1}{\lambda_i} \quad (2.1.1)$$

Momentum conservation is achieved by satisfying the phase matching condition:

$$\Delta k = k_p - k_s - k_i = 0 \quad \text{or} \quad n_p \omega_p - n_s \omega_s - n_i \omega_i = 0 \quad (2.1.2)$$

Normally, the signal has a higher frequency than the idler. What frequencies or wavelengths (the signal and the idler) will be generated in the down-conversion process is governed by the phase-matching and energy conservation conditions as given in equations (2.1.1) and (2.1.2).

The spontaneous down conversion process generates a very weak emission with quite low coherence at the signal and idler wavelengths (parametric fluorescence) and requires a high second-order susceptibility of the nonlinear crystal. To attain directly applicable intensity of the signal or the idler, the conversion efficiency needs to be improved significantly. Therefore, we have to send the newly generated waves again to the nonlinear crystal and repeat the phase-matched interactions. This is why we build up OPAs or OPOs for practical applications.

In an OPA, because of extremely high pump power density (GW/cm^2), a parametric superfluorescence power level at the same order of magnitude as that of the pump can be achieved in a single transition through nonlinear crystal. That means a single pump pulse is already enough to generate applicable signal power through parametric interaction.

In a practical device of an OPA, the strong pump beam is split into multiple parts by beam splitters, so that a large pump pulse is divided into multiple small pump pulses with lower intensities. Thus, the OPA process consists of several stages. In the first stage, the first pump pulse with the smallest delay is focused into the nonlinear crystal to generate parametric superfluorescence (at the signal frequency). The intensity of the first pump pulse should be lower than the supercontinuum generation threshold. In the second stage, the generated superfluorescence is sent back to the nonlinear crystal. The signal should be delayed such that it arrives at the crystal simultaneously with the second pump pulse. Efficient interaction between them amplifies the signal significantly. This stage may also be used as a preamplification process, and the power amplification can be accomplished in the third stage, where the preamplified signal is sent into the crystal again and interacts with the third pump pulse after appropriate delay. Increasing the number of amplification stages can improve the coherence and stability of the OPA emission. [26]

If we put the nonlinear crystal in a resonator, oscillation of the signal (or idler) can build up. Such a device is called an OPO.

The difference between an OPO and an OPA can be summarized as follows: (1) An OPA requires extremely powerful pump pulses (typically mJ-pulse energy) and can operate with single-pulse pumping, while an OPO operates with very low pump threshold (typically nJ-pulse energy) but requires a successive pump pulse train. (2) An OPA generates higher energy pulses at lower repetition rate (typically $\mu\text{J} - \text{mJ}$ at

kHz repetition rate), whereas an OPO produces nJ pulses at much higher repetition rate (typically 80 MHz). (3) High repetition rate implies high signal-to-noise ratio. Therefore, an OPO generally has lower amplitude noise than an OPA. (4) Owing to the spatial confinement by the resonator, the output beam from an OPO has much higher spatial quality than that from an OPA. (5) The output from an OPO has higher coherence properties and consequently higher spectral qualities than that from an OPA [27].

Therefore, when compared with an OPA, an OPO is more advantageous in much higher spatial and spectral qualities of the generated pulses, higher coherence properties, lower amplitude noise, and its easier ways to control the tunability. Moreover, high-repetition-rate operation is of special or critical importance for some applications, where an OPO cannot be replaced with an OPA. Using the output from an OPO as the injection seed of an OPA provides the opportunity to produce high-quality giant pulses [28].

In an OPO, the interaction times of the pump with the signal pulses, called cavity lifetime of the signal, is dependent on the output coupling rate of the cavity mirrors and cavity losses. There are singly resonant (SRO, only the signal) and doubly resonant (DRO, both the signal and the idler) OPOs. We will only talk about singly resonant OPOs.

Since gain is available only in the nonlinear crystal when the pump pulse is present, for femtosecond OPOs it is necessary to use a synchronous pumping scheme, where the pump laser has the same cavity length as the OPO so that the signal pulse can always meet the pump pulse in the crystal.

The optical parametric oscillator operates in a different way if compared with a laser. A laser derives its gain from the energy in the upper energy levels of the atoms or molecules, which has been stored through excited transitions between different states. The tuning range or bandwidth of a laser is limited because these transitions have inherent linewidths. The lasing of a laser can be achieved only when the “population inversion” is realized and the gain in the medium exceeds the total cavity loss. In contrast, “population inversion” is not required for an OPO and the gain is derived from the pump wave through a nonlinear frequency conversion process. Tunability of an OPO depends mainly on the phase-matching conditions and dispersion characteristics of the nonlinear crystal.

2.1.3 Solutions to the coupled equations for optical parametric processes

The coupled equations are the main tools to investigate the optical parametric processes theoretically, which can be derived from the Maxwell's equations. Here we will discuss the three-frequency parametric interaction processes, which apply to SHG, SFG, DFG, and OPA.

In this chapter, we just intend to calculate the conversion efficiencies of the parametric interactions considering only the influence from the phase-mismatch. Interactions between monochromatic waves with slowly varying amplitudes in lossless nonlinear media will be studied. The influences from the group velocity mismatch (GVM), group velocity dispersion (GVD), which are very important for ultrashort (i. e., femtosecond) pulsed OPOs, will be analyzed in Chapter 2.4.

Thus, the coupled equations for optical parametric processes can be generally written as [25,29]:

$$\frac{\partial}{\partial z} E_1(z) = j \frac{4\pi}{n_1 \lambda_1} d_{\text{eff}} E_3(z) E_2^*(z) \exp(j\Delta kz) \quad (2.1.3 \text{ a})$$

$$\frac{\partial}{\partial z} E_2(z) = j \frac{4\pi}{n_2 \lambda_2} d_{\text{eff}} E_3(z) E_1^*(z) \exp(j\Delta kz) \quad (2.1.3 \text{ b})$$

$$\frac{\partial}{\partial z} E_3(z) = j \frac{4\pi}{n_3 \lambda_3} d_{\text{eff}} E_1(z) E_2(z) \exp(-j\Delta kz) \quad (2.1.3 \text{ c})$$

where $E_i(z)$ ($i=1, 2, 3$) are the amplitudes of the electric fields of the interaction waves: $E_i(\omega_i; z, t) = E_i(z) \exp[i(k_i z - \omega_i t)] + c.c.$; n_i ($i = 1, 2, 3$) are the refractive indices of the nonlinear medium at the interaction wavelengths λ_i ; d_{eff} is the effective susceptibility of the medium; $\Delta k = k_3 - k_1 - k_2$ is the phase velocity mismatch amount between the pump and the generated waves; the energy conservation condition is implied in the coupled equations: $\frac{1}{\lambda_3} = \frac{1}{\lambda_1} + \frac{1}{\lambda_2}$.

The equations in (2.1.3) can be solved both analytically and numerically. Table 2.1.1 lists the analytical solutions to the coupled equations for different processes without pump depletion taken into account. Fig. 2.1.2 shows numerical solutions under different phase-matching conditions. At a given amount of phase mismatch amount ($\Delta k \neq 0$), the conversion efficiency from the pump to the signal will change oscillatory from zero to the peak value with increasing the interaction length (L),

creating the so-called Maker-fringes. The Maker-fringes were firstly observed experimentally by Maker et al. [30] when bright and dark second harmonic fringes were generated as a crystal was rotated about an axis perpendicular to the pump beam axis. The number of fringes is equal to $L/(2L_C)$, where L_C is the coherence length ($\Delta k L_C = \pi$) for the studied process, as also shown in Fig 2.1.2.

Table 2.1.1 Analytical solutions to the coupled equations for different processes [1]

Processes	Conversion efficiency (SI units)
SHG ($2\omega = \omega + \omega$)	$\frac{8\pi^2 d_{eff}^2 L^2 I_\omega \sin^2(\Delta k L / 2)}{\varepsilon_0 n_\omega^2 n_{2\omega} c \lambda_\omega^2 (\Delta k L / 2)^2}$
SFG ($\omega_S = \omega_{P1} + \omega_{P2}$)	$\frac{8\pi^2 d_{eff}^2 L^2 I_{P1} \sin^2(\Delta k L / 2)}{\varepsilon_0 n_{P1} n_{P2} n_S c \lambda_S^2 (\Delta k L / 2)^2}$
DFG ($\omega_D = \omega_{P1} - \omega_{P2}$)	$\frac{8\pi^2 d_{eff}^2 L^2 I_{P1} \sin^2(\Delta k L / 2)}{\varepsilon_0 n_{P1} n_{P2} n_D c \lambda_D^2 (\Delta k L / 2)^2}$
OPO ($\omega_P = \omega_S + \omega_i$)	$\frac{8\pi^2 d_{eff}^2 L^2 I_P \sin^2(\Delta k L / 2)}{\varepsilon_0 n_P n_s n_i c \lambda_s^2 (\Delta k L / 2)^2}$

For femtosecond interaction, the value of L should be the effective interaction length instead of the practical medium length. The phase-matching bandwidth is defined as the full width at half maximum (FWHM) of the function of $\frac{\sin^2(\Delta k L / 2)}{(\Delta k L / 2)^2}$, or $\text{sinc}^2(\Delta k L / 2)$, where $|\Delta k L| \leq 0.886\pi$, as illustrated in Fig. 2.1.3.

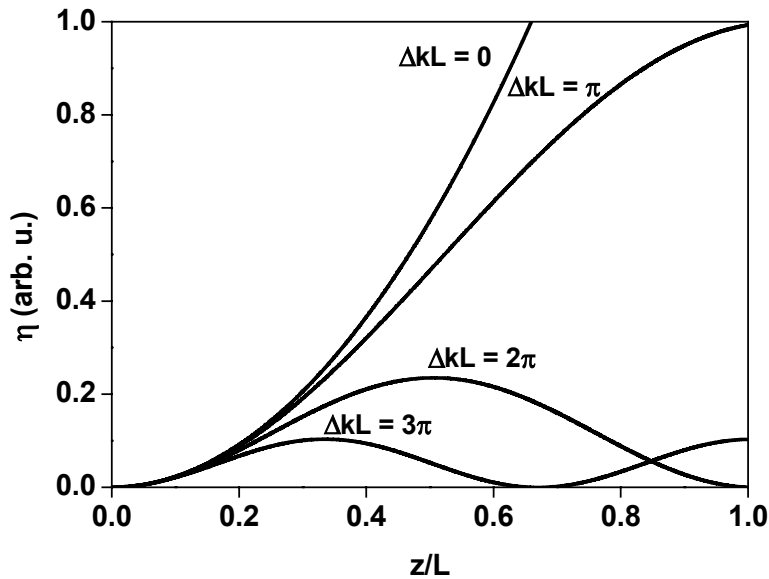


Fig. 2.1.2 Conversion efficiency as a function of position (z) in a nonlinear medium (L), varying the phase mismatch for the OPO process.

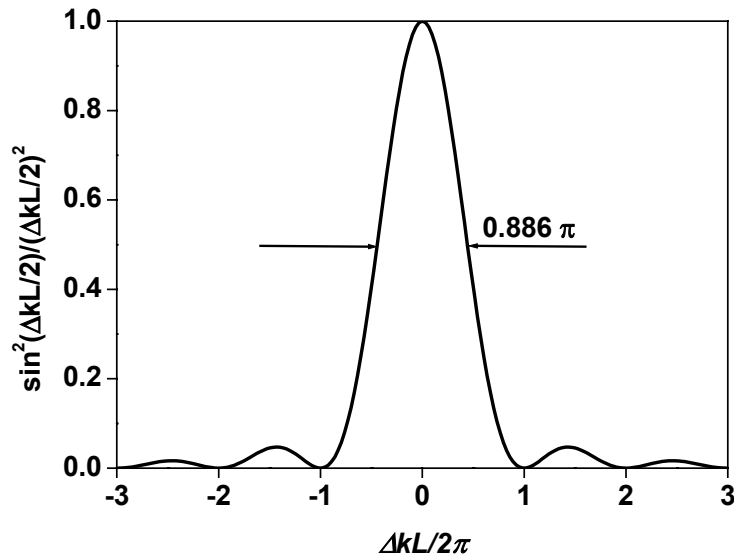


Fig. 2.1.3 Plot of the sinc^2 function ($\text{sinc}^2(x) = \sin^2 x / x^2$) and phase-matching bandwidth.

With perfect phase matching ($\Delta k=0$), the conversion efficiency can become large so that the pump depletion has to be considered when solving the coupled equations. In Ref. 1 (pp. 38-45), analytical solutions to the coupled equations and some theoretical discussions are presented. Here we just demonstrate the pump depletion effect by solving the coupled equations using a set of practical parameters.

For type-II noncritical phase matching of a KTP OPO ($\theta=90^\circ$, $\phi=0^\circ$) (discussed in Chapter 2.4), we know $d_{\text{eff}}=7.6$ pm/V. We pump the KTP OPO with a Ti:sapphire laser having the following parameters:

- Center wavelength: 800 nm
- Repetition rate: 80 MHz
- Pulse duration: 100 fs
- Signal wavelength: 1141.4 nm (based on perfect phase matching)
- Idler wavelength: 2674.6 nm

Assuming a pump power of 1 W and beam diameter of 100 μm at the focus in the KTP crystal, the peak intensity of the pump pulse can be calculated:

$$I_0 = \frac{2P}{\pi w_0^2 \cdot R \cdot \tau} \approx 3.2 \text{ GW} / \text{cm}^2$$

where P is the pump power, w_0 is the radius of the pump beam at the focus, R is the repetition rate, and τ is the pulse duration. The amplitude of the electric field of the pump can be calculated by

$$|E_p| = \sqrt{\frac{I_0}{2\varepsilon_0 n c}} \approx 5.85 \times 10^7 \text{ V/m}$$

where $n=1.760$ is the refractive index of KTP at the pump wavelength, $c=2.997 \times 10^8$ m/s is the velocity of light in vacuum, and $\varepsilon_0=8.85 \times 10^{-12}$ F/m is the permittivity of free space. The refractive indices of KTP at the signal and idler wavelengths are 1.745 and 1.715, respectively.

We also assume that the amplitude of the intracavity signal wave has the same value as that of the pump wave, $|E_s|=5.85 \times 10^7$ V/m.

Substituting above parameters into the coupled equations and solving the equations numerically, we can get the intensities of the signal and the idler as well as the depleted pump versus the position in the KTP crystal (z). The results of the calculation are shown in Fig. 2.1.4.

It is obvious in Fig. 2.1.4 that the pump gets completely depleted at about $z = 0.6$ mm, where the signal and the idler reach their peak intensities. Thereafter, since no energy can be provided for the signal and the idler, their intensities decrease with increasing the crystal length, and energy is transferred from the signal and the idler back to the pump. This process will be repeated for further interactions if the crystal is sufficiently long. We only demonstrated an ideal case using the results in Fig. 2.1.4 for understanding the OPO process, since we did not consider influences from the phase mismatch, the group velocity mismatch (GVM) and group velocity dispersion (GVD), and we calculated only single-path interaction. The influences from GVM and GVD will be discussed in Chapter 2.4.

Please also refer to the references [31-34] for different methods of solving the coupled equations.

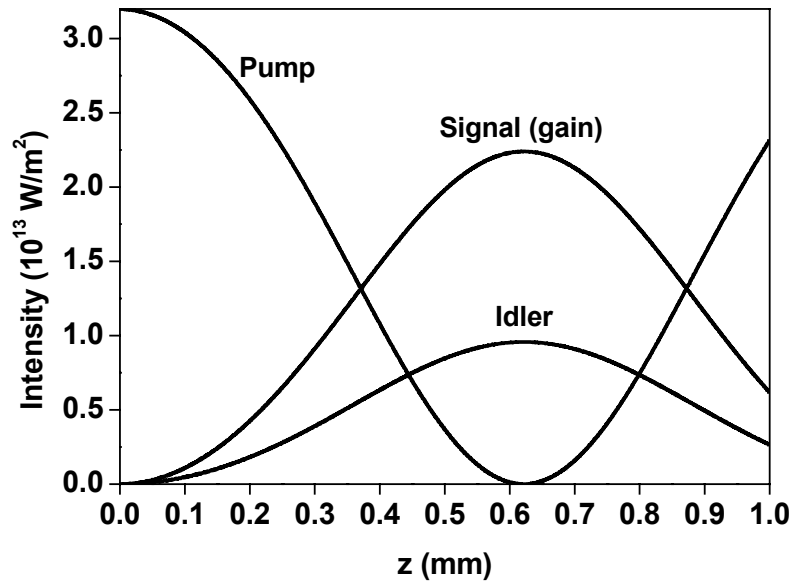


Fig. 2.1.4 A practical example of solving the coupling equations for perfect phase matching ($\Delta k=0$) with the pump depletion included. Dispersion of the material (GVM and GVD) was not considered.

2.1.4 Tuning methods of OPOs

Tunability is the most important characteristics of OPOs. Here we summarize the commonly employed methods for tuning the signal wavelength of a SPOPO. Detailed discussion and theoretical calculations will be given in the following chapters.

(1) Pump wavelength tuning

According to the phase-matching conditions of the OPOs based on birefringent or periodically poled crystals, the signal gains maximum amplification at perfect phase matching. Therefore, when the pump wavelength is changed, the signal wavelength has to change correspondingly to keep the perfect phase matching. Tuning the signal wavelength with varying pump wavelength is called “pump wavelength tuning” of an OPO. The tuning range depends mainly on the tuning range of the pump wavelength, phase-matching conditions for the specific nonlinear crystal, and the cavity bandwidth.

(2) Cavity length tuning

In synchronous pumping, the OPO must have the same cavity length as the pump laser, so that the signal pulse arrives simultaneously with the pump pulse at the crystal to get most efficient interaction. Because of dispersion of the nonlinear crystal, the signal will be delayed differently at different wavelengths. In other words, signal pulses have different round-trip times in the cavity at different center wavelengths. When the cavity length of the OPO is changed slightly, the signal has to change its wavelength to keep constant cavity length or constant round-trip time. Cavity length tuning can be achieved easily by tuning the voltage on a piezoelectric transducer (PZT) onto which one of the cavity mirrors is mounted. Therefore, this method is the most commonly and frequently used to tune the signal wavelength of a SPOPO. This is also the basis for stabilizing the operation of a SPOPO, when the change of the signal wavelength at the output is fed back to control the voltage on the PZT, forming a closed loop.

(3) Intracavity wavelength tuning elements

Inserting a wavelength selection element (such as a birefringent filter) into the OPO cavity or using a diffraction-grating [35] as one of the end mirrors can also be employed to tune the signal wavelength. When inserting a wavelength selection device, the dispersion of the inserted glass and transmission bandwidth must be considered in advance for femtosecond operation of the SPOPO.

(4) Grating period tuning

Grating period tuning applies only to quasi-phase-matched OPOs. According to the phase-matching conditions of QPM (discussed in Chapter 2.3), at a given pump wavelength, the signal wavelength is a function of the poling period.

(5) Temperature tuning

The refractive indices of nonlinear crystals are functions of temperature. Indices of some birefringent crystals, e.g., LBO, are very sensitive to the change of the ambient temperature. Temperature tuning can be used as the main tuning method for OPOs based on such crystals.

Based on the thermal expansion effect, the grating periods of periodically poled crystals for QPM OPOs are also functions of temperature. Changing the temperature also changes slightly the grating periods. So, for QPM OPOs, temperature tuning also

combines the effect of grating period tuning, resulting in larger tuning rates and larger tuning ranges.

Temperature tuning methods can be realized by mounting the crystal in an oven and controlling its temperature.

(6) Angle tuning

Angle tuning methods applies mainly to birefringently and critically phase-matched OPOs. [36] At a given pump wavelength, the signal wavelength corresponds to a specific phase-matching angle. Changing the phase-matching angle tunes the signal wavelength to the value of perfect phase matching. Obviously, angle tuning is much more complicated, and also experimentally more challenging due to the intracavity beam displacement when rotating the crystal than other methods; therefore it is less commonly used.

2.2

Birefringent phase matching (BPM) and tuning characteristics of BPM OPO

2.2.1 Birefringent phase matching methods

In three - wave nonlinear processes (SHG, SFG, DFG), useful output power levels are obtained only when a fixed phase relationship is maintained between input and output beams as they travel through the crystal. The process used to maintain this relationship is called phase matching [1]. The phase matching process can most easily be understood by considering the interaction to occur between an optical wave and an identical nonlinear polarization source wave at the same frequency, where the polarization wave is generated by two other optical waves at different frequencies. As long as the optical wave and the source nonlinear polarization travel with the appropriate relative phase, energy is transferred constructively into the optical wave. If the optical wave and the source polarization travel at different phase velocities, the efficiency of the interaction is reduced as energy is transferred alternatively from the polarization wave to the optical wave, then back to the polarization wave while they propagate through the nonlinear medium. The distance over which maximum transfer of energy occurs between the polarization wave and the optical wave is the coherence length for the interaction. [29]

Birefringent phase matching is a conventional and most important phase-matching technique. The basic idea of BPM is that the interaction waves of different frequencies are polarized differently, so that their corresponding phase velocities can be adjusted and their wave vectors can satisfy the phase matching conditions.

Before introducing these phase-matching methods in detail, we need to explain some important and commonly applied terminologies in phase matching:

(I) Uniaxial and biaxial crystals

In uniaxial crystals, there is a single axis of symmetry, commonly designated the Z-axis, which coincides with the principal optical axis. This principal optical axis is defined as the one where both polarizations propagate at the same group velocity. Thus the principal refractive indices are $n_x=n_y=n^o$ and $n_z=n^e$. When $n^o < n^e$, the crystal is called a positive uniaxial crystal, as shown in Fig. 2.2.1. It is called a negative

uniaxial crystal when $n^o > n^e$. For a propagation at an angle θ with respect to the Z-axis, the extraordinary waves has an index given by:

$$\frac{1}{[n^e(\theta)]^2} = \frac{\cos^2 \theta}{[n^o]^2} + \frac{\sin^2 \theta}{[n^e]^2} \quad (2.2.1)$$

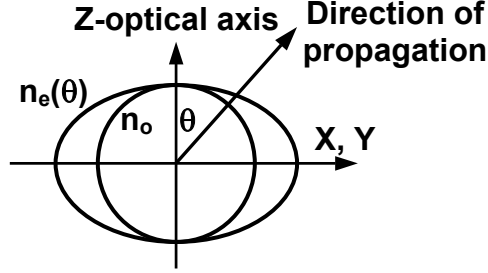


Fig. 2.2.1 Uniaxial crystal.

In biaxial crystals, there are two optical axes, which by convention are taken to lie in the XZ plane (see Fig. 2.2.2). The optic axes make an angle Ω with respect to the Z-axis, given by

$$\sin \Omega = \frac{n_z}{n_y} \left(\frac{n_y^2 - n_x^2}{n_z^2 - n_x^2} \right)^{1/2} \quad (2.2.2)$$

and are situated symmetrically about the Z-axis. It is also convention to take $n_z > n_y > n_x$. For light propagating along the optic axes, the refractive index is independent of polarization. The general case of propagation at an angle θ with respect to the Z-axis and an azimuthal angle ϕ with respect to the X-axis is desired for phase matching. The refractive indices of the two allowed modes of propagation are determined by solving the Fresnel equation:

$$\frac{\sin^2 \theta \cos^2 \phi}{n^{-2} - n_x^{-2}} + \frac{\sin^2 \theta \sin^2 \phi}{n^{-2} - n_y^{-2}} + \frac{\cos^2 \theta}{n^{-2} - n_z^{-2}} = 0 \quad (2.2.3).$$

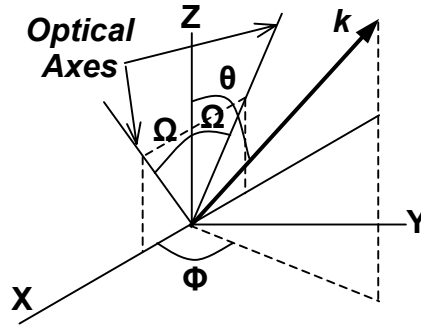


Fig. 2.2.2 Coordinate system for a biaxial crystal.

(II) Ordinary and extraordinary indices

In anisotropic materials there are two normal modes of propagation for each frequency. These waves are orthogonally polarized and travel at different phase velocities. In uniaxial crystals, for example, one of these waves, called the ordinary wave, sees a constant index of refraction independent of its direction of propagation. This is called the ordinary index n^o . The second wave, called the extraordinary wave, sees a refractive index $n^e(\theta)$ which is dependent on its direction of propagation. The angle θ describes the direction of propagation relative to one of the principal axes of the medium.

(III) Type I and type II phase matching:

For OPO, type I phase matching refers to the situation where the signal and the idler waves have the same polarization. In type II phase matching, the signal and the idler have orthogonal polarizations.

For SHG, there is only one pump. In type I phase-matching, the pump is either ordinary or extraordinary wave (e.g., ee \rightarrow o or oo \rightarrow e). In type II phase matching, the pump is polarized so that one of its orthogonal components is ordinary and the other is extraordinary (e.g., eo \rightarrow e or oe \rightarrow o).

(IV) Critical and noncritical phase matching

The situation where the phase-matching angle θ_{pm} is 90^0 is referred to as noncritical phase matching (NCPM), while the case of $\theta_{pm} \neq 90^0$ is called critical phase matching (CPM).

Noncritical phase matching is advantageous over critical phase matching for two reasons. First, it is less sensitive to beam divergence, which lowers the conversion efficiency. Second, the walk-off angle for this case is zero, which places less constraint on the beam size and the crystal length.

The phase matching conditions for SHG, SFG, and OPO processes can be given as:

$$\text{SHG: } 2\vec{k}_\omega = \vec{k}_{2\omega}$$

$$\text{SFG: } \vec{k}_{p_1+p_2} - \vec{k}_{p_1} - \vec{k}_{p_2} = 0$$

$$\text{OPO: } \vec{k}_p - \vec{k}_s - \vec{k}_l = 0$$

For collinear propagation, they reduce to:

$$\text{SHG: } n_{\omega} = n_{2\omega} \text{ or } n_{\lambda} = n_{\lambda/2} \quad (2.2.4)$$

$$\text{SFG: } (\omega_{p1} + \omega_{p2})n_{p1+p2} - \omega_{p1}n_{p1} - \omega_{p2}n_{p2} = 0 \quad (2.2.5)$$

$$\text{OPO: } \omega_p n_p - \omega_s n_s - \omega_i n_i = 0 \text{ or } \frac{n_p}{\lambda_p} - \frac{n_s}{\lambda_s} - \frac{n_i}{\lambda_i} = 0 \quad (2.2.6)$$

where \vec{k} is the wave vector and the footnotes P, S, I denote the pump, the signal, and the idler, respectively.

At the same time, the energy conservation condition should also be considered, e.g., for an OPO:

$$\omega_p = \omega_s + \omega_i \text{ or } \frac{1}{\lambda_p} = \frac{1}{\lambda_s} + \frac{1}{\lambda_i} \quad (2.2.7)$$

Using formulas (2.2.6) and (2.2.7), one can obtain the pump tuning characteristics (signal or idler wavelength versus pump wavelength) of an OPO.

There are multiple BPM methods, including scalar angle phase matching, vector angle phase matching, temperature phase matching [1]. In the following, we will mainly talk about the scalar angle phase matching method.

The task of angle phase matching is to find the phase matching angle (θ_{pm}) for a desired frequency conversion process and parameters of given interaction waves. Next, we discuss the calculation of the phase matching angles in uniaxial and biaxial crystals.

A. Phase matching angles for uniaxial crystals (e.g., BBO, LiNbO₃)

First, we need to determine which type of phase matching will be adopted, type I or type II.

Second, we solve the equation (2.2.1) in conjunction with one of (2.2.4), (2.2.5), and (2.2.6) for different processes. The energy conservation condition should also be considered. Then the phase matching angle can be obtained.

The formulas for phase-matching angles for SHG and SFG processes in uniaxial crystals are given in Table 2.2.1 and Table 2.2.2 [1], respectively. In the formulas, o means the ordinary wave, e means the extraordinary wave, ω means the fundamental wave and 2ω means the SHG wave. In Table 2.2.2, $p1$ and $p2$ denote the first and the second pump waves, s denotes the sum frequency wave.

2.2.1 Birefringent phase matching methods

For the OPO process, we just need to change the subscripts in the formulas in table 2.2.2: $s \rightarrow P, p1 \rightarrow S, p2 \rightarrow I$, where P, S, I stand for the pump, the signal, and the idler in the OPO process.

Table 2.2.1 Angles phase matching formulas for SHG in uniaxial crystals

Type I

oo \rightarrow e

$$\sin^2 \theta_{pm} = \frac{(n_{2\omega}^e)^2}{(n_{\omega}^o)^2} \left[\frac{(n_{2\omega}^o)^2 - (n_{\omega}^o)^2}{(n_{2\omega}^o)^2 - (n_{2\omega}^e)^2} \right] \quad (2.2.8)$$

ee \rightarrow o

$$\sin^2 \theta_{pm} = \frac{(n_{\omega}^e)^2}{(n_{2\omega}^o)^2} \left[\frac{(n_{2\omega}^o)^2 - (n_{\omega}^o)^2}{(n_{\omega}^e)^2 - (n_{\omega}^o)^2} \right] \quad (2.2.9)$$

Type II

oe \rightarrow e or eo \rightarrow e

$$\frac{n_{2\omega}^o}{\sqrt{1 + \left[\frac{(n_{2\omega}^o)^2}{(n_{2\omega}^e)^2} - 1 \right] \sin^2 \theta_{pm}}} - \frac{\frac{1}{2} n_{\omega}^o}{\sqrt{1 + \left[\frac{(n_{\omega}^o)^2}{(n_{\omega}^e)^2} - 1 \right] \sin^2 \theta_{pm}}} = \frac{1}{2} n_{\omega}^o \quad (2.2.10)$$

eo \rightarrow o or oe \rightarrow o

$$\sin^2 \theta_{pm} = \frac{4n_{2\omega}^o (n_{\omega}^e)^2 (n_{2\omega}^o - n_{\omega}^o)}{(2n_{2\omega}^o - n_{\omega}^o)^2 [(n_{\omega}^e)^2 - (n_{\omega}^o)^2]} \quad (2.2.11)$$

Table 2.2.2 Angle phase matching formulas for SFG in uniaxial crystals

Type I

oo \rightarrow e

$$\sin^2 \theta_{pm} = \frac{(n_s^e)^2}{\left[(\lambda_s / \lambda_{p1}) n_{p1}^o + (\lambda_s / \lambda_{p2}) n_{p2}^o \right]^2} \left[\frac{(n_s^o)^2 - \left[(\lambda_s / \lambda_{p1}) n_{p1}^o + (\lambda_s / \lambda_{p2}) n_{p2}^o \right]^2}{(n_s^o)^2 - (n_s^e)^2} \right] \quad (2.2.12)$$

ee \rightarrow o

$$\frac{(\lambda_s / \lambda_{p1}) n_{p1}^o}{\sqrt{1 + \left[\frac{(n_{p1}^o)^2}{(n_{p1}^e)^2} - 1 \right] \sin^2 \theta_{pm}}} + \frac{(\lambda_s / \lambda_{p2}) n_{p2}^o}{\sqrt{1 + \left[\frac{(n_{p2}^o)^2}{(n_{p2}^e)^2} - 1 \right] \sin^2 \theta_{pm}}} = n_s^o \quad (2.2.13)$$

Table 2.2.2 (continued)

Type II

oe→e

$$\frac{n_s^o}{\sqrt{1 + \left[\frac{(n_s^o)^2}{(n_s^e)^2} - 1 \right] \sin^2 \theta_{pm}}} - \frac{(\lambda_s / \lambda_{p2}) n_{p2}^o}{\sqrt{1 + \left[\frac{(n_{p2}^o)^2}{(n_{p2}^e)^2} - 1 \right] \sin^2 \theta_{pm}}} = (\lambda_s / \lambda_{p1}) n_{p1}^o \quad (2.2.14)$$

eo→e

$$\frac{n_s^o}{\sqrt{1 + \left[\frac{(n_s^o)^2}{(n_s^e)^2} - 1 \right] \sin^2 \theta_{pm}}} - \frac{(\lambda_s / \lambda_{p1}) n_{p1}^o}{\sqrt{1 + \left[\frac{(n_{p1}^o)^2}{(n_{p1}^e)^2} - 1 \right] \sin^2 \theta_{pm}}} = (\lambda_s / \lambda_{p2}) n_{p2}^o \quad (2.2.15)$$

eo→o

$$\sin^2 \theta_{pm} = \frac{(n_{p1}^e)^2}{(n_{p1}^e)^2 - (n_{p1}^o)^2} \frac{[n_s^o - (\lambda_s / \lambda_{p2}) n_{p2}^o]^2 - (\lambda_s / \lambda_{p1})^2 (n_{p1}^o)^2}{[n_s^o - (\lambda_s / \lambda_{p2}) n_{p2}^o]^2} \quad (2.2.16)$$

oe→o

$$\sin^2 \theta_{pm} = \frac{(n_{p2}^e)^2}{(n_{p2}^e)^2 - (n_{p2}^o)^2} \frac{[n_s^o - (\lambda_s / \lambda_{p1}) n_{p1}^o]^2 - (\lambda_s / \lambda_{p2})^2 (n_{p2}^o)^2}{[n_s^o - (\lambda_s / \lambda_{p1}) n_{p1}^o]^2} \quad (2.2.17)$$

Here we give an example to calculate the phase matching angle in a BBO crystal for the doubling of the pump wave at 1200 nm.

We employ type I phase matching. There will be two possibilities: ee→o and oo→e.

For the case of (ee→o), the pump beam (at 1200 nm) will be an extraordinary wave and the SHG will be an ordinary wave. Using the Sellmeier equations given in appendix A, we can find that the BBO crystal is a negative uniaxial crystal, meaning $n^e < n^o$ and $n^e \leq n^e(\theta) \leq n^o$. Consequently the phase matching condition for (ee→o), $n^e(\theta, 1200 \text{ nm}) = n^o(600 \text{ nm})$, cannot be satisfied.

Therefore, we have to use the configuration of (oo→e). The pump beam will be used as an ordinary wave and the doubled wave will be an extraordinary wave. Using the Sellmeier equations of BBO, we calculate the ordinary and extraordinary indices, $n^o(1200 \text{ nm}) = 1.65247$, $n^o(600 \text{ nm}) = 1.66948$, $n^e(600 \text{ nm}) = 1.55142$. Substituting these values into formula (2.2.8), the phase matching angle can be calculated to be 21.22° .

From the formulas given in Table 2.2.1 and Table 2.2.2, it can be found that sometimes no analytical solutions can be obtained, then we have to use numerical methods.

B. Phase matching angles for biaxial crystals (e.g., LBO, KTP)

To find the phase matching angle in biaxial crystals, we need to solve the Fresnel equation given in (2.2.3) in conjunction with (2.2.4), (2.2.5), or (2.2.6) for different frequency conversion processes. The energy conservation condition should also be considered.

In biaxial crystals, the two independent solutions to the Fresnel equation correspond to the refractive indices of two orthogonal modes of propagation in a particular direction (θ, ϕ) . Generally, the designations of ordinary and extraordinary do not apply, except for propagation in the principal planes. However, it is still possible to define type I phase matching as parallel pump polarizations, and type II phase matching as orthogonal pump polarizations.

Because solving the Fresnel equation to find the phase matching angle for biaxial crystals is quite complicated, we will not discuss it here in detail. Please refer to [1, 37, 38] in the literature for a detailed discussion. For simplicity, we will discuss only the NCPM cases in biaxial crystals and take the KTP crystal as an example to explain the BPM technique for OPO process in subsections 2.2.3, 2.2.4, and 2.2.5. At the end of this chapter we will describe briefly temperature phase matching of an LBO OPO.

2.2.2 Phase matching bandwidth for OPO processes

A finite phase mismatch in the parametric fluorescence process is due to two sources [1]: (1) a finite input bandwidth of frequencies $\Delta\omega = -(\omega_I - \omega_0) = \omega_S - \omega_{S0}$, where the subscript 0 refers to that frequency for which there is perfect phase matching; (2) an angular spread in the signal and idler wave vectors as shown in Fig. 2.2.3.

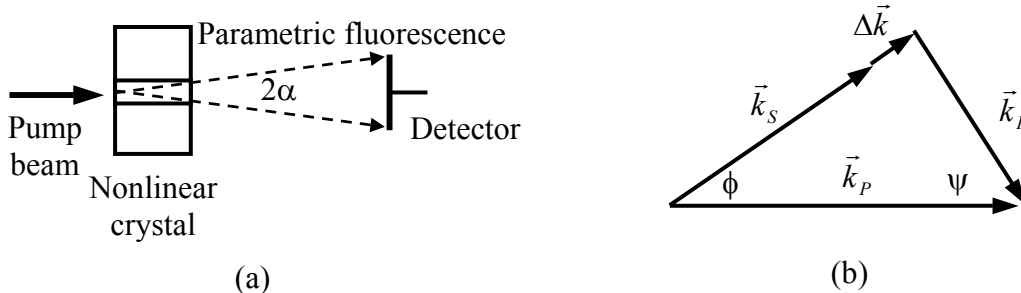


Fig. 2.2.3 Optical parametric generation and signal power collection geometry.

To calculate the phase matching bandwidth, we start with the formula of the phase mismatch amount for the OPO process

$$\Delta k = k_p - k_s - k_l = \frac{n_p \omega_p}{c} - \frac{n_s \omega_s}{c} - \frac{n_l \omega_l}{c} \quad (2.2.18)$$

where c is the light velocity in vacuum.

Suppose the central frequency of the signal is ω_{0s} and there is a shift of $\Delta\omega_s$ from ω_{0s} within the signal bandwidth. According to the energy conservation condition, $\omega_p = (\omega_{0s} + \Delta\omega_s) + (\omega_{0l} - \Delta\omega_l)$, where $\Delta\omega_l$ is the shift from central frequency of the idler (ω_{0l}) within the idler bandwidth. However, since $\omega_p = \omega_{0s} + \omega_{0l}$, we can conclude that $\Delta\omega_s = \Delta\omega_l = \Delta\omega$. After such a shift of the signal (idler) frequency, the formula for phase mismatch can be rewritten as

$$\begin{aligned} \Delta k &= \frac{n_p \omega_p}{c} - \frac{\left(n_s + \frac{dn_s}{d\omega_s} \Delta\omega \right) (\omega_s + \Delta\omega)}{c} - \frac{\left(n_l - \frac{dn_l}{d\omega_l} \Delta\omega \right) (\omega_l - \Delta\omega)}{c} \\ &= \frac{(n_p \omega_p - n_s \omega_s - n_l \omega_l) - \left[\left(n_s + \frac{dn_s}{d\omega_s} (\omega_s + \Delta\omega) \right) - \left(n_l - \frac{dn_l}{d\omega_l} (\omega_l - \Delta\omega) \right) \right] \Delta\omega}{c} \\ &= - \left(\left. \frac{dk_s}{d\omega_s} \right|_{\omega_s = \omega_{0s}} - \left. \frac{dk_l}{d\omega_l} \right|_{\omega_l = \omega_{0l}} \right) \Delta\omega \\ &= -b \Delta\omega \quad (2.2.19) \end{aligned}$$

Inbetween it was already considered that $n_p \omega_p - n_s \omega_s - n_l \omega_l = 0$ for perfect phase matching and $\frac{dk}{d\omega} = \frac{d}{d\omega} \left(\frac{n\omega}{c} \right) = \frac{n + \frac{dn}{d\omega} \omega}{c}$ with $\Delta\omega \ll \omega_s, \Delta\omega \ll \omega_l$, and let

$$b = \left. \frac{dk_s}{d\omega_s} \right|_{\omega_s = \omega_{0s}} - \left. \frac{dk_l}{d\omega_l} \right|_{\omega_l = \omega_{0l}}$$

According to the analysis in Chapter 2.1, the small gain approximation of one-pass gain of the signal wave is a sinc^2 function, which is defined as:

$$G \approx (gL)^2 \frac{\sin^2(\Delta k L / 2)}{(\Delta k L / 2)^2} = (gL)^2 \text{sinc}^2(\Delta k L / 2) \quad (2.2.20)$$

where L should be the effective interaction length between the engaged waves.

We also define that the signal bandwidth for perfect phase matching in terms of the FWHM of the sinc^2 curves, corresponding to $\Delta kL/2 \approx 0.443\pi$. Therefore, the bandwidth of the generated signal wave by a single pump wavelength can be calculated by

$$\Delta\omega = \frac{0.886\pi}{|b|L} \quad (2.2.21)$$

The signal bandwidth is more frequently described in terms of wavelength. Then the above formula can be converted to

$$\Delta\lambda \approx \frac{\lambda_s^2}{L \left[\left(n_s - \lambda_s \frac{dn_s}{d\lambda_s} \Big|_{\lambda_s=\lambda_{s0}} \right) - \left(n_l - \lambda_l \frac{dn_l}{d\lambda_l} \Big|_{\lambda_l=\lambda_{l0}} \right) \right]} \quad (2.2.22)$$

In fact, the pump wave has its own bandwidth, so that each spectral component excites a signal with certain bandwidth. Consequently, the resultant signal bandwidth should be the overlap of all of these sub-generations. The pump threshold is another important factor limiting the signal bandwidth that can be excited by a pump spectrum with specific shape, bandwidth, and intensity.

2.2.3 The KTP (KTiOPO₄) crystal

KTP [38], or Potassium Titanyl Phosphate, is an outstanding crystal for many applications in nonlinear optics and electrooptics. Its large optical nonlinearity (see Table 2.2.3), high optical damage threshold (10 GW/cm², 560 nm, 30 ps, 10 Hz), wide acceptance angle, low insertion loss ($\alpha < 1\%$) and thermal stable phase-matching properties make KTP particularly suitable for frequency doubling of infrared lasers operating near 1 μm (e.g. Nd lasers) and for OPOs. Additionally, large linear electro-optic r coefficients and low dielectric constants make it attractive for electro-optic applications, such as modulators and Q-switches.

The KTP crystal is a colorless orthorhombic biaxial nonlinear optical crystal belonging to the $mm2$ symmetry class. The transparency range of KTP is from 0.35 μm to 4.5 μm . The morphology of natural KTP crystals is shown in Fig. 2.2.4. [38]

KTP decomposes on melting ($\sim 1150^\circ\text{C}$), and hence normal melt processes cannot be used to grow this material. Two techniques can be employed to grow large single KTP crystals: hydrothermal and flux techniques. [38]

Hydrothermally grown KTP crystals normally have low concentration of vacancies and defects, implying high damage threshold and low conductivity. Therefore, such

crystals are also appropriate for periodically poling. However, high temperature and high pressure are required by this technique, and the growing process is slow and complicated, leading to high costs and limited sizes of the KTP crystals.

The flux technique is essentially a high-temperature solution growth technique in which the KTP crystallizes out of a molten KTP/flux composition when cooled. [38] A significant advantage of flux technique is that it operates at atmospheric pressures and hence does not require sophisticated pressure equipment. However, uniform temperatures and high levels of temperature control are required. Flux growing technique is well established and the KTP crystals can be grown in large sizes with good homogeneity. Price of flux grown KTP crystals is also acceptable. But this kind of KTP has high vacancy concentration, leading to its sensitivity to photorefractive damage (“grey tracking”) and a high mobility of the K^+ ions in the lattice. The high ionic conductivity causes difficulties in electrical poling technique. The conductivity of flux-grown KTP crystals has to be reduced if they are to be poled electrically. [39]

The linear-, nonlinear-, and electro-optical properties of KTP crystal grown by the flux and hydrothermal techniques are similar, though some differences between them have been observed in some of the dielectric properties and in the high-power optical damage characteristics.

The one-pole Sellmeier equations of KTP crystal is as given in Appendix A.

Table 2.2.3 *Nonlinear-optical coefficients of KTP near 1 μ m*

d_{31}	d_{32}	d_{33}	d_{24}	d_{15}
6.5 pm/V	5.0 pm/V	13.7 pm/V	7.6 pm/V	6.1 pm/V

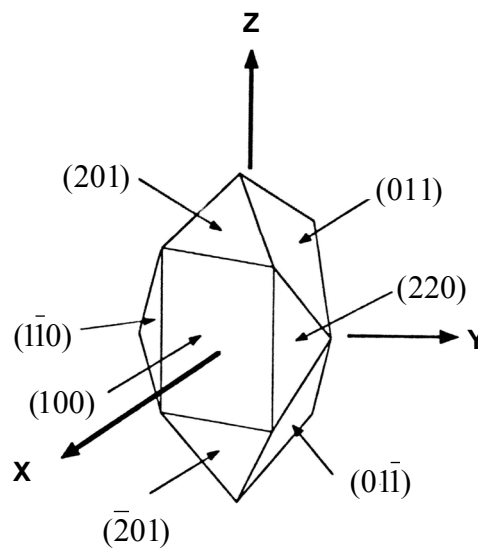


Fig. 2.2.4 *Natural KTP crystal morphology.*[38]

2.2.4 Noncritical phase matching (NCPM) of a KTP OPO

There are three possibilities of NCPM in biaxial crystals, with the crystal cut in the Y - Z plane (X -cut), in the X - Z plane (Y -cut), and in the X - Y plane (Z -cut).

First, we give the effective nonlinear susceptibility (d_{eff}) of biaxial crystals for the propagation in the principal plane under Kleinman symmetry [1], as shown in Table 2.2.4, so that we can compare the efficiencies of the OPO process under different configurations of phase matching.

Table 2.2.4 Formulas for d_{eff} of biaxial crystals under Kleinman Symmetry ($d_{24}=7.6\text{pm/V}$ and $d_{15}=6.1\text{pm/V}$ for KTP crystal)[38]

Crytal class	Principal plane	ooe, oeo, eoo	eeo, eoe, oee
$mm2$	XY	0	$d_{15}\sin^2\phi + d_{24}\cos^2\phi$
	YZ	$d_{15}\sin\theta$	0
	XZ	$d_{24}\sin\theta$	0

In table 2.2.4, θ is the angle between the direction of propagation and the Z -axis, ϕ is the angle between the projection of the wave vector onto the X - Y plane and the X -axis.

Theoretical analysis found that for Ti:sapphire laser pumped KTP OPOs (pump wavelength from about 700 nm to 900 nm), type-I NCPM processes are prohibited, and only two type-II NCPM processes are possible when cutting the crystals in the Y - Z and X - Z planes, respectively.

A. NCPM for a X -cut biaxial crystal (KTP)

The crystal will be cut in the plane perpendicular to the X -axis, namely in the Y - Z plane. All of the interaction waves will propagate in the direction of X -axis, meaning $\theta = 90^\circ$ and $\phi = 0^\circ$, so that the phase matching will be achieved in the X - Z plane. Consequently d_{eff} is equal to d_{24} . In this case, the type II NCPM process can be achieved only when the pump and the signal are polarized in Y direction and the idler is polarized in Z direction, as illustrated in Fig. 2.2.5. Therefore the phase matching condition can be written as:

$$\frac{n_Y}{\lambda_p} - \frac{n_Y}{\lambda_s} - \frac{n_Z}{\lambda_I} = 0$$

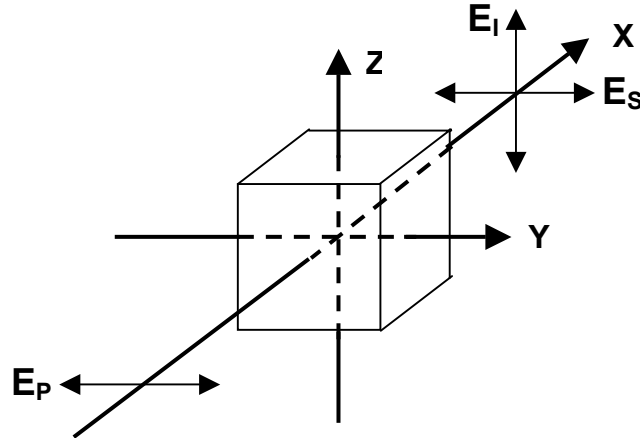


Fig. 2.2.5 Type II noncritical phase matching for the OPO process in the X-Z plane of a biaxial crystal.

B. NCPM in a Y-cut biaxial crystal (KTP)

In this case, the crystal will be cut in the X-Z plane and the noncritical phase matching will be achieved in the Y-Z plane. The advantage of this configuration is the slightly shorter signal wavelength when pumping with a Ti:sapphire laser at 800 nm if compared with the X-cut configuration. The pump, the signal and the idler will propagate in the direction of Y-axis, meaning $\theta=90^\circ$ and $\phi=90^\circ$. In this case, the type II NCPM process can be achieved only when the pump and the signal are polarized in X direction and the idler is polarized in Z direction, as illustrated in Fig. 2.2.6. The effective nonlinear coefficient (d_{eff}) becomes d_{15} , which is smaller than that for the NCPM in X-Z plane. The phase matching conditions can be written as:

$$\frac{n_X}{\lambda_P} - \frac{n_X}{\lambda_S} - \frac{n_Z}{\lambda_I} = 0$$

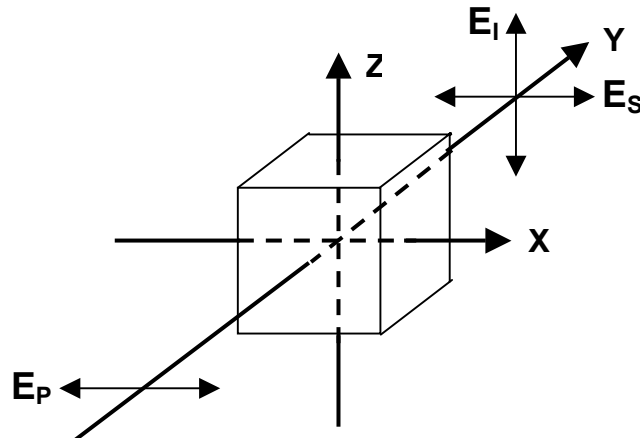


Fig. 2.2.6 Type-II noncritical phase matching for the OPO process in the Y-Z plane of a biaxial crystal.

2.2.5 Tuning characteristics of a noncritically phase-matched KTP OPO

As long as the phase matching configuration (cutting angles of the crystal, type I or type II phase matching, polarization of the pump beam) is determined, the tuning of the signal wavelength versus pump wavelength will be fixed. The tuning curves can be calculated by solving the equation of the phase matching condition in conjunction with the energy conservation condition.

We show the tuning characteristics of the signal and idler wavelengths in Fig. 2.2.7.

As already discussed above, the OPO process that is phase matched in the X - Z plane is more efficient than that phase matched in the Y - Z plane, the ratio between the efficiencies of these two processes is $(7.6/6.1)^2 \approx 1.55$. Therefore the X -cut configuration is mostly employed for a KTP OPO. However, there is a shift of about 50 nm between the tuning curves of the signal wavelength for the phase matching in the X - Z plane and in the Y - Z plane. For the first case, it is almost not possible to tune the signal to a shorter wavelength than 1050 nm. For applications using KTP OPO as the laser source and using relatively shorter signal wavelength (e.g., around 1050 nm), the phase matching in the Y - Z plane is more suitable.

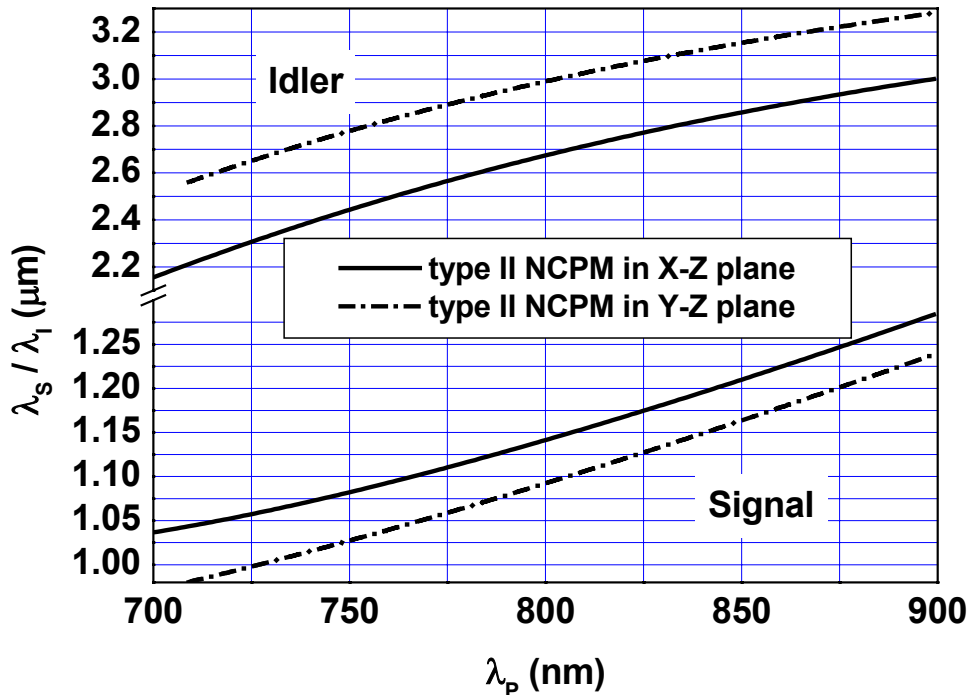


Fig. 2.2.7 Tuning characteristics of the signal (λ_s) and idler (λ_i) wavelengths versus pump wavelength (λ_p) of a type II noncritically phase-matched KTP OPO.

2.2.6 Temperature phase matching: LBO OPO

LBO (lithium triborate, LiB_3O_5) is a biaxial crystal, which was discovered by Chen et al. [40] shortly after the discovery of the BBO crystal [41]. Because of its excellent nonlinear optical properties, LBO is a very attractive material for pulsed optical parametric oscillators and amplifiers [42]. LBO has a short wavelength transmission limit of 160 nm, making it extremely suitable for applications in the UV. Because of its sensitive thermal dependence [43, 44] of the principal refractive indices, LBO has a wide temperature tunability, which is also the most important feature of it. OPOs based on LBO reported so far covered the spectral range from 306 nm to 2500 nm for temperature tuning from room temperature (20°C) to 200°C. Ruffing et al. [45] demonstrated a high power picosecond LBO OPO tunable in the blue spectral range (457 ~ 479 nm), which operated with a conversion efficiency of 74% (signal + idler) under a pump power of 9 W at 355 nm. J. D. Kafka et al. [46] reported a 40-fs LBO OPO pumped by a cw mode-locked Ti:sapphire laser, which generated up to 400 mW average signal power tunable from 1.1 to 1.6 μm using 2 W pump power.

Although LBO has a moderate nonlinear coefficient (~ 1 pm/V), it offers several major advantages: (1) non-critical phase matching provides a collinear pump and signal geometry that facilitates the initial alignment procedure, and there is no walk-off between the pump and signal beams, meaning a longer interaction length and higher gain; (2) LBO exhibits lower group velocity mismatch, allowing longer crystals for higher gain; (3) it has a low GVD, sub-130 fs pulses can be achieved without intracavity dispersion compensation; (4) a LBO OPO can be easily tuned through changing the temperature; (5) it has a wide transparency range (0.16~2.6 μm), a large birefringence, which is applicable for the generation of radiation tunable from the near UV to the near IR; (6) the surface-damage threshold of LBO is the highest of any NLO crystal measured so far.

In this chapter, we will describe mainly type I noncritical phase matching of an LBO OPO pumped by a Ti:sapphire laser and its temperature tuning characteristics.

For a Ti:sapphire laser pumped LBO OPO, there are two possibilities for type II NCPM with: P-SI (Pump-Signal, Idler): X-XZ (X-ZX), X-XY (X-YX). In one configuration, the pump and the signal (idler) are polarized in the direction of X-axis, the idler (signal) is polarized in the direction of Z-axis; in the other configuration, the pump and the signal (idler) are polarized in the direction of X-axis, the idler (signal) is

polarized in the direction of Y-axis. For type I phase matching, there is only one possibility: P-SI: Y-ZZ; the pump is polarized in the direction of Y-axis, while the idler is polarized in the direction of Z-axis, as shown in Fig. 2.2.8.

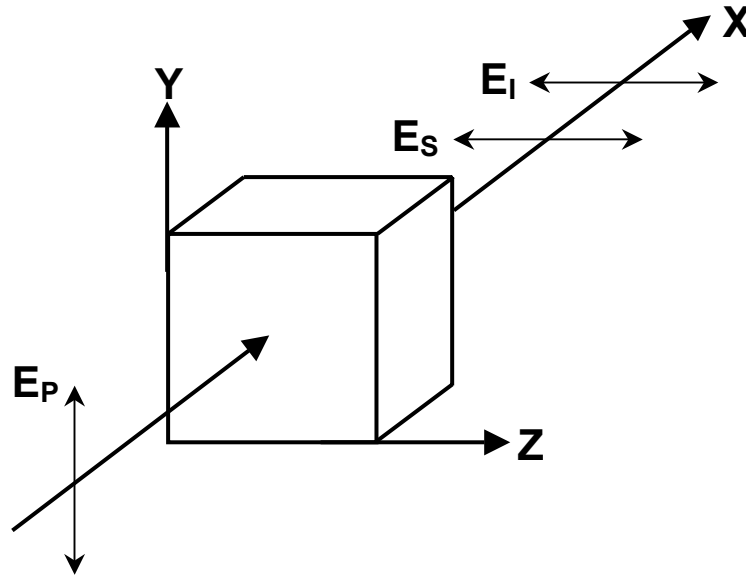


Fig. 2.2.8 Type I noncritical phase matching of LBO OPO.

To predict the phase matching temperature accurately, we need the precise Sellmeier equations and thermal dependence of the refractive indices of LBO. Here we use the Sellmeier equations given by Velsko et al. [43] and the dependence of the refractive indices on the temperature given by Tang et al. [44]:

$$n^2 = A + \frac{B}{\lambda^2 + C} + D\lambda^2$$

	A	B	C	D
n_X	2.4543	1.1413×10^{-2}	-9.4981×10^{-3}	-1.3900×10^{-2}
n_Y	2.5382	1.2830×10^{-2}	-1.1387×10^{-2}	-1.7034×10^{-2}
n_Z	2.5854	1.3065×10^{-2}	-1.1617×10^{-2}	-1.8146×10^{-2}

$$\frac{dn_x}{dT} = -2.0342 \times 10^{-7} - 1.9697 \times 10^{-8} T - 1.4415 \times 10^{-11} T^2$$

$$\frac{dn_y}{dT} = -1.0748 \times 10^{-5} - 7.1034 \times 10^{-8} T - 5.7387 \times 10^{-11} T^2$$

$$\frac{dn_z}{dT} = -8.5998 \times 10^{-7} - 1.5476 \times 10^{-7} T + 9.4675 \times 10^{-10} T^2 - 2.2375 \times 10^{-12} T^3$$

By the integration

$$n = n_0 + \int_{T_0}^T \frac{dn}{dT} dT, \quad T_0 = 20^\circ\text{C},$$

we can calculate the temperature dependent refractive indices of LBO. Then using the phase matching condition:

$$\Delta k(T) = 2\pi \left(\frac{n_p(T)}{\lambda_p} - \frac{n_s(T)}{\lambda_s} - \frac{n_l(T)}{\lambda_l} \right) = 0 \quad \text{with} \quad \frac{1}{\lambda_p} = \frac{1}{\lambda_s} + \frac{1}{\lambda_l},$$

we can calculate the temperature tuning characteristics of a LBO OPO.

Figure 2.2.9 demonstrates the temperature tuning characteristics of a type-I NCPM LBO OPO pumped at 775 nm and at 810 nm. The expected signal tuning ranges are from 1.18 μm to 1.55 μm , and from 1.35 μm to 1.6 μm , respectively.

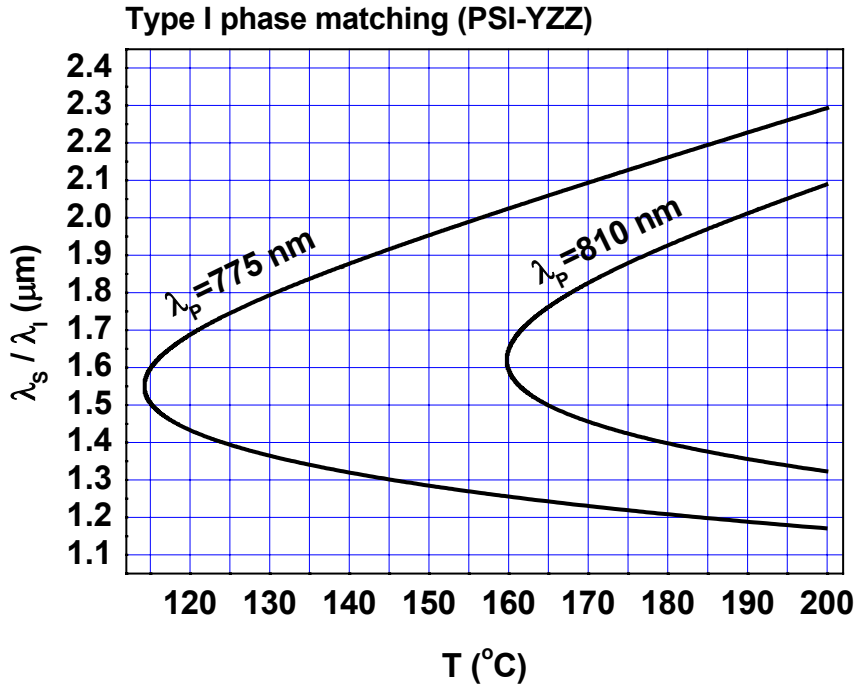


Fig. 2.2.9 Temperature tuning of a type I NCPM LBO OPO pumped at 775 nm.

2.3

Quasi-phase matching (QPM) and tuning characteristics of QPM OPOs

2.3.1 Quasi-phase matching

Quasi-phase matching is an alternative technique to birefringent phase matching for compensating phase velocity dispersion in frequency-conversion applications.

In birefringent phase matching, many desirable OPO implementations are limited by problems occurring in this method, such as Poynting-vector walk-off, low effective nonlinear coefficient, and inconvenient phase-matching temperatures and angles [6]. In addition, in birefringent phase matching the range of the wavelengths over which a particular crystal can be used is determined by the dispersion of the indices of refraction for light polarized along the principal axes and by the second-order nonlinear susceptibility tensor. Nonlinear optical coefficients derived from this tensor relate the magnitude of the nonlinear response in a designated crystallographic direction to inputs of specified polarizations. Efficient nonlinear conversion requires not only that the phase-matching conditions be satisfied for the wavelengths of interests, but also that the nonlinear optical coefficient corresponding to the chosen polarization directions be large. [1]

However, in a first-order quasi-phase-matched device, the nonlinear coefficient is modulated with a period twice the coherence length of the interaction to offset the accumulated phase mismatch. A significant advantage of quasi-phase matching is that any interaction within the transparency range of the material can be noncritically phase matched at a specific temperature, even interactions for which birefringent phase matching is impossible [6]. Another benefit is that the interacting waves can be chosen so that coupling occurs through the largest element of the $\chi^{(2)}$ tensor. For example, the large nonlinearity and noncritical phase-matching capabilities of periodically poled lithium niobate (PPLN) have permitted the exploitation of its high parametric gain to generate wavelengths in the mid-IR region. In an OPO configuration, one can reach the largest nonlinear coefficient in PPLN (d_{33}) by polarizing the pump, signal, and idler waves parallel to the z axis ($e \rightarrow e+e$), yielding a

gain enhancement over the birefringently phase-matched process of $\left(\frac{2 d_{33}}{\pi d_{31}}\right)^2 \approx 20$

[6], and it is also broadly tunable, from approximately 0.95 to 5.4 μm , and it can produce nearly transform limited pulses over its entire tuning range. The ability of the femtosecond PPLN OPO to produce high-average power pulses with an all-solid-state pump source makes it especially attractive in terms of its reliability and maintenance costs. An additional advantage of this configuration is that the extraordinary polarization experiences lower absorption loss through the transmission window of the material than does the corresponding ordinary polarization. For these reasons, synchronously pumped OPOs based on PPLN have proved to be useful tools to generate wavelengths as long as 5.4 μm .

A. Basic ideas of quasi-phase matching

Armstrong et al. [7] were the first to suggest ways to achieve QPM. For a frequency-conversion process, such as an OPO or a SHG process, the phase mismatch is accumulated with increasing the interaction length (or length of the crystal). After a coherence length, the conversion efficiency reduces and energy flows back from the signal or from the doubled wave to the pump. For a crystal length much longer than the coherence length, the efficiency will behave in the way of the Marker fringes, as described in Chapter 2.1. If the nonlinear coefficient is modulated with a period twice the coherence length, in other words, the nonlinear coefficient changes its sign after each coherence length, the accumulated phase mismatch can be offset. Consequently, the conversion efficiency increases continuously with interaction length. This phase-matching technique is called quasi-phase matching. Meanwhile, we should keep in mind that the group velocity mismatch between the interacting waves and pulse duration of them largely limit the effective interaction length and modify the strength of coupling between these waves.

The most direct technique for QPM is that the nonlinear crystal is divided into segments each one coherence length long with each segment then rotated relative to its neighbours by 180° about the axis of propagation, see Fig. 2.3.1. Because of the lack of inversion symmetry, this has the effect of the changing the sign of the components of the nonlinear susceptibility tensor ($\chi^{(2)}$). Hence the nonlinear polarization wave is shifted by π radians after each coherence length. The coherence

length for frequency conversion process is sometimes only a few micrometers. It is difficult to fabricate such thin segments of nonlinear crystals and to control the thickness of them precisely. This has inhibited the development of QPM in the past, especially for visible and ultraviolet wavelengths. An electric-field poling technique was developed in 1990s [6] to reproducibly manufacture PPLN suitable for applications in infrared optical parametric oscillators and second harmonic generators, as will be demonstrated in subsection 2.3.2.

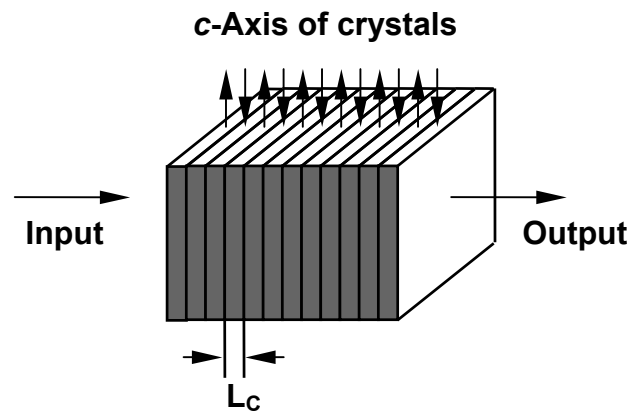


Fig.2.3.1 Schematic of quasi-phase matching technique using a stack of uniaxial crystals of alternating c -axis directions. L_C , coherence length for the parametric process.

B. Theoretical analysis

For simplicity, let us consider the case of a stack consisting of nonlinear dielectric slabs for QPM, as shown in Fig.2.3.2. The principles of QPM should be the same for a periodically poled bulk crystal.

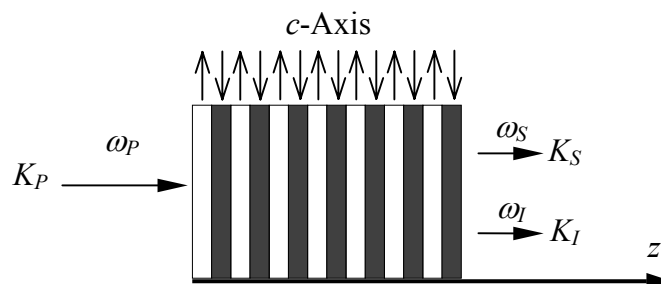


Fig. 2.3.2 Geometry of periodical poling for quasi-phase matching.

As shown in Fig. 2.3.2, during the optical parametric generation process, the incident pump beam (ω_P, k_P) excites the signal (ω_S, k_S) and the idler (ω_I, k_I) waves, which propagate in the same direction of z . The corresponding coupled equations can be written as:

$$\frac{\partial}{\partial z} E_S(z) = (-1)^M i \frac{(2\pi)^2}{n_S \lambda_S} \mu \chi^{NL} E_P(z) E_I(z)^* \exp(i\Delta kz) \quad (2.3.1)$$

$$\frac{\partial}{\partial z} E_I(z) = (-1)^M i \frac{(2\pi)^2}{n_I \lambda_I} \mu \chi^{NL} E_P(z) E_S(z)^* \exp(i\Delta kz) \quad (2.3.2)$$

$$\frac{\partial}{\partial z} E_P(z) = (-1)^M i \frac{(2\pi)^2}{n_P \lambda_P} \mu \chi^{NL} E_S(z) E_I(z)^* \exp(i\Delta kz) \quad (2.3.3)$$

where E_P , E_S , and E_I are the amplitudes of the electric fields of the pump (P), the signal (S), and the idler (I), respectively; n_P , n_S , and n_I are the corresponding refractive indices of the pump, the signal, and the idler waves in the periodically poled crystal;

$\Delta k = 2\pi \left(\frac{n_P}{\lambda_P} - \frac{n_S}{\lambda_S} - \frac{n_I}{\lambda_I} \right)$ is the phase mismatch amount; to include the periodical change of the poling direction of the nonlinear crystal, we introduced the factor $(-1)^M$, where $M = \text{integer}[z/(m \cdot l_c)]$ and m is the order of quasi-phase matching.

Fig. 2.3.3 demonstrates the solutions to the coupled equations under different orders of quasi-phase matching.

From the Fourier expansion, the effective nonlinear coefficient for the QPM interaction is [6]:

$$d_Q = d_{eff} G_m \quad (2.3.4)$$

where $G_m = \frac{2}{m\pi} \sin(m\pi D)$ is the corresponding Fourier coefficient and $D = l/\Lambda$ is called the duty factor that is given by the length of reversibly poled domain divided by the poling period (or the grating period) Λ , which is twice the coherence length l_c for the same process in a single-domain material:

$$\Lambda = 2l_c = \frac{2\pi}{k_P - k_S - k_I} \quad (2.3.5)$$

It is understandable from formula (2.3.4) and Fig. 2.3.3 that only odd-order QPM process can gain efficient conversion, since d_Q is equal to zero when m is an even number and D is equal to 50%.

For first-order quasi-phase matching ($m=1$) with a 50% poling duty cycle, the effective nonlinear coefficient can be simplified as:

$$d_Q = \frac{2}{\pi} d_{eff}$$

and the phase matching condition can be written as:

$$\Delta k_Q = k_p - k_s - k_l - \frac{2\pi}{\Lambda} = 0 \quad (2.3.6)$$

or

$$\frac{n_p}{\lambda_p} - \frac{n_s}{\lambda_s} - \frac{n_l}{\lambda_l} - \frac{1}{\Lambda} = 0 \quad (2.3.7)$$

In case of low gain, the single-pass parametric power amplification in a crystal of length L is [47]:

$$G(L) = \frac{|E_S(L)|^2}{|E_S(0)|^2} - 1 \approx \frac{2\omega_s\omega_l d_Q^2 I_P}{n_s n_l n_p \epsilon_0 c^3} L^2 \operatorname{sinc}^2\left(\frac{\Delta k_Q L}{2}\right) \quad (2.3.8)$$

where I_P is the pump intensity, which has the same form as that for a BPM process.

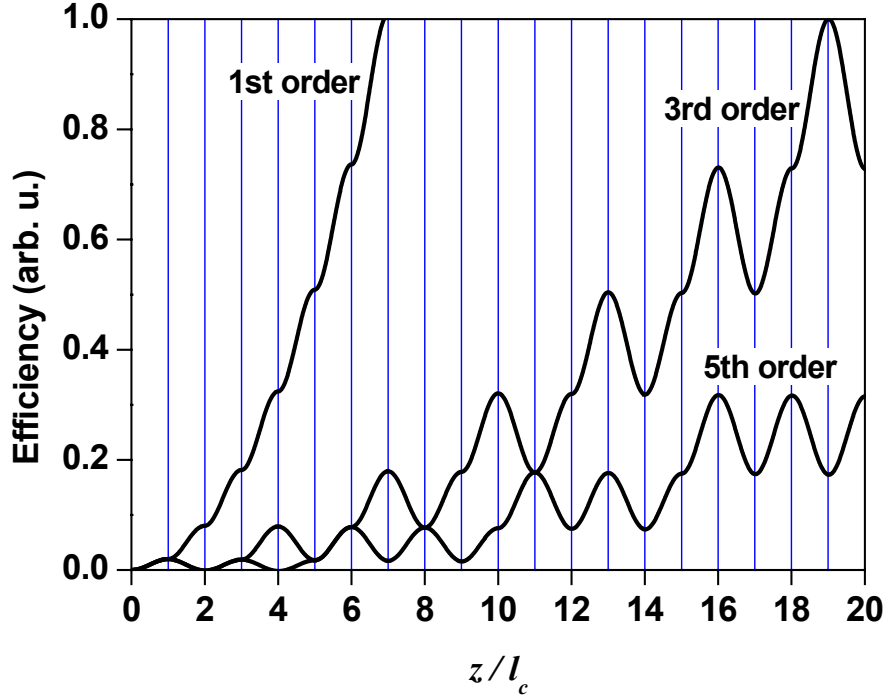


Fig.2.3.3 Conversion efficiency of the OPO process under 1st, 3rd, and 5th orders of QPM, where z is the position in the crystal, l_c is the coherence length of the first-order OPO process.

2.3.2 LiNbO₃ and PPLN

Lithium Niobate (LiNbO₃) [48, 49] possesses a combination of unique electro-optic, acoustic, piezoelectric, pyroelectric and non-linear optical properties, making it suitable for applications in acoustic, electro-optical and non-linear optical devices, high-temperature acoustic transducers, receivers and transmitters of acoustic vibrations, air force acceleration meters, acoustic wave delay lines, deflectors, generators of non-linear distorted waves, acoustic filters, electro-optical Q-modulators (Q-switch), converters, frequency doublers and resonators in laser systems, non-linear elements in parametric light generators, etc. An indispensable condition of some of these applications is a high degree of optical uniformity of lithium niobate crystals used for fabrication of active elements.

In the field of nonlinear optics, LiNbO₃ crystals are widely used as frequency doublers for wavelengths > 1 μm and optical parametric oscillators pumped at 1064 nm as well as quasi-phase-matched devices. Due to its large electro-optic (E-O) and acousto-optic (A-O) coefficients, LiNbO₃ crystals are the most commonly used material for Pockels cells, Q-switches and phase modulators, waveguide substrate, and surface acoustic wave (SAW) wafers, etc.

The LiNbO₃ crystal series include some other crystals, such as MgO:LiNbO₃, ZnO:LiNbO₃, and Fe:LiNbO₃, which have some special properties that are more suitable for some specific applications. For instance, compared with LiNbO₃ crystals, MgO:LiNbO₃ crystals exhibit their particular advantages for NCPM frequency doubling of Nd:Lasers, frequency mixing and optical parametric oscillators. The SHG efficiencies of over 65% for pulsed Nd:YAG lasers and 45% for cw Nd:YAG lasers have been achieved in MgO:LiNbO₃ crystals. MgO:LiNbO₃ is also a good crystal for optical parametric oscillators and amplifiers, quasi-phase-matched doublers and integrated waveguides. MgO:LiNbO₃ crystals have also a much higher resistance to the photorefractive effects than the normal LiNbO₃ crystals, which increases a lot the efficiencies of QPM doubling and OPO processes. MgO:LiNbO₃ has similar effective nonlinear coefficients as pure LiNbO₃. Its Sellmeier equations (for MgO dopant 7 mol%) are:

$$n_o^2 = 4.8762 + \frac{0.11554}{\lambda^2 - 0.04674} - 0.033119\lambda^2$$

$$n_e^2 = 4.5469 + \frac{0.094779}{\lambda^2 - 0.04439} - 0.026721\lambda^2$$

Some other physical and optical properties are summarized in Table 2.3.1.

Table 2.3.1 Basic physical and optical properties of lithium niobate (LiNbO₃) [48, 49]

PROPERTY	VALUE
Chemical formula	LiNbO ₃
Crystallographic system	Trigonal, space group R3c
Lattice Constants, Å	a=5.148 c= 13.863
Molecular Weight	147.9
Point group	3m
Density, g/cm ³	4.644
Transmission Range, μm	0.42 – 5.2
Dielectric Constant	29
Melting Temperature, °C	1255±5
Curie point, °C	1140±5
Thermal Conductivity, W/(m K) at 300 K	5.6
Thermal Expansion, K ⁻¹ at 300 K α _a (perpendicular) α _c (parallel)	15×10 ⁻⁶ 4.1×10 ⁻⁶
Specific Heat, cal/(g K)	0.15
Hardness (Mohs)	~5
Bandgap, eV	4.0
Solubility in water	None
Electro-Optical Coefficients, pm/V	r ₃₃ =30.8, r ₃₁ =8.6 r ₂₂ =3.4, r ₅₁ =28
SAW Velocity, m/s	3490 – 3890
Optical Damage Threshold, MW/cm ²	10 – 100
Birefringence Gradient	< 5 × 10 ⁻⁵
Absorption coefficient	~0.1%/cm q 1064 nm
NLO coefficients	d ₃₃ = 34.4 pm/V d ₃₁ = d ₁₅ = 5.95 pm/V d ₂₂ = 3.07 pm/V
Efficiency NLO Coefficients	d _{eff} =5.7 pm/V or ~14.6 x d ₃₆ (KDP) for frequency doubling at 1300 nm; d _{eff} =5.3 pm/V or ~13.6 x d ₃₆ (KDP) for OPO pumped at 1064 nm; d _{eff} =17.6 pm/V or ~45 x d ₃₆ (KDP) for quasi-phase-matched structures.
Electro-Optic Coefficients	g ₃₃ ^T = 32 pm/V, g ₃₃ ^S = 31 pm/V, g ₃₁ ^T = 10 pm/V, g ₃₁ ^S = 8.6 pm/V, g ₂₂ ^T = 6.8 pm/V, g ₂₂ ^S = 3.4 pm/V,

To understand the principle of periodic poling of a bulk LiNbO₃ crystal, we need to have some knowledge of ferroelectric crystals [50]. A ferroelectric crystal exhibits an electric dipole moment even in the absence of an external electric field. In the ferroelectric state, the center of positive charge of the crystal does not coincide with the center of the negative charge, as shown in Fig.2.3.4(a). When the externally applied field exceeds a certain threshold value, the center of the positive charge will shift to another stable position so that the polarity of the crystal will be reversed, as shown in Fig. 2.3.4(b). Above the Curie point (T_C), the ferroelectricity will disappear (Fig. 2.3.4(c)).

A qualitative picture of ferroelectricity in LiNbO₃ is shown in Fig. 2.3.5. [6] Polarity of a ferroelectric domain is determined by the offset of the metal ions either above or below the oxygen layers. Domain reversal involves reorienting the crystal from one stable configuration to the other, which can be effected by the application of an external electric field. Significant domain reversal occurs when the applied field exceeds a certain value referred to as the coercive field, which is $\sim 21\text{kV/mm}$ for LiNbO₃ at room temperature. Some techniques can be applied to prevent backreversal of the reversed domains, as discussed in detail in Ref. 46.

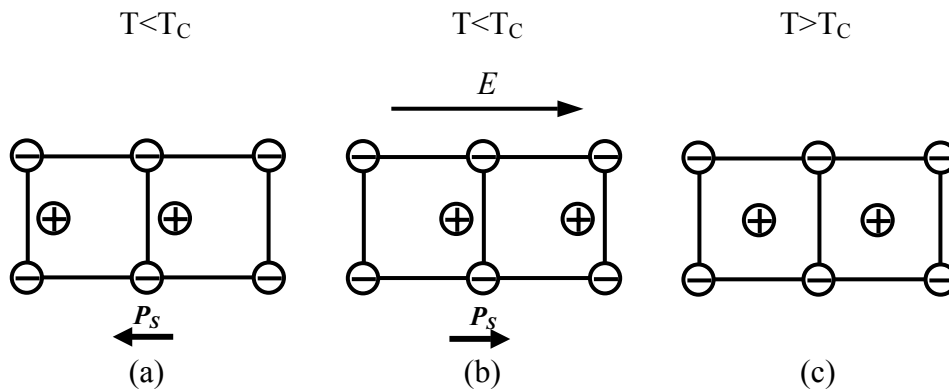


Fig 2.3.4. Poling of ferroelectric crystals. T_C , transition temperature or Curie point; P_s , polarity of the studied domain of the crystal; E , applied electric field.

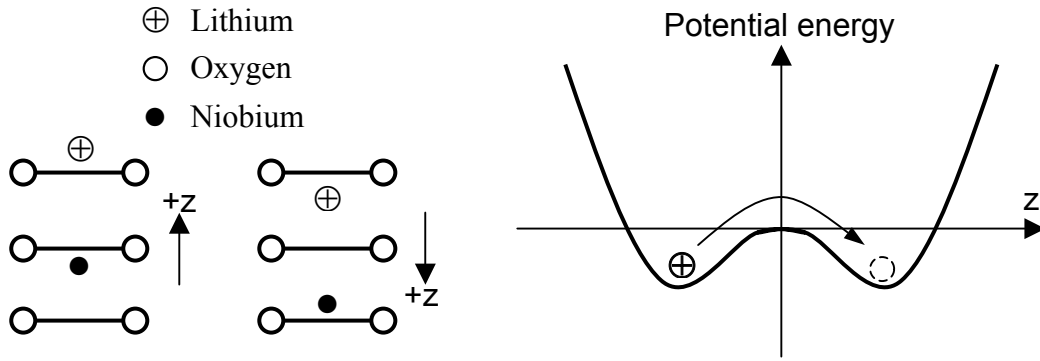


Fig 2.3.5. *Qualitative picture of ferroelectricity in LiNbO₃. Domain polarity can be reversed by application of a field sufficient to move the ions from the one stable location to the other.*

The techniques for ferroelectric domain reversal with an external electric field have produced PPLN [51, 52, 53], PPLT (periodically poled LiTaO₃) [54], and PPKTP [55]. In this approach, domain periodicity is precisely defined by a lithographic mask by standard microfabrication techniques. Myers et al. [6] developed an electric-field poling process that yields uniform PPLN in thick substrates for efficient QPM frequency-conversion applications. The arrangement for this technique is demonstrated in Fig. 2.3.6. They used a standard optical-grade LiNbO₃ wafer and patterned a positive electrode with the desired structure on the +z surface of the wafer. Two methods were used for the fabrication of the electrode. In the first approach, a 0.2- μm -thick Al grating was patterned by lift-off lithography. A 0.2- μm -thick layer of photoresist was applied over the grating, leaving a portion of the metal pattern exposed. Contact was made to the exposed metal with a liquid electrolyte consisting of LiCl in deionized water. In the second variant, a grating pattern of photoresist is covered by an Al film and then covered by the electrolyte. Please refer to Ref. 46 for comparison between these two variants. For the negative electrode, liquid electrolyte was applied directly in the bare $-z$ surface. The liquid electrode fixture consisted of two electrolyte-containing chambers, which squeezed the LiNbO₃ sample between O-rings. This arrangement permitted application of fields exceeding 25kV/mm without breakdown of the sample.

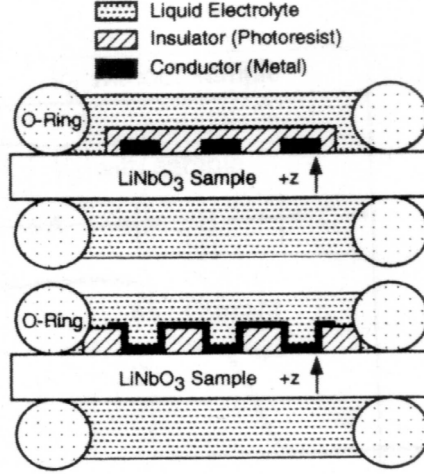


Fig. 2.3.6 Electrode configurations for electric-field poling. [6]

2.3.3 Tuning characteristics of the PPLN OPO

There are several methods for tuning the signal wavelength of a PPLN OPO: pump wavelength tuning, grating period tuning, temperature tuning, and cavity length tuning methods. Since the cavity length tuning method is applicable for all OPOs, we will discuss only the first three tuning methods in this section, all of which are based on the phase matching condition of a PPLN OPO.

The precise expression of the phase matching conditions of a PPLN OPO can be written as:

$$\Delta k_Q = 2\pi \left(\frac{n_p(T)}{\lambda_p} - \frac{n_s(T)}{\lambda_s} - \frac{n_i(T)}{\lambda_i} - \frac{1}{\Lambda(T)} \right) = 0 \quad \text{with} \quad \frac{1}{\lambda_p} = \frac{1}{\lambda_s} + \frac{1}{\lambda_i} \quad (2.3.9)$$

At a given grating period and a fixed temperature (T) of PPLN, the signal wavelength (λ_s) is a function of the pump wavelength (λ_p). Tuning the signal (idler) wavelength by changing the pump wavelength is called pump wavelength tuning. At a fixed pump wavelength and a fixed temperature of PPLN, the signal (idler) wavelength is a function of the grating period. Tuning the signal wavelength by changing the grating period of PPLN is called grating period tuning. The refractive index of PPLN is a function of temperature, and the grating period also changes with temperature because of the thermal expansion characteristics of the material, so that at a given pump wavelength and a given grating period at room temperature, the signal wavelength can be tuned by changing the temperature of the PPLN crystal, this is called temperature tuning.

A. Pump wavelength tuning

If we fix A and T and use the Sellmeier equations for LiNbO_3 given in Appendix A, we can solve the equation (2.3.9) numerically and obtain the pump wavelength tuning characteristics of the PPLN OPO, as shown in Fig. 2.3.7. In the calculations, we used pump wavelengths typical for a Ti:sapphire laser (760 nm ~ 840 nm). The temperature of the crystal was set to 100°C.

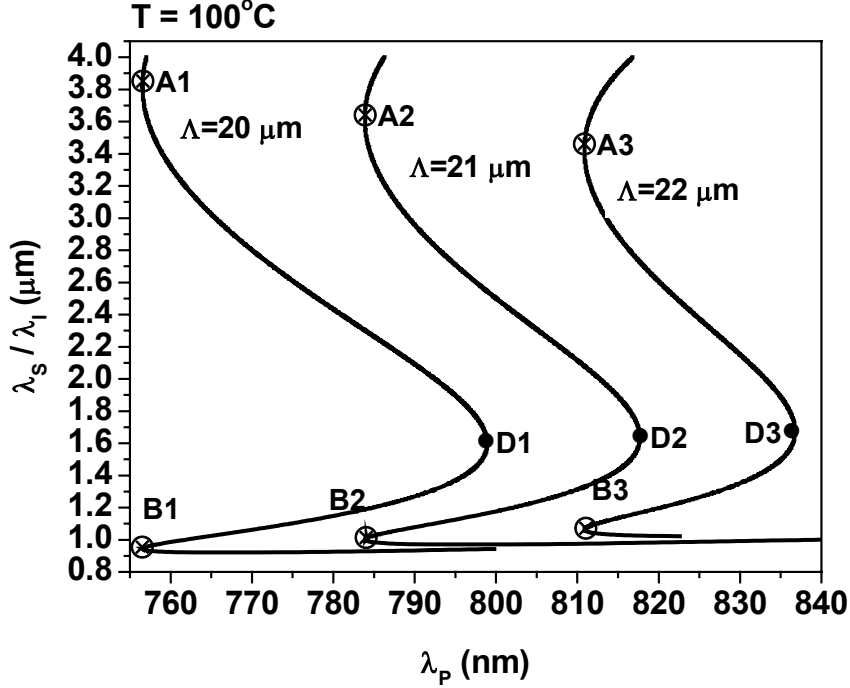


Fig. 2.3.7 Pump wavelength tuning of PPLN OPO pumped with a Ti:sapphire laser for grating periods equal to 20, 21, and 22 μm , respectively. D1, D2, and D3 are the degeneracy points of the three tuning curves; A1 and B1, A2 and B2, A3 and B3 correspond to the idler and signal wavelengths that have similar group velocities in PPLN (besides the degeneracy points) for the three tuning curves, respectively.

It can be found that for a given grating period there is a limited pump wavelength range for perfect QPM, e.g., when $\Lambda = 20 \mu\text{m}$, the phase-matched pumping range is from about 760 nm to 800 nm. The QPM pump range shifts to longer wavelengths with increasing grating period. It can also be found that the tuning curves turn back on themselves because the corresponding interactions straddle the region where the curvature of the dispersion changes its sign [6]. A consequence of this behaviour is that the parametric gain bandwidth is extremely large, implying a large signal bandwidth excited by a much smaller pump bandwidth. In other words, the tuning rate is very large. We can explain this by some further theoretical analysis.

We can rewrite the phase matching conditions for QPM and BPM process as:

$$\frac{n_p}{\lambda_p} = \frac{n_s}{\lambda_s} + \frac{n_i}{\lambda_i} + \frac{1}{\Lambda} \text{ (QPM)} \quad \text{or} \quad \frac{n_p}{\lambda_p} = \frac{n_s}{\lambda_s} + \frac{n_i}{\lambda_i} \text{ (BPM)}$$

Since Λ is a constant, if we perform differentiation operations with respect to λ_p on both sides of the above two equations, we will get the same result. The left-hand side is:

$$-\frac{n_p}{\lambda_p^2} + \frac{1}{\lambda_p} \frac{dn_p}{d\lambda_p} = -\frac{1}{\lambda_p^2} \left(n_p - \lambda_p \frac{dn_p}{d\lambda_p} \right) = -\frac{1}{\lambda_p^2} \frac{c}{v_p} \quad (2.3.10 \text{ a})$$

where v_p is the group velocity of the pump wave. The right-hand side reads:

$$\begin{aligned} & -\frac{n_s}{\lambda_s^2} \frac{d\lambda_s}{d\lambda_p} + \frac{1}{\lambda_s} \frac{dn_s}{d\lambda_s} \frac{d\lambda_s}{d\lambda_p} - \frac{n_i}{\lambda_i^2} \frac{d\lambda_i}{d\lambda_p} + \frac{1}{\lambda_i} \frac{dn_i}{d\lambda_i} \frac{d\lambda_i}{d\lambda_p} \\ &= -\frac{1}{\lambda_s^2} \left(n_s - \lambda_s \frac{dn_s}{d\lambda_s} \right) \frac{d\lambda_s}{d\lambda_p} - \frac{1}{\lambda_i^2} \left(n_i - \lambda_i \frac{dn_i}{d\lambda_i} \right) \frac{d\lambda_i}{d\lambda_p} \\ &= -\frac{1}{\lambda_s^2} \frac{c}{v_s} \frac{d\lambda_s}{d\lambda_p} - \frac{1}{\lambda_i^2} \frac{c}{v_i} \frac{d\lambda_i}{d\lambda_p} \quad (2.3.10 \text{ b}) \end{aligned}$$

where v_s and v_i are group velocities of the signal and idler waves respectively. On the other hand, since $\frac{1}{\lambda_p} = \frac{1}{\lambda_s} + \frac{1}{\lambda_i}$, we can get another relation expressed as:

$$-\frac{1}{\lambda_i^2} \frac{d\lambda_i}{d\lambda_p} = -\frac{1}{\lambda_p^2} + \frac{1}{\lambda_s^2} \frac{d\lambda_s}{d\lambda_p}$$

Substituting this relation into (2.3.10 b) and reconstructing the equation, we obtain:

$$-\frac{1}{\lambda_p^2} \frac{c}{v_p} = -\frac{1}{\lambda_s^2} \frac{c}{v_s} \frac{d\lambda_s}{d\lambda_p} + \left(-\frac{1}{\lambda_p^2} + \frac{1}{\lambda_s^2} \frac{d\lambda_s}{d\lambda_p} \right) \frac{c}{v_i}$$

A very important formula can then be reached:

$$\boxed{\frac{d\lambda_s}{d\lambda_p} = \frac{v_i^{-1} - v_p^{-1}}{v_i^{-1} - v_s^{-1}} \frac{\lambda_s^2}{\lambda_p^2}} \quad (2.3.11)$$

It can be concluded from the formula (2.3.11) that the tuning rate of the signal wavelength with changing the pump wavelength depends mainly on the group velocity mismatch between the signal and the idler waves and that between the pump and the idler waves. The smaller the group velocity mismatch between the signal and the idler waves or the larger that between the idler and the pump waves, the larger the tuning rate and the tuning range of the signal wave. The tuning rate becomes infinite when the signal and the idler have the same group velocity. This happens at the

degeneracy points (as marked by $D1\sim D3$ in Fig. 2.3.7) and also when the signal wavelength is very short while the idler wavelength becomes very long so that the signal and the idler waves can possibly have equal group velocities (as marked by $A1\sim A3$ and $B1\sim B3$ in Fig. 2.3.7). Fig. 2.3.8 shows the dispersion characteristics of PPLN. The refractive index changes its curvature at about $1.925\mu\text{m}$, where the GVD becomes zero. At longer wavelength than $1.925\mu\text{m}$ the GVD becomes negative, which means that the group velocity will decrease with increasing wavelength. Consequently, it is possible for two waves to have the same group velocity if their wavelengths are located on either side of $1.925\mu\text{m}$. This is why there is another position (signal or idler wavelength) besides the degeneracy point in the tuning range where the signal and the idler at different wavelengths have the same group velocity. If the pump wavelength is shorter than 700 nm , since the group velocity of the signal is always smaller than the idler so that the value of (2.3.11) is positive all over the corresponding tuning range, so the curvature of the tuning curve is positive and does not change throughout the tuning range. When the pump wavelength is longer than $1.0\mu\text{m}$, the signal propagates faster than the idler, so the sign of the value of (2.3.11) is negative, which results in a negative curvature of the tuning curve. In the middle part of the pumping range, the signal propagates faster than the idler in one segment, and it propagates slower than the idler in the other segment, so there are two points in the tuning curve where the signal and the idler have the same group velocity and the tuning rate becomes infinite. These processes are described in Fig. 2.3.9.

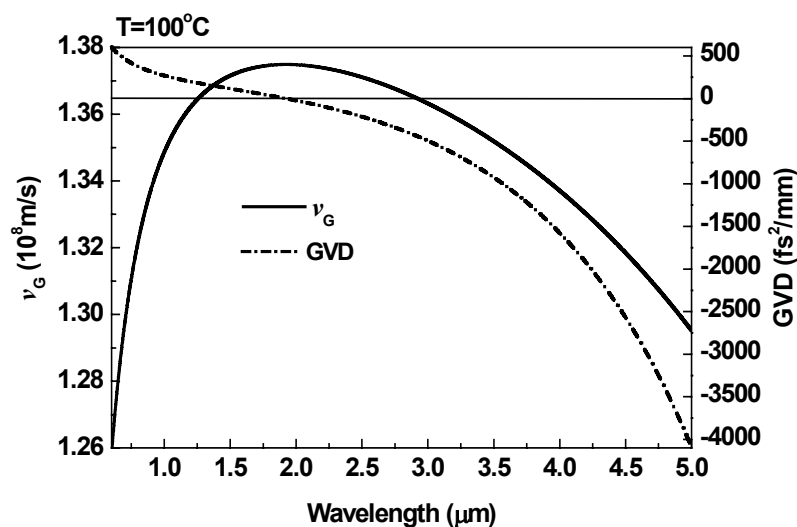


Fig. 2.3.8 Dispersion characteristics (group velocity v_G and GVD) of PPLN at 100°C .

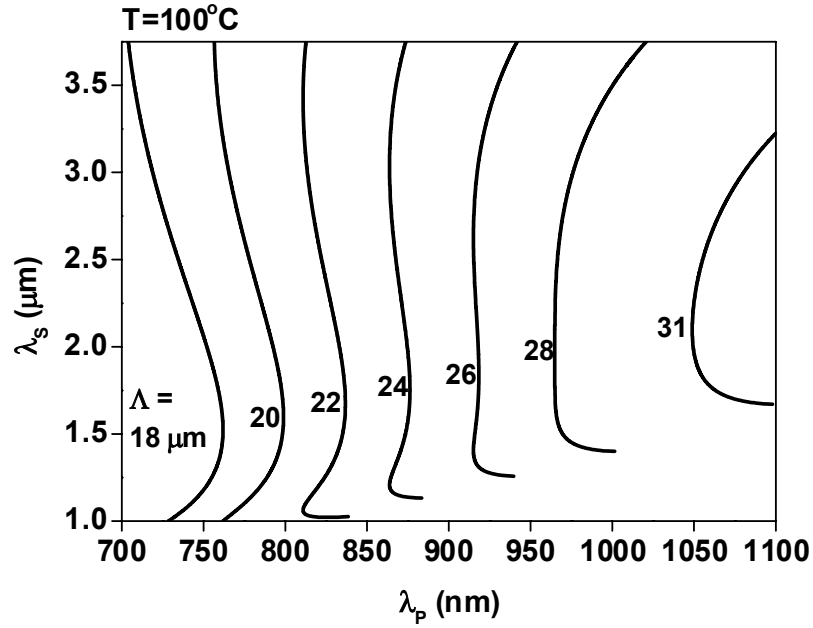


Fig. 2.3.9 Changing of the curvature of the tuning curves with pump wavelength and grating period of PPLN OPO.

B. Grating period tuning

If we fix λ_p and T , we can solve the equation in (2.3.9) numerically to find the function of λ_s versus Λ . Some examples of the calculations are presented in Fig. 2.3.10.

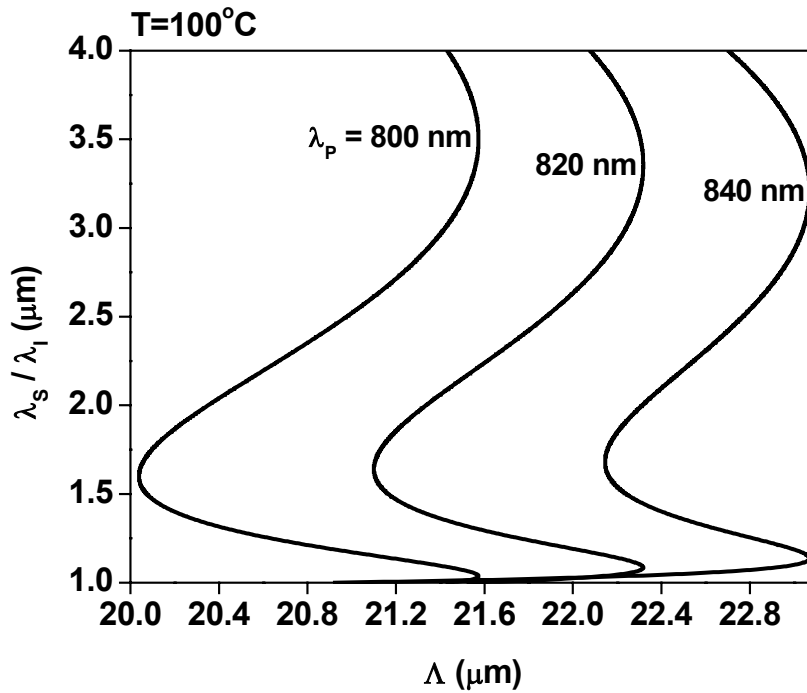


Fig. 2.3.10 Grating period tuning of PPLN OPO.

Using similar methods described in subsection 2.3.3.A, we can obtain the expression for the tuning rate of the signal wavelength when changing the grating period:

$$\boxed{\frac{d\lambda_s}{d\Lambda} = \frac{\lambda_s^2}{\Lambda^2} \left(\frac{c}{v_I} - \frac{c}{v_S} \right)^{-1}} \quad (2.3.12)$$

Obviously, the tuning rate depends on the GVM between the signal and the idler. Similar to the case of pump wavelength tuning, there are two turning-back points in the tuning range, with one located at the degenerate wavelength and the other located where very short signal wavelength and very large idler wavelength correspond to equal group velocities. The tuning rate is also inversely proportional to the square of the grating period. The grating periods that are applicable for a given pump wavelength at a given temperature can be changed in a range of about 1 μm , which becomes smaller with increasing pump wavelength. Therefore, when designing a PPLN crystal for a known pump laser, multiple poling gratings with periods varying in a range of 1~2 μm are normally produced in a bulk LiNbO_3 , enabling optimization of QPM.

Because the pump wave propagates slower than the idler in the studied tuning ranges, the value of (2.3.12) is opposite to that of (2.3.11). This is why we observe opposite curvatures of the tuning curves in Fig. 2.3.7 and in Fig. 2.3.10.

C. Temperature tuning

Temperature tuning characteristics of a PPLN OPO can be obtained when solving the equation (2.3.9) with a constant pump wavelength and a fixed grating period.

Temperature tuning is very important for PPLN OPOs, since it enables QPM at any wavelength within the transparency range of the PPLN crystal.

Two mechanisms make effects during temperature tuning. First, the refractive index of the crystal changes with temperature; second, the grating period is a function of temperature because of the thermal expansion effect. We must include these two factors simultaneously when calculating the temperature tuning curves. It was found that the variation of the grating period with temperature has much more influence on the tuning characteristics than that of the refractive index. So, the temperature tuning curves look somewhat similar to the grating period tuning curves, as demonstrated in Fig. 2.3.11. It is obvious that smaller grating periods are required at higher

temperatures for a given pump wavelength. The tuning rate of the signal wavelength with changing the temperature can also be derived as

$$\frac{d\lambda_s}{dT} = \frac{\lambda_s^2 \Lambda_{25^\circ C} \left(\frac{c}{v_I} - \frac{c}{v_S} \right)^{-1} [\alpha + 2\beta(T - 25^\circ C)]}{\Lambda^2} \quad (2.3.13),$$

where $\alpha=1.54 \times 10^{-5} \text{K}^{-1}$, $\beta=5.3 \times 10^{-9} \text{K}^{-2}$ [56] are the thermal expansion coefficients. We can conclude that the tuning rate is inversely proportional to the square of the grating period, inversely proportional to the GVM between the signal and the idler, whereas linearly proportional to the temperature. Therefore, we can observe in Fig. 2.3.11 that a higher tuning rate corresponds to a higher temperature and smaller grating period. Similar tuning-back phenomena observed in grating period tuning curves can also be observed in Fig. 2.3.11.

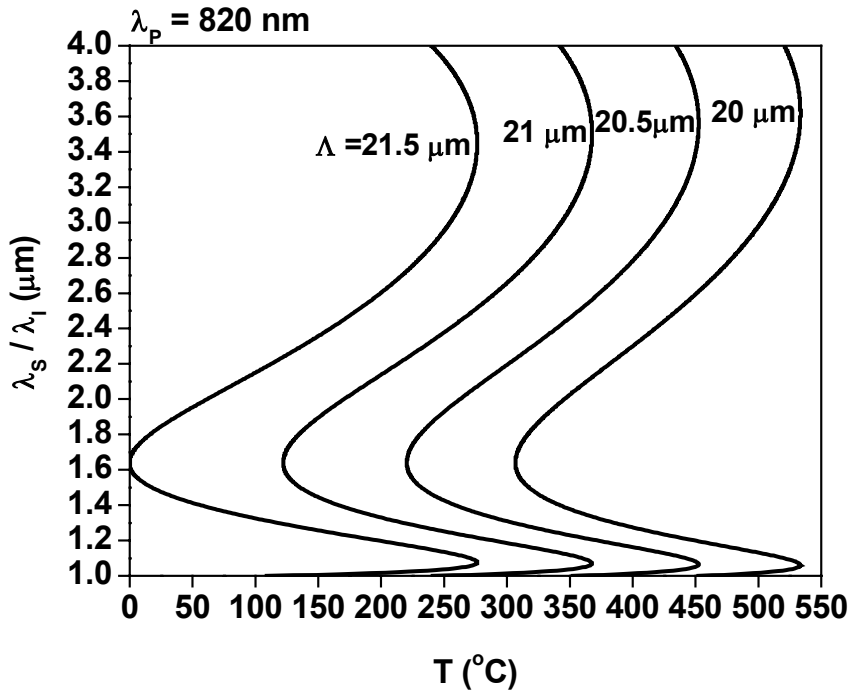


Fig. 2.3.11 Temperature tuning of PPLN OPO.

2.3.4 Design of a PPLN crystal

The main task of designing a PPLN crystal is to find the required grating period and the crystal length for an expected frequency conversion process. For a PPLN OPO, we should determine at first the pump wavelength (λ_p) and the desired signal wavelength (λ_s). By solving the following equations,

$$\left. \begin{aligned} \frac{n_z(\lambda_p)}{\lambda_p} - \frac{n_z(\lambda_s)}{\lambda_s} - \frac{n_z(\lambda_I)}{\lambda_I} - \frac{1}{\Lambda} = 0 \\ \frac{1}{\lambda_p} = \frac{1}{\lambda_s} + \frac{1}{\lambda_I} \end{aligned} \right\} \quad (2.3.13)$$

we can obtain the required grating period for a first-order QPM OPO. Since for QPM all of the interaction waves (the pump, the signal, and the idler) are polarized in the direction of Z-axis of the PPLN crystal, we used only n_z in the phase matching condition. Fig. 2.3.12 demonstrates how to select a grating period for a PPLN OPO pumped with a Ti:sapphire laser and operating in the near-infrared at 100°C. For example, pumping at 800 nm, a grating period of about 21 μm is required for generating signal wavelength of 1.2 μm .

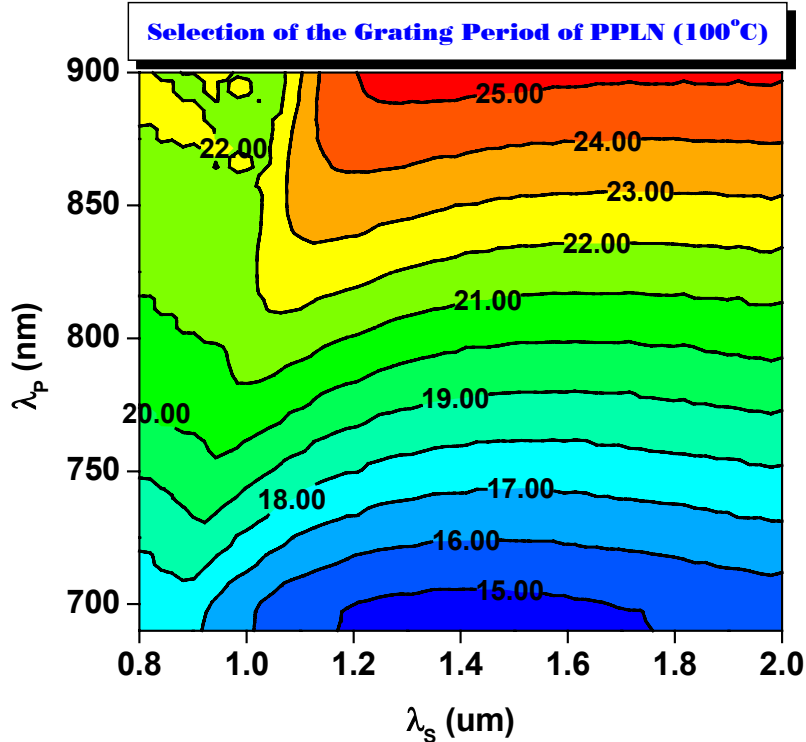


Fig. 2.3.12. Selection of the grating period of a PPLN crystal for a Ti:sapphire laser pumped OPO operating in the NIR at 100°C.

The crystal length is limited by the GVM between the interaction waves. Normally we consider mainly the GVM between the pump and the signal. Assuming that the signal and the pump have similar pulse duration τ_P , we can design the crystal length by the criteria

$$L_{eff} \leq 2\tau_P (v_P^{-1} - v_S^{-1})^{-1},$$

where L_{eff} is the effective interaction length, and v_P, v_S are the group velocities of the pump and the signal, respectively. The practical crystal length is normally a little longer than L_{eff} .

Figure 2.3.13 gives the GVM between the interaction waves in a PPLN OPO when the grating period is $21 \mu\text{m}$ at 100°C . For instance, the GVM between the pump and the signal is about 220 fs/mm when pumping a PPLN OPO at 800 nm . If $\tau_P \approx 30 \text{ fs}$, then $L_{eff} \leq 0.273 \text{ mm}$; if $\tau_P \approx 100 \text{ fs}$, then $L_{eff} \leq 0.91 \text{ mm}$.

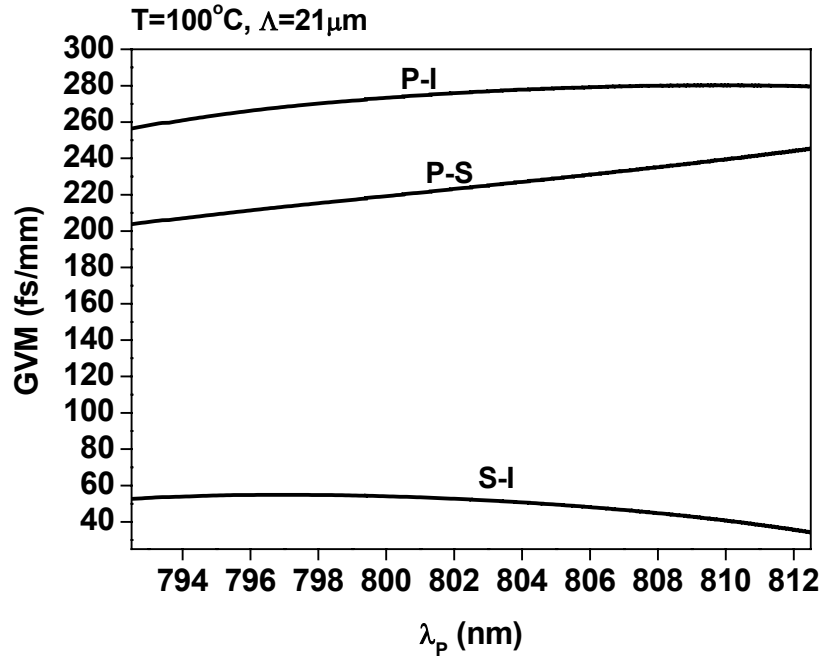


Fig. 2.3.13. GVM between the interaction waves in a PPLN OPO. P-I, P-S, and S-I mean the GVM between the pump and the idler, between the pump and the signal, and between the signal and the idler, respectively.

2.3.5 PPKTP and PPKTP OPO

By means of a multi-step lithographic and electric field poling process, a permanent change in the nonlinear properties of KTP crystal has been achieved. The PPKTP's high nonlinear coefficient and non-critically phase-matched interaction allow very high conversion efficiencies at low pump intensities.

There are several advantages of PPKTP over PPLN for applications in QPM frequency conversion processes. First, in the manufacturing stage, the poling of LiNbO₃ needs a coercive field as large as ~21 kV/mm; while, the coercive field required for poling KTP is only about ~2 kV/mm. Large coercive field limits the possible crystal thickness of PPLN to ~0.5 mm. The much lower coercive field for KTP allows successful poling on samples of at least 1 mm thickness. [13] Second, KTP has a much higher photorefractive damage threshold than LiNbO₃, permitting room-temperature operation without temperature control. However, satisfactory operation of PPLN requires heating the crystal in a temperature-controlled oven. [56] Third, using KTP instead of LiNbO₃ eliminates the long-term crystal degradation when operating at high average power.

Similar to the operation of PPLN, all of the interaction waves of the PPKTP OPO are polarized in the direction of the Z-axis of the crystal, namely, the nonlinear susceptibility d_{33} will be utilized. However, the value of d_{33} (16.9pm/V) of KTP is smaller than that (27pm/V) of LiNbO₃, so that a PPKTP OPO will have a lower conversion efficiency than a PPLN OPO. In principle, the pump threshold of a PPKTP OPO will also be a little higher than that of the PPLN OPO. The phase matching condition of the PPKTP OPO has the same form as that of a PPLN OPO, as given by (2.3.9).

The calculated pump wavelength tuning and grating period tuning characteristics of a PPKTP OPO pumped by a Ti:sapphire laser are presented in Fig. 2.3.14 and Fig. 2.3.15, respectively. Because the GVD of KTP becomes zero at about 1.765 μm and becomes negative at longer wavelengths, the turning-back phenomenon can be observed in the tuning curves too.

It can be concluded from Fig. 2.3.14 that for pumping at 800 nm the optimal grating period should be about 28 μm . Because the degeneracy point increases with increasing pump wavelength and grating period, using a longer pump wavelength and a larger grating period would be more appropriate for an OPO operating at

wavelengths that are slightly shorter than the degeneracy point, e.g., the configuration of $\Lambda=29 \mu\text{m}$ and $\lambda_p=820 \text{ nm}$ would be a better choice for an OPO operating at $1.55 \mu\text{m}$ than the configuration of $\Lambda=28 \mu\text{m}$ and $\lambda_p=800 \text{ nm}$.

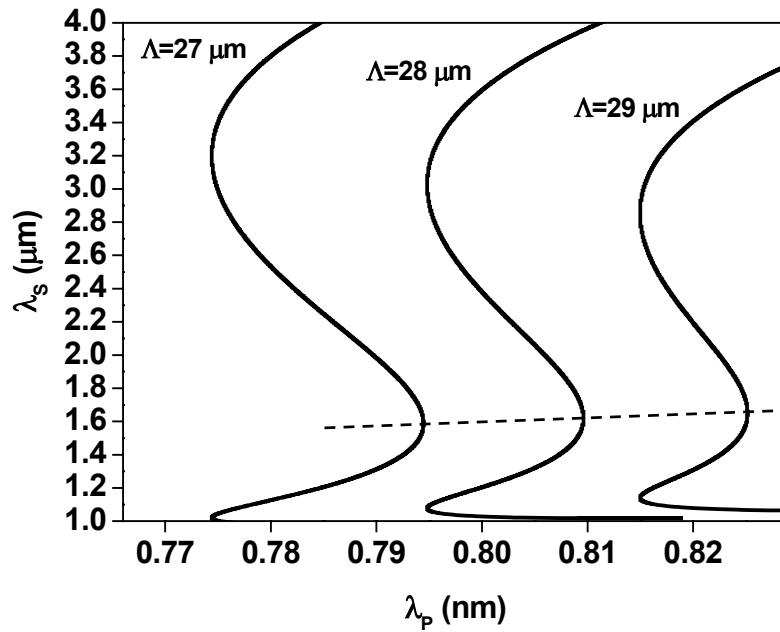


Fig. 2.3.14 Pump wavelength tuning of a PPKTP OPO.

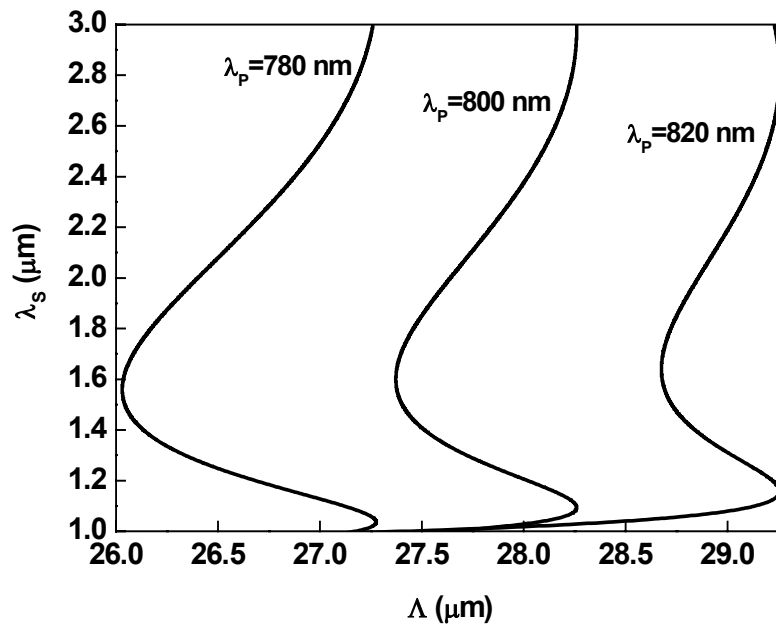


Fig. 2.3.15 Grating period tuning of PPKTP OPO.

Fig. 2.3.16 demonstrates how to select a grating period using a given pump wavelength and an expected signal wavelength.

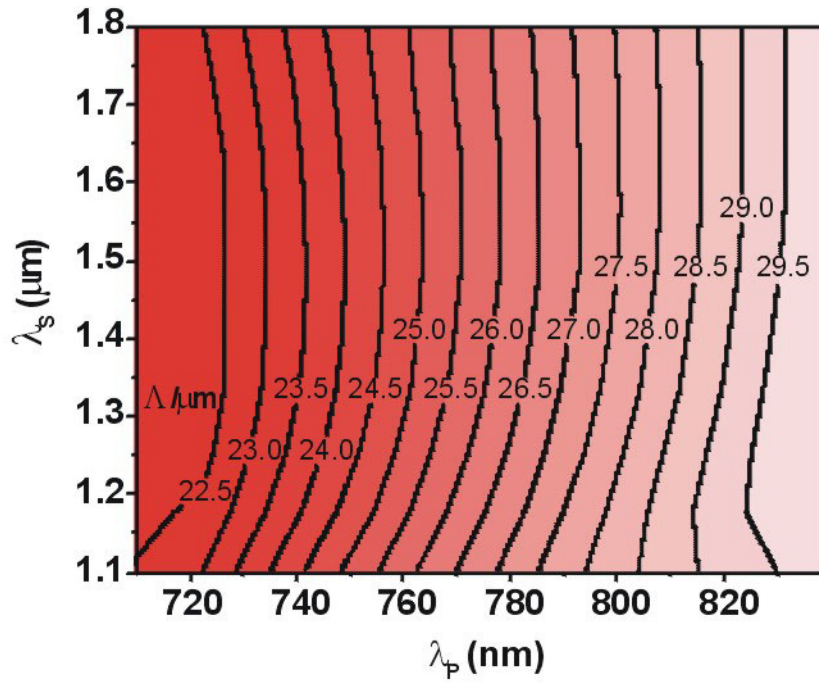


Fig. 2.3.16 Selection of grating period of PPKTP OPO.

2.4

Dispersion characteristics of OPO crystals and optical glasses; pulse broadening effects

Dispersion characteristics of optical crystal and glasses are of key importance for ultrafast laser systems. Group velocity dispersion or group delay dispersion (GDD) is the most important index to evaluate the dispersion characteristics of the laser or OPO crystals and the glasses inserted into the resonator or in the beam path. Based on GDD, we can easily estimate degree of pulse broadening effects and design the compensation configuration, so that we can achieve ultrashort-pulsed operation of the laser systems. Group velocity mismatch between the interaction waves passing through the nonlinear crystal is another important factor leading to pulse broadening for an OPO. Together with the pump pulse duration and the expected signal pulse duration, it determines the effective interaction length of the pulses in the crystal.

2.4.1 GVD and GVM

A. GVD

The group velocity of the laser pulses propagating in a nonlinear optical medium is defined as:

$$v_G = \frac{c}{n - \lambda \frac{dn}{d\lambda}} \quad (2.4.1)$$

where c is the velocity of light in vacuum, n is the refractive index of the nonlinear medium, λ is the center wavelength of the laser pulses. Then the GVD can be derived as:

$$\frac{dv_G}{d\lambda} = \frac{\lambda v_G^2}{c} \frac{d^2n}{d\lambda^2} \quad (2.4.2).$$

In most cases, we evaluate the GVD of the optical materials using the group velocity dispersion parameter (k''), which is defined as:

$$k'' = \frac{d^2k}{d\omega^2} = \frac{\lambda^3}{2\pi c^2} \frac{d^2n}{d\lambda^2} \quad (2.4.3)$$

where $k = \frac{n\omega}{c}$ is the wave vector, ω is the circular frequency of the incident wave, and consequently:

$$\frac{dv_G}{d\lambda} = \frac{\omega^2 v_G^2}{2\pi c} \frac{d^2 k}{d\omega^2} \quad (2.4.4)$$

B. GVM

In frequency conversion processes, such as SHG, SFG, DFG, OPO or OPA, two or more waves interact with each other while propagating through the nonlinear medium. Due to dispersion of the material, different waves propagate at different group velocities. In case of interaction on the femtosecond scale, the interacting pulses may get separated after propagating some distance in the medium, which means that there is a reduced effective interaction length. The GVM is a quantitative evaluation of this effect, which is defined as:

$$\Delta v_G = \left(\frac{1}{v_{G,i}} - \frac{1}{v_{G,j}} \right)^{-1} \quad (2.4.5)$$

where $v_{G,i}$ and $v_{G,j}$ are the group velocities of the two interacting waves i and j .

The effective interaction length L_{eff} for wave i and wave j can thus be calculated by the following formula:

$$L_{eff} = 2\tau_p |\Delta v_G| = 2\tau_p \left| \left(\frac{1}{v_{G,i}} - \frac{1}{v_{G,j}} \right)^{-1} \right| \quad (2.4.6)$$

where τ_p is the incident pulse duration at FWHM. It is supposed that wave i and wave j have a similar pulse duration. In case of sub-100 fs operation, to restrict the broadening in pulse length to less than $\sim 10\%$, the crystal length should be chosen as $L_{eff}/4$. [57, 58]

Some theoretical work regarding the pulse broadening effect induced by GVM will be presented in detail in subsection 2.4.3.

2.4.2 Dispersion characteristics of some typical OPO crystals

Figure 2.4.1 shows the GVD of some typical OPO crystals, including KTP, KTA, RTA, CTA, PPLN, PPKTP, and LBO. Their Sellmeier equations are as summarized in Appendix A. In addition to the wavelength of the incident beam, the GVD is also dependent on the polarization of the incident beams and the type of phase matching. So, when we talk about the GVD of OPO crystals, we should determine first how the

2.4.2 Dispersion characteristics of some typical OPO crystals

phase matching is achieved and how the incident beam is polarized. Table 2.4.1 gives the conditions for the calculation of the curves in Fig. 2.4.1. The incident beam should refer to the signal of the OPO. We consider only the near IR spectral range for the signal wavelength from 1000 nm to 1800 nm.

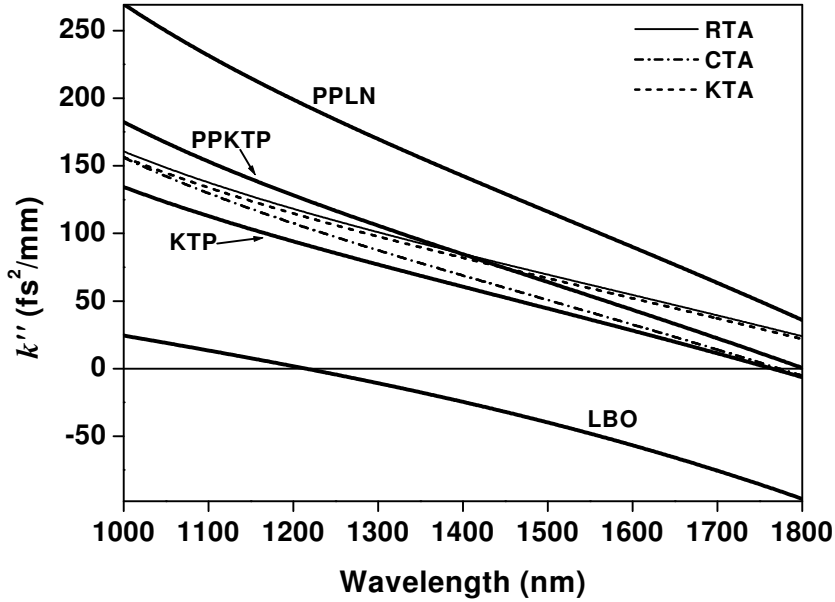


Fig. 2.4.1 Group velocity dispersion characteristics of some typical OPO crystals.

Table 2.4.1 Phase-matching and polarization conditions for the calculations of the curves in Fig. 2.4.1.

Crystal	Polarization of incident beam (direction of principal axis)	Phase matching
KTP	Y	Type II, NCPM ooe (PSI): $\hat{\epsilon}=90^\circ, \phi=0^\circ$
KTA	Y	Type II, NCPM ooe (PSI): $\hat{\epsilon}=90^\circ, \phi=0^\circ$
RTA	Y	Type II, NCPM ooe (PSI): $\hat{\epsilon}=90^\circ, \phi=0^\circ$
CTA	Y	Type II, NCPM ooe (PSI): $\hat{\epsilon}=90^\circ, \phi=0^\circ$
PPLN	Z	QPM, eee (PSI)
PPKTP	Z	QPM, eee (PSI)
LBO	Z	Type I, NCPM ooe (PSI): $\hat{\epsilon}=90^\circ, \phi=0^\circ$

According to Fig. 2.4.1, PPLN has the largest GVD among all of the studied crystals. KTP has much smaller GVD than PPKTP. The LBO crystal has very small dispersion around 1.2 μm , and the GVD of LBO becomes negative when the

wavelength is longer than 1.215 μm , which should be considered when designing the intracavity GVD compensation mechanism.

We give the GVM values between the pump and the signal (P-S), the signal and the idler (S-I), and between the pump and the idler (P-I) for KTP and PPKTP crystals in Fig. 2.4.2 and Fig. 2.4.3. The GVM characteristics of PPLN is given in Fig. 2.3.13 in Chapter 2.3.

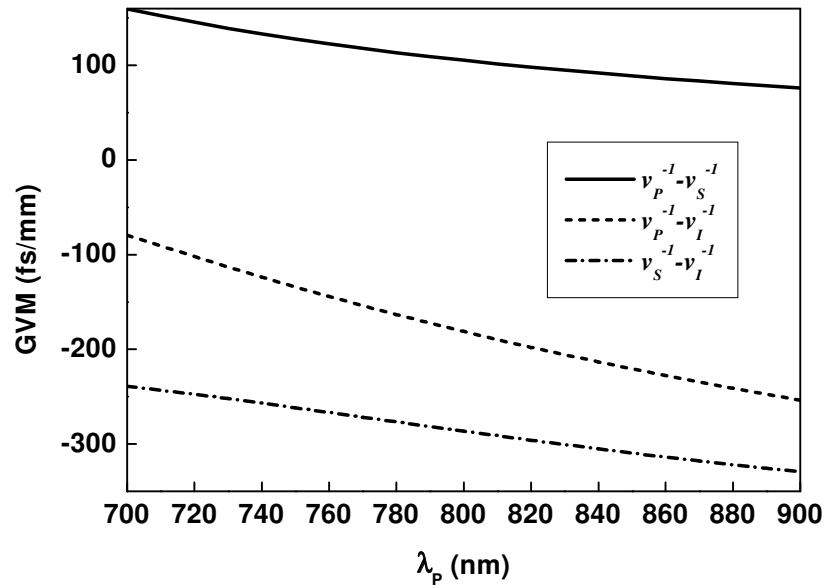


Fig. 2.4.2 GVM between the interaction waves of a KTP OPO vs. pump wavelength (λ_p).

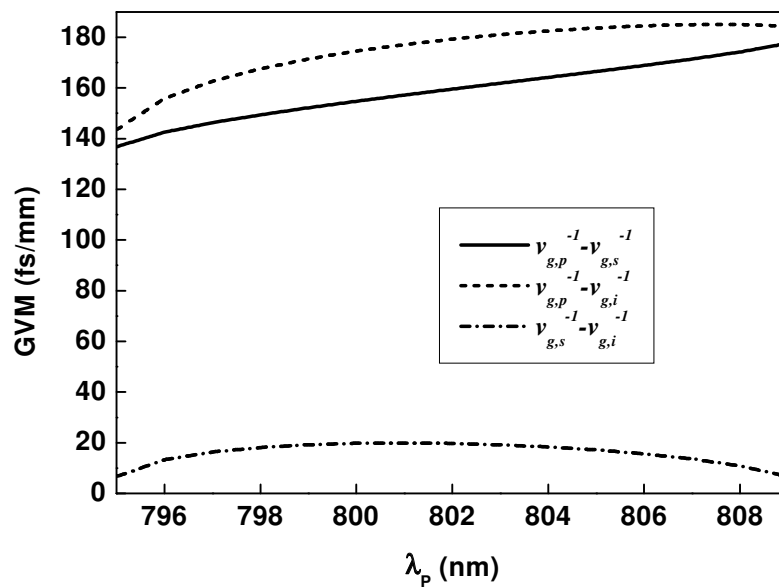


Fig. 2.4.3 GVM between the interaction waves of a PPKTP OPO vs. pump wavelength. The poling period of PPKTP is 28 μm .

2.4.3 Pulse broadening effects induced by GVM

To understand the pulse shaping and broadening effect induced by GVM, we developed a simplified numerical method to solve the coupled equations for optical parametric process, in which the GVM and GVD can be both included.

Different work [32-34, 59, 60] has been done to solve the coupled equations for optical parametric processes. Complicated derivations and complicated numerical methods were introduced to find solutions to the coupled equations given in (2.4.7).

$$\begin{cases} \left(\frac{\partial}{\partial z} + \frac{1}{v_s} \frac{\partial}{\partial t} \right) E_s = iK_s E_I^* E_P \exp(j\Delta kz) \\ \left(\frac{\partial}{\partial z} + \frac{1}{v_I} \frac{\partial}{\partial t} \right) E_I = iK_I E_S^* E_P \exp(j\Delta kz) \\ \left(\frac{\partial}{\partial z} + \frac{1}{v_P} \frac{\partial}{\partial t} \right) E_P = iK_P E_S E_I \exp(-j\Delta kz) \end{cases} \quad (2.4.7)$$

where $K_i = \frac{2\pi d_{eff}}{n_i \lambda_i}$, $i = P, S, I$, and E_S , E_I , and E_P are the amplitudes of the electric fields of the signal, the idler, and the pump, respectively.

Here we introduce acceptable approximations and use a very simple numerical method to solve the equations in (2.4.7). In our analysis, we considered only the NCPM case, where all of the interaction waves propagated in the same direction. Suppose the three interacting pulses (P , S , and I) have the same starting point at $(0, t)$. Because of the group velocity mismatch among the three interaction waves, a specific position z in the direction of propagation in the crystal corresponds to different time

points for the three pulses, which are $t - \frac{z}{v_s}$ for E_S , $t - \frac{z}{v_I}$ for E_I , and $t - \frac{z}{v_P}$ for E_P .

Thus, the amplification in the amplitude of the electric field of E_S at (z, t) results from the interaction between E_I^* and E_P at $(z, t - \frac{z}{v_I} + \frac{z}{v_s})$ and $(z, t - \frac{z}{v_P} + \frac{z}{v_s})$,

respectively. Similar relations can also be obtained for E_I and E_P . Considering these

relations will result in the elimination of the factors of $\frac{1}{v_i} \frac{\partial}{\partial t} E_i$ ($i = P, S, I$) in the

equations in (2.4.7). So the following modified coupled equations can be obtained:

$$\begin{cases} \frac{\partial}{\partial z} E_S(z,t) = iK_S E_I^* \left(z, t - \frac{z}{v_I} + \frac{z}{v_S} \right) E_P \left(z, t - \frac{z}{v_P} + \frac{z}{v_S} \right) \exp(j\Delta kz) \\ \frac{\partial}{\partial z} E_I(z,t) = iK_I E_S^* \left(z, t - \frac{z}{v_S} + \frac{z}{v_I} \right) E_P \left(z, t - \frac{z}{v_P} + \frac{z}{v_I} \right) \exp(j\Delta kz) \\ \frac{\partial}{\partial z} E_P(z,t) = iK_P E_S \left(z, t - \frac{z}{v_S} + \frac{z}{v_P} \right) E_I \left(z, t - \frac{z}{v_I} + \frac{z}{v_P} \right) \exp(-j\Delta kz) \end{cases} \quad (2.4.8)$$

To solve the equations in (2.4.8) numerically, we divide the nonlinear crystal into multiple slabs, as shown in Fig. 2.4.4.

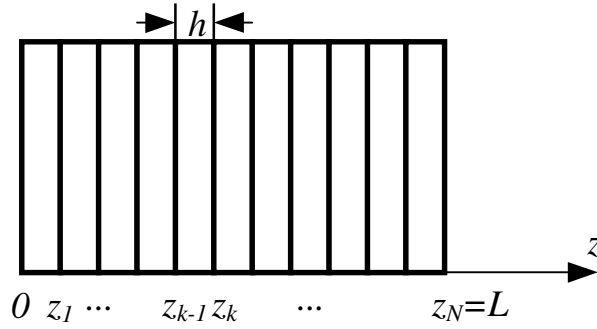


Fig. 2.4.4 Division of the crystal for solving the modified coupling equations in (2.4.8).

If the thickness of each slab (h) is small enough so that the term of $\frac{\partial}{\partial z} E_i(z,t)$ ($i=P, S, I$) can be replaced by $\frac{E_i(z_k, t) - E_i(z_{k-1}, t)}{z_k - z_{k-1}}$, where $k=1 \sim N$, $N = \text{integer}(L/h)$,

$h = z_k - z_{k-1}$, L is the total length of the crystal, the equations in (2.4.8) can be rewritten as:

$$\begin{cases} E_S(z_k, t) = \frac{E_S(z_{k-1}, t) + jhK_S E_I^* \left(z_{k-1}, t - \frac{z_{k-1}}{v_I} + \frac{z_{k-1}}{v_S} \right) E_P \left(z_{k-1}, t - \frac{z_{k-1}}{v_P} + \frac{z_{k-1}}{v_S} \right) \exp(j\Delta kz_k)}{1 - h^2 K_S K_I \left| E_P \left(z_{k-1}, t - \frac{z_{k-1}}{v_P} + \frac{z_{k-1}}{v_S} \right) \right|^2} \\ E_I(z_k, t) = \frac{E_I(z_{k-1}, t) + jhK_I E_S^* \left(z_k, t - \frac{z_k}{v_S} + \frac{z_k}{v_I} \right) E_P \left(z_{k-1}, t - \frac{z_{k-1}}{v_P} + \frac{z_{k-1}}{v_I} \right) \exp(j\Delta kz_k)}{1 - h^2 K_S K_I \left| E_P \left(z_{k-1}, t - \frac{z_{k-1}}{v_P} + \frac{z_{k-1}}{v_I} \right) \right|^2} \\ E_P(z_k, t) = \frac{E_P(z_{k-1}, t) + jhK_P E_S \left(z_k, t - \frac{z_k}{v_S} + \frac{z_k}{v_P} \right) E_I \left(z_k, t - \frac{z_k}{v_I} + \frac{z_k}{v_P} \right) \exp(-j\Delta kz_k)}{1 + h^2 K_I K_P \left| E_S \left(z_k, t - \frac{z_k}{v_S} + \frac{z_k}{v_P} \right) \right|^2} \end{cases}$$

where we have substituted the expressions of E_I and E_P into E_I , those of E_S and E_P into E_I , and those of E_S and E_I into E_P , and have included small gain approximation when considering very small h . Then we can solve the coupled equations numerically from slab to slab.

The GVD can be included when considering that each wave has a spectral distribution. We can first digitize the spectrum of each field and then solve the coupled equations for each spectral component. Since each spectral component has its own group velocity, it will be shifted and broadened differently in the time domain when compared with others. Overlapping all of the spectral components will give us the overall influence from both GVM and GVD on the pulse shape and pulse duration.

Here we take only the GVM into account and analyze how the signal, pump, and idler pulses change in shape and in duration when they pass through a certain amount of nonlinear crystal. In the following simulations, we considered a KTP OPO pumped by a Ti:sapphire laser at 800 nm, which is noncritically phase-matched (type II), so that the signal oscillates at 1141.4 nm and the idler is generated at 2674.6 nm. The pump pulses were assumed to be about 100 fs long ($\tau_P = 100$ fs). All of the interaction pulses are Gaussian. The calculations were done for a single-pass interaction between the pump, the signal, and the idler.

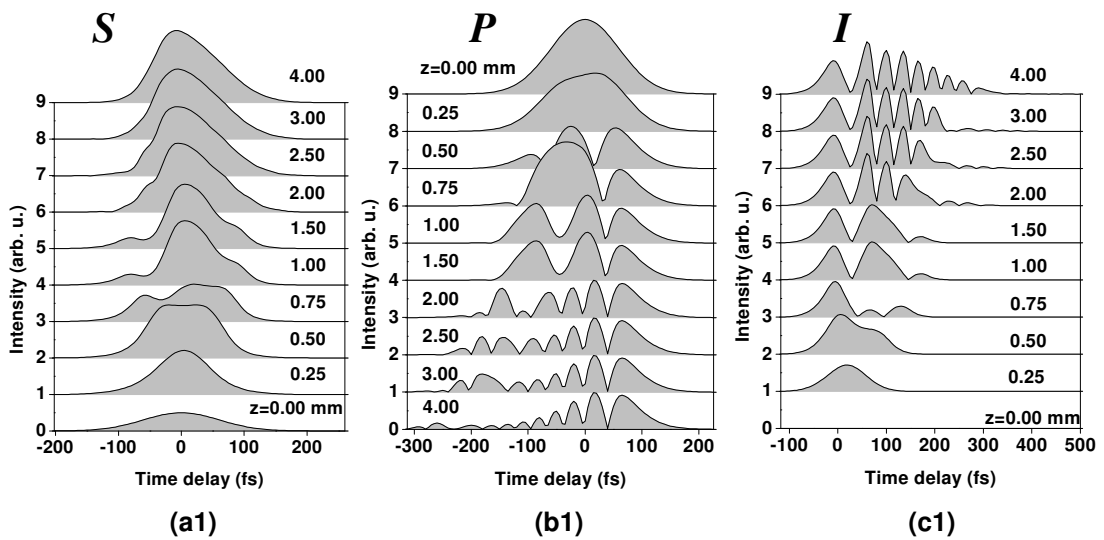
In the initial state, the signal is assumed to have the same pulse duration as the pump and there is no idler wave generated. We assumed perfect phase matching ($\Delta k=0$) for the interaction. The delay between the pump and the signal is normally adjusted through cavity length tuning of the OPO. Since the signal propagates faster than the pump in the KTP crystal, it should arrive a little later than the pump at the front surface of the crystal to get sufficient interaction with the pump. There should exist an optimal delay for the highest conversion efficiency from the pump to the signal.

Figure 2.4.5 (a1), (b1), and (c1) present the variation of the intensity and pulse shape of the signal (S), the pump (P), and the idler (I), respectively, when assuming that the signal and the pump arrive at the KTP crystal simultaneously. Due to the separation between the pump and the signal pulses, the signal pulse did not change any more after propagating by about 2 mm. While the idler propagated slightly slower than the signal, the pump pulse was depleted further and the idler pulse increased slowly with increasing the crystal length. Very structured pump and idler pulse shapes

can be observed. In Fig. 2.4.5 (a2), (b2), and (c2), the delay between the signal and the pump was increased to $\tau_p/2$ (50 fs). Obviously, the signal pulse gained more amplification, the pump pulse got more depleted, and the idler became more structured. The effective interaction length increased to 2.5 mm, where the signal pulse shape did not change any more. When the delay between the signal and the pump was increased to τ_p (100 fs), as shown in Fig. 2.4.5 (a3), (b3), and (c3), the gain in the signal increased further, but less energy was transferred from the pump to the idler, so that the pump was not depleted as largely as in the case of $\tau_p/2$ delay in the later stage of interaction. The signal and idler pulses became narrower when compared with Fig. 2.4.5 (a2) and (c2). The signal pulse shape did not change any more after 3 mm of interaction. For $2\tau_p$ (200 fs) delay between the pump and the signal, more energy was transferred to the signal than in all above cases, and consequently, the gain in the idler was much less, as shown in Fig. 2.4.5 (a4), (b4), and (c4). But the signal pulse was largely broadened and a quite long tail can also be observed in the idler pulse.

Comparing the results in Fig. 2.4.5, we can conclude that the optimal delay between the pump and the signal is around τ_p , where the largest gain in the signal pulse and the shortest signal pulse duration can be achieved, which corresponds to about 30 μm lengthening of the OPO cavity.

The simulation results in Fig. 2.4.5 can be comparable to those given in Ref. [59].



2.4.3 Pulse broadening effects induced by GVM

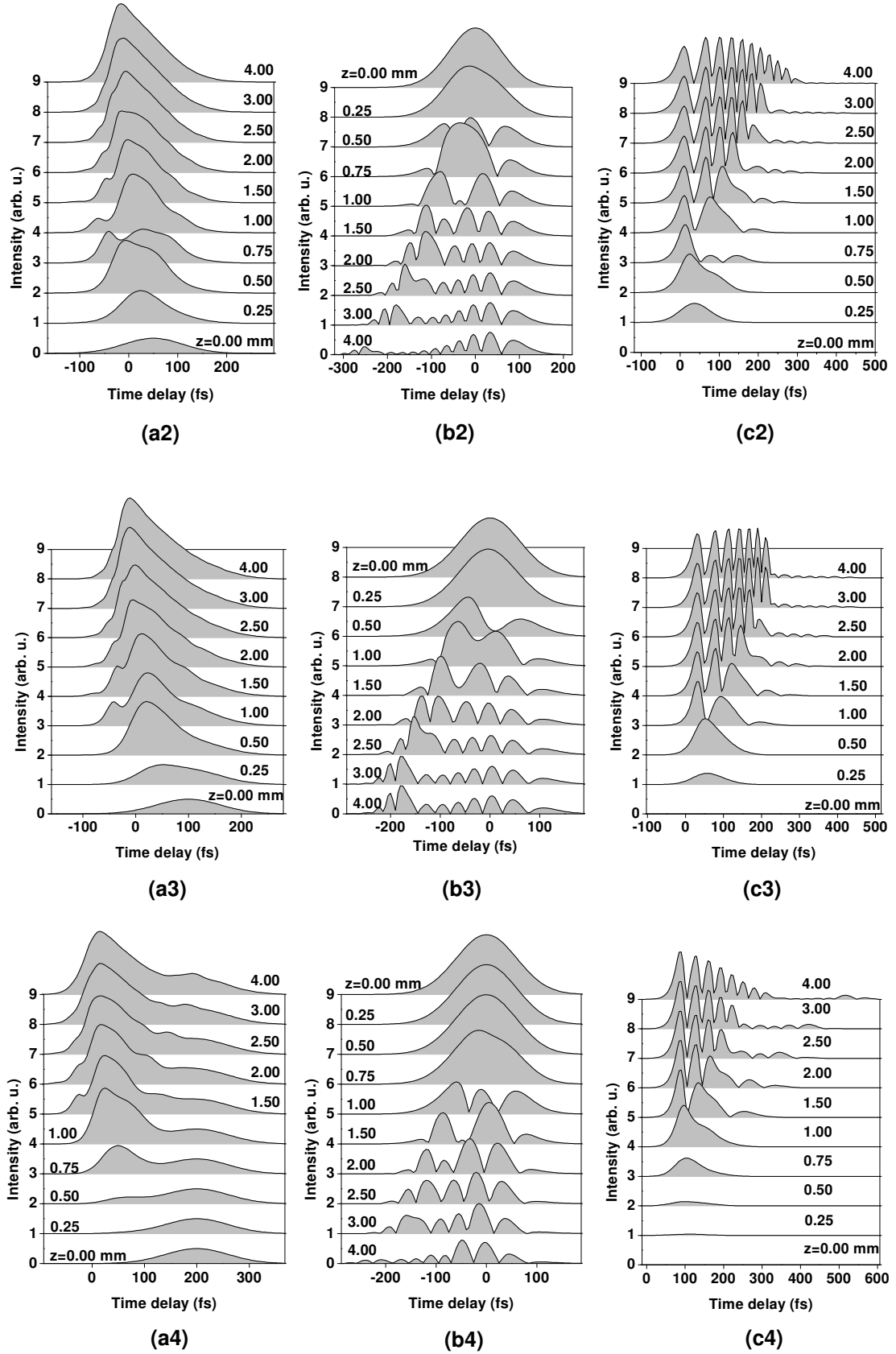


Fig. 2.4.5 Variation of the pulse shapes and pulse durations of the signal, the pump, and idlers after a certain length of interaction in the KTP crystal. The delay between the signal and the pump (the signal behind the pump) was: 0, $\tau_p/2$, τ_p , and $2\tau_p$ in the four groups of data, respectively.

In above simulations, the phase mismatch for the OPO process was assumed to be 0. If we consider the spectral bandwidths of both the pump and the signal, as well as the phase matching bandwidth, the simulations will match more closely the practical cases. For simplicity, we give a fixed value of phase mismatch and solve the coupled equations for a interaction length of 3 mm and a delay of 100 fs between the signal and the pump pulses which initially are both 100 fs long. Fig. 2.4.6 shows the simulation results. It is obvious that the gain in the signal and the idler and the depletion in the pump decrease with increasing Δk . When Δk is smaller than 2π , there is significant gain in the signal and idler pulses and the pump can be largely depleted. When Δk is about 10π , there is almost no gain in the signal pulses and very little idler was generated, and the pump pulse remains almost unchanged.

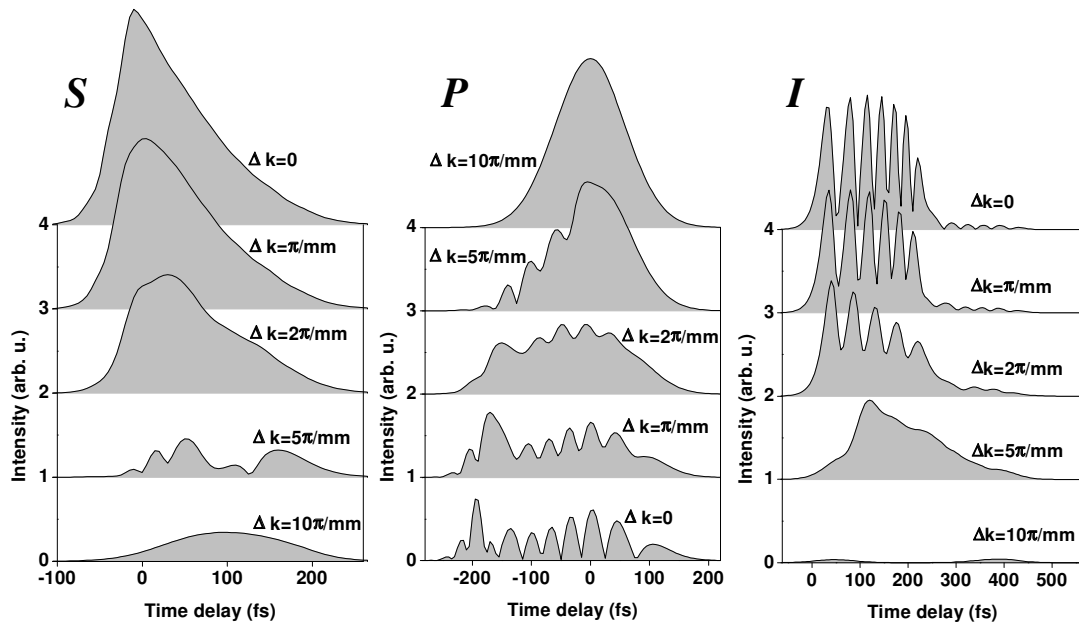


Fig. 2.4.6 Variation of the signal (*S*), the pump (*P*), and the idler (*I*) pulses for a single-pass interaction between them in a KTP OPO. The signal and pump pulses were assumed to be 100 fs long and the signal pulse is delayed 100 fs from the pump. The KTP crystal is 3 mm long.

2.4.4 Dispersion characteristics of some optical glasses and pulse broadening effects

GVD leads to a linear chirp of the pulses that propagate through the nonlinear material, consequently the pulses will get broadened, which can be described quantitatively by the following formula [61]:

$$\tau_p(z) = \tau_0 \sqrt{1 + \left(\frac{z}{z_d}\right)^2} \quad (2.4.9)$$

where τ_0 is the unchirped pulse duration before entering the dispersive material, τ_p is the pulse duration after passing through the material, z is the propagating path length in the material, z_d is called the characteristic length that is defined as:

$$z_d = \frac{1}{4 \ln 2} \frac{\tau_0^2}{d^2 k / d\omega^2} \quad (2.4.10).$$

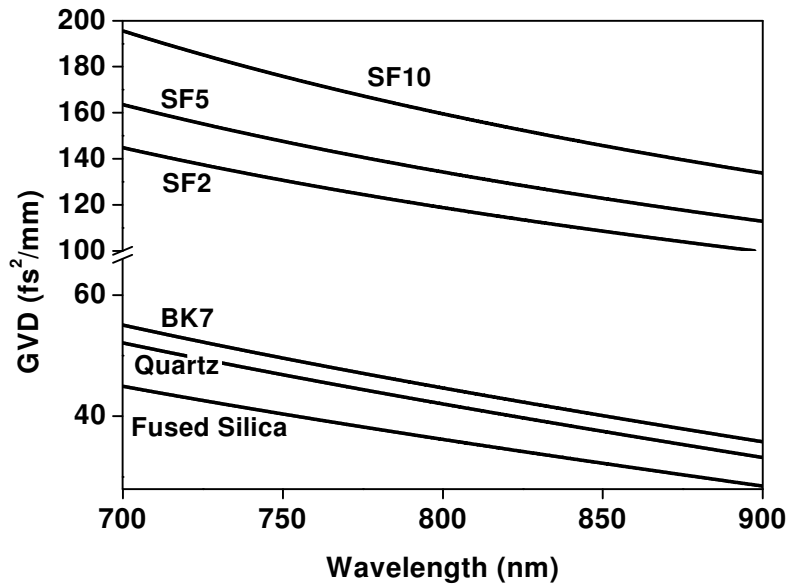
The GVD is included in z_d by the $d^2 k / d\omega^2$. Obviously, if we know the initial pulse duration, GVD and the length of the material, we can easily estimate the pulse duration after passing through the material. Some detailed discussions about chirping and broadening of pulses propagating in dispersion materials, as well as the derivation of formula (2.4.9) are given in [61].

In addition to the nonlinear crystals, some common glasses, such as BK7, fused silica, quartz, SF2, SF5, and SF10, which are normally the materials of the output couplers, the lenses, the prisms, or the beam splitters, etc., also introduce dispersion to the signal pulses of the OPO inside or outside the cavity. Fig. 2.4.7 (a) and (b) present the GVD of these glasses for two spectral ranges: 700 - 900 nm and 1000 - 1600 nm, respectively.

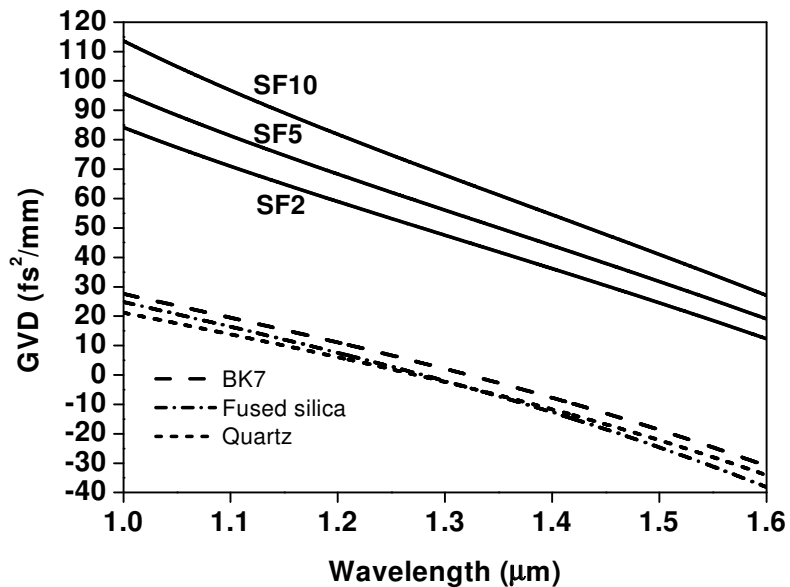
If the pulses propagate through multiple optical components, we should go from one component to the next to calculate the broadened pulse duration and finish all of the components separately, instead of accumulating the total amount of the glass at first and then calculating the broadening.

Figure 2.4.8 (a) through (f) illustrate the broadening effects when the pulses pass through three types of glasses: BK7, fused silica, and quartz. The pulses were assumed to be centered at 800 nm and 1200 nm and changed in duration from 10 fs to 60 fs. We can conclude from Fig. 2.4.8 that shorter pulses are more strongly broadened when they pass through the same amount of dispersion material. Since the three kinds of glasses have a much larger GVD at 800 nm than at 1200 nm, the broadening effect at 800 nm is also much more serious than at 1200 nm. When the pulses are longer than 40 fs, there is almost no broadening to the input pulses at 1200 nm. According to our calculations, pulses longer than 100 fs (at 800 nm) will be broadened very little when they pass through the above three glasses. All of the above three glasses have a zero GVD around 1.3 μm , and the GVD of them becomes

negative at longer wavelengths, so that the input transform-limited pulses will get negatively chirped. Prism-pairs made of such glasses cannot be used to compensate for intracavity GVD in lasers or OPOs or to compress extracavity pulses at longer wavelength than 1.3 μm .



(a)



(b)

Fig. 2.4.7 GVD of some common glasses for the spectral ranges of (a) 700-900 nm and (b) 1000-1600 nm.

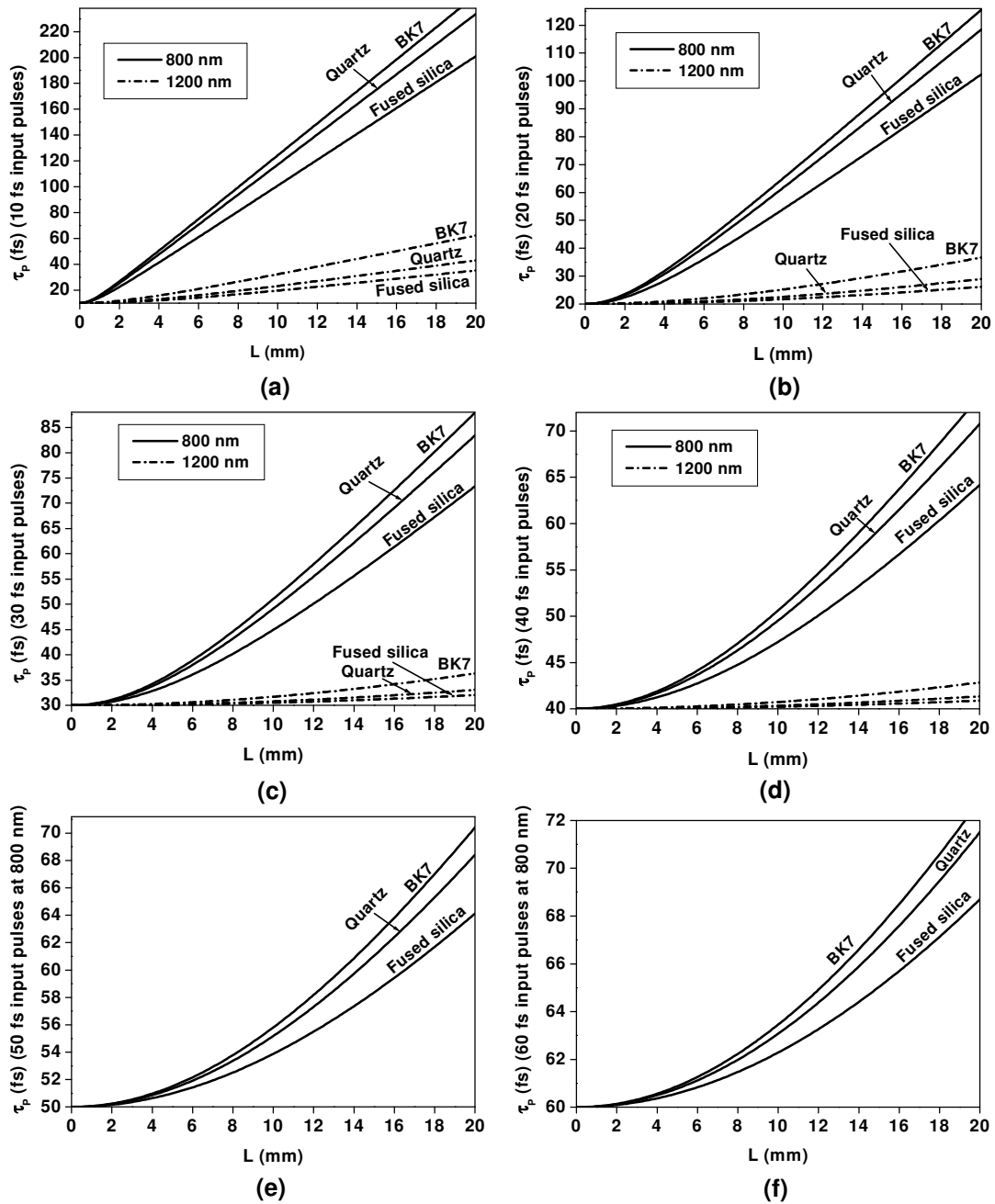


Fig. 2.4.8 Pulse broadening characteristics in BK7, Fused silica and Quartz glasses at different input pulse durations.

2.5

GVD compensation and pulse compression methods

2.5.1 Prism pair

A. Negative GDD created by a prism pair [61]

A prism pair as depicted in Fig. 2.5.1 can introduce negative GDD to the input pulses, therefore serving as a device for intracavity GVD compensation or extracavity pulse compression.

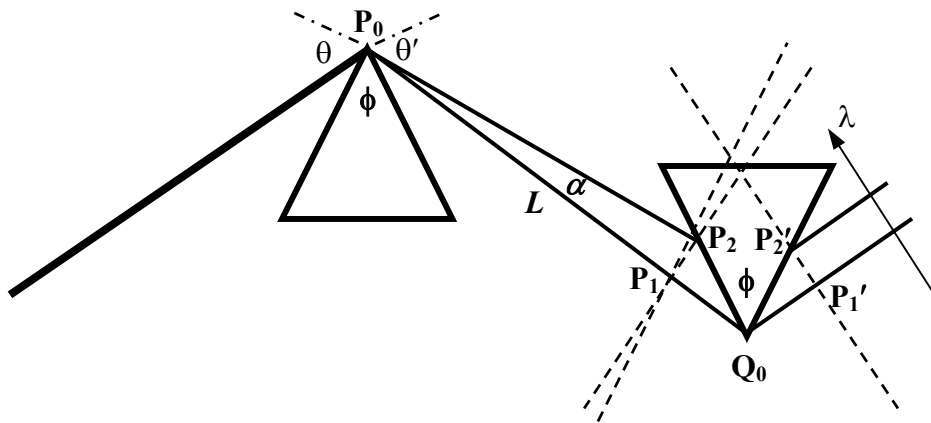


Fig. 2.5.1 Angular dispersion induced by a prism pair.

The compensation for GVD by prism pairs is based on the angular dispersion induced by the prisms to the incidence laser beam. As shown in Fig. 2.5.1, the laser beam is incident at Brewster angle for a center wavelength (λ_0) on the apex (P_0) of the first prism. The dispersed and spread-out beam hits also on the apex of the second prism (Q_0). Because the two prisms are parallel to each other with their apexes aligned in opposite directions, the beam at the output of the second prism becomes parallel again. The angular dispersion that takes place between the two prisms is designated by the angle $\alpha(\lambda)$ which is a function of wavelength. Since $\alpha(\lambda)$ is a very small angle, the wavefront at $\overline{P_1 P_2}$ has approximately the same phase as that at $\overline{P_1' P_2'}$. The optical path length of $\overline{P_0 P_1}$ corresponds to the shortest spectral component of the laser beam. Then at the point of P_1 , the optical path length of any other spectral components can be expressed as:

$$l(\lambda) = \overline{P_0 P_1} \cos \alpha ,$$

and the phase delay can be written as:

$$\Psi_\alpha = \frac{2\pi}{\lambda} \overline{P_0 P_1} \cos \alpha .$$

Because of the small value of α and the normally large distance between the two prisms ($\overline{P_0 P_1} \gg \overline{P_1 Q}$), $\overline{P_0 P_1}$ can be approximate to the distance between the apexes of the prisms (L), so that

$$\Psi_\alpha = \frac{2\pi}{\lambda} L \cos \alpha = \frac{\omega}{c} L \cos \alpha$$

where $\omega = \frac{2\pi c}{\lambda}$ is the angular frequency and c is the velocity of light in vacuum.

Then the GDD induced by the angular dispersion can be derived as

$$\frac{d^2 \Psi_\alpha}{d\omega^2} = -\frac{L}{c} \left\{ \sin \alpha \left[2 \frac{d\alpha}{d\omega} + \omega \frac{d^2 \alpha}{d\omega^2} \right] + \omega \cos \alpha \left(\frac{d\alpha}{d\omega} \right)^2 \right\} \quad (2.5.1)$$

Because α is very small, we can assume $\sin \alpha \approx 0$ and $\cos \alpha \approx 1$, so that (2.5.1) can be approximately written as

$$\frac{d^2 \Psi_\alpha}{d\omega^2} = -\frac{\omega L}{c} \left(\frac{d\alpha}{d\omega} \right)^2 \quad (2.5.2)$$

Obviously, formula (2.5.2) creates a negative value, which is the reason why a prism pair can be used to compensate for the positive GVD from optical crystals and glass elements.

To calculate (2.5.2) we need to specify $d\alpha/d\omega$. Considering

$$\frac{d\alpha}{d\omega} = \frac{d\alpha}{dn} \frac{dn}{d\omega} \quad \text{and} \quad \frac{dn}{d\omega} = -\frac{\lambda^2}{2\pi c} \frac{dn}{d\lambda}$$

where n is the refractive index of the prism material, we only need to calculate $d\alpha/dn$.

We use the geometry shown in Fig. 2.5.2 to determine $d\alpha/dn$.

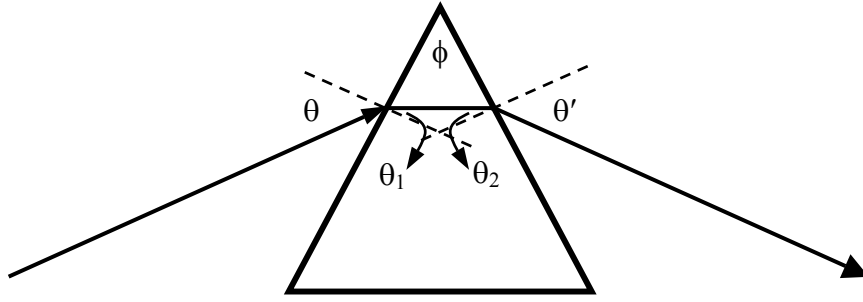


Fig. 2.5.2 Geometry of the prism to determine the angular dispersion.

The following relationships can be derived on the basis of Fig. 2.5.2:

$$\sin \theta = n \sin \theta_1 \quad (2.5.3)$$

$$\sin \theta' = n \sin \theta_2 \quad (2.5.4)$$

$$\theta_1 + \theta_2 = \phi \quad (2.5.5)$$

From (2.5.3), (2.5.4), and (2.5.5), we can obtain

$$\cos \theta \frac{d\theta}{dn} = \sin \theta_1 + n \cos \theta_1 \frac{d\theta_1}{dn} \quad (2.5.6)$$

$$\cos \theta' \frac{d\theta'}{dn} = \sin \theta_2 + n \cos \theta_2 \frac{d\theta_2}{dn} \quad (2.5.7)$$

$$\frac{d\theta_2}{dn} = -\frac{d\theta_1}{dn} \quad (2.5.8)$$

Since θ is fixed, $\frac{d\theta}{dn} = 0$, we can derive that

$$\frac{d\theta_2}{dn} = -\frac{d\theta_1}{dn} = \frac{1}{n} \operatorname{tg} \theta_1 \quad (2.5.9)$$

From (2.5.6), (2.5.7), and (2.5.9), we can derive that

$$\frac{d\theta'}{dn} = \frac{\sin \theta_2}{\cos \theta'} + \frac{\cos \theta_2}{\cos \theta'} \operatorname{tg} \theta_1 \quad (2.5.10).$$

Considering Brewster angle incidence at λ_0 , $\theta'|_{\lambda_0} = \theta$ and $\theta_1|_{\lambda_0} = \theta_2|_{\lambda_0}$ and substituting these relations together with (2.5.3) into (2.5.10), we can obtain easily

$$\left. \frac{d\theta'}{dn} \right|_{\lambda_0} = 2 \quad (2.5.11)$$

According to Fig. 2.5.1 and Fig. 2.5.2, it is understandable that $\frac{d\alpha}{dn} = \frac{d\theta'}{dn}$. Consequently, the formula (2.5.2) can be rewritten as

$$\boxed{\Psi_{\alpha}''(\lambda_0) = \frac{d^2\Psi_{\alpha}}{d\omega^2}\bigg|_{\lambda_0} = -4L \frac{\lambda_0^3}{2\pi c^2} \left(\frac{dn}{d\lambda}\bigg|_{\lambda_0} \right)^2} \quad (2.5.12)$$

Formula (2.5.12) is the final expression for the single-path negative GVD at λ_0 created by the prism pair.

B. Positive GVD induced by a prism pair

Because the laser beam propagates through some amount of the prism material, some additional positive GDD will be introduced to the laser pulses, which should also be considered while calculating the total amount of GDD created by the prism pairs.

Suppose the cumulative mean glass path through the prisms is l , then the positive GDD parameter can be calculated simply by

$$\Psi_P''(\lambda_0) = \frac{d^2\Psi_P}{d\omega^2}\bigg|_{\lambda_0} = \frac{\lambda_0^3 l}{2\pi c^2} \frac{d^2 n}{d\lambda^2}\bigg|_{\lambda_0} \quad (2.5.13)$$

If we know the material of the prisms, $\frac{d^2 n}{d\lambda^2}\bigg|_{\lambda_0}$ can be determined easily. Therefore,

we just need to find the mean path length (l) of glass that the pulses go through. We assume that the center wavelength (λ_0), at which the Brewster angle was specified, has a mean path length. In other words, we can think that this wavelength propagates in the spatially mid-way between paths of the longer and shorter ends of the laser spectrum. Then l depends mainly on the incident beam size and the material of the prisms. Suppose that the diameter of the laser beam at incidence is D , the Brewster angle at λ_0 is θ ($\tan\theta = n_0$, n_0 is the refractive index of the prism material at λ_0), and the incidence laser pulses have a spectral bandwidth of $\Delta\lambda$, we can obtain the expression of l after some simple geometric analysis:

$$l = \frac{2 \left(D + \left| \frac{dn}{d\lambda} \right| \Delta\lambda L \right) \sin \frac{\phi}{2}}{\cos \theta} \quad (2.5.14)$$

Substituting (2.5.14) into (2.5.13), we can obtain the positive GDD introduced by the prism inside the light path:

$$\Psi_P''(\lambda_0) = \frac{\lambda_0^3}{2\pi c^2} \frac{2 \left(D + \left| \frac{dn}{d\lambda} \right| \Delta \lambda L \right) \sin \frac{\phi}{2} \left| \frac{d^2 n}{d\lambda^2} \right|_{\lambda_0}}{\cos \theta} \quad (2.5.15)$$

The total GDD introduced by a single pass through a prism pair is given by the summation of (2.5.12) and (2.5.15):

$$\Psi_T''(\lambda_0) = \Psi_\alpha''(\lambda_0) + \Psi_P''(\lambda_0) \quad (2.5.16)$$

C. Design of prism pairs for intracavity GVD compensation or extracavity pulse compression

It can be deduced from Fig. 2.5.1 that behind the second prism the spectral components of the laser pulses are spatially separated and spread out in the direction perpendicular to the propagation. We can select a certain wavelength by just placing a slit in the laser beam behind the second prism. In a laser cavity, however, or at the output of a laser for practical applications, we expect a single laser beam with all its spectral components overlapped, meaning that no transverse displacement of any spectral components (spatial chirp) is allowed. Therefore, we can apply two configurations of prism pairs for practical design, as illustrated in Fig. 2.5.3 (a) and (b). In this way, the value of (2.5.16) should be doubled ($2\Psi_T''$) to calculate the practical GDD introduced by the prism pair(s). A slit can be put between the prism P2 and the high reflection mirror M in Fig. 2.5.3(a) or between the prisms P2 and P3 in Fig. 2.5.3(b) to serve as a wavelength selection or tuning device.

The GDD of the prism pairs is still adjustable by translating the apexes of the prisms inward or outward with respect to the laser beam.

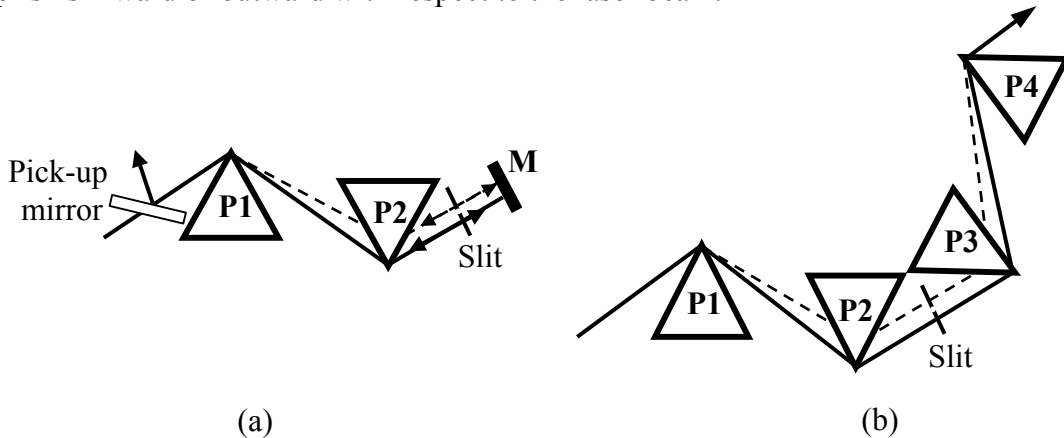


Fig. 2.5.3 Configurations of prism pairs without transverse displacement of spectral components.

To design a prism-pair system for intracavity GVD compensation, we need to know the following parameters in advance:

- (1) Expected center wavelength of the oscillating laser pulses (λ_0).
- (2) Expected bandwidth ($\Delta\lambda$) (or the transform-limited pulse duration) of the oscillating pulses.
- (3) GVD of the laser gain medium (laser or OPO crystals) and length of the medium.
- (4) GVD of other intracavity optical components (the amount of dispersion glasses) that the laser pulses will pass through.

The parameters to be designed for a prism-pair system include:

- (1) Material of the prisms (refractive index and GVD of the material).
- (2) Apex angle of each prism (ϕ).
- (3) Distance between the paired prisms (L).

In the following discussion, we assume a linear (standing-wave) cavity for a laser or an OPO to be studied, so that the prism-pair configuration in Fig. 2.5.3(a) will be our choice. The pick-up mirror in Fig. 2.5.3 (a) should be removed out of the laser beam.

Then the prism-pairs can be designed in the following way:

- Select a glass material with low third-order dispersion for the prisms.
- Calculate the Brewster for the prism material at λ_0 using $\tan\theta=n_0$, where θ is the Brewster angle and n_0 is the refractive index at λ_0 .
- Calculate the apex angle of each prism using $\phi=2\sin^{-1}(\sin\theta/n_0)$.
- Calculated the total GDD (fs^2 , GVD \times Length of the medium) of the crystals and all of the glass components: Ψ_O'' in the laser or OPO cavity.
- Estimate the diameter of laser beam in the cavity and substitute it into (2.5.14), then calculate the distance between the two prisms by substituting (2.5.12) and (2.5.15) into (2.5.16) and solving the equation:

$$\Psi_T'' = -\Psi_O'' \quad (2.5.17)$$

This concludes the design of a prism pair for intracavity GVD compensation.

Here we give an example designing a prism-pair system for a 10 fs Ti:sapphire laser using a 4.75 mm Ti:sapphire crystal and operating at a center wavelength of 800 nm and a repetition rate of 80 MHz:

We use fused silica as the material for the prisms. The Brewster angle for fused silica at 800 nm is $\theta = 55.469^\circ$, then the apex angle of the prisms is $\phi = 69.063^\circ$.

The GVD of sapphire was calculated (using the Sellmeier equations in Appendix A) to be $58.1812 \text{ fs}^2/\text{mm}$, so that the 4.75 mm Ti:sapphire crystal creates a single-path intracavity GDD of 276.36 fs^2 .

Assuming that the intracavity beam diameter of the laser is 4 mm, the first order ($dn/d\lambda$) and second order ($d^2n/d\lambda^2$) dispersion of fused silica are $-0.0173/\mu\text{m}$ and $0.04/\mu\text{m}^2$, respectively. The GVD of fused silica is $36.22 \text{ fs}^2/\text{mm}$.

Transform-limited 10 fs pulses correspond to a spectral bandwidth (at FWHM) of about 92 nm ($\Delta\lambda \approx 92 \text{ nm}$).

Since we used the single-path GDD of the Ti:sapphire crystal, we should also use single-path GDD from the prism-pair. Solving the equation (2.5.17), we can obtain the distance between the two prisms, which is $L = 584.4 \text{ mm}$.

In practice, we use a larger distance between the prisms than the value of L given above and translate the prism (P1) a little more into the laser beam, so that we have enough flexibility to adjust the compensation.

The design procedure of prism pairs for extracavity pulse compression is almost the same as that for intracavity compensation. We just need to estimate how much the intracavity pulses are positively chirped and how much extracavity glass (including the output coupler) the output pulses will pass through, and then determine the positive GDD to be compensated for. The prism pairs can be designed similarly as described above.

Figure 2.5.4 illustrates the variation of the GDD (double pass, at 800 nm) introduced by a prism pair made of fused silica versus the distance between the two prisms. We assumed that the incident beam diameter was 4 mm and the two lines correspond to a spectral bandwidth of 100 nm and 30 nm, respectively.

In practice, the divergence of the intracavity laser beam influences both the diameter of the laser beam and the difference between the beam sizes on the two prisms. This will change considerably the positive GDD introduced by the prisms, which makes it difficult to design precisely the distance between the prisms. This is also one of the reasons why we should better initially use a longer distance than the calculated value and allow space for later adjustment.

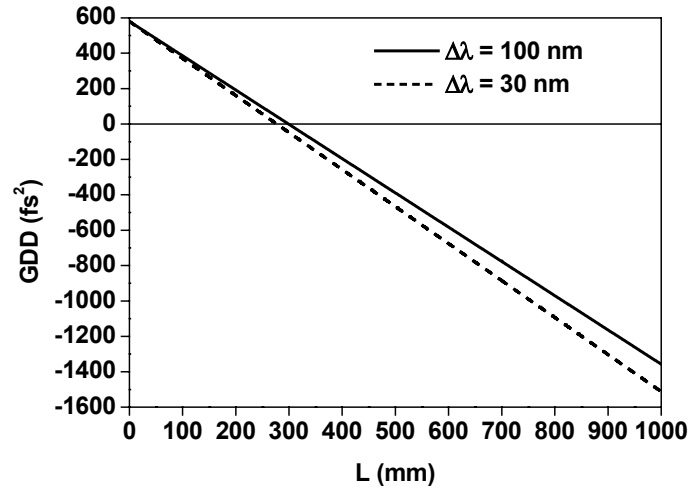


Fig. 2.5.4 GDD of a prism pair versus the distance (L) between the two prisms.

2.5.2 Grating pair

Gratings can produce larger angular dispersion than prisms. The resulting negative GVD can be utilized to compress pulses. Due to the low transmission efficiency (< 80%) of the gratings, prism pairs rather than grating pairs are mostly used intracavity. Grating pairs are more suitable for the shaping of high-power pulses, avoiding undesired nonlinear optical effects in the glass materials. [61]

Figure 2.5.5 shows the arrangement of a pair of parallel gratings (G1 and G2) creating negative GDD, where β is the incidence angle, $\beta'+\alpha$ is the diffraction angle for the wavelength of λ , λ_0 is the wavelength at which $\alpha=0$, b is the normal separation between G1 and G2.

According to Fig. 2.5.5, the path length from A to the wave front at $\overline{CC_0}$ at wavelength λ can be expressed as:

$$L(\lambda) = \overline{ABC} = \frac{b}{\cos(\beta'+\alpha)} [1 + \cos(\beta + \beta'+\alpha)] \quad (2.5.18)$$

And the corresponding phase delay is

$$\Psi_L(\lambda) = \frac{2\pi}{\lambda} L(\lambda) \quad (2.5.19)$$

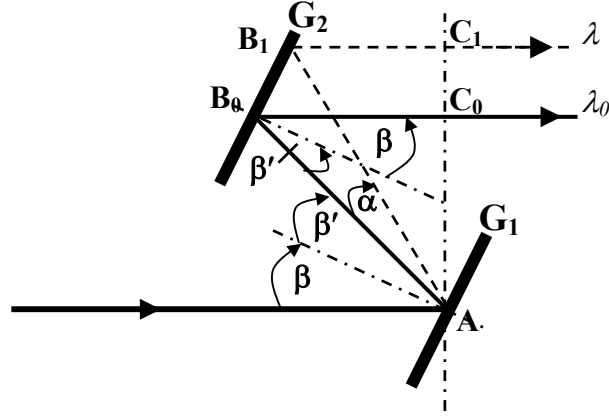


Fig. 2.5.5 Grating pair producing negative GDD.

The peculiarity of a grating is that it introduces an additional phase shift of 2π at each groove of G2. If assuming the grating constant d , the total phase shift due to the grooves can be written as:

$$\Psi_R(\lambda) = 2\pi \frac{btg(\alpha + \beta')}{d} \quad (2.5.20)$$

The total phase delay introduced by the prism pair is given by the summation of (2.5.19) and (2.5.20):

$$\Psi(\lambda) = \Psi_L(\lambda) + \Psi_R(\lambda) \quad (2.5.21)$$

Using the grating equations

$$\sin \beta - \sin \beta' = -\frac{\lambda_0}{d} \quad (2.5.22)$$

$$\sin \beta - \sin(\beta' + \alpha) = -\frac{\lambda}{d} \quad (2.5.23)$$

we can obtain $\frac{d\alpha}{d\omega} = -\frac{\lambda^2}{2\pi c \cdot \cos(\beta' + \alpha)d}$ and $\left. \frac{d\alpha}{d\omega} \right|_{\lambda_0} = -\frac{\lambda^2}{2\pi c \cdot \cos \beta' d}$.

Thus the final expression for the GDD produced by the grating pair is

$$\left. \frac{d^2\Psi}{d\omega^2} \right|_{\lambda_0} = -\frac{b\lambda_0^3}{2\pi c^2 d^2 \cos^3 \beta'} \quad (2.5.24)$$

Obviously, a grating pair produces negative GDD to the incident laser pulses.

The transverse displacement of the spectral components at the output of the second grating can be compensated by using two pairs of grating in sequence or by sending the beam back with a high reflection mirror. As a result, the overall dispersion doubles. Tunability can be achieved by changing the grating separation b . Unlike prisms, the GDD of the grating pair is always negative.

2.5.3 Chirped mirrors

The invention of chirped mirrors by Kuhl [62] and Szipöcs [63, 64] et al. set a new milestone in the generation of ultra-short pulses, especially in the generation of sub-10 fs pulses.

Chirped mirrors have advantages over the prisms and gratings: (1) High efficiency. Chirped mirrors can have a reflection rate as high as that of normal dielectric mirrors, e.g., reaching 99.8%. (2) Large compensation bandwidth. Chirped mirrors can produce a nearly constant negative GDD over a large spectral range with a very little oscillation around the target design. (3) Simple arrangement. Chirped mirrors can be used just like normal dielectric mirrors. Ultra-short-pulsed laser systems with chirped mirrors can be arranged very simply and compactly when compared with the systems using prisms or gratings.

The basic idea of chirped mirrors is: A wave packet of a given center wavelength is most efficiently reflected by a corresponding quarter-wave stack. Therefore, if multiple layers with increasing thicknesses are deposited on a substrate, longer wavelengths will penetrate deeper into the structure and will consequently experience more group delay when reflected back from the mirror. As a result, a negative GDD will be produced. The monotonic variation of the thickness of the layers can be achieved through dielectric coating with alternate layers of high- and low-index materials and with different thickness. Such a structure constitutes a so-called chirped dielectric mirror. Please refer to [64] for detailed discussions about the theory and design of chirped mirrors.

Chirped mirrors have an important drawback. The impedance mismatch of the chirped mirror structure to the ambient medium (air) causes unwanted spectral oscillations around the target function. The oscillation amplitude increases dramatically with mirror bandwidth. This kind of oscillation influences considerably the smoothness of the tuning of an OPO. This problem can be solved by the so-called double-chirped mirrors (DCM, [65]). The impedance of the chirped mirror section is matched to the low-index or high-index material of the coating, which is then matched to the ambient air by an additional anti-reflection (AR) coating on top of the chirped mirror, as shown in Fig. 2.5.6.

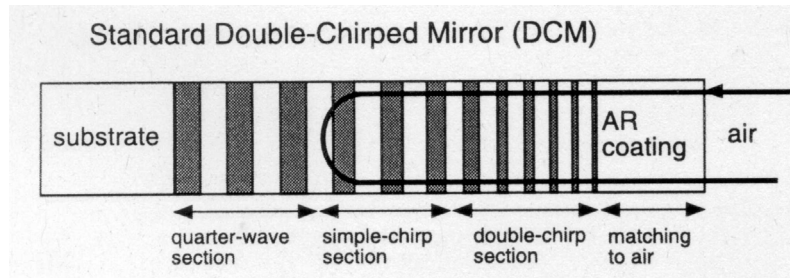


Fig. 2.5.6 Structure of double-chirped mirrors (DCM). [65]

Matuschek et al. [66] developed a novel technique of chirped mirrors, which suppresses detrimental dispersions by design. This is achieved by separating the chirped mirror stack from the AR section, coating them on two non-interfering surfaces of a substrate, as shown in Fig. 2.5.7. This is called back-side-coated (BASIC) technique.

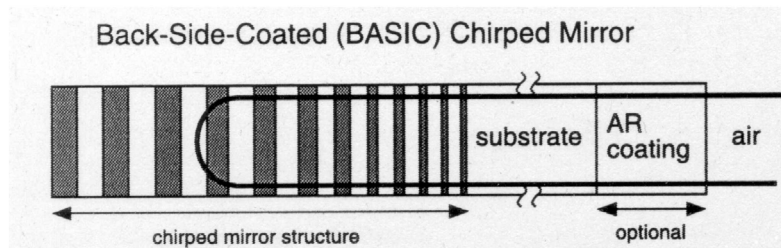


Fig. 2.5.7 Structure of back-side-coated (BASIC) chirped mirrors [66].

2.5.4 Glass slabs

Here we put forth a new method that can be possibly used for intracavity GVD compensation or extracavity pulse compression for OPOs. We introduce an intracavity glass plate made of BK7, fused silica, quartz, etc. Similar method (using a fused silica Littrow prism) was first used by Tomaru et al. [67, 68] in a femtosecond Cr^{4+} :YAG laser operating at $1.55 \mu\text{m}$ for intracavity dispersion compensation.

As discussed in Chapter 2.4, the GVDs of some glasses become zero at shorter wavelengths in the near IR when compared with the operating wavelength of the OPO and then become negative at longer wavelengths. Table 2.5.1 lists the zero-GVD points of the BK7, fused silica, and quartz glasses, as well as their negative GVD

values at 1.55 μm . Table 2 lists the zero-GVD points of PPKTP, PPLN crystals and their positive GVD values at 1.55 μm .

Table 2.5.1 *Zero and negative GVD characteristics of BK7, Fused Silica, and Quartz*

Glass	Zero-GVD wavelength	GVD at 1.55 μm
BK7	1322 nm	-24.72 fs ² /mm
Fused Silica	1273 nm	-27.98 fs ² /mm
Quartz	1279 nm	-31.12 fs ² /mm

Table 2.5.2 *Zero GVD characteristics of PPKTP and PPLN crystals*

Crystal	Zero-GVD wavelength	GVD at 1.55 μm
PPKTP	1798 nm	53.23 fs ² /mm
PPLN	1924 nm	103.34 fs ² /mm

Therefore, it is feasible to compensate the positive GVD from a nonlinear crystal with a glass plate having a designed thickness if the OPO operates at a wavelength longer than ~ 1350 nm. Since quartz has large birefringence, fused silica and BK7 glasses would be preferred, and fused silica is even better than BK7 glass.

For instance, compensating the GVD of a 1-mm PPKTP crystal at 1.55 μm needs about 1.9-mm fused silica or about 2.2-mm BK7 glass; compensating the positive GVD of a 1-mm PPLN crystal at 1.55 μm needs about 3.7-mm fused silica or 4.2-mm BK7 glass. Since such glasses as BK7, fused silica, quartz, have negative GVDs at wavelengths as long as 1.55 μm , they cannot be used as prism materials for compensation.

It should be noted that the GVDs of some nonlinear crystals become zero also at very short wavelengths, e.g., the GVD of LBO becomes zero at about 1215 nm. In this case, neither prisms nor glass plates can be used to compensate for the positive GVD from the crystal.

The most important advantages of using a glass plate for GVD compensation include: (1) Low cost. A glass plate even with high polishing quality ($\lambda/10$) and very small wedge ($<10''$) is at least several times cheaper than a pair of prisms or a pair of gratings. One chirped mirror costs even more. (2) Easy to deal with. We just need to place the glass plate at Brewster angle in the cavity or outside the cavity in the laser beam. The insertion loss is very low. No complicated alignment is needed. (3) Much more smooth and flat compensation curves than other methods. The compensation

curve of GDD vs. wavelength of a glass plate is much flatter than that of a prism pair or a grating pair, and also much smoother than that of the chirped mirrors. Fig. 2.5.8 shows a comparison between the compensation curves of GDD vs. wavelength of a fused silica plate, a prism pair made of SF10 glass, where they both create about -100 fs^2 GDD at 1.55 μm . It was assumed that the bandwidth of the pulses to be compensated is 100 nm. The curves in Fig. 2.5.8 were calculated for single path compensation.

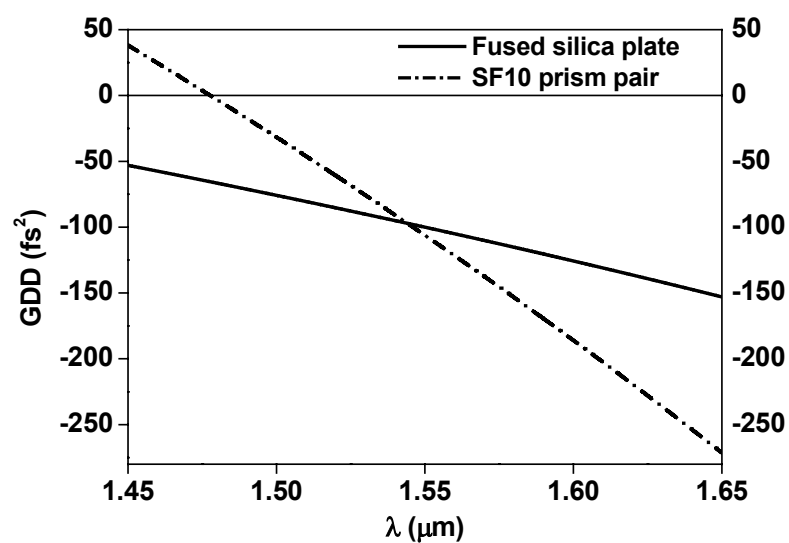


Fig. 2.5.8 Comparison between the compensations by a fused silica plate and by a SF10 prism pair.

Section III Experiments

3.1

32-fs KTP OPO [69-71]

3.1.1 Introduction

The KTP OPO is a typical birefringently phase-matched optical parametric oscillator. Because of the large nonlinearity, stable physical and chemical characteristics, high optical damage threshold, wide acceptance angles, and thermally stable phase-matching properties of the KTP crystal, the KTP parametric oscillator has proved to be highly successful for generating ultrashort pulses in the near- and mid-IR spectral region. [72]

A variety of research has been demonstrated for femtosecond KTP OPOs, especially after the full development of Kerr-lens mode-locked Ti:sapphire lasers.[17, 73-80] The first reported OPO synchronously pumped with femtosecond pulses was also based on KTP, which was pumped intracavity by a standard colliding-pulse mode-locked (CPM) dye laser [73]. The Kerr-lens mode-locked Ti:sapphire laser led to a new level of performance in the high-repetition-rate femtosecond OPO. To make use of the large effective nonlinear susceptibility of KTP and to reduce the walk-off between the interaction waves, noncritical type II phase matching ($\theta=90^\circ$, $\phi=0^\circ$, $o \rightarrow o+e$) was commonly employed for KTP OPOs. Intracavity compensation for the positive GVD from the KTP crystal was normally necessary to achieve sub-100fs operation of the OPOs. [73-79] Using an intracavity prism-pair compressor, signal pulses as short as 40 fs were generated in a sub-100 fs Ti:sapphire laser pumped KTP OPO [75]. Superior to the prism pairs, chirped mirrors are more effective for intracavity GDD compensation in OPOs, which have the advantages of the flexibility for designing the wavelength dependence of the GDD, easier adjustment and optimization of the cavity, low insertion losses, and insensitivity of the created GDD to the beam path. [17] There are also disadvantages for the chirp-mirror method. First, the compensation amount cannot be adjusted continuously. Second, there is always an oscillation of the compensation curve versus wavelength, sometimes this oscillation has large amplitude so that the OPO signal wavelength cannot be tuned continuously.

In our work with the KTP OPO, we used chirped mirrors with approximately $-80 \sim -140 \text{ fs}^2$ GDD for intracavity GVD compensation. A sub-30 fs Ti:sapphire laser operating at about 80 MHz repetition rate was used as the pump. The OPO was capable of producing nearly chirp-free 32 fs sech^2 signal pulses with a tuning range of 1140 nm – 1200 nm and an average power larger than 40 mW at 80 MHz at a pump power of about 800 mW. The pump threshold of the OPO was measured to be about 270 mW.

3.1.2 Experimental setup and pump characteristics

We used an eight-mirror ring cavity to construct the KTP OPO, as shown in Fig. 3.1.1,

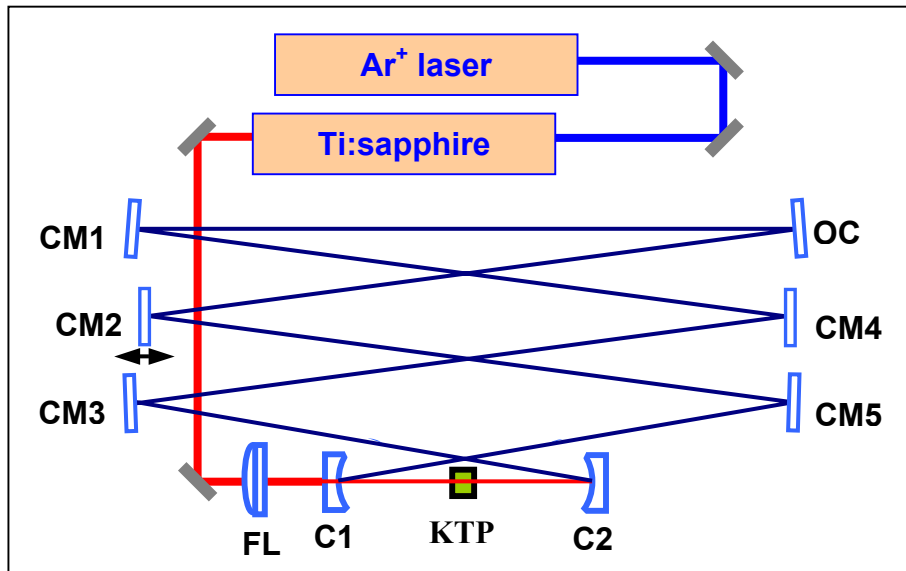


Fig. 3.1.1 Experimental setup.

where $\text{CM}_1 \sim \text{CM}_5$ are chirped mirrors for intracavity GVD compensation. CM_2 is mounted on a piezoelectric transducer with 45- μm translation range for cavity length tuning. OC is an output coupler with $T=3\sim 4\%$. C_1 and C_2 are two curved mirrors with $r = -100 \text{ mm}$. The focusing lens (FL) has a focal length of 60 mm. We used a 2 mm thick KTP crystal with type II noncritical phase matching ($o \rightarrow o+e$, $\theta=90^\circ$, $\phi=0^\circ$).

The Ar^+ laser pumped Kerr-lens mode-locked Ti:sapphire laser with a repetition rate of about 80 MHz provided the pump beam for the OPO. The pulse duration ranges from about 21 fs to 30 fs. The autocorrelation of the pump pulses was

measured using a Michelson autocorrelator with GaAs photodiode through two-photon absorption, as shown in Fig. 3.1.2. The inset shows the measured spectrum of the pulses. Nearly transform-limited 21 fs pulses at about 800 nm with a time-bandwidth product of 0.445 were obtained from the Ti:sapphire laser. Fig. 3.1.3 shows the output power of the Ti:sapphire laser versus the pump power of the Ar⁺ laser. For stable mode locking, the pumping range of the Ar⁺ laser should be from 4.5 W to 8.5 W. In mode locking, the wavelength of the Ti:sapphire laser can be tuned from 760 nm to 840 nm.

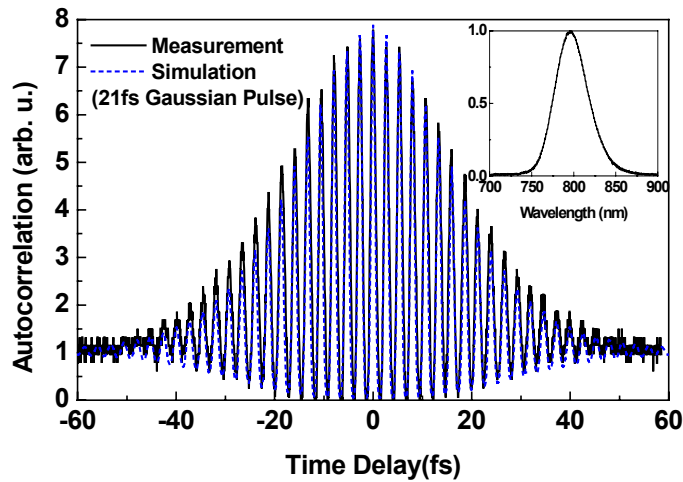


Fig. 3.1.2 Measurements of autocorrelation and corresponding spectrum (inset) of the Ti:sapphire laser pulses. The dashed curve is the simulation of autocorrelation for 21-fs Gaussian pulses.

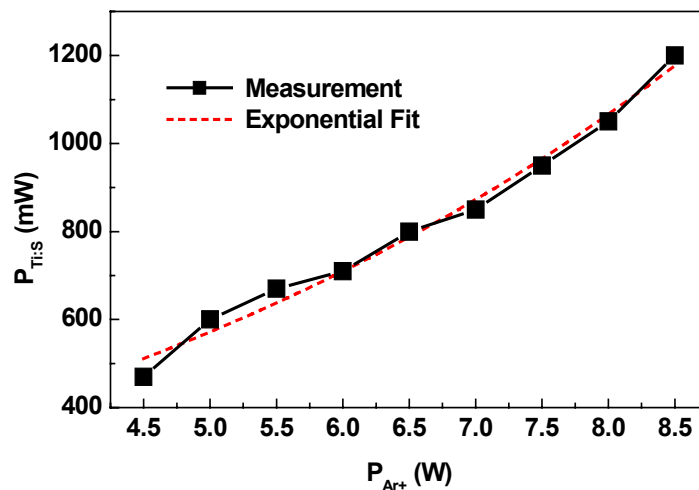


Fig. 3.1.3 Output power of the Ti:sapphire laser versus pump power from the Argon ion laser.

3.1.3 Pulse characteristics of the KTP OPO

To get the shortest pulses from the KTP OPO, we tried different configurations with different numbers of chirped mirrors and output couplers with different transmission rates. The best configuration for getting the shortest pulse duration is as described in Fig. 3.1.1 with 5 chirped mirrors and a 3~4% output coupler. The intracavity GDD characteristics are shown in Fig. 3.1.4.

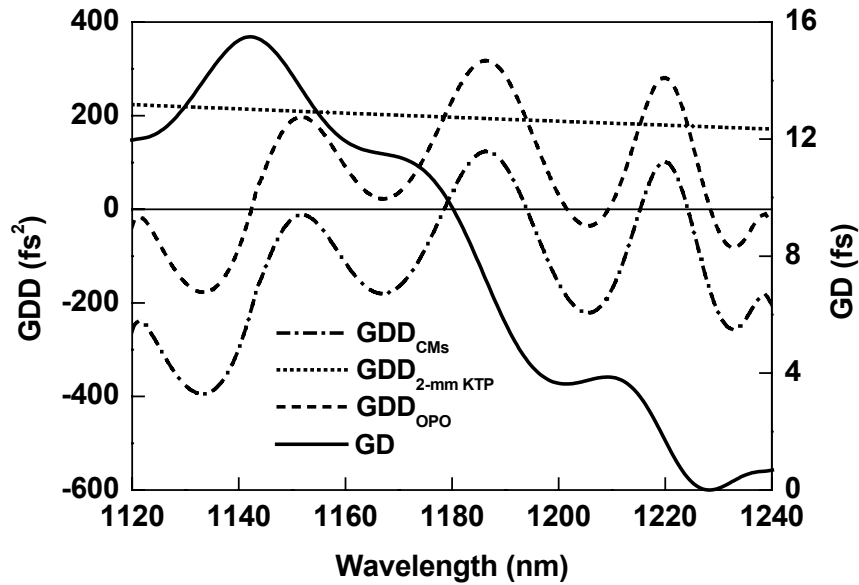


Fig. 3.1.4 GDD characteristics of the chirped mirrors (GDD_{CM}), the KTP crystal ($GDD_{2\text{-mm KTP}}$), and the OPO (GDD_{OPO}). The right scale corresponds to the group delay of the signal versus wavelength (GD).

The intracavity GDD is positive over the tuning range of the OPO signal wavelength from 1140 nm to 1210 nm, so that positive tuning was observed with the signal wavelength when changing the cavity length, namely a longer signal wavelength oscillated at a longer cavity length. The shortest pulse duration was measured at about 1180 nm, where the intracavity GDD became zero and the broadest spectral bandwidth of 53 nm was obtained for the signal wave. The corresponding pump wavelength is about 824 nm.

When measuring the autocorrelation of the OPO signal pulses, since it was difficult to find a beam splitter for 1200 nm, we used a simple 1-mm quartz plate as a beam splitter with the signal beam incident at about 75° to achieve best contrast in the autocorrelation curve. The autocorrelation trace was recorded with a Si photodiode

through two-photon absorption, as demonstrated in Fig. 3.1.5. The measured autocorrelation and corresponding spectrum of the signal pulses are shown in Fig. 3.1.6.

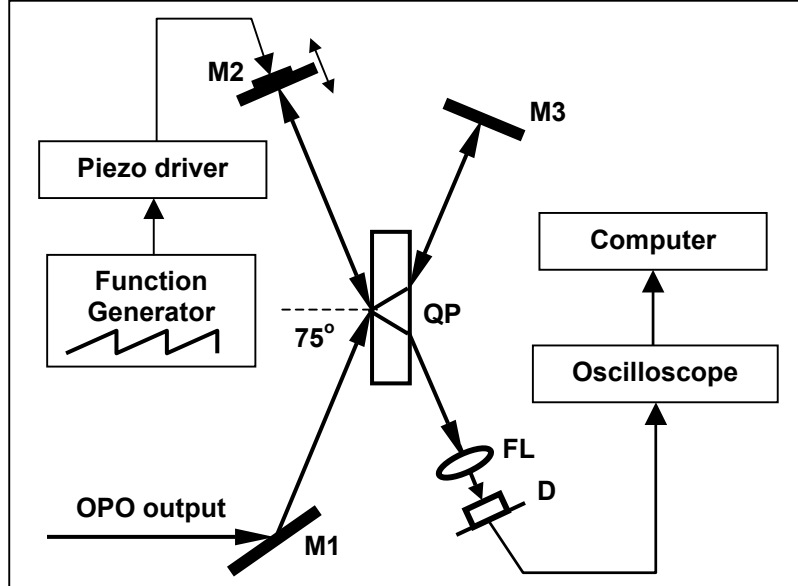


Fig. 3.1.5 Setup for the autocorrelation measurement of the signal pulses. M1-M3, high reflectors; QP, 1-mm quartz plate; FL, focusing lens; D, photodiode.

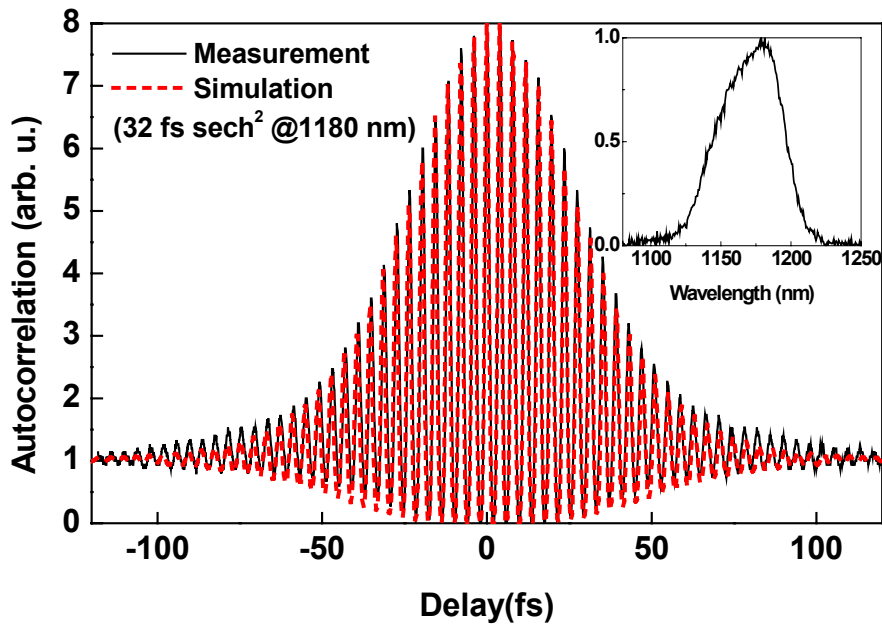


Fig. 3.1.6 Autocorrelation measurement of the signal pulses. Inset: corresponding spectrum.

However, before the signal pulse reaches the photodiode, it needs to propagate through about 10mm quartz and BK7 glass (3 mm output coupler, > 2 mm quartz plate, 5 mm focusing lens). Taking this into account, the intracavity signal pulses are actually about 28 fs long according to the calculations based on the formula (2.4.9) in Chapter 2.4.

3.1.4 Cavity length tuning effects

The mirror CM2 of the OPO was mounted onto a piezoelectric transducer to enable cavity length tuning. For the output power characteristics, as shown in Fig. 3.1.7, the piezo was driven by a sawtooth function with a period of 50 s and an amplitude of 10 V, so that the cavity length was changed in a range of about 9 μm . However, the OPO was maintained lasing within only about 3.5 μm of cavity length mismatch. The highest signal power is about 40 mW when pumping with 900 mW, corresponding to about 4.4% power conversion efficiency.

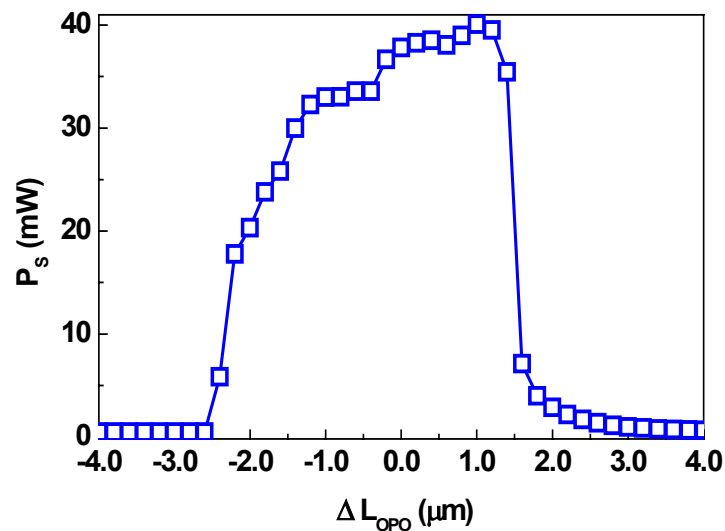


Fig. 3.1.7 Signal power (P_s) versus cavity length detuning (ΔL_{OPO}).

The cavity length detuning effects can be understood as follows: For the case of positive intracavity GDD, when the cavity length is increased, the signal wavelength has to shift to a longer value so that signal wave is delayed more strongly and keeps synchronous with the pump. Similarly, a shorter signal wavelength oscillates at a shorter cavity length; For negative intracavity GDD, an opposite process will take place. Fig. 3.1.8 shows several signal spectra over the tuning range when changing the

cavity length. By only cavity length tuning, the signal wavelength can be tuned from 1140 nm to 1180 nm. The largest bandwidth appeared near the center of the cavity length tuning range. Integration of the spectra separately gives information of the pulse energy at different wavelengths. The largest bandwidth corresponds to the smallest pulse energy, as depicted by the open circles. Comparing with the power characteristics shown in Fig. 3.1.7, we can conclude that there is a large variation of the pulse duration over the tuning range and the shortest pulse really appears at the largest bandwidth as expected.

In Fig. 3.1.8, one can observe a mirror imaging effect of the signal spectra around 1155 nm, while the spectra themselves are not symmetric. This can be explained by the complicated process governed by group velocity dispersion of the KTP crystal, the group velocity mismatch between the pump and the signal, and the phase matching conditions. We can simply describe this process as follows: At shorter cavity length, the signal may arrive at the KTP crystal simultaneously with or a little earlier than the pump. Because the signal propagates faster than the pump, while shorter-wavelength components in the signal spectrum propagate slower than longer-wavelength components, the shorter-wavelength components can possibly interact more efficiently with the pump than the longer-wavelength components and consequently gain more amplification. This is why we observed the unsymmetrical shapes of the signal spectra when the center wavelengths are shorter than 1160 nm. If the signal arrives later than the pump at the KTP crystal, the longer-wavelength components will be able to interact with and consequently deplete the whole pump spectrum, so that the shorter-wavelength components can only interact with the depleted pump and get less amplified. This is the reason for the asymmetrical shapes observed for the signal spectra centered at wavelengths longer than 1170 nm. As a result, there should be an optimal delay of the signal pulses from the pump pulses or an optimal cavity length detuning amount, where a nearly symmetrical and broadest signal spectrum can be obtained.

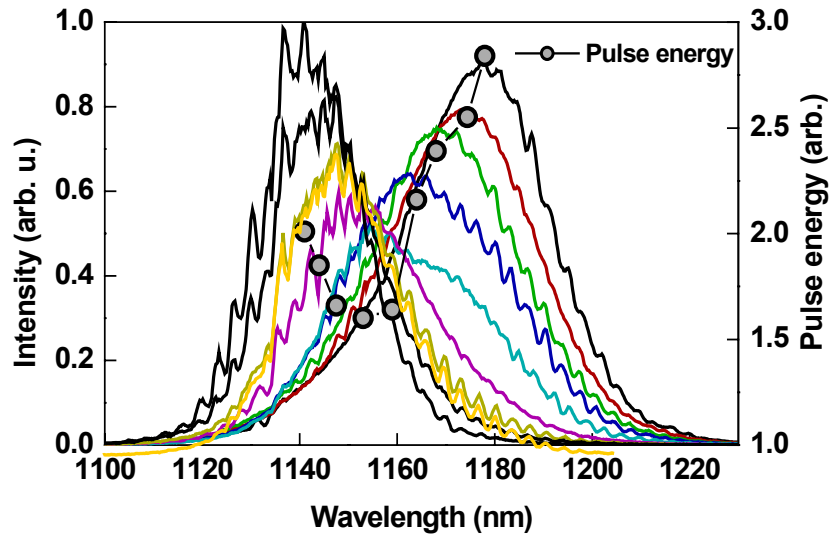


Fig. 3.1.8 Spectra of the signal over the cavity length tuning range and the corresponding pulse energy.

3.1.5 Pump wavelength tuning effects

The signal wavelength can be tuned from 1160 nm to 1210 nm when changing the pump wavelength from about 806 nm to 838 nm, as demonstrated in Fig. 3.1.9. It can be observed that the signal bandwidth decreases while the pulse energy (integration of the spectrum over wavelength) increases with increasing the pump wavelength. Fig. 3.1.10(a) shows the theoretical and experimental pump wavelength tuning curves of the KTP OPO. There is an obvious shift of the experimental data from the theoretical curve, which is about 10 nm. To explain these phenomena, we need to consider the influence from dispersion effects of the Ti:sapphire crystal, as shown in Fig. 3.1.10(b).

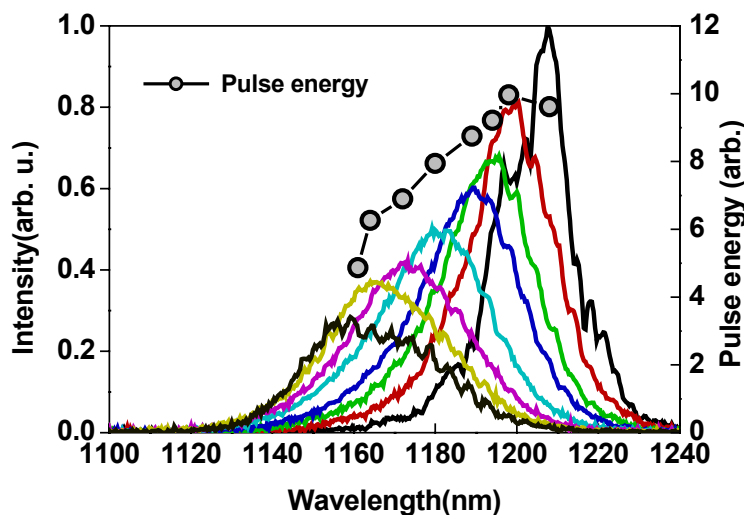


Fig. 3.1.9 Pump wavelength tuning effects: Signal spectra and pulse energy.

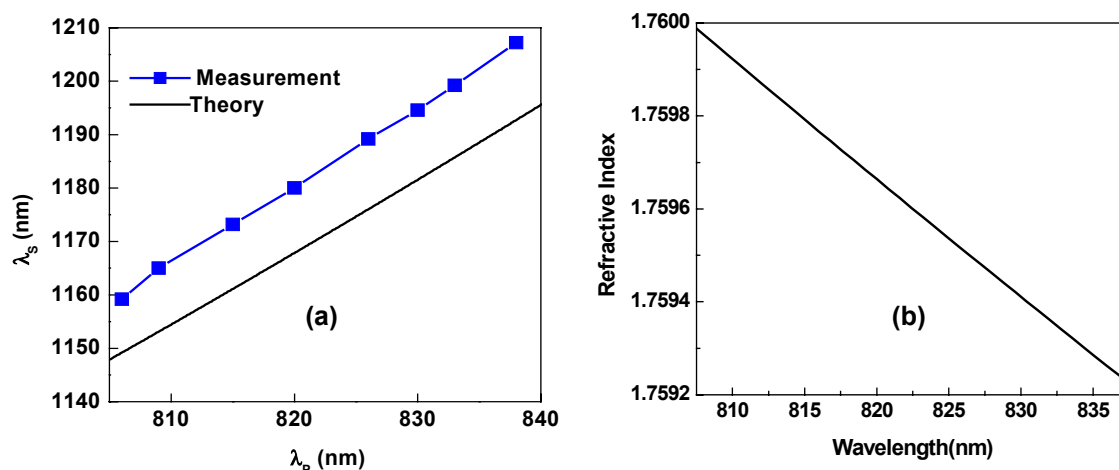


Fig. 3.1.10 (a) Theoretical (solid line) and measured (closed squares) pump wavelength tuning curves; (b) Dispersion characteristics of sapphire.

From 805 nm to 840 nm, the refractive index of sapphire reduces from 1.76 to 1.7592. The 0.0008 difference creates a cavity length reduction of about 7.6 μm (double pass) for the pump laser with a 4.75 mm Ti:sapphire crystal, which is equivalent to increasing the cavity length of the OPO by the same amount while increasing the pump wavelength. Therefore, in addition to the increasing of the signal wavelength with the pump wavelength, there is an additional shift of the signal wavelength to the longer values, this is the main reason for the approximate 10 nm difference between the theoretical the experimental curves in Fig. 3.1.10 (a).

3.1.6 Pump threshold

We measured two groups of pump threshold data for pumping with sub-30 fs and 100 fs pulses, respectively, as shown in Fig. 3.1.11. In both cases, the repetition rate of the pump pulses is approximately 80 MHz. For sub-30 fs pumping, the threshold pump power is about 275 mW, corresponding to a pulse energy of 3.4 nJ. For ~ 100 fs pumping, the threshold pump power is 250 mW, corresponding to a pulse energy of 3.1 nJ. We did not find an obvious difference between these two cases. But according to the theory by J. Hebling et al. [81], the threshold pump pulse energy should be almost 3 times larger for 30 fs pumping than for 100 fs pumping. Reasons for this disagreement are not quite clear.

The higher pump threshold under shorter pump pulses can be explained by two mechanisms. First, with shorter pump pulses, the interaction length between the pump and the signal is reduced and the signal gains lower amplification. Second, shorter pulse duration corresponds to larger bandwidth and the pulse energy is distributed to more spectral components, so that higher pulse energy is needed to make more spectral components exceed the threshold energy. On the other hand, for similar pulse energy, shorter pulses provide much higher peak powers, which should also affect the operation of the OPO.

Certainly, there are still other factors that influence the measurement of the pump threshold, such as the measurement method, the status of the alignment of the OPO cavity, the matching between the tuning range of the OPO and the cavity bandwidth, etc.

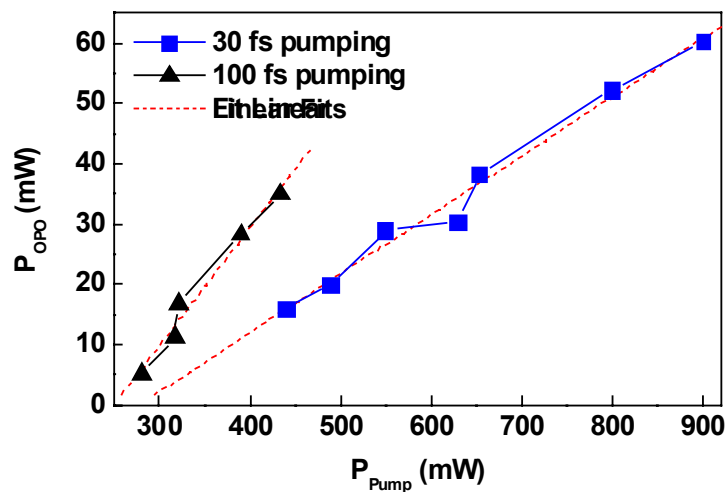


Fig. 3.1.11 Pump threshold measurement for pumping with ~ 30 fs and ~ 100 fs pulses: output power of OPO (P_{OPO}) vs. pump power (P_{Pump}) of the Ti:sapphire laser.

3.2

Generation of femtosecond visible pulses from an OPO

3.2.1 Introduction

Synchronously pumped optical parametric oscillators generating picosecond or femtosecond pulses in the near- or mid-infrared region have a variety of applications. Intracavity and extracavity SHG and SFG processes are effective methods to extend the tuning range of the OPOs to the visible. Ultrashort tunable pulses in the visible are very useful for spectroscopy. Green and blue coherent radiation has also some other applications. By inserting a BBO crystal into an additional focus in the cavity of Ti:sapphire laser pumped KTP OPOs, highly efficient intracavity SHG of the signal [2, 78,82] and SFG between the signal and the pump [82] have been achieved. Intracavity and extracavity efficient SFG processes by a KTP crystal in a Nd:YAG laser pumped AgGaS₂ OPO were reported by E. C. Cheung et al. [83]. Another method to generate visible light from an OPO is to pump with the second harmonic of the Ti:sapphire laser [84], so that the OPO oscillates in the visible range. In this case, high power of the Ti:sapphire laser is needed. All above methods to generate visible light need an additional nonlinear crystal, requiring a high pump power and a complex setup. Signal frequency doubling and optical parametric oscillation processes were achieved simultaneously within a single KTP crystal in case of a small polarization misorientation [85]. Insertion of an additional intracavity half-wave plate [86] strongly enhanced the SHG intensity. Using a half-wave plate and polarizing beam splitters to split the pump beam into *s* and *p* components, with the *p* polarized component pumping the OPO and the *s* polarized one taking part in the SFG process, a single-crystal SFG – OPO was achieved by K. G. Köprülü et al. [87].

Quasi-phase-matching is a very efficient technique to generate femtosecond and picosecond pulses from an optical parametric oscillator. Making use of the large nonlinear coefficients (e.g. d_{33} for PPLN), one can achieve a much higher efficiency and a much lower pump threshold in a quasi-phase-matched OPO if compared with a birefringently phase-matched one. Another great advantage of QPM is that any interactions within the transparency range of the nonlinear crystal can be phase matched and multiple orders of QPM can be achieved simultaneously, so that

frequency mixing processes can be managed in the same device. Higher order QPM techniques have also been utilized for efficient intracavity SHG or SFG in PPLN OPOs. A 3rd order quasi-phase-matched generation of femtosecond green pulses was achieved through SHG of the signal in a PPLN OPO [87]. Also based on third order QPM, efficient SFG between the signal and the pump to generate green light was observed in a picosecond PPLN OPO [88]. Burr and Tang [89] observed an estimated 200 mW output power in the blue through SFG between the signal and the pump in a PPLN OPO pumped with 1.6 W Ti:sapphire laser. It was suggested by Y. Q. Lu, et al. [8] that the periodically poled optical superlattice Nd:MgO:LiNbO₃ has great potential for constructing a blue or green radiation source through self-frequency-doubling. Quasi-phase-matched SHG and THG processes were achieved in a quasiperiodic optical superlattice of LiTaO₃ arranged in a Fibonacci sequence [90], and visible light was generated with a conversion efficiency of up to ~5%-20%. With aperiodical poling techniques for SHG [91, 92], the visible pulses generated through intracavity and extracavity SHG can be compressed simultaneously. Second-order QPM based on a periodically poled LiTaO₃ with 3.3 μm grating period and 75% duty cycle was reported for SHG of 680-nm diode lasers [93], which can also be applied to double the frequencies in the IR spectral region to generate visible light using larger grating periods.

In our work with the PPLN OPO, we found that optimizing the duty cycle of the poling period in PPLN is a promising method to achieve higher order QPMs for the SFG and SHG processes. We proved both experimentally and theoretically that a small deviation of the duty cycle from 50%, which has a small influence on the odd-order QPM, will substantially increase the efficiencies of the even-order QPM, so that multiple higher orders of QPM can be achieved simultaneously in the same OPO device to generate the visible light. In our case, a ~56% duty cycle built up an efficient 4th order QPM for SFG in the blue and an efficient 2nd order QPM for SHG in the red with little reduction in the efficiency of the 1st order QPM for the OPO process. A simultaneous 3rd QPM SHG process for the generation of the green light is still kept efficient. Thus, using only 480 mW pump power, in addition to an up to 50 mW output of the signal pulses tunable from 1040 nm to 1350 nm, we also obtained femtosecond pulses of up to 14 mW in the blue, 12 mW in the green and 18 mW in the red. More interestingly, we observed another 3rd order quasi-phase-matched

process producing a mutual enhancement between the blue light and the red light generation. The efficiency of the visible light generation can still be much improved through further optimizing the duty cycle of the poling period.

This chapter is organized as follows. In section 3.2.2, we first present some common methods for generating visible light from an OPO, including some work done by others as mentioned in section 3.2.1. In section 3.2.3, we describe our experimental and theoretical work concerning extracavity and intracavity doubling of the signal frequency in a KTP OPO. From section 3.2.4 to section 3.2.7, we demonstrate our experimental work of generating visible pulses from a femtosecond PPLN OPO using a $\sim 56\%$ poling duty cycle. In section 3.2.4, we present our experimental results with the spectra and output power of the visible pulses over the whole tuning range. In section 3.2.5, we give a comprehensive explanation to the mechanism responsible for the efficient generation of the visible light. In section 3.2.5-A, we describe our method to determine the duty cycle of the poling period of PPLN. In section 3.2.5-B, we analyze in detail how the $\sim 56\%$ duty cycle greatly improves the efficiency of the 2nd and the 4th order QPM. In section 3.2.5-C, we make a comparison between the experimental results and the theoretical calculations, which is very helpful for better understanding and further confirmation of our analysis. In section 3.2.5-D, we present numerical simulations for optimizing the duty cycle. In section 3.2.5-E, we explain the synchronous operation effects between the generation of the blue and the red light. In section 3.2.6, we characterize the generated pulses, including the signal, the SFG in the blue and the SHG in the red. Section 3.2.7 shows other characteristics of the OPO, including the pump spectrum depletion effect which is very important for optimizing the pump wavelength, the pump bandwidth and the pump threshold of the OPO (section 3.2.7-A); the two-stage operation effect with tuning the cavity length which results from the over-compensation of the intracavity GVD by chirped mirrors (section 3.2.7-B); and the self-phase-modulation effects which influence the structure of the SHG spectrum (section 3.2.7-C).

3.2.2 Some typical methods for intracavity SHG and SFG

A typical ring cavity configuration of a synchronously pumped OPO for intracavity SHG is shown in Fig. 3.2.1. A BBO crystal is inserted into another focus of the ring cavity, which is formed by two additional curved mirrors M5 and M6. T. Albrecht et al. [2] used a 200 μm thick BBO crystal that was cut for type I ($o+o\rightarrow e$) phase matching at 600 nm for normal incidence. M5 and M6 have a curvature radius of -80 mm and they are additionally coated for antireflection ($T>85\%$) from 500 nm to 675 nm. 150 mW visible pulses (290 fs) at 570 nm were generated with a pump power of 1.4W. They used a twofold reduced synchronous length for the OPO cavity, so that the OPO and the visible pulses operate at 152 MHz (with 76 MHz pumping).

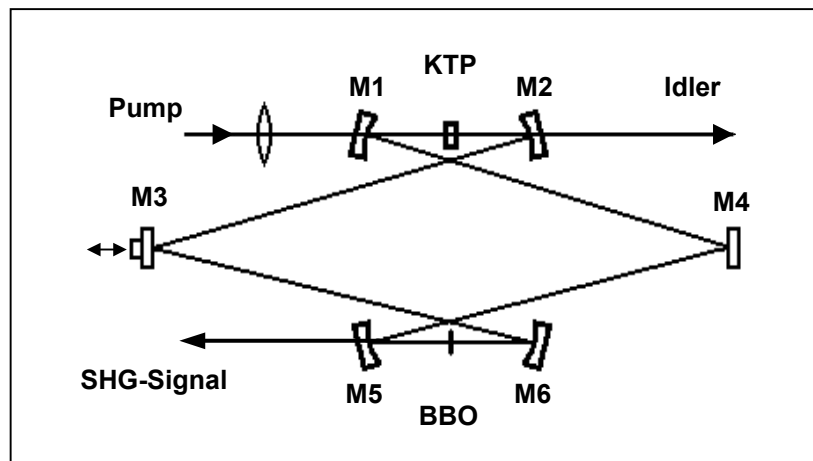


Fig. 3.2.1 Resonator of a SHG-OPO. [2]

A Shirakawa et al. [82] achieved intracavity SFG and SHG in the same cavity of a Ti:sapphire laser pumped KTP OPO using a 0.3 mm BBO crystal cut at $\theta=22.4^\circ$ and $\phi=0^\circ$ for type I ($o+o\rightarrow e$) phase matching, as shown in Fig. 3.2.2. For SFG, the residual pump pulses were delayed using an extracavity light path, so that the pump and the signal pulses arrive at the BBO crystal at the same time. The selection between the SHG and SFG output was performed by slightly changing the angle of BBO crystal. The tuning ranges are from 426 nm to 483 nm and from 520 nm to 585 nm for SFG and SHG processes, respectively. Femtosecond visible pulses with an average power of 330 mW were generated with a pump power of 1.3 W.

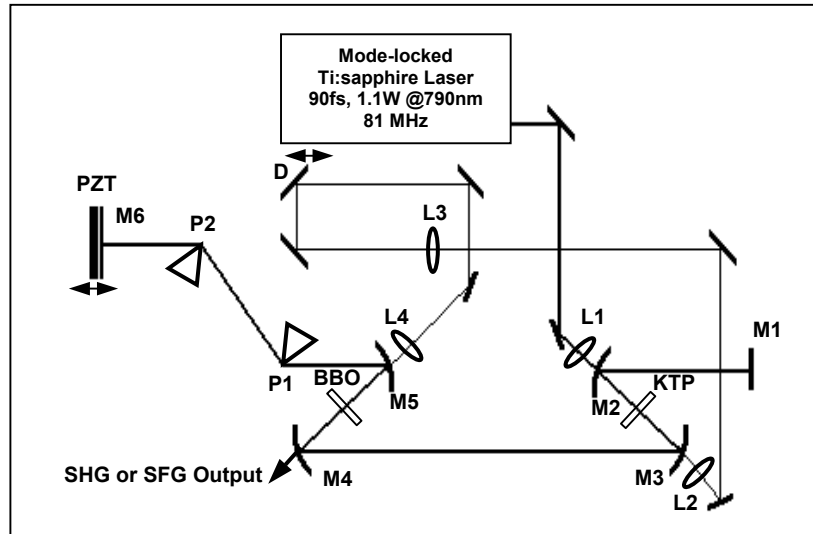


Fig. 3.2.2 Schematic of the intracavity-frequency-mixed OPO. [82]

A self-doubling KTP OPO pumped by a Ti:sapphire laser was reported by T. Kartaloglu et al.[86], where no additional crystal was inserted into the cavity. The SHG process was achieved simultaneously with OPO process in the same KTP crystal. To achieved phase matching of the SHG process, a half-wave plate (HWP) was placed into the cavity, which was used to couple some of the p -polarized signal beam into s polarization. Fig. 3.2.3 depicts the experimental setup. With this method, femtosecond pulses in the green were generated with an efficiency of 29% when pumping with 700 mW. A single-crystal sum-frequency-generating KTP OPO was also reported by the same group [87], as described in Fig. 3.2.4. The polarization direction of the p -polarized pump laser (Ti:sapphire laser) was first rotated by a HWP and then split into p and s components by a polarizing beam splitter (PBS). The p component was used for OPO pumping, while the s component was used for SFG between the signal and the pump. Another PBS was used to combine the p and s components before the entrance of the OPO. The OPO generated blue output beam at 487 nm with 43% power-conversion efficiency when pumping with a 1.6-W Ti:sapphire laser.

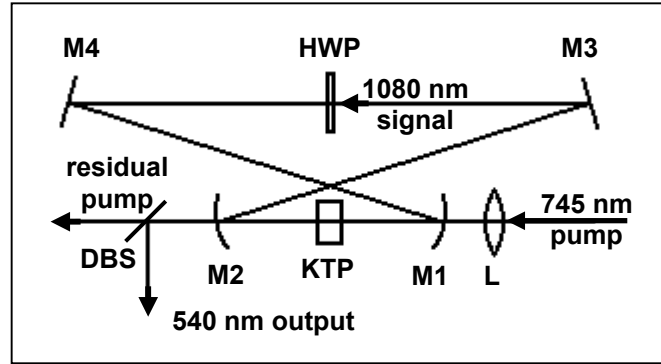


Fig. 3.2.3 Self-doubling OPO setup. [86]

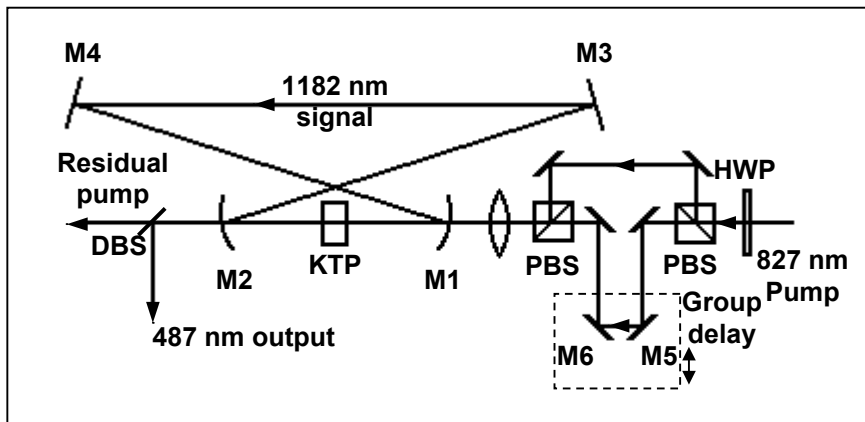


Fig. 3.2.4 Experimental setup of the SFG – OPO. [87]

3.2.3 Example: Intracavity and extracavity SHG and SFG in a KTP OPO using a BBO crystal

A. Extracavity SHG and SFG

We performed extracavity SHG and SFG experiments with a Ti:sapphire-laser-pumped KTP OPO. A 2-mm thick KTP crystal cut at $\theta=90^\circ$ and $\phi=0^\circ$ for type II ($o \rightarrow o+e$) phase matching was used for the OPO which consists of a six-mirror ring cavity (see Fig. 3.2.5). A 1-mm BBO crystal was used for the SHG of the signal at about 1100 nm, which was cut at an internal angle of $\theta=22.4^\circ$ for type I ($o+o \rightarrow e$) phase matching and normal incidence. To achieve extracavity SFG between the signal and the pump, the BBO crystal needs to be rotated about 2° ($\theta \approx 25^\circ$) from the normal incidence position. The residual pump beam was recollimated and delayed before combining it with the signal beam. The signal or the combined beam was focused by a

quartz lens of 50-mm focal length. The generated visible beam was recollimated with another lens of 100-mm focal length.

In our application for spectroscopy, we expect at least 10 mW of doubled signal power at about 550 nm. With 1-W Ti:sapphire laser pumping (at 800 nm center wavelength, 80 MHz repetition rate, and about 200 fs pulse duration), we obtained 130 mW signal power at about 1100 nm. After doubling, we measured only 1~2 mW visible light at 550 nm, which is far less than required. Fig. 3.2.6 shows the conversion efficiencies of SHG using 1-mm and 2-mm BBO crystals. For 1-mm BBO (Fig. 3.2.6(a)), at least 280 mW signal power is needed to generate 10 mW visible power. With 130 mW signal power, the conversion efficiency of SHG is lower than 2%, so we can obtain at most 2 mW power after doubling. The efficiency can be much improved by using a 2-mm BBO crystal. As shown in Fig. 3.2.6(b), with 130 mW signal power, the conversion efficiency of SHG is a little less than 7%, so that about 9 mW visible power can be expected. But the visible power can still not satisfy the requirements. We can conclude from above analysis that extracavity SHG requires considerably higher output power from the OPO. Therefore, low efficiency is a big disadvantage of extracavity SHG to generate visible pulses from an OPO.

For the SFG process, we just need to recollimate the residual pump beam and combine it with the output signal beam. The delay between the pump and signal has to be adjusted so that the signal and the residual pump pulses reach the BBO crystal simultaneously. The combined beam would be focused into the BBO crystal by the same focusing lens for the SHG process. Due to low efficiency, we measured only less than 0.5 mW power at the SFG wavelength (~460 nm).

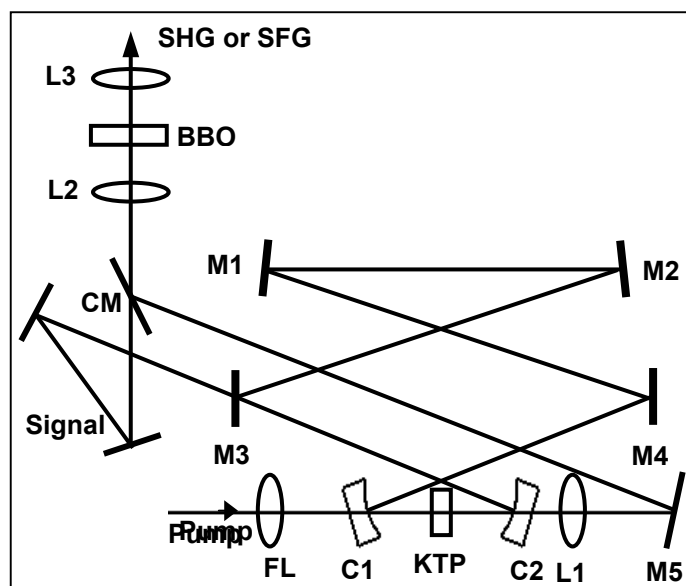


Fig. 3.2.5 Setup of the extracavity SHG - and SFG - OPO. M1, M2, M4, flat chirped mirrors for GVD compensation; M3, output coupler; C1, C2, curved mirrors ($r=-100$ mm); CM, combination mirror which is antireflection coated at the signal wavelength and high reflection coated at the pump wavelength. FL, focusing lens.

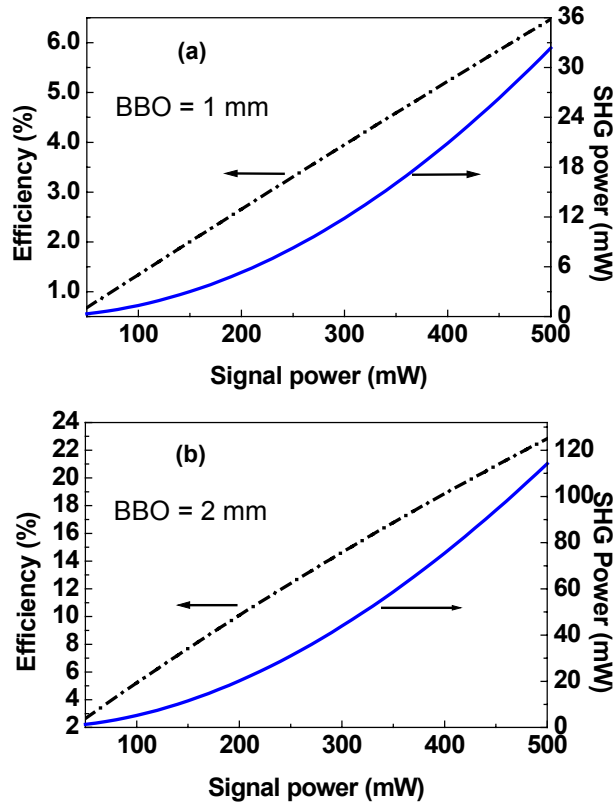


Fig. 3.2.6 Extracavity SHG of the KTP OPO signal at 1150 nm using (a) 1mm and (b) 2mm BBO crystal.

B. Intracavity SHG and SFG

The experimental setup for intracavity doubling of a KTP OPO is shown in Fig. 3.2.7. A 200-fs Ti:sapphire laser operating at 80 MHz repetition rate and ~1 W average output power was used as the pump laser. An 8-mirror ring cavity constitutes the KTP OPO. The 2-mm KTP crystal is X-cut with $\theta=90^\circ$ and $\phi=0^\circ$ for type II ($o \rightarrow o+e$) phase matching. The curved mirrors C1 and C2 have a curvature radius of -200 mm. M1 - M4 are chirped mirrors to compensate for intracavity GVD. For efficient generation of visible light, we did not use an output coupler for the OPO. C3 and C4 with a curvature radius of -100 mm were used to form another focus where a 2-mm BBO crystal was inserted. The BBO crystal was cut with an internal angle of 22° for type I phase matching for the doubling of the signal at about 1150 nm. The distance between C1 and C2 was optimized to 20.6 cm, and most efficient SHG was observed when the distance between C3 and C4 was 10.2 cm.

The doubled signal wavelength was tunable from about 540 nm to 630 nm when the pump wavelength was tuned from about 760 nm to 870 nm. The incidence angle of the signal beam on the BBO crystal needs to be changed from about -1° to about 2°

when tuning the visible light from 540 nm to 630 nm, since the internal cutting angle (22°) was designed for the doubling of about 1150 nm. Fig. 3.2.8 shows the measured power versus doubled signal wavelength. The highest power was 106 mW which was measured at 576 nm. According to Fig. 3.2.6(b), 106 mW output power at about 550 nm corresponds to an OPO signal power of about 500 mW. Because the curved mirror C4 was not coated for high transmission in the visible spectral range, the generated visible light is estimated to be higher than the measured results.

At a given pump wavelength, the center of the visible spectrum could be tuned in a very limited range (< 3 nm) by tuning the OPO cavity length, while the bandwidth of the visible light changed significantly. As shown in Fig. 3.2.9, when the center wavelength was tuned from about 546.5 nm to 548 nm by tuning the cavity length, the bandwidth was changed from 1.7 nm to about 6 nm, which also means that the visible pulse duration can be changed largely. The reasons include: (1) The 4 chirped mirrors introduced too much negative GDD at some wavelengths, so that the intracavity GVD was far overcompensated, resulting in largely reduced tuning rate. A very small tuning range can be obtained even with a large cavity length mismatch. (2) The chirped mirrors did not have satisfactorily constant GDD distributions over the compensation range, instead, the compensation curves oscillate with an amplitude larger than 200 fs^2 , especially at wavelengths outside the specified compensation range from 1100 nm to 1300 nm, so that the total intracavity GDD changed very fast even with a small change of wavelength. The tuning characteristics can be much enhanced when improving the GDD characteristics of the chirped mirrors.

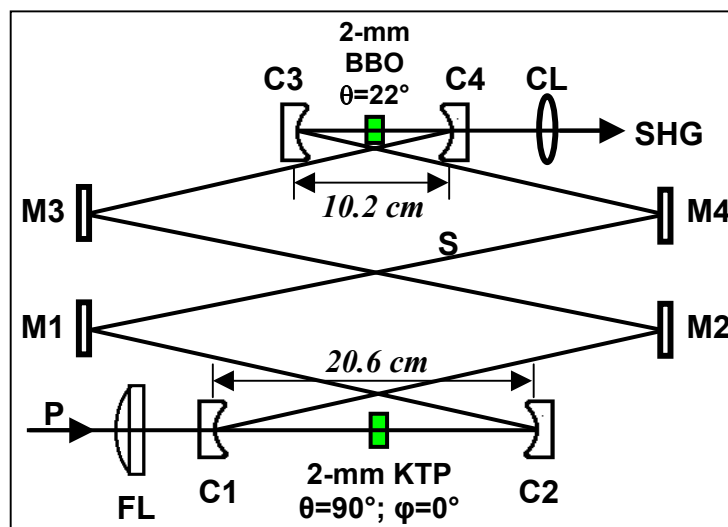


Fig. 3.2.7 Experimental setup for intracavity SHG of a KTP OPO. C1, C2, curved mirrors, $r=-200$ mm; C3, C4, curved mirrors, $r=-100$ mm; M1-M4, chirped mirrors; FL, focusing lens, $f=100$ mm; CL, collimating lens, $f=100$ mm.

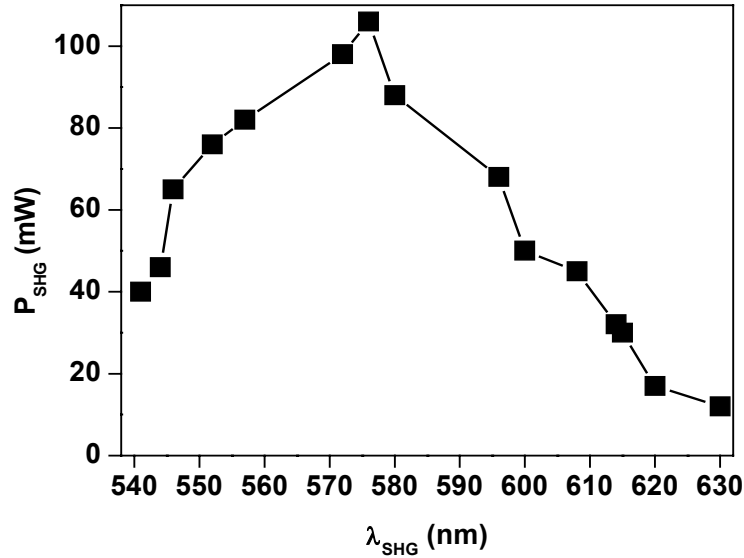


Fig. 3.2.8 Output power (P_{SHG}) versus doubled signal wavelength (λ_{SHG}) at a pump power of 800 mW and a repetition rate of 80 MHz.

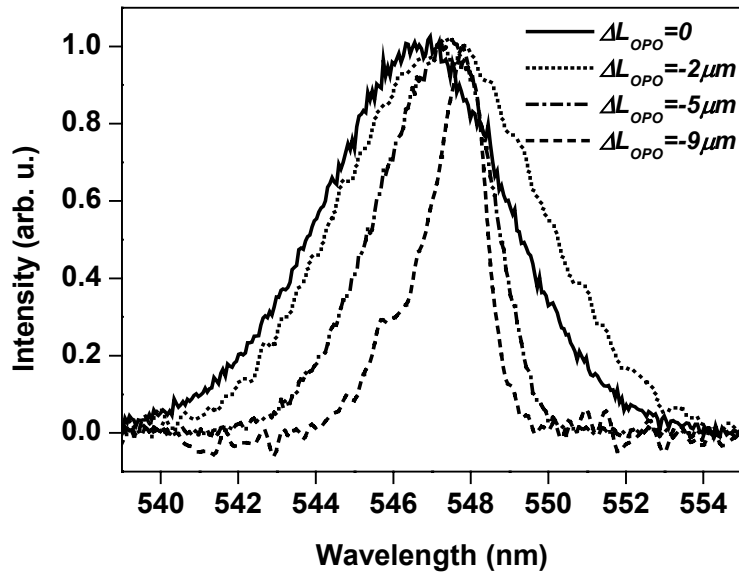


Fig. 3.2.9 Shift of the signal spectrum and variation of the bandwidth with tuning the cavity length (ΔL_{OPO}) of the OPO.

For SFG between the pump and the signal, we just need to couple the depleted pump wave transmitting through the curved mirror C2 into the BBO crystal through the curved mirror C3 after appropriate delay, so that the signal and the pump arrive at the BBO crystal simultaneously. The tilting angle of the BBO crystal with respect to the propagation direction of the incident beams needs to be optimized to get efficient conversion into the SFG wave. Here we do not present experimental work for the SFG process.

3.2.4 Efficient SHG and SFG processes in a PPLN OPO: experiments and results [94]

We used a six-mirror ring cavity for the PPLN OPO, as shown in Fig. 3.2.10. A Kerr-lens mode-locked Ti:sapphire laser provides the pump beam tunable from 760 nm to 835 nm at a repetition rate of about 80 MHz and a pulse duration of about 30 fs. We synchronously pumped the OPO with 460~480 mW, measured before the plano-convex focusing lens (FL). Chirped mirrors [17,24] (M1 and M3) were used to compensate for the group velocity dispersion of the PPLN crystal. The GDD characteristics of the chirped mirrors will be given in section 3.2.7-B. M3 is mounted onto a 45- μm piezoelectric transducer to achieve cavity length tuning. M2 (R=98%~99%) and M4 (R \approx 99.9%) are high reflectors, so that only 1~2% of the signal power was coupled out through M2. C1 and C2 are curved mirrors with a curvature radius of -100 mm. X is a 0.5 mm thick PPLN crystal which is antireflection coated on both sides at 1200 nm and 800 nm. There are multiple periodically poled gratings in the PPLN crystal, varying from about 20.5 μm to 21.5 μm . The crystal is mounted onto a X-Y translation stage to optimize the position of the crystal and to tune the grating period. To remove the photorefractive damage effect, the crystal is heated by an OMEGA CN8201-T1 Temperature & Process Controller. In our experiments, the crystal was heated to 100°C. Generated visible light and the residual pump laser are collimated by a lens (CL) with a focal length of 100 mm. To separate different visible beams and to separate the visible light from the pump and the idler waves, we used a BK7 prism (SP) with an apex angle of 45°. The power of the generated visible light and the depleted pump laser was measured about 1 m behind the prism separately using a calibrated MELLES GRIOT Broadband Power/Energy Meter. All of the visible spectra were measured with an ANDO AQ-6315A Optical Spectrum Analyzer with a resolution of 0.5 nm.

With the oscillation of the signal, we observed quite bright and nearly white light coupling out through the curved mirror C2. After separated by the prism, at least four colors in the visible were observed when tuning the signal wavelength. Spectrum analysis tells us that the blue light is the SFG between the pump and the signal, the green, the yellow and the red light is the SHG of the signal at different wavelengths. Some of the yellow light is also from the SFG between the pump and the idler.

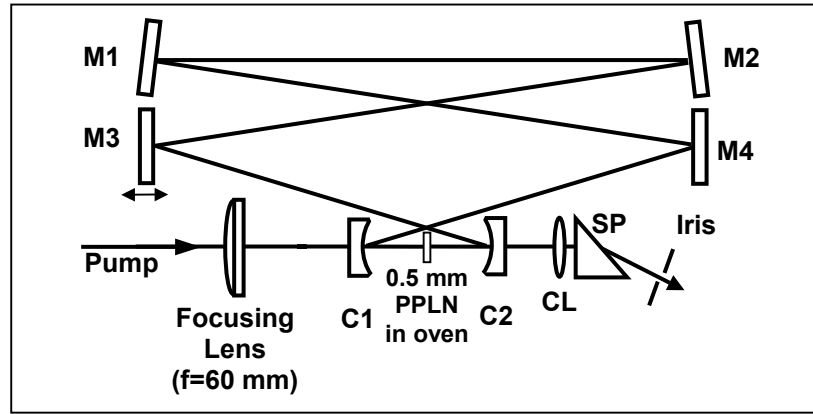


Fig. 3.2.10 Experimental setup: *M1, M3* chirped mirrors; *M2*, 1~2% output coupler, *M4* ($R=99.9\%$) high reflector; *C1, C2* curved mirrors ($r=-100$ mm); *CL*, collimating lens; *SP*, 45° BK7 prism.

To cover the whole tuning range of the visible light, we first fixed the grating period and optimized the pump wavelength using the depletion hole in the pump spectrum, which will be discussed in detail in section 3.2.7-A. Then we recorded the spectra and the output power of the visible light with changing the cavity length. Repeating above steps at different grating periods, we obtained the tuning and output characteristics of the visible light. The tuning range can still be further extended with changing the temperature. Due to the upper limit of the heater, the crystal cannot be heated higher than 120°C , so that we cannot perform a systematic experimental study. Fig. 3.2.11 presents the possible tuning range with some typical spectra and output power characteristics of the visible light. It can be seen in Fig. 3.2.11(a) that the possible tuning range of the SFG between the signal and the pump is from 460 nm to about 500 nm. The highest output power was 14 mW at 486 nm, when the grating period was tuned to about $21\ \mu\text{m}$, the depletion hole in the pump spectrum was at about 803 nm, and the signal oscillated at about 1234 nm. The bandwidth of SFG wave was larger than 1.6 nm. As shown in Fig. 3.2.11(b), the SHG wave is tunable from 520 nm to 660 nm when tuning the signal wavelength from 1040 nm to 1320 nm, and two peak powers were 12 mW at 540 nm and 18 mW at 617 nm. The most efficient generation of the green and the red light was observed at a similar grating period of about $21\ \mu\text{m}$ but at different pump wavelengths. The red light was most intensive when pumping at 803 nm and the signal oscillated at 1234 nm. The highest green power was measured when the pump spectrum was centered at about 790 nm and the signal became intensive at 1080 nm. The bandwidth of the green light is

about 3 nm, and that of the red light is about 4 nm. A quite large bandwidth (15 nm) was measured at about 660 nm.

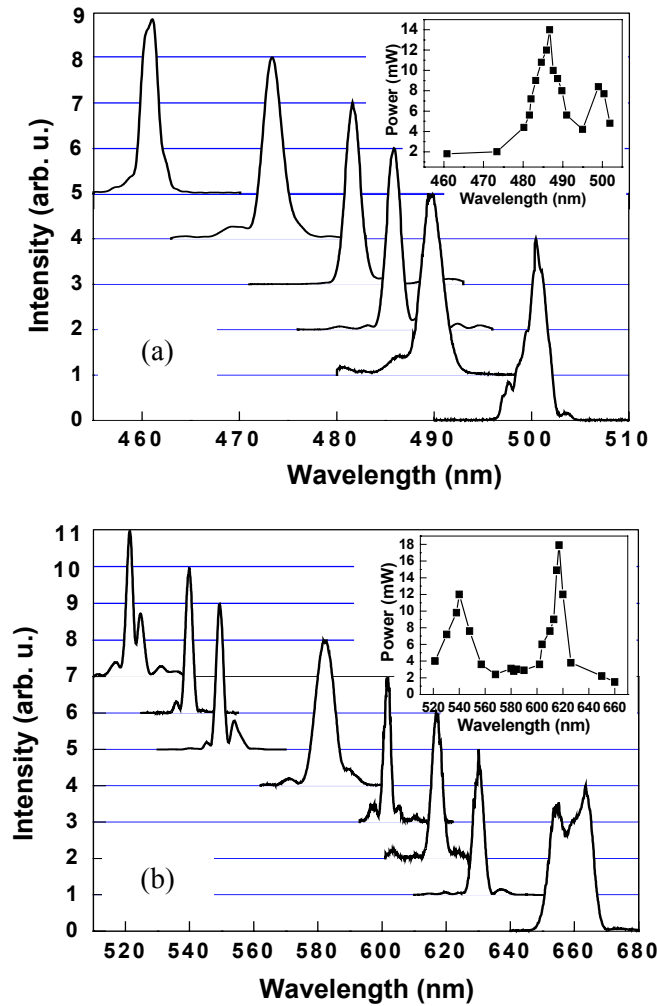


Fig. 3.2.11 Tuning characteristics of (a) SFG and (b) SHG. Inset: output power versus wavelength.

An obvious synchronous operation effect was observed with the SFG process in the blue and the SHG process in the red, they reach their peak powers almost simultaneously, so that a total output power of more than 30 mW was measured in the visible. The curved mirror C2 has reflection coefficients of about 10% for the red light, 20% for the green light, and 30% for the blue light. So, the actually generated visible power should be about 20 mW at 617 nm, 14 mW at 540 nm, and 20 mW at 486 nm, corresponding to conversion efficiencies of about 4%, 3% and 4%, respectively. Since the red and blue radiation is generated almost simultaneously, a total conversion efficiency of 8 % was achieved in the visible. We also pumped the

OPO with a reduced power of only 300 mW, and up to 10 mW in the blue, 12 mW in the red and 7 mW in the green were generated.

The walk-off among the visible beams is hardly observed. Perfectly round TEM₀₀ modes were observed in all visible beams without distortion from photorefractive effects when the crystal is heated to 100 °C. The transverse modes of the visible beams recorded by a CCD camera are shown in Fig. 3.2.12. Comparing with the brightness of the depleted pump beam in the picture, we can distinguish the intensity difference between the visible beams. Since the beams were separated by a prism, the positions of the visible beams relative to the depleted pump beam give us some information about their wavelength. After recollimation, the visible beams can be used directly for application purposes. The OPO runs in a quite stable way and the pump threshold was measured to be as low as 70 mW. The generated visible light is already sufficient in both tuning range and output power for femtosecond spectroscopy where visible power in the order of 10 mW is needed.

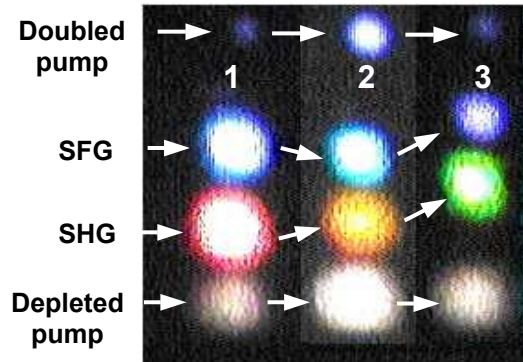


Fig. 3.2.12 Transverse modes of the visible beams. 1-SHG in the red, 2- SHG in the yellow, 3- SHG in the green.

3.2.5 Mechanisms for the efficient visible light generation

To understand the mechanism of the efficient visible light generation, we examined precisely the wavelengths of the interaction waves and the corresponding grating periods in PPLN. The following two relationships were obtained:

$$\Lambda \approx 3\Lambda_{SHG,G} \quad (3.2.1)$$

$$\Lambda \approx 2\Lambda_{SHG,R} \approx 4\Lambda_{SFG,B} \quad (3.2.2)$$

where Λ is the practical grating period in PPLN for parametric oscillation, $\Lambda_{SHG,G}$ and $\Lambda_{SHG,R}$ are the grating periods required by the 1st order QPM SHG of green light from

520 nm to 550 nm and the red light from 600 nm to 625 nm, respectively; $\Lambda_{\text{SFG,B}}$ is the grating period required by the 1st order QPM SFG of blue light from 475 nm to 495 nm. We can conclude from (3.2.1) and (3.2.2) that the generation of the green light through SHG is based on third order QPM, while the generation of the red (SHG) and the blue light (SFG) is based on second- and fourth-order QPM, respectively. According to the theory of QPM [1, 95], an even-order QPM process yields zero conversion efficiency for a poling period with 50% duty cycle. To explain the efficient generation of the visible light, we have to consider a duty cycle that is not equal to 50%.

A. Determination of the duty cycle

To determine the duty cycle of the poling period, we measured the efficiency of the SHG of the pump (Ti:sapphire laser) versus pump wavelength. It is found that the 8th order QPM at about 809 nm is much more efficient than the 7th order at 838 nm and the 9th order at about 778 nm. The 7th and the 9th orders have almost the same conversion efficiency as that of the non-phase-matched processes, as shown in Fig. 3.2.13. Then we performed a series of simulations by solving the coupled equations given in [29] for the 7th - 9th order quasi-phase-matched SHG processes in a 0.5 mm PPLN at $T=100$ °C. Fig. 14(a) gives the calculated efficiencies of the 7th -9th order QPM when the duty cycle is changed from 50% to 62.5%. A comparison between our measurement and the simulation results enables us to restrict the duty cycle to a small range from about 55% to 57%. The result with a 56.25% duty cycle agrees perfectly with the experiment. Fig. 3.2.14(b) shows how the efficiencies of the 7th – 9th orders of QPM increase with the crystal length at a 56.25% duty cycle, from which we can see details of their behavior.

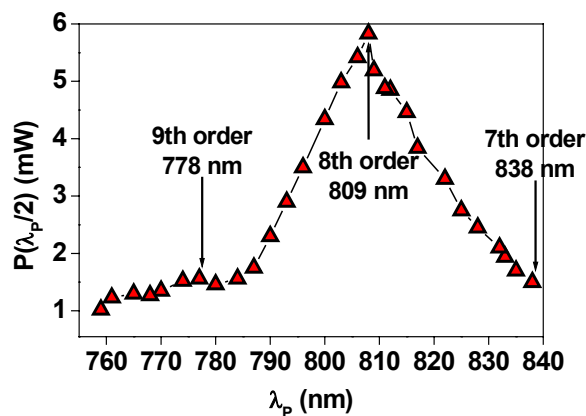


Fig. 3.2.13 Power of the doubled pump ($P(\lambda_p/2)$) versus pump wavelength (λ_p).

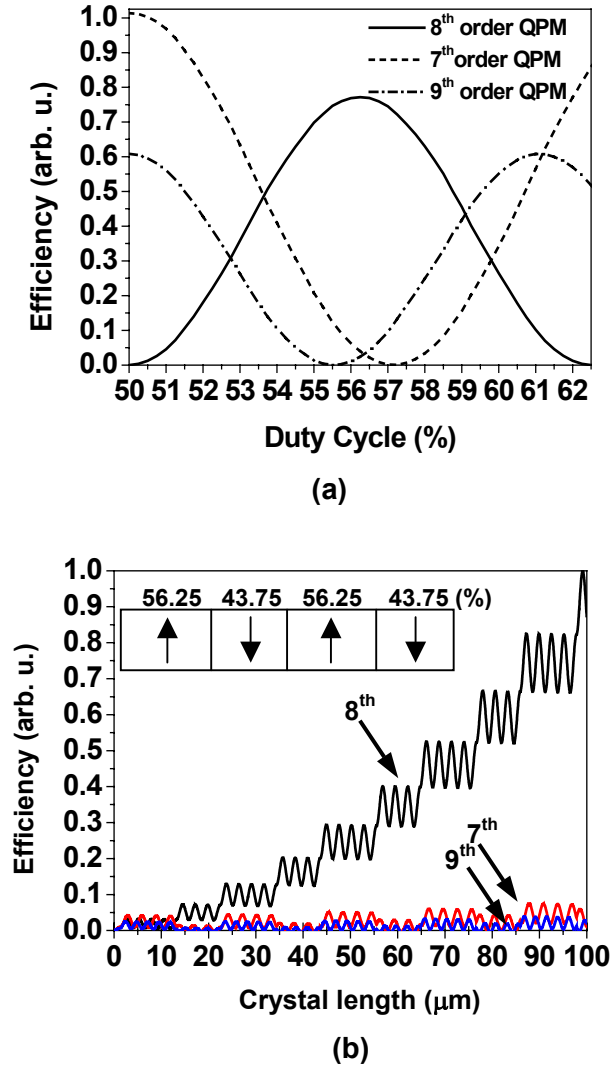


Fig. 3.2.14 Calculated conversion efficiencies of the 7th – 9th order QPM versus (a) duty cycle and (b) length of the crystal with a 56.25% duty cycle.

B. Efficient 4th and 2nd order QPM supported by a ~56% duty cycle

For the convenience of discussion, we assume an exact 56.25% duty cycle to be located in the PPLN in the following theoretical analysis. Fig. 3.2.15(a) shows the assumed poling structure in the crystal and the behavior of the 4th order and the 2nd order QPM, which are obtained by solving the coupled equations for SFG and SHG processes, respectively. From A₁ to B₁, the SFG experiences two complete non-phaseshifted periods and the SHG experiences one complete non-phaseshifted period, where they gain no amplification. From B₁ to D₁, the SFG is quasi-phaseshifted at 4th order with alternating domain lengths of $l_{c1}/2$ and $7l_{c1}/2$ and the SHG is quasi-phaseshifted at the 2nd order with alternating domain lengths of $l_{c2}/4$ and $7l_{c2}/4$, where $l_{c1}=L_C/4$, $l_{c2}=L_C/2$ and $L_C=\lambda/2$ are the coherence lengths required by

the SFG, SHG and the OPO processes, respectively. We can also think that a 2nd order QPM with alternating domain lengths of $l_{c1}/2$ and $3l_{c1}/2$ enhances the SFG process, since from C₁ to D₁, the SFG does not increase. The above processes are repeated for the next grating period (Λ). So, the even-order quasi-phase-matched interactions occupy only part of the crystal length, which reduces largely the efficiencies of these processes. Fig. 3.2.15(b) shows the increase of the conversion efficiencies of the 2nd, 3rd, and 4th orders of QPM with the crystal length for a 0.5 mm PPLN, which support the SHG in the red and green, and the SFG in the blue, respectively. The 3rd order QPM is about twice as efficient as the 4th and the 2nd order QPM. After the interaction length of 0.5 mm, the 4th order and the 2nd order quasi-phase-matched processes gained almost the same amount of increase. Because of the cavity bandwidth, the signal has less intracavity intensity near 1080 nm than around 1240 nm. Therefore, less green power was measured than for red and blue light, although the green light is generated with a more efficient QPM. According to the simulations, we also found a less than 10% decrease in the 1st order QPM and a 30% decrease in the 3rd order QPM for a 0.5 mm PPLN due to the 56.25% duty cycle, which means that more green light and signal wave could have been generated if using a 50% duty cycle.

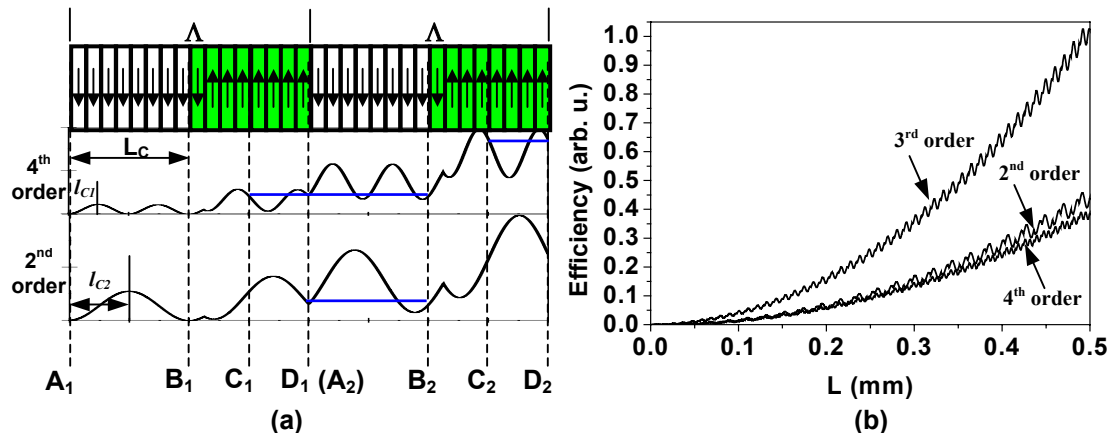


Fig. 3.2.15 (a) Mechanism of the 4th and the 2nd order QPM with a 56.25% duty cycle, where $l_{c1}=L_c/4$ and $l_{c2}=L_c/2$ are the coherence lengths for the 4th and 2nd order QPMs, respectively, L_c is the coherence length of the OPO process and $\Lambda=2L_c$ is the practical grating period. The horizontal lines across the curves correspond to non-gain processes. (b) Conversion efficiencies of the 2nd, 3rd, and 4th order QPMs versus crystal length of PPLN for 56.25% poling duty cycle.

C. Optimization of the duty cycle and theoretical simulations

Changing the duty cycle can optimize the efficiency of even-order QPM that supports the generation of the desired wavelength, so that we can make use of the energy to the largest extent for our purposes. Here we simply apply the theory of Fejer et al. [95] to give an approximate evaluation. Though in this theoretical work only SHG process was considered, because we can think of SHG as a special case of SFG process, it is still reasonable to apply this theory to analyzing SFG processes. In QPM, the conversion efficiency is proportional to d_Q^2 , where $d_Q = \frac{2d_{eff}}{\pi m} \sin(\pi m D)$ is the effective nonlinear coefficient for the QPM interaction, d_{eff} is the effective nonlinear coefficient of the same process in single-domain bulk material, m is the order of QPM, and D is the duty cycle. We plot the conversion efficiencies (η) of different orders of QPM as functions of duty cycle (D) in Fig. 3.2.16. The efficiency of the 1st-order QPM is maximum at 50% duty cycle and reduces to about 85% of the maximum value at about 62.5% duty cycle. The peak efficiency of the 2nd-order QPM is at 75% duty cycle, where the efficiency of the 1st-order is already reduced to about 60% of the maximum. The most efficient 3rd-order QPMs appear at 50% and about 83.3% duty cycles. The peak efficiency of 4th-order QPM is much lower than those of 2nd and 3rd orders, which is at 62.5% and 87.5% duty cycles. To achieve efficient higher order QPM, we should first keep efficient 1st-order. If we set the lower limit of the 1st-order efficiency to 85% of the maximum, the upper limit of the shift from the 50% duty cycle would be about 12.5%, corresponding to the most efficient 4th-order QPM at 62.5% duty cycle.

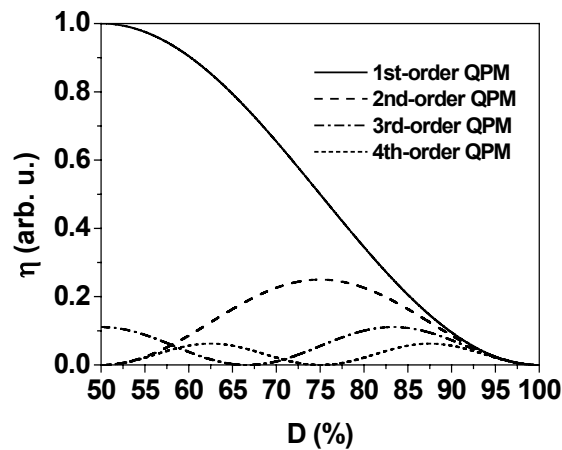


Fig. 3.2.16 Calculated conversion efficiencies of 1st-, 2nd-, 3rd- and 4th-order QPM versus poling duty cycle.

Using above theory we can only analyze 1st and higher orders of QPM independently, so that we cannot include the coupling and depletion among them. To understand the mechanisms more clearly and explain them more exactly, we performed theoretical simulations of the behavior of all of the efficiently generated waves, including the OPO-process-generated the signal, the SHG processes of both the pump and the signal, the SFG between the pump and the signal, and the SFG between the pump and the idler. The simulation applies a series of duty cycles for optimization. In order to give a complete analysis and make our simulations more close to the practical cases, we used practical conditions or parameters for the pump and the operation of the OPO with a large variation range, and also included the cavity loss and output coupling to simulate steady-state operation. We emphasized how the poling duty cycle affects the characteristics of all of the interactions and how to optimize the poling duty for the efficient generation of a desired wavelength. We also explained how the synchronous operation between the SHG of the signal and the SFG between the pump and the signal took place. Since our method and theoretical model can be used universally for analogous processes, we described this part in detail and separately in Chapter 3.3.

3.2.6 Temporal characteristics of the generated waves

Figure 3.2.17 shows the interferometric autocorrelation measurement and corresponding spectrum of the signal. In the autocorrelation data, the solid line is the measurement and the dashed line is the simulation with 65 fs Gaussian pulses. The time-bandwidth product is about 0.5. Fig. 3.2.18(a) and 3.2.18(b) present the intensity autocorrelation measurements of the SFG in the blue and the SHG in the red, respectively. We measured the visible pulses with an NT&C autocorrelator [96] with a SiC photodiode ($2 \times 2 \text{ mm}^2$) through two-photon absorption. The pulses at 486 nm were measured to be 240 fs long with a time-bandwidth product of 0.487; while a pulse duration at 617 nm was measured to be 210 fs with a larger time-bandwidth product of 0.613. The visible pulses were largely broadened as compared with the signal and the pump pulses. Calculations found that in a 0.5 mm PPLN the pulse broadening effect resulting from the GVD can be neglected for a pulse longer than 60 fs even at 486 nm. But the visible pulses need to pass through more than 20 mm BK7 glass (including one of the curved mirrors (5 mm), the collimating lens (2 mm), the

prism (10 mm), the rotator of the autocorrelator (~ 1.5 mm) and a focusing lens (2 mm)) before reaching the photodiode, this will expand the visible pulses considerably. On the other hand, the GVM between the interaction waves (1170 fs/mm between the SFG at 486 nm and the signal at 1240 nm, 937 fs/mm between the SFG and the pump at 800 nm, 564 fs/mm between the SHG at 617 nm and the corresponding signal) may be the main reason for the large broadening of the visible pulses.

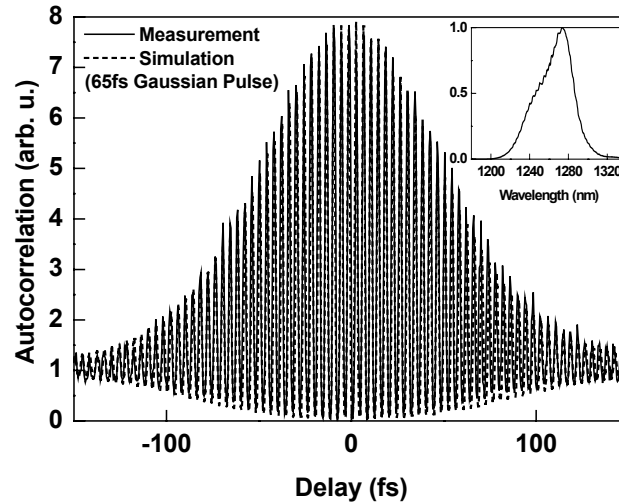


Fig. 3.2.17 Interferometric autocorrelation measurement of the signal pulses (solid line) and theoretical simulation with 65 fs Gaussian pulses (dashed line). Inset: corresponding spectrum.

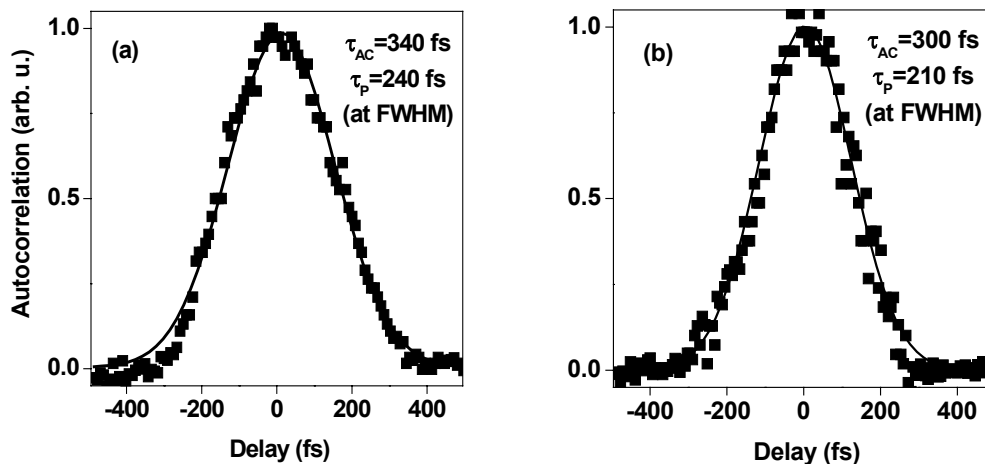


Fig. 3.2.18 Intensity autocorrelation measurement (filled squares) of the visible pulses at (a) 486 nm and (b) 617 nm. The solid lines are Gaussian fits to the experimental data. τ_{AC} and τ_p denote the autocorrelation width and corresponding pulsewidth.

3.2.7 Operation characteristics of the PPLN OPO

A. Pump spectrum depletion

A very important phenomenon observed in our 30 fs Ti:sapphire laser pumped PPLN OPO is the pump spectrum depletion effect resulting from a limited phase matching bandwidth. Fig. 3.2.19 shows the pump wavelength tuning behavior and phase matching bandwidth of a 0.5 mm PPLN crystal with a grating period of 21 μm at 100 °C. A large phase matching bandwidth can be found for the signal wavelength, which is nearly 180 nm when pumping at 800 nm. This implies that the generation of a large signal bandwidth requires a much smaller pump bandwidth. Even under perfect phase matching ($\Delta kL=0$), a signal bandwidth of 100 nm centered at 1200 nm corresponds to a pump bandwidth of only 8.5 nm, as demonstrated by the region marked by the dashed lines in Fig. 3.2.19.

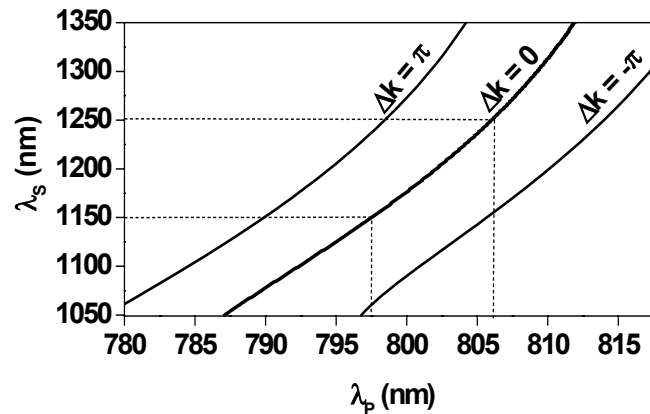
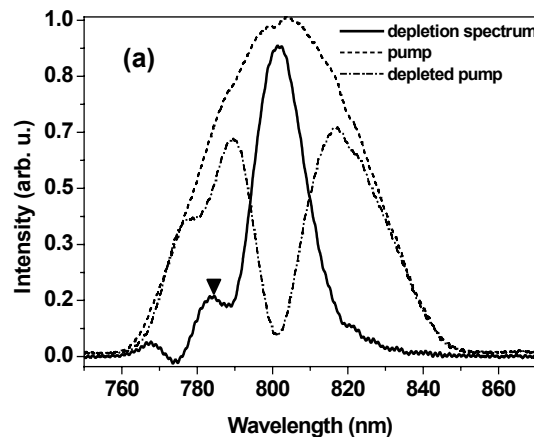


Fig. 3.2.19 Phase matching bandwidth of a 0.5 mm PPLN with a grating period of 21 μm and at 100°C, where L is the crystal length, Δk is the phase mismatch between the signal and the pump, the dashed lines show the correspondence between a 100 nm signal bandwidth and a 8.5 nm pump bandwidth at perfect phase matching.

When pumping a PPLN OPO with sub-100 fs pulses, corresponding to a bandwidth larger than 10 nm at FWHM, a depletion hole will be normally observed in the pump spectrum. In our case, the pump has a bandwidth of about 45 nm, corresponding to a pulse duration of about 21 fs when assuming transform limited operation. However, the pump pulses are in fact about 30 fs long according to the autocorrelation measurement. Fig. 3.2.20(a) gives the depleted (dash-dot line) and undepleted pump (dash line) spectra, as well as the depletion spectrum (solid line) which is defined as the difference between the above two spectra. The depletion spectrum is about 16 nm at FWHM and about 20 nm at 30% the maximum. These values of the depletion

spectrum were found typical for different pumping spectra. The smaller peak in the depletion spectrum results from the simultaneous oscillation of another signal wavelength. The depth of the depletion hole relates directly to the depletion of the pump power and the generated signal power. When tuning the cavity length, the signal wave needs to change its group velocity by shifting in its wavelength in order to keep synchronous pumping. However, different signal wavelengths deplete the pump spectrum at different positions for perfect phase matching. So, the depletion hole will shift over the pump spectrum with changing cavity length, as shown in Fig. 3.2.20(b). In fact, changing the cavity length to tune the signal wavelength combines two tuning mechanisms: cavity length tuning and pump wavelength tuning. This is the main reason why a large tuning range (over 300 nm) can be achieved by only tuning the cavity length. For birefringently phase matched OPOs (e.g., KTP OPOs), the tuning of the signal wavelength versus pump wavelength normally varies slowly or nearly linearly in a relatively small range. The signal bandwidth is mostly comparable to the pump bandwidth so that the depletion hole effect is rarely observed and the tuning range with changing the cavity length is much smaller than a PPLN OPO. In principle, the tuning range of a PPLN OPO can still be extended when using a larger pump bandwidth provided that the cavity bandwidth is larger than the potential tuning range. But at a given pump power, enlarging the pump bandwidth will reduce the intensity distributed on each spectral component and will thus increase the pump threshold. In this case, pump power needs to be increased accordingly to make more spectral components in the pump spectrum operate above the pumping threshold. In practice, the signal bandwidth is smaller than the theoretical value at a given pump bandwidth, due to the intracavity GVD and GVM, due to the cavity bandwidth, and due to the pumping threshold.



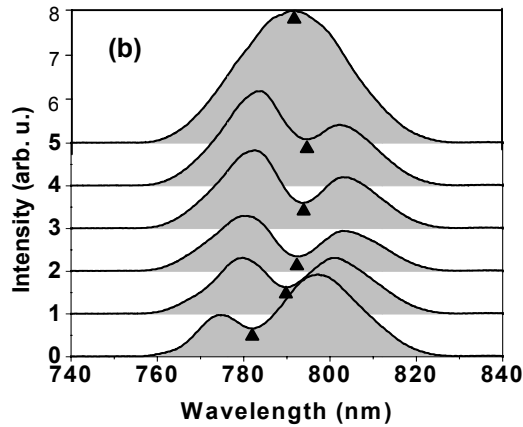


Fig. 3.2.20 Pump spectrum depletion. (a) Depletion hole and depletion spectrum. (b) Shift of the depletion hole (filled triangles) with tuning the cavity length of the OPO.

The depletion hole in the pump spectrum is very useful to optimize the operation of the PPLN OPO. First, the center wavelength of the pump can be optimized by monitoring the shift of the depletion hole with tuning the cavity length of the OPO, which should be able to move over the whole pump spectrum at an optimal pump wavelength. For longer or shorter pump wavelength, the depletion hole can only shift over the spectral range shorter or longer than the center pump wavelength, resulting in a smaller tuning range of both the signal wavelength and the cavity length. Second, using the width of the depletion hole, we can optimize the pump bandwidth so that the pump energy is utilized to the largest extent without reducing the signal bandwidth. Thus, if the depletion in the pump power is increased, a higher efficiency and a lower pump threshold of the OPO will consequently be achieved. According to our systematic measurements, most efficient pumping is achieved when the pump bandwidth at FWHM is approximately equal to the bandwidth of the depletion spectrum at 30% of the maximum. Fig. 3.2.21 shows the conversion efficiency of the OPO versus the pump bandwidth when pumping with about 500 mW at 795 nm. The most efficient operation of the OPO was achieved at a pump bandwidth of about 20 nm at FWHM, where the depletion spectrum is about 20 nm at 30% of the maximum and about 17 nm at FWHM. The pump power was depleted by 57%. Further narrowing the pump bandwidth will decrease the conversion efficiency and reduce the signal bandwidth. Certainly a smaller pump bandwidth corresponding to longer pulse duration will increase the interaction length and thus decrease the pump threshold.

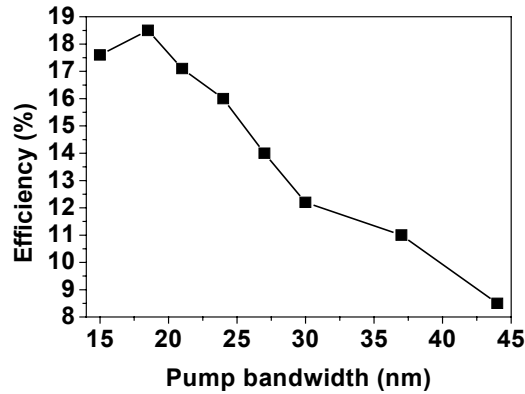


Fig. 3.2.21 Conversion efficiency (the ratio between the signal power and the pump power) of the PPLN (grating period $21 \mu\text{m}$) OPO versus pump bandwidth with the center pump wavelength optimized to 795 nm and the pump power fixed at about 500 mW .

B. Cavity length detuning: experiment and theory

Because of efficient SFG and SHG processes and excessive intracavity compensation for GVD, the variation in the signal power with tuning of the cavity length is quite different from the results of previous work with a KTP OPO [17]. An obvious two-stage operation effect was observed with the PPLN OPO, meaning the OPO turns on and off twice during the cavity length detuning process.

The HR mirror M2 of the cavity has a reflection of about 98~99% from 1100 nm to 1300 nm . Up to 50 mW signal power was measured behind it. The piezoelectric crystal on M3 was driven by a sawtooth wave of a period of 100 s and an amplitude of 18 V , generating a traveling range of $8.1 \mu\text{m}$ and a cavity length detuning amount of about $16.2 \mu\text{m}$. Fig. 3.2.22 shows the powers of the depleted pump and the generated waves (the signal, the SHG in the red and the SFG in the blue) versus cavity length detuning. In regime I, where efficient visible light generation appears, both the signal and the pump are largely depleted. Since the pump needs not only to support the oscillation of the signal but also to take part in the SFG process, the pump power is depleted by 28% which is larger than in other regimes. The cavity length tuning range for efficient visible light generation is only about $1.5\sim 2 \mu\text{m}$. In regime II, little visible light can be detected, and less than 38 mW signal power was measured with 18% pump depletion. The OPO nearly turns off after regime II and the first stage is finished. In the second stage, up to 50 mW signal power was measured with a 23% depletion of the pump power. The signal power changes smoothly and slowly with

tuning the cavity length, but little power was measured in the visible. The tuning rate of the signal wavelength is much smaller than in regime I. In this regime, yellow light with low power was observed, which was proven to be the SFG between the pump and the idler. It can also be concluded from the above measurement that the SHG and SFG processes are very wavelength-sensitive and they are not simply non-phase-matched processes based on a large signal power.

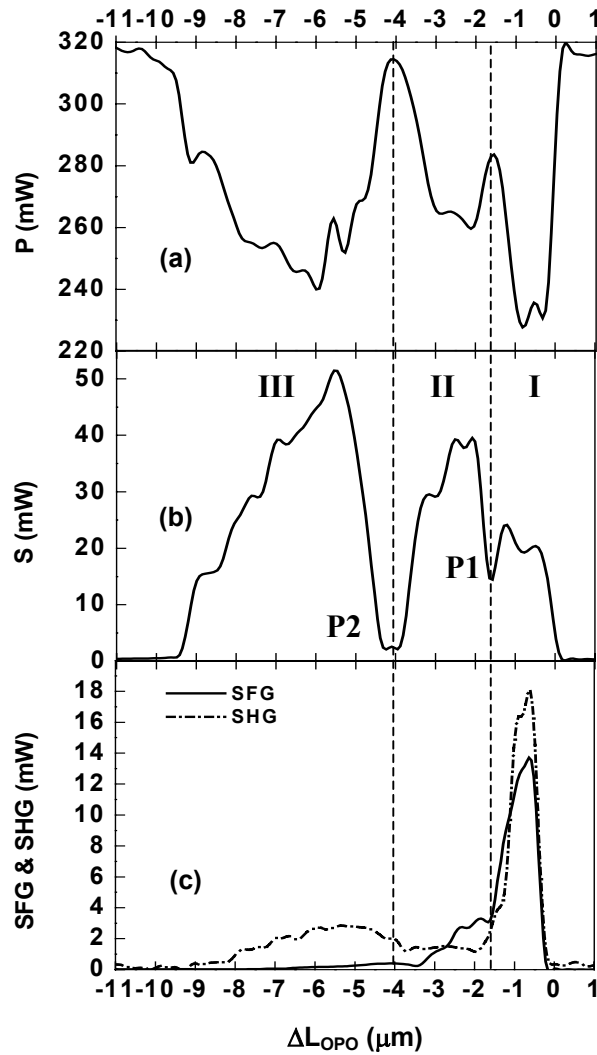


Fig. 3.2.22 Power characteristics of (a) the pump $[P]$, (b) the signal $[S]$, and (c) the SHG and SFG waves versus cavity length detuning $[\Delta L_{OPO}]$.

The cavity length detuning effects (variation of the signal wavelength and power with cavity length) results directly from the intracavity GDD and the compensation by chirped mirrors.

Since in our OPO the contribution of the non-chirped mirrors to the intracavity GDD (GDD_{OPO}) is negligible in comparison to the GDD of the chirped mirrors (GDD_{CM}) (see Fig. 3.2.23(a)) and the GDD of the PPLN crystal (GDD_{PPLN}), we can write

$$GDD_{OPO} = GDD_{CM} + GDD_{PPLN}. \quad (3.2.3)$$

By definition the GDD is

$$GDD = \frac{d\tau}{d\omega} = -\frac{\lambda^2}{2\pi c} \cdot \frac{d\tau}{d\lambda}, \quad (3.2.4)$$

where $\tau = GD$ is the group delay, c the velocity of light in vacuum, ω the angular frequency and λ the corresponding wavelength. Increasing the length of the OPO cavity which operates synchronously to the pump at a wavelength λ_0 by ΔL_{OPO} , the signal at λ_0 is delayed by

$$\Delta\tau = \frac{\Delta L_{OPO}}{c}. \quad (3.2.5)$$

Following Eqs. (3.2.3) – (3.2.5), the OPO can maintain synchronous operation by shifting its wavelength to λ_l determined by:

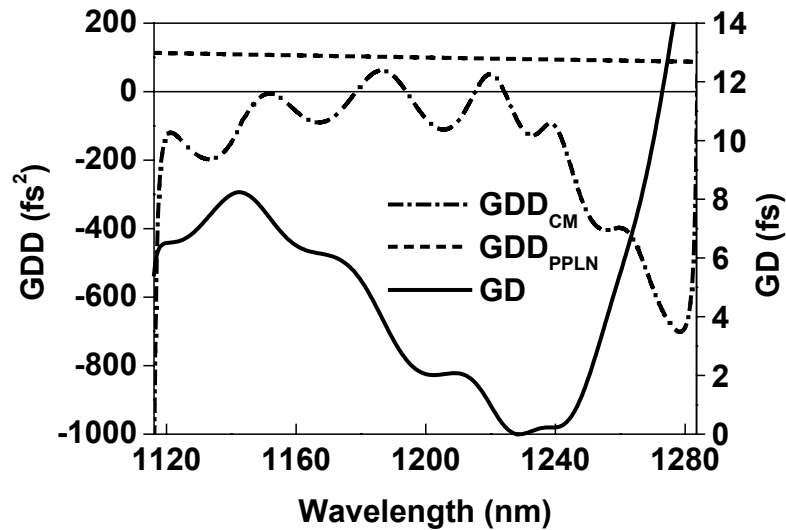
$$\Delta L_{OPO} = -c \int_{\lambda_0}^{\lambda_l} \frac{d\tau}{d\lambda} d\lambda = 2\pi c^2 \int_{\lambda_0}^{\lambda_l} \frac{GDD_{OPO}}{\lambda^2} d\lambda. \quad (3.2.6)$$

According to Eq. (3.2.6), the wavelength dependence of the cavity group delay $\Delta\tau(\lambda)$ depicted in Fig. 3.2.23(a) determines the tuning of the OPO with changing cavity length. Fig. 3.2.23 (b) shows the inverse relation $\lambda = \lambda(c\Delta\tau) = \lambda(\Delta L_{OPO})$ and compares the theoretical curve (solid line) with experimental data. In the range from 1120 nm to 1280 nm, for which GDD_{CM} data are available, the experiment agrees fairly well with the theory. For signal wavelengths longer (shorter) than 1220 nm, λ_s increases (decreases) with shorter cavity length. The wavelength at which the GDD_{OPO} becomes zero and the GD has a minimum will oscillate first when shortening the cavity from the longer end. This wavelength was found to be at about 1220 nm. Wavelengths with equal group delays will oscillate simultaneously, so that dual signal wavelength operation is observed in the cavity [8]. The upper branch

exhibits a tuning gap between 1280 nm and 1298 nm (region around $P2$ in Fig. 3.2.22(b)) caused by a sharp rise of the intracavity GDD , reaching positive values at 1283 nm. Therefore the group delay will decrease above 1283 nm. However, for negative intracavity GDD the group delay of the signal pulses must increase with decreasing the cavity length to maintain synchronism with the pump pulses. A similar effect is observed around 1120 nm (see the dip at $P1$ in Fig. 3.2.22(b)) where GDD_{CM} becomes strongly negative.

For wavelengths longer than 1298 nm, the GDD is expected to become strongly negative again. The intracavity group delay of the signal pulses will be correspondingly increased and the signal pulses become synchronized to the pump pulses, so that the OPO operates in a second stage.

The tuning rate in the positive GDD region is much larger than that in the negative GDD region. Because of cavity bandwidth, the OPO cannot operate at wavelengths shorter than 1050 nm and longer than 1350 nm. Experiments also showed that with largely negative intracavity GDD the OPO could operate much more stable and efficiently, but the tuning rate of the signal wavelength became smaller when changing the cavity length.



(a)

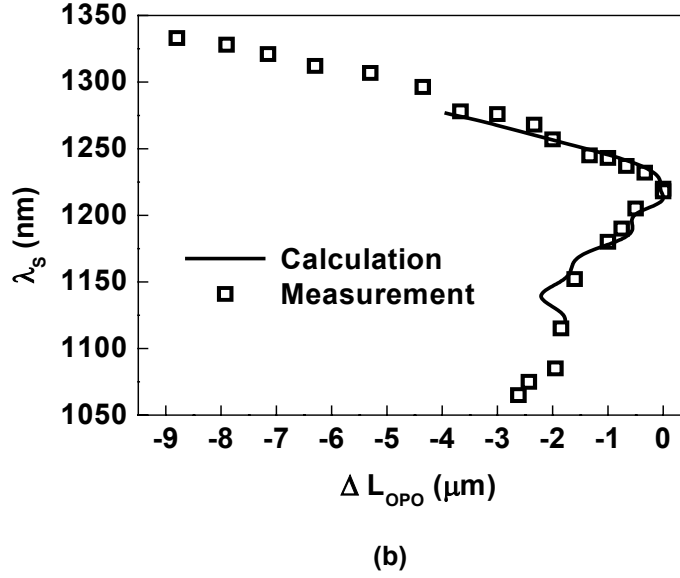


Fig. 3.2.23 Cavity length tuning effects with intracavity GDD compensated by chirped mirrors. (a) GDD of the chirped mirrors (dash-dotted line) and PPLN (dashed line), and the relative group delay (GD, solid line) vs. wavelength. (b) Comparison of tuning of the signal wavelength with the cavity length change (ΔL_{OPO}) between theory (solid line) and measurement (opened squares).

C. Self-phase-modulation (SPM) effects

As shown in Fig. 3.2.11, multiple peaks are sometimes observed in the SFG and SHG spectra, which result from the depleted pump spectrum and the structured signal spectrum. Pump spectrum depletion leaves two peaks on both sides of the depletion hole. The SFG is the interaction not only between the signal and the depletion spectrum but also between the signal and the peaks left in the pump spectrum. So, two small wings sometimes appear in the SFG spectra. Because of high intracavity intensity of the signal wave and high nonlinear refractive coefficient of the PPLN crystal ($n_2=5 \times 10^{-15} \text{ cm}^2\text{W}^{-1}$, see Z-scan measurement of PPLN discussed in Chapter 3.6), significant self-phase-modulation effects were observed in the femtosecond PPLN OPO, which are identified by broadened and structured signal spectra [71]. Assuming 65 fs signal pulses and 60 μm diameter of the signal beam at the focus in the crystal, for an output power of 40 mW and 2 % output coupling, the highest intensity at the focus in the crystal is about $27 \text{ GW}/\text{cm}^2$. The accumulated single-pass phase shift is about 0.11π at maximum using $\phi_{\text{max}} = \frac{2\pi}{\lambda} n_2 I_0 L$ [79], which means the maximum nonlinear phase shift experienced by a pulse centered at λ and with

maximum intensity I_0 propagating through a length L of crystal with nonlinear refractive index n_2 . The average photon lifetime in the cavity is about 50 round trips for a 2% output coupler, creating a maximum phase shift of about 5.5π . The SPM-effect-induced positive GDD [91] in the signal pulse can be eliminated by the over-compensation by the chirped mirrors, so that nearly Gaussian-shaped signal spectra were observed in the net negative GDD region in spite of even higher signal intensity. Fig. 3.2.24 shows the tuning of the signal spectra. Because the SPM effects depend on the signal intensity, they become less obvious at low signal power. On the other hand, the GVD of PPLN becomes smaller with increasing wavelength. The signal spectra are more structured at shorter wavelengths than at longer wavelengths because of high signal power and positive GVD in PPLN. At wavelengths longer than 1300 nm, the signal spectrum becomes Gaussian-shaped, though a larger signal was detected. This resulted from the much larger negative intracavity GVD .

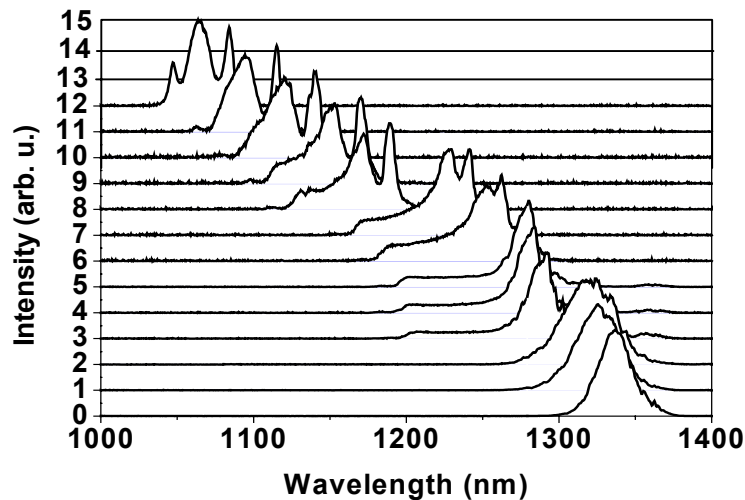


Fig. 3.2.24 Broadened and structured signal spectra when tuning the cavity length result from self-phase-modulation effects.

3.2.8. Conclusions

We summarized and compared different methods for generating visible pulses from an OPO and demonstrated mainly the efficient generation of visible femtosecond pulses through higher-order QPM in a PPLN OPO. Up to 8% conversion efficiency into the visible was achieved with only 480 mW pump power using a ~56% duty cycle of the poling period. Optimizing the duty cycle can improve significantly the conversion efficiency into the visible. Using higher pump power, much more visible light can be generated.

Theoretical analysis proved that our method using an intentionally designed poling duty cycle is very promising to achieve efficient intracavity SHG and SFG processes in a PPLN OPO. We can also conclude that multiple orders of QPM can be managed in the same PPLN, so that efficient frequency mixing processes between the interaction waves in a PPLN OPO can be achieved simultaneously without using any other nonlinear crystals or optical components. Our theory modeling the intracavity GDD nicely explains the cavity length detuning behavior. Through the self-SHG and self-SFG processes, the tuning range of the PPLN OPO is largely extended and the device becomes more versatile for spectroscopy applications. The pump spectrum depletion effect is very useful to optimize the pumping spectrum and the operation efficiency of the PPLN OPO, so that the lowest pump threshold can be reached. Significant SPM effects in tightly focused femtosecond OPO result in broadened and structured signal spectra, which can give rise to multiple peaks in the generated visible spectra.

3.3

Coupling among multiple higher-order QPM processes in a PPLN OPO

In Chapter 3.2 we discussed how a poling duty cycle that is not equal to 50% (e.g., ~56%) enabled even-order QPM processes and how multiple higher-order (even and odd order) QPM processes operate simultaneously and efficiently in a single PPLN OPO. A 4th-order QPM SFG between the pump and the signal and a 2nd-order QPM SHG of the signal were described both experimentally and theoretically. The theoretical analysis considered these processes separately. The coupling between them as well as some other possible efficient interactions were not taken into account. A more exact model is required to deal with this problem for better understanding of the mechanisms and more complete investigating of the observed phenomena.

In this chapter, we give a more exact theoretical model by incorporating all of the observed efficient processes into one set of differential equations derived from the coupled equations for different QPM processes of three-wave parametric interactions. The simulation results demonstrate the coupling relations and dependence among the interacting waves and reveal more efficient interactions. Here we will also introduce some weak coupling processes that will be described as degenerate processes. The synchronous operation between the SHG of the signal and the SFG between the pump and the signal will be investigated precisely. Using practical operation parameters and considering the steady-state oscillation of the signal make our simulation results reflect the real behavior of the OPO, so that perfect agreement between simulation and measurement can be obtained.

3.3.1 Higher-order processes in a PPLN OPO

As reference and basis for our simulation, we use the same experimental set-up and measurement results as given in Chapter 3.2. We first present all of the observed generation of new waves in addition to the pump, the signal, and the idler. Fig. 3.3.1 illustrates all of the measured spectra from 350 nm to 700 nm when the PPLN OPO operated at about 1305 nm. The spectrum centered at about 652.6 nm is generated through doubling of the signal. The double-peaked spectrum centered at about 400 nm

is the doubled pump. Oscillation of the signal resulted in a depletion hole in the pump spectrum, and therefore in the doubling spectrum. The double-peaked spectrum centered at about 494 nm is the SFG between the pump and the signal. Depletion of the pump spectrum left two peaks on both sides of the depletion hole, which led to the double peaks in the SFG spectrum. The spectrum at about 581 nm is the SFG between the pump and the idler. The spectrum at about 681 nm is the SFG between the pump and the idler.

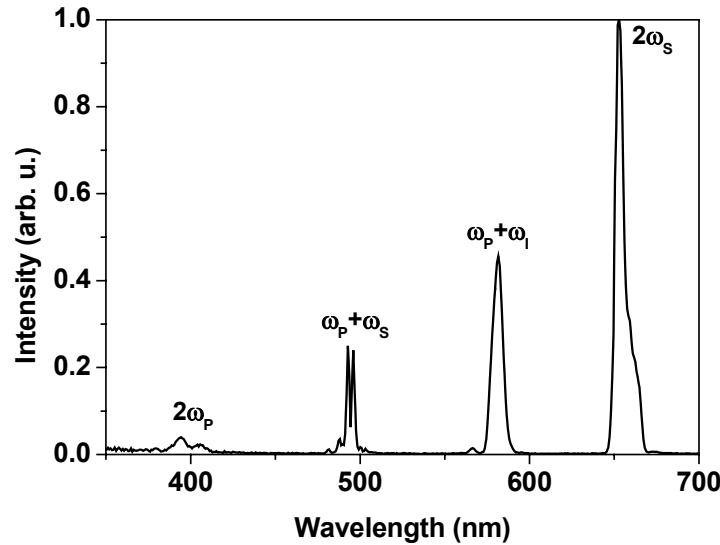


Fig. 3.3.1 Observed spectra in the visible and UV regions when the OPO signal operates at about 1305 nm. ω_p , ω_s , and ω_i are the frequencies of the pump, the signal, and the idler. “+” means the SFG between the frequencies on both sides of it and “2” means SHG of the frequency behind it.

Because of a non-50% duty cycle of PPLN, both even and odd orders of QPM can operate efficiently. Therefore, we need to study the OPO process more completely by including all possibly efficient interactions. Considering that efficient interactions take place only for intensive waves, especially in case of higher-order processes, we only took care of the pump- or signal-involved processes. However, our simulation found that only the processes listed in Table 3.3.1 produced efficient generation of new frequencies, which also agrees with our observations as shown in Fig. 3.3.1. In Table 3.3.1, the subscripts S , P , I denote the signal, the pump and the idler; $SHG1$ and $SHG2$ stand for the doubling of the pump and the signal, respectively; $SFG1$ is the SFG between the pump and the signal, and $SFG2$ is the SFG between the pump and the idler.

Table 3.3.1 Efficient processes existing simultaneously in a PPLN OPO.

Processes	Frequency conversions	$d_{33}^{a)}$ (pm/V)	Order of QPM
1. OPO	$\omega_p \rightarrow \omega_s + \omega_l$	23.8	1
2. SHG1: doubling of P	$2\omega_p \rightarrow \omega_{SHG1}$	31.5	7, 8, 9
3. SHG2: doubling of S	$2\omega_s \rightarrow \omega_{SHG2}$	26.0	1 ^{b)} , 2, 3
4. SFG1: SFP between P and S	$\omega_p + \omega_s \rightarrow \omega_{SFG1}$	28.2	3, 4, 5
5. SFG2: SFG between P and I	$\omega_p + \omega_l \rightarrow \omega_{SFG2}$	26.1	2

a) $d_{33}=27$ pm/V for the SHG of 1064 nm. [6]

b) The order of the QPM for SHG of the signal is approximately equal to 1, instead, it is a little larger than 1, when the signal oscillates at about 1.5 μ m.

The first column from the left of Table 3.3.1 lists the numbered processes, the second column presents the frequency conversion relationships between correspondingly interaction waves, the third column gives the effective second-order nonlinear coefficient of PPLN for each process, and the fourth column gives the possible orders of QPM for each process.

The second-order optical nonlinear coefficient d_{33} of PPLN was calculated approximately using the Miller's scaling and the value of d_{33} for SHG of 1064 nm given in Ref. 8, which is 27 pm/V. The Miller's scaling is given by

$$\Delta_{ijk} = \frac{d_{ijk}(-\omega_1 - \omega_2; \omega_1, \omega_2)}{\chi_{ii}(\omega_1 + \omega_2)\chi_{jj}(\omega_1)\chi_{kk}(\omega_2)},$$

where Δ_{ijk} has little dispersion, d_{ijk} is the second-order nonlinear coefficient, and the χ 's are linear susceptibility tensor elements ($\chi_{ii}(\omega)=n_i^2-1$, where n_i is the refractive index for light at frequency ω polarized along the i axis). [97,98,99]

The same rule of subscription will be used in the following discussion for the wavelength (λ_i), the refractive index (n_i), and the electric field (E_i), with $i=P, S, I, SHG1, SHG2, SFG1, SFG2$. Our discussion below will also be concentrated on the 5 processes and the 6 generated waves.

3.3.2 “Degenerate” higher-order QPM processes

Before introducing the theoretical model for simulation, it is worth mentioning some weak coupling interaction that may be QPM at higher orders.

Here we apply the concept of “degeneracy” to describe two or more higher-order QPM processes that generate the same frequency.

Based on the energy conservation condition of an OPO, namely $\omega_p = \omega_s + \omega_i$, we can obtain easily the following relationships:

$$\omega_p + \omega_s = 2\omega_s + \omega_i \quad (3.3.1)$$

$$\omega_p + 2\omega_s = \omega_s + (\omega_p + \omega_s) \quad (3.3.2)$$

$$\omega_p + (\omega_p + \omega_s) = \omega_s + 2\omega_p \quad (3.3.3)$$

Equation (3.3.1) implies that the SFG between the signal and the pump and the SFG between the doubled signal and the idler will generate the same frequency (wavelength): ω_{SFG1} (λ_{SFG1}). The left side of equation (3.3.2) is the SFG between the pump and the doubled signal, and the right side is the SFG between the signal and the SFG between the pump and the signal. These two processes also generate the same frequency. In equation (3.3.3), one of the two equivalent processes is the SFG between the signal and the doubled pump on the right side, and the other is the SFG between the pump and the SFG between the pump and the signal on the left side.

Though the equations of (3.3.1), (3.3.2), and (3.3.3) can be concluded for any OPO, the two processes on both sides of each of these equations can NOT be phase-matched simultaneously in a birefringently phase-matched OPO. In a QPM OPO, the two processes can be QPM at different orders, so that they can possibly become efficient simultaneously. Especially in case of the non-50% poling duty cycle, any of them may become strongly coupled in a certain spectral range. Consequently, the corresponding effects may affect the behavior of other generated waves and the OPO process.

Based on the phase-matching conditions for the OPO, the SFG between P and S ($SFG1: \omega_p + \omega_s$), the doubling of S ($SHG2: 2\omega_s$), and the SFG between *the doubled* S and I ($SFG3: 2\omega_s + \omega_i$), we have the following relationships:

$$\text{OPO: } \frac{n_p}{\lambda_p} = \frac{n_s}{\lambda_s} + \frac{n_i}{\lambda_i} + \frac{1}{\Lambda_{OPO}} \quad (3.3.4)$$

$$\omega_p + \omega_s: \frac{n_{SFG1}}{\lambda_{SFG1}} = \frac{n_p}{\lambda_p} + \frac{n_s}{\lambda_s} + \frac{1}{\Lambda_{SFG1}} \quad (3.3.5)$$

$$2\omega_s: \frac{n_{SHG2}}{\lambda_{SHG2}} = \frac{n_s}{\lambda_s} + \frac{n_s}{\lambda_s} + \frac{1}{\Lambda_{SHG2}} \quad (3.3.6)$$

$$2\omega_S + \omega_I: \frac{n_{SFG3}}{\lambda_{SFG3}} = \frac{n_{SHG2}}{\lambda_{SHG2}} + \frac{n_I}{\lambda_I} + \frac{1}{\Lambda_{SFG3}} \quad (3.3.7)$$

where Λ_{OPO} , Λ_{SFG1} , Λ_{SHG2} , Λ_{SFG3} are the grating periods for the 1st-order QPM processes given by equations (3.3.4) through (3.3.7).

From (3.3.4) to (3.3.7), we can easily derive the following relationship:

$$\boxed{\frac{1}{\Lambda_{OPO}} + \frac{1}{\Lambda_{SFG1}} = \frac{1}{\Lambda_{SHG2}} + \frac{1}{\Lambda_{SFG3}}} \quad (3.3.8)$$

If substituting $\Lambda_{SFG1} = \Lambda_{OPO} / 4$ and $\Lambda_{SHG2} = \Lambda_{OPO} / 2$ into (3.3.8), we can conclude that:

$$\Lambda_{SFG3} = \Lambda_{OPO} / 3 \quad (3.3.9)$$

Equation (3.3.9) tells us that if *SFG1* is supported by a 4th-order QPM and *SHG2* is enhanced by a 2nd-order QPM, the SFG between the doubled signal and the idler (*SFG3*) will be automatically phase matched at the 3rd-order.

Similarly, if we substitute $\Lambda_{SFG1} = \Lambda_{OPO} / 5$ and $\Lambda_{SHG2} = \Lambda_{OPO} / 3$ into (3.3.8), we obtain the same relationship as (3.3.9). This means that if *SFG1* is QPM at the 5th order and the *SHG2* is QPM at the 3rd order, the generation of *SFG3* will be again automatically supported by 3rd-order QPM.

From equation (3.3.2) and (3.3.3) we can derive:

$$\boxed{\frac{1}{\Lambda_{SHG2}} + \frac{1}{\Lambda_{SFG4}} = \frac{1}{\Lambda_{SFG1}} + \frac{1}{\Lambda_{SFG5}}} \quad (3.3.10)$$

$$\boxed{\frac{1}{\Lambda_{SFG1}} + \frac{1}{\Lambda_{SFG6}} = \frac{1}{\Lambda_{SHG1}} + \frac{1}{\Lambda_{SFG7}}} \quad (3.3.11)$$

where *SFG4* and *SFG5* stand for the two processes on the left and right sides of equation (3.3.2), respectively; and *SFG6* and *SFG7* correspond to the processes on both sides of equation (3.3.3). Here we do not discuss in detail the QPM orders of the processes of *SFG4* ~ *SFG7*.

In our initial simulation, all of the possible efficient interactions (the pump- or the signal-involved processes), including the processes expressed by equations (3.3.1)~(3.3.3), were taken into account. It was found that for a pump intensity lower than 20 GW/cm² the above mentioned degenerate processes have very little influence on the processes listed in Table 3.3.1. In this chapter, we intend to compare our simulation to our experimental work where a pump intensity of about 2.86 GW/cm²

was applied, therefore, we will not include these degenerate processes in our model in subsection 3.3.4.

3.3.3 Simulation model: The modified coupled equations

Based on the coupled equations for three-wave parametric interactions we incorporated the processes in Table 3.3.1 into one set of differential equations:

$$\left\{ \begin{array}{l} \frac{dE_S}{dz} = jq \left[K_{S,1} E_P E_I^* e^{j\Delta k_1 z} + K_{S,3} E_{SHG2} E_S^* e^{j\Delta k_3 z} + K_{S,4} E_{SFG1} E_P^* e^{j\Delta k_4 z} \right] \quad (3.3.12.a) \\ \frac{dE_P}{dz} = jq \left[K_{P,1} E_S E_I e^{-j\Delta k_1 z} + K_{P,2} E_{SHG1} E_P^* e^{j\Delta k_2 z} + K_{P,4} E_{SFG1} E_S^* e^{j\Delta k_4 z} \right. \\ \left. + K_{P,5} E_{SFG2} E_I^* e^{j\Delta k_5 z} \right] \quad (3.3.12.b) \\ \frac{dE_I}{dz} = jq \left[K_{I,1} E_P E_S^* e^{j\Delta k_1 z} + K_{I,5} E_{SFG2} E_P^* e^{j\Delta k_5 z} \right] \quad (3.3.12.c) \\ \frac{dE_{SHG1}}{dz} = jq \left[K_{SHG1,2} E_P^2 e^{-j\Delta k_2 z} \right] \quad (3.3.12.d) \\ \frac{dE_{SHG2}}{dz} = jq \left[K_{SHG2,3} E_S^2 e^{-j\Delta k_3 z} \right] \quad (3.3.12.e) \\ \frac{dE_{SFG1}}{dz} = jq \left[K_{SFG1,4} E_S E_P e^{-j\Delta k_4 z} \right] \quad (3.3.12.f) \\ \frac{dE_{SFG2}}{dz} = jq \left[K_{SFG2,5} E_P E_I e^{-j\Delta k_5 z} \right] \quad (3.3.12.g) \end{array} \right.$$

where

$$K_{S,1} = \frac{\omega_S d_{eff}}{n_S c} \frac{2}{\pi} \sin(\pi D)$$

$$K_{S,3} = \frac{\omega_S d_{eff}}{n_S c} \frac{2}{m_3 \pi} \sin(m_3 \pi D)$$

$$K_{S,4} = \frac{\omega_S d_{eff}}{n_S c} \frac{2}{m_4 \pi} \sin(m_4 \pi D)$$

$$K_{P,1} = \frac{\omega_P d_{eff}}{n_P c} \frac{2}{\pi} \sin(\pi D)$$

$$K_{P,2} = \frac{\omega_P d_{eff}}{n_P c} \frac{2}{m_2 \pi} \sin(m_2 \pi D)$$

$$K_{P,4} = \frac{\omega_P d_{eff}}{n_P c} \frac{2}{m_4 \pi} \sin(m_4 \pi D)$$

$$K_{P,5} = \frac{\omega_P d_{eff}}{n_P c} \frac{2}{m_5 \pi} \sin(m_5 \pi D)$$

$$K_{I,1} = \frac{\omega_I d_{eff}}{n_I c} \frac{2}{\pi} \sin(\pi D)$$

$$K_{I,5} = \frac{\omega_I d_{eff}}{n_I c} \frac{2}{m_5 \pi} \sin(m_5 \pi D)$$

$$K_{SHG1,2} = \frac{\omega_{SHG1} d_{eff}}{n_{SHG1} c} \frac{2}{m_2 \pi} \sin(m_2 \pi D)$$

$$K_{SHG2,3} = \frac{\omega_{SHG2} d_{eff}}{n_{SHG2} c} \frac{2}{m_3 \pi} \sin(m_3 \pi D)$$

$$K_{SFG1,4} = \frac{\omega_{SFG1} d_{eff}}{n_{SFG1} c} \frac{2}{m_4 \pi} \sin(m_4 \pi D)$$

$$K_{SFG2,5} = \frac{\omega_{SFG2} d_{eff}}{n_{SFG2} c} \frac{2}{m_5 \pi} \sin(m_5 \pi D)$$

and the phase mismatch amount for the five processes are expressed respectively as:

$$\Delta k_1 = 2\pi \left(\frac{n_P}{\lambda_P} - \frac{n_S}{\lambda_S} - \frac{n_I}{\lambda_I} \right)$$

$$\Delta k_2 = 2\pi \left(\frac{n_{SHG1}}{\lambda_{SHG1}} - \frac{2n_P}{\lambda_P} \right)$$

$$\Delta k_3 = 2\pi \left(\frac{n_{SHG2}}{\lambda_{SHG2}} - \frac{2n_S}{\lambda_S} \right)$$

$$\Delta k_4 = 2\pi \left(\frac{n_{SFG1}}{\lambda_{SFG1}} - \frac{n_P}{\lambda_P} - \frac{n_S}{\lambda_S} \right)$$

$$\Delta k_5 = 2\pi \left(\frac{n_{SFG2}}{\lambda_{SFG2}} - \frac{n_P}{\lambda_P} - \frac{n_I}{\lambda_I} \right).$$

$m_i = \frac{\Lambda \cdot \Delta k_i}{2\pi}$ are the orders of QPM for different processes with $i=2, 3, 4, 5$, and A

is the practical grating period of PPLN.

The periodic poling and the poling duty cycle are included by the parameter q that is defined as:

$$q = \begin{cases} +1, & 0 \leq V < D \\ -1, & D \leq V < \Lambda \end{cases}, \text{ with } V = (z - \text{int}(z/\Lambda) \cdot \Lambda) / \Lambda. D \text{ is the poling duty cycle.}$$

The function of $\text{int}(z/\Lambda)$ takes only the integer part of the value of z/Λ , where z is the position in the PPLN crystal in the propagation direction of the interacting waves.

The OPO process corresponds to the first terms in equations (3.3.12.a), (3.3.12.b), and (3.3.12.c); the SHG of the pump corresponds to the second term in equation (3.3.12.b) and in equation (3.3.12.d); the SHG of the signal corresponds to the second term in equation (3.3.12.a) and in equation (3.3.12.e); the SFG between the pump and

the signal is characterized by the third term in equation (3.3.12.a), the third term in equation (3.3.12.b), and in equation (3.3.12.f); the SFG between the pump and the idler is described by the fourth term in equation (3.3.12.b) and in equation (3.3.12.g).

In the model, we did not consider the group velocity mismatch (GVM) between interacting waves, which leads to shortening of the effective interaction length, reduction of the efficiency, and broadening the interacting pulses. In our model the spectrum of each wave was considered to be composed of a single line (or a single wavelength). Above approximations proved to be reasonable and effective to evaluate only the conversion efficiencies of the studied processes.

We used the measured output power (20 ~ 50 mW) of the signal as a reference to estimate the intracavity signal power (1 ~ 2.5 W for 2% output coupling) and employed the corresponding intensity and field amplitude as the initial signal input of the simulation. We also converted the practical pump power of 500 mW into the intensity and the amplitude of the field in the crystal with the reflection loss from the focusing lens and the curved mirror included. We made use of formulas $I = \frac{2P}{\pi w_0^2 R \tau}$

and $E = \sqrt{\frac{I}{2\epsilon_0 n c}}$ to relate the power, the intensity, and the amplitude of the electric

field, where P is the average power, I is the intensity, E is the amplitude, w_0 (30 μm) is the radius of the beam waist in the crystal, τ (40fs for the pump, 60 fs for the signal) is the pulse duration, R (80MHz) is the repetition rate, n is the refractive index, c (2.997×10^8 m/s) is the velocity of light in vacuum, and ϵ_0 (8.85×10^{-12} F/m) is the dielectric constant in vacuum.

In the simulation, it is assumed that the PPLN crystal is 0.5 mm long and heated to 100°C, and it has a grating period of 21 μm . A 2% output coupler was assumed and a 14% total cavity loss (including a 10% absorption by the PPLN crystal, a 2% output coupling, and a 2% reflection loss from other cavity mirrors) for the signal was estimated for the six-mirror ring cavity. The pump wavelength was tuned from 760 nm to 840 nm and the signal wavelength was scanned from 1000 nm to 1600 nm.

An important point in our simulation is that the output coupling and the steady state oscillation of the signal were considered. To sustain the steady oscillation of the signal, the single-path gain of the signal should be equal to a single round-trip loss, including the reflection losses from the mirrors and the absorption from the crystal

and the output coupling. The totally estimated 14% cavity loss of the signal was used as an important parameter to control reasonable signal intensity in the crystal. We used an iteration method to find the steady state signal intensity in the crystal versus the signal wavelength over the tuning range while the pump intensity was kept constant over the whole range of the pump wavelength.

3.3.4 Simulation results and discussion

A. Behavior of the higher-order QPM enhanced generation

Figure 3.3.2 shows the intensities of the generated visible light as a function of wavelength with the poling duty cycle changed from 50% to 66%. The degenerate point of the phase-matching curve of PPLN with a 21- μm grating period appears at 1.6 μm of the signal wavelength and 818 nm of the pump wavelength, limiting the tuning ranges of the SFG and SHG waves.

Figure 3.3.2(a) describes the behaviour of the SFG between the signal and the pump (*SFGI*). From 440 nm to 540 nm there appear 3 peak intensities at about 457 nm, 486 nm, and 530 nm, which are quasi-phase-matched at 5th, 4th, and 3rd order, respectively. Corresponding bandwidths are about 2.5 nm, 4 nm, 6.6 nm at FWHM, which can also be understood as the phase-matching bandwidths. It is quite clear that the odd-order QPM SFG processes are most efficient at 50% duty cycle and the efficiency decreases with increasing the duty cycle. The efficiency of the 3rd-order process is much higher than that of the 4th- and 5th-order processes. There is no generation at 486 nm for the 4th-order QPM at a 50% duty cycle. The efficiency of the 4th-order process increases with increasing the duty cycle and reaches its maximum at a little less than 62% duty cycle.

Figure 3.3.2 (b) demonstrates the variation of intensities of the \sim 1st-, 2nd-, and 3rd-order QPM SHG of the signal with wavelength at different poling duty cycles. The peak intensities of these three orders of QPM occur at the doubled signal wavelengths of \sim 750 nm, \sim 620 nm, and \sim 540 nm, respectively. The corresponding phase matching bandwidths are \sim 25 nm, \sim 15 nm, and \sim 10 nm, implying much larger tuning range of the SHG of the signal than that of the SFG between the signal and the pump. In fact, we could not achieve exact 1st order QPM SHG process of the signal near 750 nm for the assumed simulation conditions, instead, the QPM order is larger than 1 and smaller than 1.2. It is again understandable that the efficiencies of the \sim 1st and the

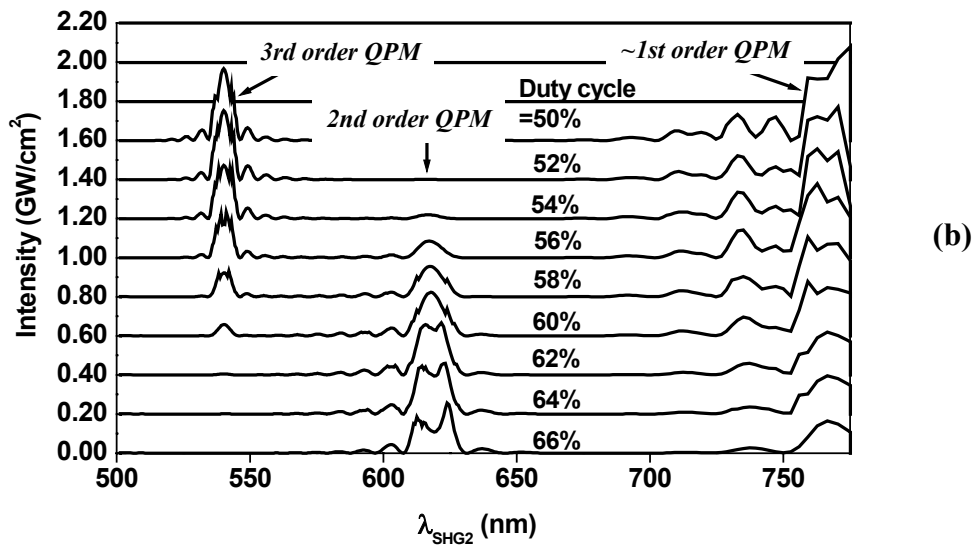
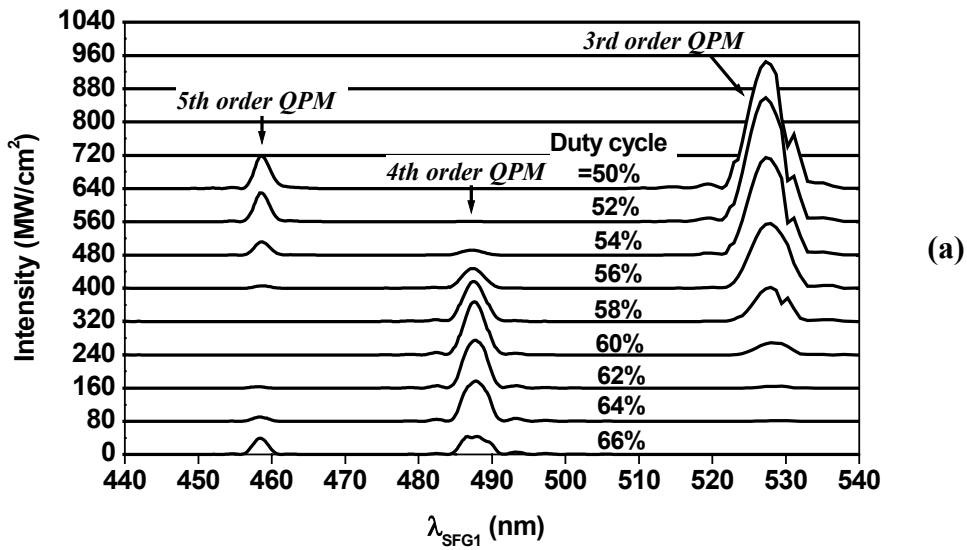
3rd-order processes are highest at 50% duty cycle and reduce with increasing the duty cycle. The 2nd-order process has a zero generation at 50% duty cycle and gain more conversion with increasing the duty cycle. The optimum poling duty cycle for the 2nd-order QPM SHG of the signal is about 64%.

If we do not consider the reduction in efficiency of the OPO process resulting from the non-50% duty cycle and the cavity loss (including the output coupling) of the signal (or the steady-state operation), the highest efficiency will be found at 75% duty cycle (see Fig. 3.2.16). SHG of the signal relies on an intensive generation of the signal, while increasing the poling duty cycle reduces the efficiency of the OPO process and results in low signal intensity. Steady-state oscillation of the signal requires a threshold signal intensity to ensure a single-path gain that is equal to the cavity loss. All of these factors determined an optimum duty cycle for the 2nd-order QPM SHG of the signal. It can be observed in Fig. 3.3.2 (b) that the intensity curves vary quite drastically near 750 nm. This is due to the degeneracy of the tuning characteristics of the PPLN OPO. Near the degeneracy point, the signal wavelength changes drastically even with a small change of the pump wavelength. In the simulation, this results in much fewer points in the calculated curves in the spectral range near the degeneracy point than in the spectral ranges far from the degeneracy point.

Figure 3.3.2 (c) shows the variation of the intensity of the SFG between the pump and the idler with wavelength at different duty cycles. Only one peak can be observed from 550 nm to 650 nm. The SFG process generating the peak intensity at about 585 nm is based on the 2nd-order QPM. The phase-matching bandwidth is about 10 nm. We did not find a optimum duty cycle for this process, since the intensity of this SFG wave increases with increasing the duty cycle. Due to the much lower intensity of the idler when compared with the pump and the signal, it is obvious that this SFG process is much less efficient than the above two.

Figure 3.3.2 (d) shows the intensity of the doubled pump as a function of wavelength at different duty cycles. For a 21- μm grating period of PPLN and a oscillation range from 1.0 to 1.4 μm , the pump wavelength needs to be tuned in a small range from about 780 nm to 810 nm. Therefore, the 9th-order QPM process at about 778 nm and the 7th-order QPM process at about 838 nm cannot be observed, and we demonstrate in Fig 3.3.2 (d) only the 8th-order process. In principle, the

highest efficiency of the 8th-order QPM SHG of the pump should be at a duty cycle of 56.25% (see Fig. 3.2.14(a)). As demonstrated in (d), the highest intensity of the doubled pump appears at ~56% duty cycle, which agrees well with our expectation. The corresponding phase-matching bandwidth is about 2 nm. Though the pump intensity is much higher than the idler, because of the higher QPM order, the highest intensity of the SHG of the pump is much lower than that of the SFG between the pump and the idler.



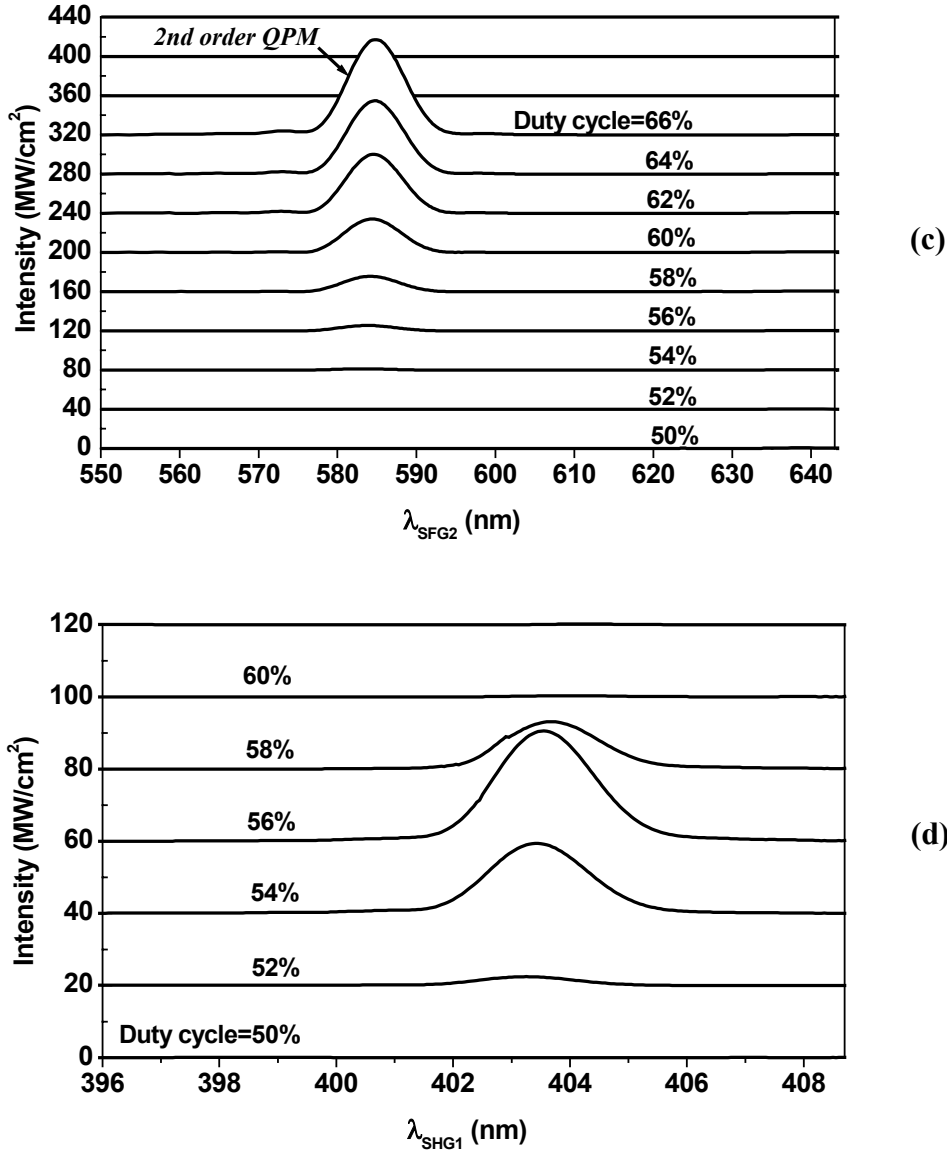


Fig. 3.3.2 Operation behaviour (intensity versus wavelength) of (a) the SFG between the signal and the pump (SFG1); (b) SHG of the signal (SHG2); (c) SFG between the pump and the idler; (d) SHG of the pump at different poling duty cycles.

B. Grating period tuning characteristics

Changing the grating period of PPLN tunes the signal wavelength and the depletion hole in the pump spectrum, resulting in a shift of the higher-order QPM ranges. Combining grating period tuning, pump wavelength tuning, and cavity length tuning methods, and using an appropriate duty cycle of PPLN, the oscillation of the OPO will be able to generate almost all wavelengths covering the visible and the near IR spectral range.

The simulation results of grating period tuning of higher-order QPM SHG of the signal and SFG between the signal and the pump are demonstrated now. Fig. 3.3.3 (a)

shows the shift of the 2nd-order QPM range for the SHG of the signal when tuning the grating period from 19 to 22 μm . The duty cycle was assumed to be 62%. The doubled signal wavelength is tunable from 590 nm to 640 nm. Fig. 3.3.3 (b) shows that the efficient generation range or QPM bandwidth of the 4th-order QPM SFG between the signal and the pump shifts from 470 nm to 500 nm when tuning the grating period of PPLN from 19 to 22 μm . A 62% duty cycle was also assumed for all the given grating periods of PPLN.

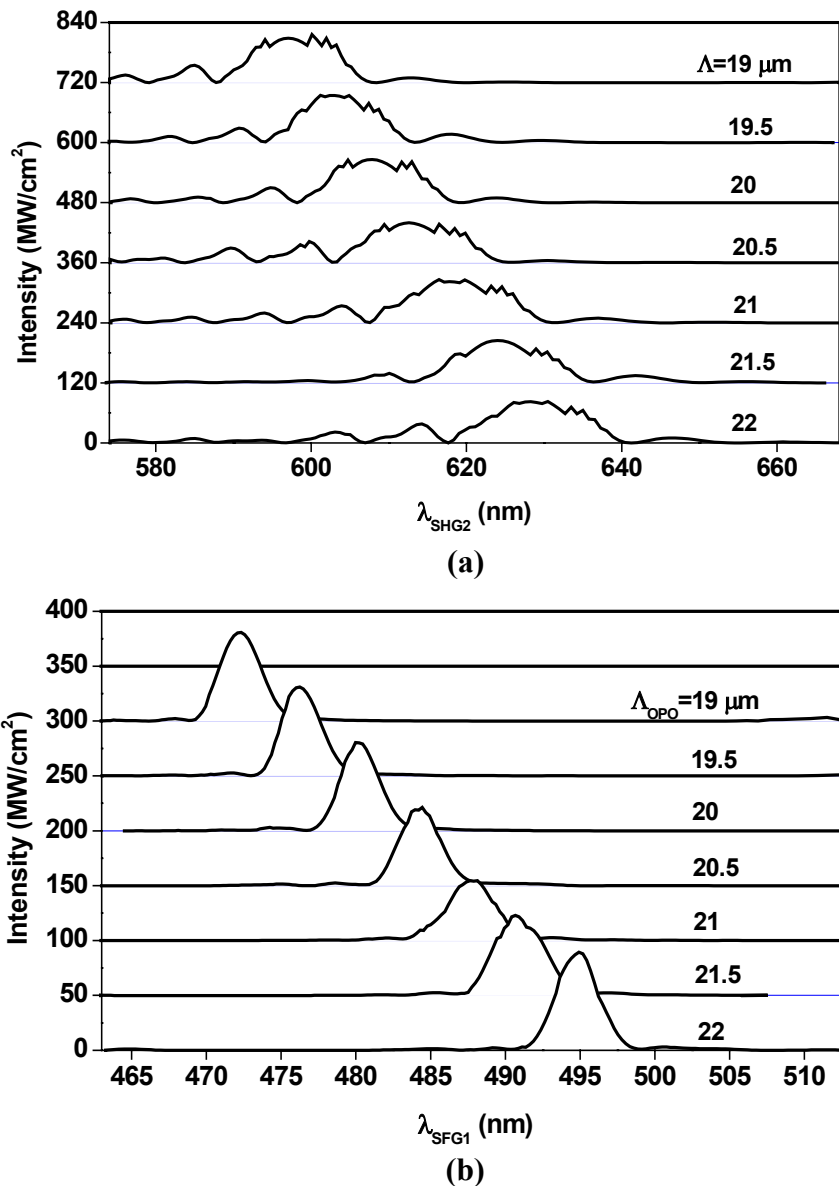


Fig. 3.3.3 Shifting of the efficient generation ranges (intensity vs. wavelength) of (a) the 2nd-order QPM SHG of the signal and (b) the 4th-order QPM SFG between the signal and the pump with tuning the grating period of PPLN (Λ_{OPO}) having a duty cycle of 62%.

C. Behavior of the signal

Figure 3.3.4 and Figure 3.3.5 describe the simulated behavior of the signal for a grating period of 21 μm of PPLN and a total cavity loss of 18% (4% output coupling rate) of the OPO.

In Fig. 3.3.4, the intracavity intensity of the signal is given as a function of the signal versus wavelength with the poling duty cycle varying from 50% to 66%. The cavity bandwidth of the OPO was not taken into account. At position A, the depletion from the 3rd-order QPM SHG of the signal and the 5th-order QPM SFG between the signal and the pump can be obviously observed for a 50% duty cycle. This depletion is reduced with increasing the duty cycle and the odd-order processes become less efficient. At position B, the 2nd-order QPM SHG of the signal and the 4th-order QPM SFG between the signal and the pump deplete the signal simultaneously and significantly. The depletion should not be neglected and it increases with increasing duty cycle. At position C, the most efficient operation of the signal should appear at about 1.45 μm for a duty cycle smaller than 60%. The average signal intensity is reduced to 50% when the duty cycle changes from 50% to 66%. At $\sim 1.24 \mu\text{m}$, the signal intensity can even be reduced to 20% if compared with the case of 50% duty cycle due to the efficient SHG of the signal and SFG between the pump and the signal.

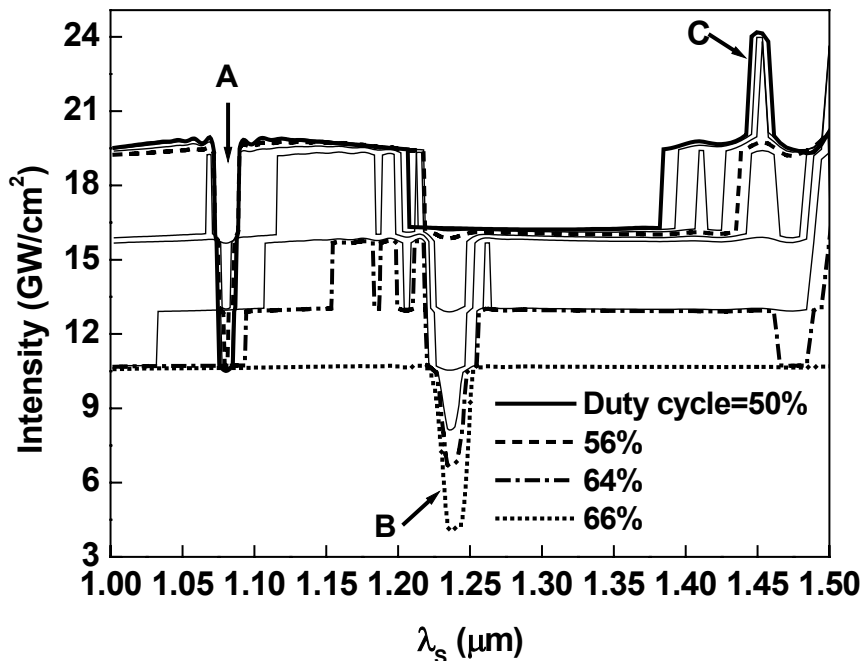


Fig. 3.3.4 Intensity of the signal vs. wavelength at different poling duty cycles of PPLN having a grating period of 21 μm .

The curves in Fig. 3.3.5 are functions of the intracavity signal intensity versus signal wavelength with the output coupling rate varying from 0% to 6% and the duty cycle fixed at 62%. An intrinsic cavity loss of 12% was assumed. An average reduction in the signal intensity of nearly 75% can be observed when the output-coupling rate is increased from 0% to 6%. The highest intensity of the signal appears at about 1.2 μm , which is about 50 GW/cm^2 in case of no output coupling, corresponding to an intracavity power of about 3.7 W. For a 2% output coupling, the intensity of the signal varies from 20~30 GW/cm^2 , corresponding to an intracavity power of 1.5~2.4 W and an output power of 30~50 mW, which is in the same order as the measurements (20~50 mW signal power for a 2% output coupler and ~56% poling duty cycle). The signal is largely depleted by the simultaneous SHG of the signal and SFG between the pump and the signal, which become considerably efficient at 62% duty cycle.

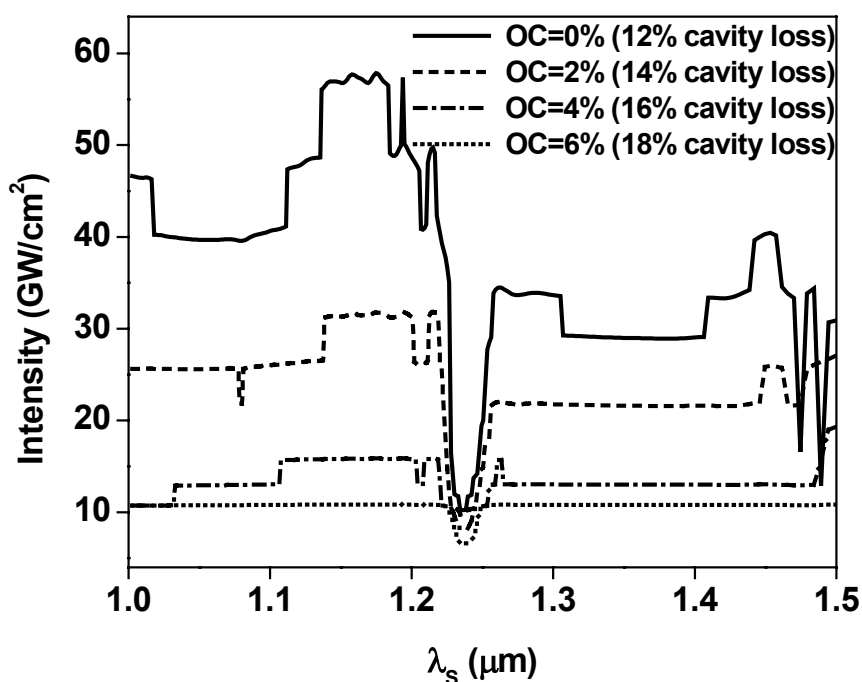


Fig. 3.3.5 Intensity of the signal vs. wavelength with the output coupling rate of the OPO varying from 0% to 6%. The PPLN has a grating period of 21 μm and a duty cycle of 62%.

D. Comparison between simulations and measurements

Figure 3.3.6 compares the simulation results with the measurement data for the SHG of the signal and the SFG between the signal and the pump. The same conditions (56% duty cycle, 21 μm grating period) were used for the simulation as those in the experiments.

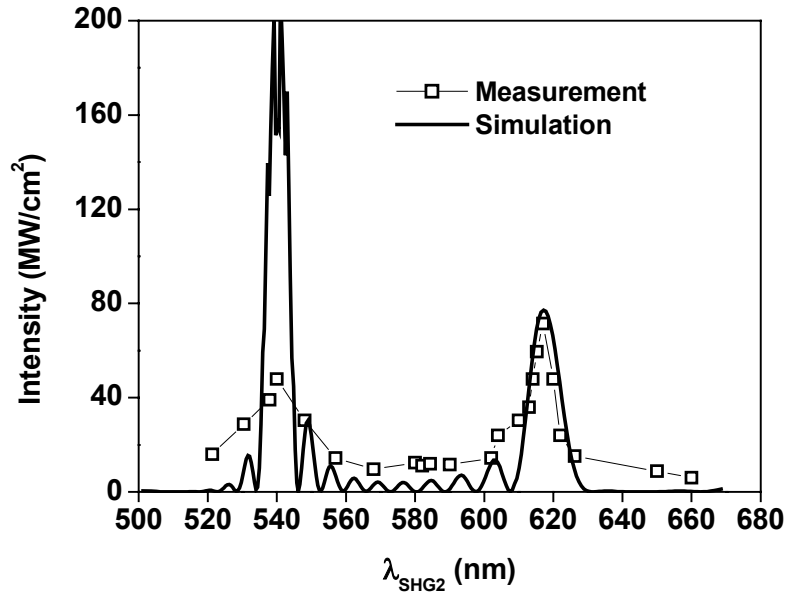
Figure 3.3.6 (a) gives both the measurement (opened squares) and simulation (solid line) data (intensity versus wavelength) for the SHG of the signal. Basically, the simulation agrees well with the measurement, especially in the range from 600 to 630 nm the simulation curve almost overlaps the measured data. At ~617 nm, a similar intensity was predicted by the simulation. Simulation also reveals that the 3rd-order process near 540 nm has much higher efficiency than the 2nd-order one centered around 617 nm, however, we measured a much lower power in the green than in the red. The reason is that the cavity bandwidth for high reflection ranges from 1100 nm to 1300 nm, and large cavity losses at 1080 nm led to lower efficiency for generating the signal and consequently lower intensity of the SHG wave.

For the comparison between the simulation (solid line) and measurement (opened squares) for the SFG between the signal and the pump, as illustrated in Fig. 3.3.6 (b), we can also conclude a perfect agreement for the range from 480 nm to 490 nm. The peak intensity at 486 nm given by the simulation, which is supported by an exact 4th-order QPM process, has almost the same value in MW/cm^2 as the measurement, implying perfect agreement between them. Another peak appearing at about 500 nm in the measurement data can be explained as the result of the deviations of the grating periods from the specified values and the poling duty cycle from our estimate. Additionally, we used a higher temperature to heat the PPLN in this measurement, giving rise to a larger poling period and resulting in an effect like grating period tuning. This also implies that temperature tuning and grating period tuning (Fig. 3.3.3 (b)) can largely extend the tuning ranges of the higher-order processes. Due to the cavity bandwidth we did not measure the relative efficient generation around 457 nm, though it is predicted by the simulation.

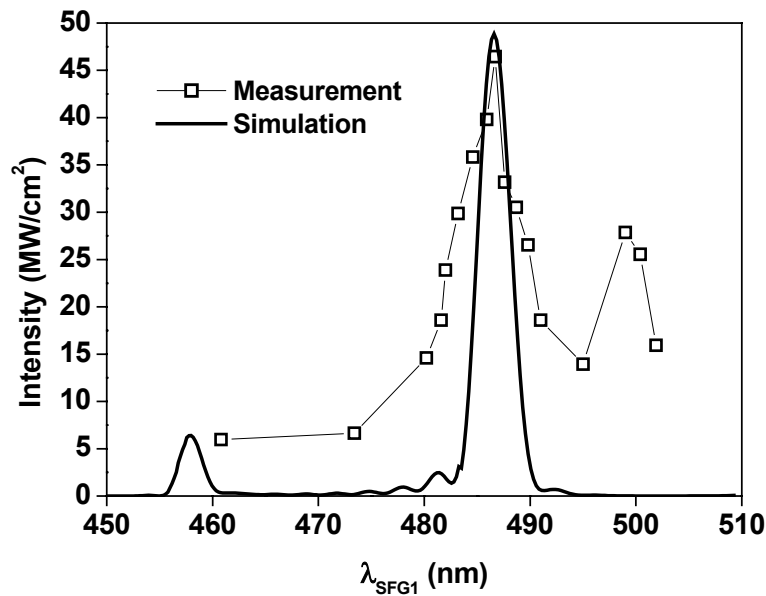
The agreement of the intensities at 486 nm and 617 nm between the simulation and the measurements also confirms the measured pulse duration at these wavelengths (see Fig. 3.2.21) when comparing the simulated values of the intensity and pulse duration of the signal.

When comparing the simulation results and the measurements, we can observe slight differences in the bandwidths for efficient generation (phase-matching bandwidth) of the two processes. There are at least three reasons for these differences: (1) Large GVM between the generated waves in the visible (SFG and SHG) and the pump and the signal waves results in a largely reduced effective interaction length for each interaction. In our simulation, we did not consider the GVM between interacting

waves and the full crystal length (0.5 mm) was used for all interactions, resulting in a largely reduced phase-matching bandwidth for each process. (2) The inhomogeneity in the poling duty cycle causes the deviation between simulation and measurement. (3) Jumping of the wavelength during measurement and unstable operation of the OPO at some spectral ranges led to error in the measured data.



(a)



(b)

Fig. 3.3.6 Comparison between simulation (solid line) and measurement (open squares) as a function of intensity versus wavelength for the processes of (a) SHG of the signal and (b) SFG between the signal and the pump.

3.3.5 Synchronous operation between “ $\omega_p + \omega_s$ ” and “ $2\omega_s$ ”

In Chapter 3.2, we mentioned the observation of the synchronous operation between the SHG of the signal (*SHG2*) and the SFG between the signal and the pump (*SFG1*) when tuning the OPO cavity length or changing the pump wavelength. A degenerate process of SFG between the idler and the doubled signal (*SFG3*), as described in subsection 3.3.2, was initially thought to synchronize these two processes of *SHG2* and *SFG1*. Though the process of *SFG3* is supported by a 3rd-order QPM, simulation showed that it has little influence (<1% the conversion efficiency) on *SFG1* and *SHG2* due to the low intensities of the idler and the doubled signal. Therefore, a second factor may play a more important role in the synchronicity between the operation of *SHG2* and *SFG1*.

Figure 3.3.7 illustrates the contour lines of the orders of QPM for *SHG2* and *SFG1* processes ($\Lambda_{\text{OPO}}/\Lambda_{\text{SHG}}$ and $\Lambda_{\text{OPO}}/\Lambda_{\text{SFG}}$) versus the signal and the pump wavelengths (λ_s and λ_p). Exact 1st-order quasi-phase matching was assumed for the OPO process. It is obvious that, when pumping in the range from 740 to 840 nm and when the signal oscillates between 1.0 and about 1.5 μm , the 2nd-order curve in (a) has almost the same distribution as the 4th-order curve in (b), and the 3rd-order curve in (a) has a similar distribution to the 5th-order curve in (b), though the curves in (b) have a slightly flatter shape than those in (a). When tuning the signal wavelength by changing the pump wavelength or by shifting the depletion hole in the pump spectrum through changing the OPO cavity length, the 2nd-order QPM SHG of the signal and the 4th-order QPM SFG between the signal and the pump become efficient almost simultaneously, or in other words, they make use of the same signal and pump wavelengths. The same conclusion can also be drawn for 3rd-order QPM SHG of the signal and 5th-order QPM SFG between the signal and the pump. For instance, a signal centered at 1234 nm is generated when using a pump wavelength of ~ 803 nm and a PPLN grating period of 21 μm , corresponding to an exact 2nd-order QPM SHG of the signal and an exact 4th-order QPM SFG between the signal and the pump. Therefore we observed simultaneously a peak power at ~ 617 nm for the SHG of the signal and a peak power at 486 nm for the SFG between the signal and the pump, as described in Section 3.2.4.

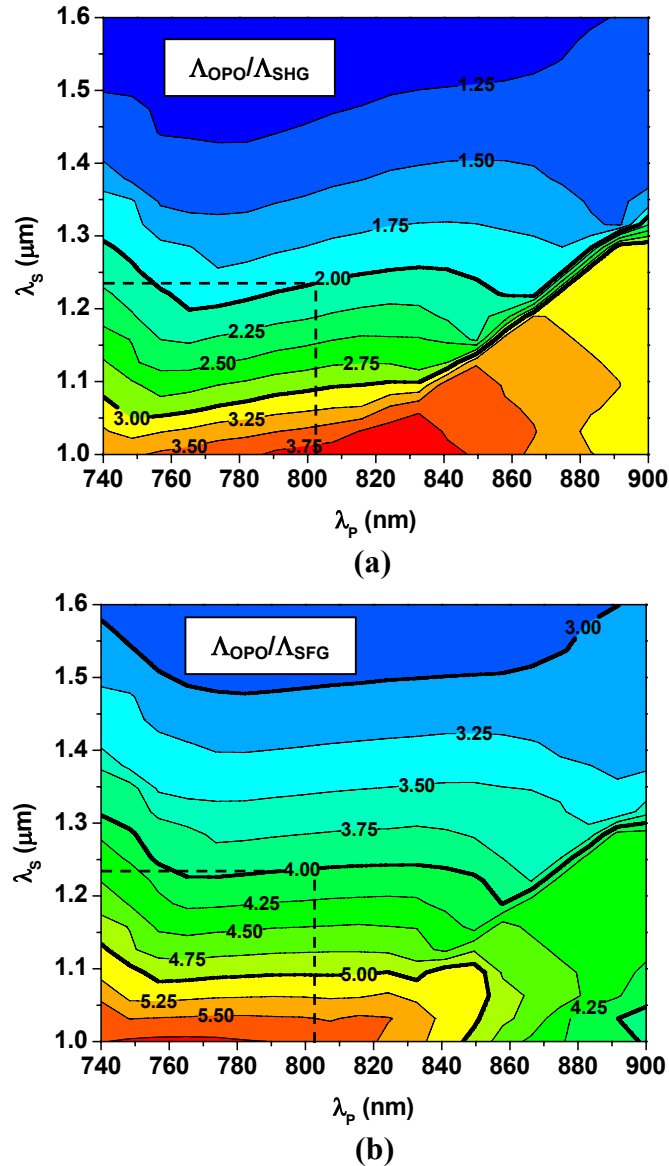


Fig. 3.3.7 Contour lines of the ratio between the practical grating period (Λ_{OPO}) and the required grating periods (Λ_{SHG} , Λ_{SFG}) by 1st order QPM (a) SHG of the signal and (b) SFG between the pump and the signal versus the pump and signal wavelengths. The two thicker curves in (a) correspond to the 2nd- and 3rd-order QPM SHG of the signal, respectively. The three thicker curves in (b) correspond to the 3rd-, 4th-, and 5th-order QPM SFG between the signal and the pump, respectively. The dashed lines show that the 4th order QPM SFG and the 2nd order QPM SHG make use of the same pump wavelength (~ 803 nm) and the same signal wavelength (~ 1234 nm).

3.4

Lower-order synchronous pumping of the PPLN OPO

3.4.1 Methods to achieve high-repetition-rate operation of a synchronously pumped OPO

There basically exist several methods to realize high repetition rate (>300 MHz) operation of a synchronously pumped OPO. Before defining these methods, we need to clarify some assumptions. Both the pump laser and the OPO are assumed to have a ring cavity or a linear (standing-wave) cavity, so that their cavity lengths or round-trip times of the pulses in the cavities can be compared directly. L_P designates the cavity length of the pump laser, and L_{OPO} designates that of the OPO. In exactly synchronous pumping, we have $L_P=L_{OPO}$.

A. $L_{OPO} = L_P/N$

First, it is possible to employ a low frequency laser pulse train to pump an OPO with an N times shorter cavity length, namely $L_{OPO} = L_P/N$, where N is an integer number. Then the OPO emits a pulse train with N times the pump repetition rate. Phillips et al. [11] have demonstrated up to 322 MHz operation of a femtosecond PPLN OPO using fourfold reduction in the OPO cavity length when pumping at 85.5 MHz repetition rate. B. Ruffing, et al. [16] achieved 1.334 GHz operation of a picosecond KTA OPO pumped by a mode-locked 83.4 MHz Nd: YVO₄ laser using a 16 times shorter cavity length for the OPO than the pump laser.

Disadvantages of this method include: (1) The large beam waist of the signal wave in the nonlinear crystal associated with the short OPO cavity length may result in a significant problem concerning mode matching between the pump and the signal. (2) The signal pulses experience more round-trip losses (correspondingly the pump threshold is increased and the tuning range is reduced), since gain is not provided for each pass through the crystal. (3) The signal pulses have periodically varying intensities, which may be a serious problem in nonlinear spectroscopy.

B. $L_{OPO} = L_P \cdot m/N$

Second, based on the first method, much longer OPO cavity lengths can be used, however, if L_{OPO} is equal to a rational fraction of the pump laser cavity length (L_P), that is $L_{OPO} = L_P \cdot m/N$, where m and N ($m < N$) are both integers and m/N is a simplest fraction. The repetition rate of the pump laser can thus be multiplied by N . Pumping with an 80 MHz Ti:sapphire laser, we have utilized OPO cavity lengths L_{OPO} of $1/2 \cdot L_P$, $2/3 \cdot L_P$, $3/4 \cdot L_P$, $3/5 \cdot L_P$, and $3/7 \cdot L_P$ and achieved OPO operation at about 160 MHz, 240 MHz, 320 MHz, 400 MHz, and 560 MHz, correspondingly.

Because of the much longer cavity length compared with method A, the mode-matching problem can be solved with this method. But the disadvantages of large round-trip losses and periodically varying signal-pulse intensities are still present using this method (see Fig. 3.4.1).

In methods A and B, L_{OPO} is smaller than L_P . Therefore we call these two methods lower-order synchronous pumping methods.

C. $L_{OPO} = N \cdot L_P$

By choosing $L_{OPO} = N \cdot L_P$ with $N = 2, 3, 4, \dots$, the OPO repetition rate remains as high as that of the pump without increasing the round-trip losses. Mode matching can be easily achieved owing to the flexibility in arranging the OPO cavity length. In this method, all of the signal pulses have equal intensities. (see Fig. 3.5.4).

This method is most suitable for pumping an OPO with a high-repetition-rate laser (> 500 MHz), where a very short cavity length (< 60 cm, ring cavity) of the OPO is required for exactly synchronous pumping.

D. $L_{OPO} = L_P \cdot N/m$

Based on method C, if we want to multiply the high repetition rate of the pump laser, we can employ the configuration of $L_{OPO} = L_P \cdot N/m$, where m and N ($m < N$) are both integers and m/N is a simplest fraction. Then the repetition rate of the pump pulses will be multiplied by m in the signal pulse train. But the signal pulses become unequal again in intensities.

In methods C and D, L_{OPO} is larger than L_P . We call these methods higher-order synchronous pumping methods.

Though the disadvantages of lower-order methods restrict their applications, they are easy ways to achieve high-repetition-rate operation of OPOs without changing to new pump sources.

In this Chapter, we discuss only the method B of lower-order synchronous pumping. Higher-order synchronous pumping based on method C will be discussed in Chapter 3.5.

3.4.2 Lower-order synchronous pumping

We explain the principles of method B of lower-order synchronous pumping by the configuration of $L_{OPO} = 3/7 \cdot L_P$, see Fig. 3.4.1. Suppose that the repetition rate of the pump pulses is $1/T$, where T is the repetition period of the pump pulses, the first pump pulse excites a signal pulse, which will travel 7 round trips before amplified by the 4th pump pulse. During these 7 round trips, the signal pulse experiences only cavity loss. Under low cavity loss and high gain of the signal pulse, a pulse train $S1$ of a repetition rate of $7/(3T)$ can be generated. Similarly, the second pump pulse will generate a second signal pulse train $S2$ also operating at $7/(3T)$ repetition rate. But $S2$ is delayed $T/7$ from $S1$. The pulses in $S2$ will also travel 7 round trips before amplified by the 5th pump pulse. A third signal pulse train will be generated by the third pump pulse, which is similarly delayed $T/7$ from $S2$. At the output, the 3 signal pulse trains will combine together, giving rise to a pulse train with a repetition rate 7 times that of the pump pulses ($7/T$). In summary, three signal pulse trains are amplified by the pump pulses numbered with $3n-2$, $3n-1$, and $3n$, respectively, where n is an integer ranging from 1 to infinite, with each operating at $7/3$ repetition rate of the pump pulses. Because the three signal pulse trains are delayed sequentially by $T/7$, combination of them gives rise to a signal pulse train operating at 7 times the repetition rate of the pump pulses. When pumping at 80 MHz, the signal pulses will operate at 560 MHz.

Based on similar principles, the following relations can be understood:

$$6/7 L_P = 5/7 L_P = 4/7 L_P = 3/7 L_P = 2/7 L_P = 1/7 L_P$$

$$5/6 L_P = 1/6 L_P$$

$$4/5 L_P = 3/5 L_P = 2/5 L_P = 1/5 L_P$$

$$3/4 L_P = 1/4 L_P$$

$$2/3 L_P = 1/3 L_P$$

where “=” means the cavity length on both sides gives rise to a similar signal pulse repetition rate and similar cavity loss.

In our experiments, a ring cavity PPLN OPO was pumped with 40 fs Ti:sapphire laser pulses tunable from 760 nm to 840 nm at a repetition rate of 80 MHz. The cavity length of the PPLN OPO was reduced to $3/7L_P$, $5/6L_P$, $3/5L_P$, $3/4L_P$, $2/3L_P$, $1/2L_P$, so that the repetition rate of the signal pulses was tuned from 80 MHz to 560 MHz with a step of 80 MHz.

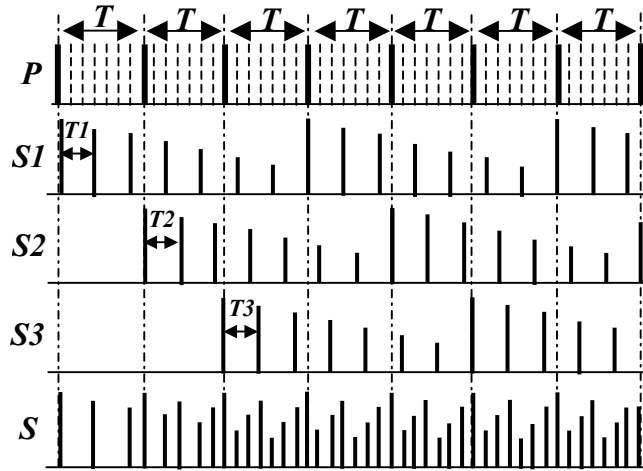


Fig. 3.4.1 Generation of 560 MHz signal pulses under 80 MHz pumping using $3/7$ cavity length for the PPLN OPO. T , repetition period of the pump pulses; $T_1=T_2=T_3=3T/7$; P , the pump pulse train; S_1 , S_2 , S_3 , the generated 3 signal pulse trains; S , the output signal pulse train.

3.4.3 Experimental setup

The cavity configuration of the PPLN OPO is shown in Fig. 3.4.2, which was designed initially for synchronous pumping at 80 MHz. The corresponding cavity length of the six-mirror ring cavity is about 374.8 cm. M1 is a chirped mirror ($R>99\%$) that is mounted on to a LPZT for cavity length tuning. M3 and M4 are high reflection mirrors ($R>99\%$). M2 is a 1~2% output coupler. The PPLN crystal (X) is 0.5 mm long. Multiple periodically poling gratings with the periods ranging from 20.5 μm to 21.5 μm are located parallel in the PPLN. In the experiments, we fixed the grating period at about 21 μm . Focal length of the focusing lens (FL, Achromat) is 60 mm. C1 and C2 are curved mirrors with $r=-100$ mm.

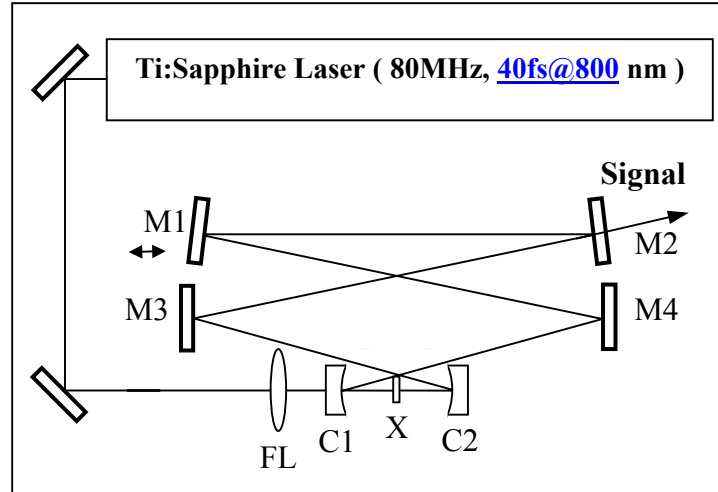


Fig. 3.4.2 *Experimental setup.*

3.4.4 Experimental results and discussions

Because our OPO cavity was initially designed for 80 MHz pumping, the sizes of the mirrors and mirror holders make it almost impossible to shorten the cavity length to <75 cm ($\sim L_P/5$). Fig. 3.4.3 shows the calculated diameter of the signal beam waist in the crystal versus cavity length. The curvature radius of the curved mirrors leads to a diameter of larger than 60 μm of the signal beam waist in the crystal when the cavity length is shorter than $L_P/3$, which cannot match the pump mode that is estimated to be smaller than 60 μm in diameter at the focus. Thus, we cannot make the OPO lase when L_{OPO} is smaller than $L_P/3$.

These factors make the method B of lower-order synchronous pumping more practical.

In the experiment, the PPLN crystal was heated to higher than 90°C to remove the photorefractive effects. The pump power was kept constant at about 500 mW for all measurements.

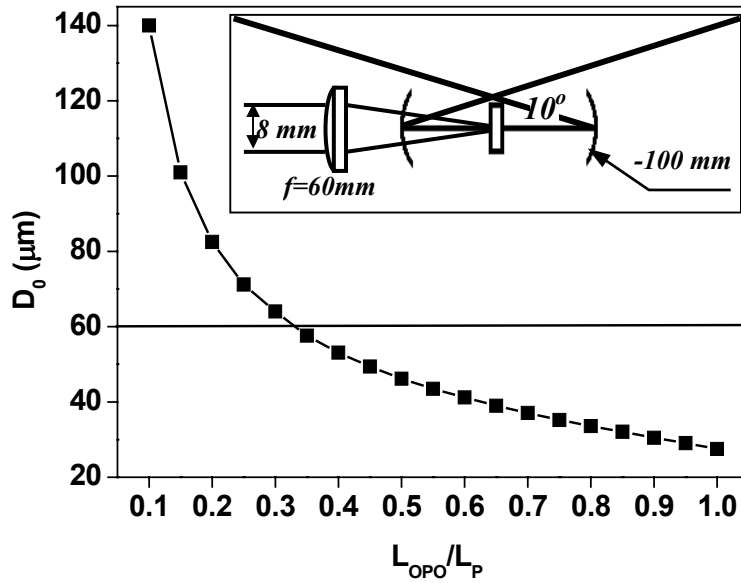


Fig. 3.4.3 Diameter of the signal beam waist (D_0) in the crystal versus cavity length.

To achieved 2 ~ 7 times multiplication of the pump repetition rate, we changed the positions of the chirped mirror (M1) and output coupler (M2) so that the cavity was shortened to $1/2 L_P$, $2/3 L_P$, $3/4 L_P$, $2/5 L_P$, $3/5 L_P$, $5/6 L_P$, $3/7 L_P$ and $5/7 L_P$. Consequently, up to 560 MHz repetition rate of the signal pulses was achieved. Higher repetition rate means more round trips and more cavity losses of signal pulses before amplified by the next pump pulse. As a result, the pump threshold is increased and the tuning range of the signal wavelength is reduced. It should be noted that, during the multiplication of the repetition rate of the signal pulses, each pump pulse was utilized. However, because of low signal intensity and consequently weak interaction, only a small part of the pump energy was converted to the signal, so that very small pump depletion was observed.

Figure 3.4.4 shows the pump threshold measurements versus repetition rate. It is understandable that the pump threshold increases with changing the order of synchronous pumping to get a higher repetition rate, since the signal pulse needs to experience more cavity loss. The lowest threshold pump power measured under the first order pumping is about 60 mW. Up to 74 mW signal power was measured at 500 mW pumping. A conversion efficiency of 15 % to the signal power was achieved. At 3/7 order synchronous pumping, only 5 mW signal power was measured and the OPO maintained oscillation within a very small range of cavity length mismatch. The threshold pump pulse energy does not change much when the repetition rate varies

from 80 MHz to 560 MHz, which ranges from 0.6 to 0.85 nJ. However, at 1/2 and 3/4 orders the lowest threshold pump pulse energies were measured, though in principle more cavity loss was introduced at 1/2 and 3/4 orders than at 1st order (exact synchronous pumping). According to Fig. 3.4.3, the optimum mode matching can be achieved around 1/2 order synchronous pumping. This may be one of the reasons. The largest threshold pump pulse energy was measured at 1/3 order synchronous pumping.

Figure 3.4.5 shows the highest output power of the OPO signal at different lower orders of synchronous pumping. There was an approximately exponential decay in the variation of the signal power with increasing the repetition rate at a constant pump power of about 500 mW.

Figure 3.4.6 shows the signal wavelength tuning range at different orders of synchronous pumping. It can be found that with increasing repetition rate by lower-order synchronous pumping, the oscillation range of the signal becomes narrower and shifts to longer wavelengths.

Figure 3.4.7 shows an autocorrelation measurement of the signal pulses and the corresponding spectrum at 160 MHz. The signal pulses were measured to be 56 fs long assuming sech^2 pulse shape, creating a time-bandwidth product of about 0.338.

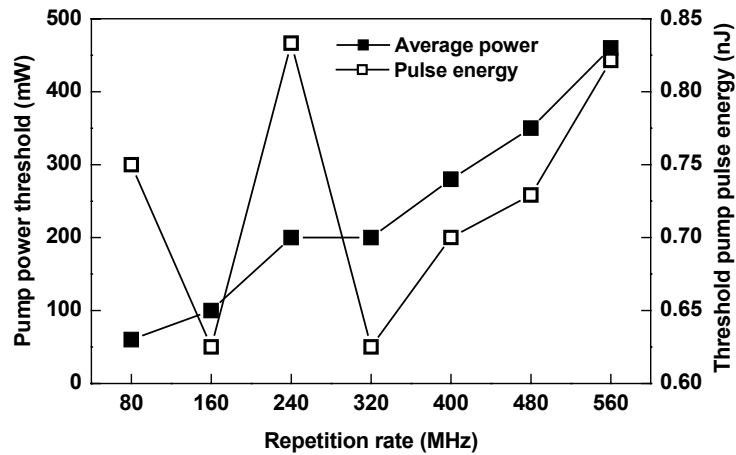


Fig. 3.4.4 Pump threshold of the PPLN OPO at different lower orders of synchronous pumping, i.e. at different repetition rates.

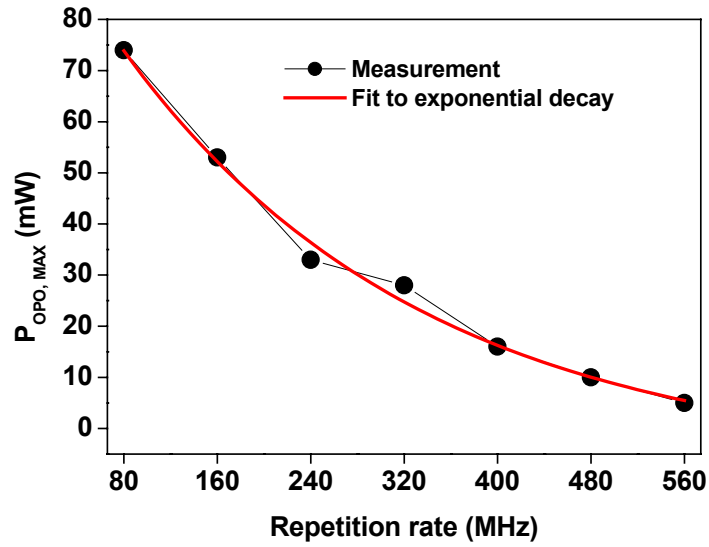


Fig. 3.4.5. Maximum output power ($P_{OPO, MAX}$) of the signal versus repetition rate at a pump power of about 500 mW.

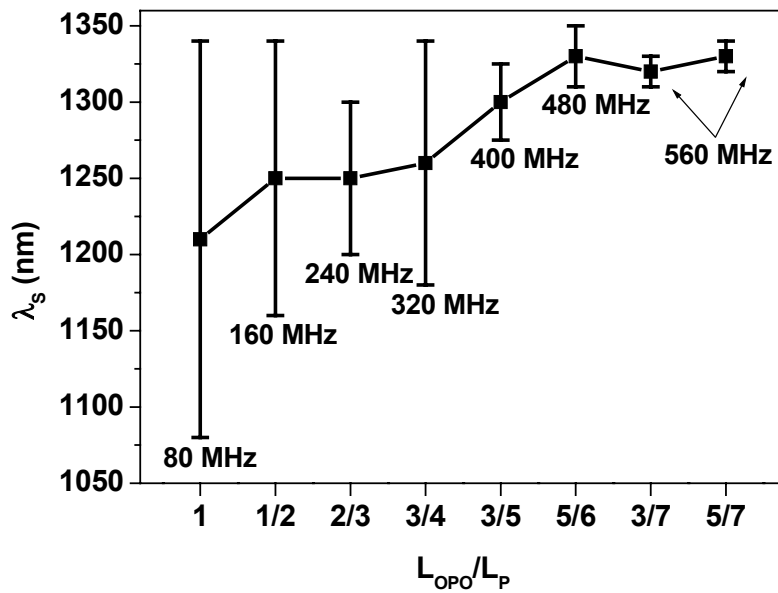


Fig. 3.4.6 Tuning range of the signal wavelength at different repetition rates. Note: the horizontal axis was not scaled in terms of the real cavity length. The scaling gives separately different configurations of lower-order synchronous pumping.

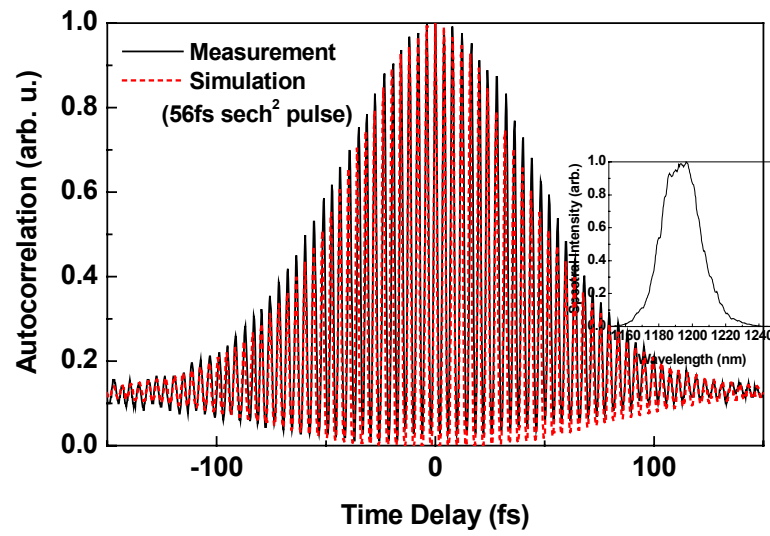


Fig. 3.4.7 Autocorrelation measurement of the signal pulses at 160 MHz repetition rate. Inset: corresponding spectrum.

3.5

Femtosecond 1 GHz PPLN OPO based on higher-order synchronous pumping

3.5.1 Introduction

High-repetition-rate femtosecond laser pulses tunable in the infrared and visible spectral range can be widely applied for time-resolved spectroscopy and pump-probe measurements with a high signal to noise ratio. Femtosecond OPOs operating at high repetition rate in the near infrared (1.3 μm and 1.55 μm) are potentially of great importance for optical communication systems to achieve high data rates and high capacity, where optical time-division multiplexing (OTDM) and wavelength-division multiplexing (WDM) need to be combined. [100] A high repetition rate OPO is distinguished by compact size and employing frequency multiplication it can serve as a high-repetition-frequency optical clock, e.g., for optical logic circuits. [101] Additionally, femtosecond OPOs provide frequency combs in the near infrared and in the visible, which is useful for applications with large frequency span, e.g., precise optical frequency measurements.[102-104]

Different methods to achieve high-repetition-rate operation of OPOs have been defined in Chapter 3.4. 2.5-GHz repetition rate has been reported for a PPLN OPO generating 7.8-ps pulses, using direct synchronous pumping [105]. A 1.334 GHz picosecond KTA OPO was reported using 1/16 order synchronous pumping. [16] Femtosecond OPOs reported so far [11] operated below 400 MHz, which was also based on lower-order (1/4 order) synchronous pumping.

In our case, we used a Kerr-lens mode-locked Ti:sapphire operating at 1 GHz [4] as the pump for the PPLN OPO. Our PPLN OPO was initially designed for pumping with low repetition rate (~ 80 MHz) laser pulses, which had a cavity length of about 374 cm. It was difficult for us to reduce this cavity length to the exact synchronous length (~ 30 cm) for 1 GHz operation due to the mode-matching problems and the sizes of the mirrors and the holders. Therefore, we employed higher-order synchronous pumping methods and achieved 1 GHz operation of the femtosecond PPLN OPO. [106]

3.5.2 Experimental setup

The experimental setup is shown in Fig. 3.5.1. A compact ring cavity femtosecond Ti:sapphire laser [4] pumped by a Millennia 10 W diode-pumped solid-state laser was used to pump the PPLN OPO. It uses chirped mirrors for dispersion control and produces (intracavity) 23 fs transform-limited pulses that were chirped to approximately 40 fs by the output coupler. The corresponding spectral bandwidth is 30 nm centered at about 800 nm. The repetition rate is tunable from 300 MHz to 3 GHz by simple rearrangement of the cavity mirrors. Typical average output powers for 1 GHz operation reaches 1.1 W for 2 % output coupling.

We also used a ring cavity for the PPLN OPO. The 0.5-mm-thick PPLN crystal contains ten sections of poling gratings with periods ranging from 20.5 μm to 21.5 μm is antireflection-coated on both sides at 1200 nm and 800 nm. The crystal is mounted on an X-Y translation stage to optimize the position of the crystal and to tune the grating period, and it was usually heated to 100 $^{\circ}\text{C}$ by an OMEGA CN8201-T1 Temperature Controller to avoid photo-refractive damage. C1 and C2 are curved mirrors with a curvature radius of $r=-100$ mm. M1 and M2 are flat mirrors.

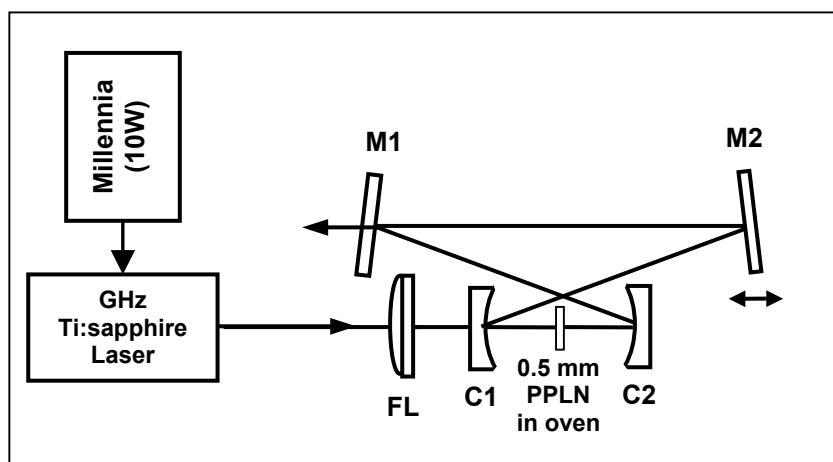


Fig. 3.5.1 Experimental setup. FL, focusing lens, $f=60$ mm; C1, C2, curved mirrors, $r=-100$ mm; M1, M2, flat mirrors;

3.5.3 Mode matching and higher-order synchronous pumping

The cavity length of a synchronously pumped OPO (L_{OPO}) should be the same as that of the pump laser (L_P). For high repetition rate (>300 MHz) operation, a quite short cavity is required, e.g., cavity length as short as 30 cm is required for 1 GHz operation. Some problems caused by very short cavity length have been briefly discussed in Chapter 3.4. Here we give more detailed and quantitative descriptions of these problems.

Shorter cavity length implies a larger beam waist in the nonlinear crystal. Fig. 3.5.2 shows the calculated contour lines of the diameter (D_0) of the signal beam waist versus ring cavity length (L_{OPO}) and curvature radius (r) of the curved mirrors. It can be found that D_0 increases quickly with reducing L_{OPO} at a given value of r (see for example the dashed horizontal line), and decreases with reducing r at a given L_{OPO} (see the dashed vertical line). In our calculations, we determined the optimum distance between the two curved mirrors (L_{CC}) providing a good signal mode. Fig. 3.5.3 illustrates our criteria to optimize L_{CC} . It is important to notice that the beam waists in the sagittal (D_{0X}) and tangential planes (D_{0Y}) are slightly different due to astigmatism. Therefore, the stability curves in Fig. 3.5.3 for the sagittal (dash-dotted line) and the tangential (solid line) planes are shifted with respect to each other when plotted in dependence on L_{CC} . Stable OPO operation is confined to the common range of the two stability curves which decreases with increasing incidence angle of the signal beam on the curved mirrors (θ), as also discussed in Chapter 3.4. In order to obtain most stable operation of the OPO, we optimized L_{CC} to the value corresponding to the intersection between the two stability curves, e.g., $L_{CC} = 105$ mm for $L_{OPO} = 1200$ mm, $r = -100$ mm, and $\theta = 5^\circ$, where $D_0 = D_{0X} = D_{0Y} \approx 60\mu\text{m}$. In principle, a shorter L_{CC} would decrease the beam diameter in the crystal. However, this results, besides the astigmatic beam distortion, in an increased spot diameter on C1 and C2 and therefore enhanced diffraction losses. This is shown by the dashed and dotted curves in Fig. 3.5.3. On the other hand, the astigmatism and the stable operation conditions set an upper limit to θ . The sizes of the mirrors and mirror holders may largely increase this angle when reducing r . In consequence, the value of r can hardly be smaller than 75 mm. According to Fig. 3.5.2, $r = -75$ mm and $L_{OPO} = 30$ cm correspond to a D_0 as large as 120 μm . For perfect mode matching, a similarly large

pump focus diameter in the crystal would be required. Then, the intensity of both the pump and the signal would be largely reduced in the interaction area. Therefore the efficiency of the OPO is reduced and the pump threshold is largely increased. At high pump repetition rate, where a much smaller pulse energy is provided, the decrease in the efficiency and increase in the pump threshold become especially critical.

Higher-order synchronous pumping (method C in Chapter 3.4) can solve above problems easily. By choosing $L_{OPO}=N \cdot L_P$ with $N=2, 3, 4, \dots$, the OPO repetition rate remains as high as that of the pump without increasing the round-trip losses. Fig. 3.5.4 demonstrates the operation of 4th-order ($L_{OPO}=4L_P$) synchronous pumping. Assuming that the pump pulses operate at 1 GHz, four signal pulse trains (S1-S4), each operating at 250 MHz will be excited, which are delayed sequentially by one repetition period of the pump laser ($T=1$ ns) from each other. The pump pulse train synchronizes the four signal pulse trains to each other, so that the sequence of S1-S4 creates a 1 GHz signal pulse train at the output.

Because of the much longer OPO cavity, higher-order synchronous pumping enables high intensity interaction between the pump and the signal by reducing the signal beam waist, and mode matching can easily be improved through optimizing the focal length of the focusing lens (f) and the values of r and L_{CC} . Obviously, all signal pulses have equal intensities in higher-order synchronous pumping, which is very important for applications such as nonlinear spectroscopy. Using higher-order synchronous pumping, the same OPO device is suitable for both low and high repetition rate operations, which makes it more flexible in applications.

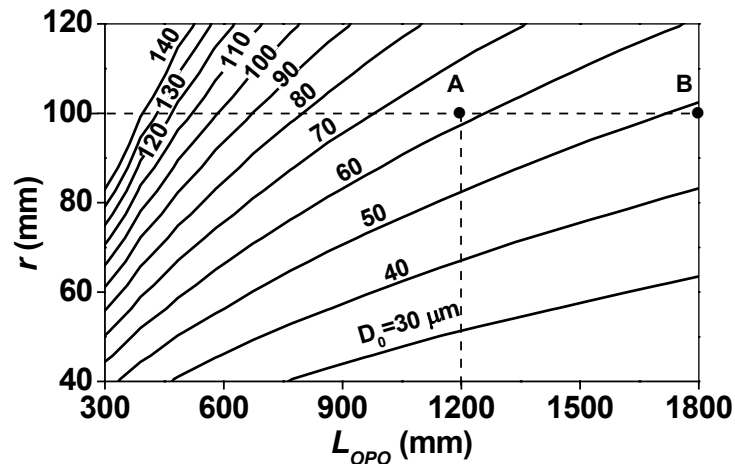


Fig. 3.5.2 Contour lines of the diameter of the signal beam waist (D_0) in PPLN crystal versus cavity length (L_{OPO}) of the OPO and the curvature radius (r) of the curved mirrors.

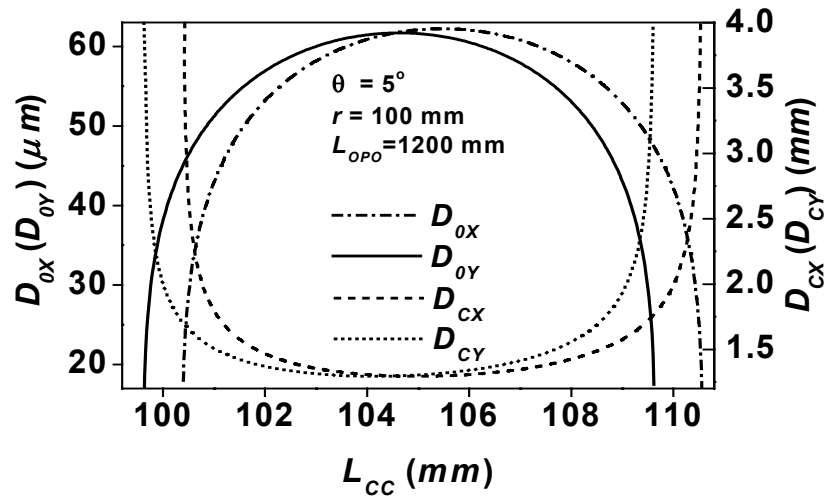


Fig. 3.5.3 Variation of the beam waist inside the PPLN crystal in the sagittal (D_{0X}) and tangential (D_{0Y}) planes as a function of L_{CC} . The dashed and dotted lines show the beam diameters in the sagittal (D_{CX}) and tangential (D_{CY}) planes on C1 and C2 as a function of L_{CC} .

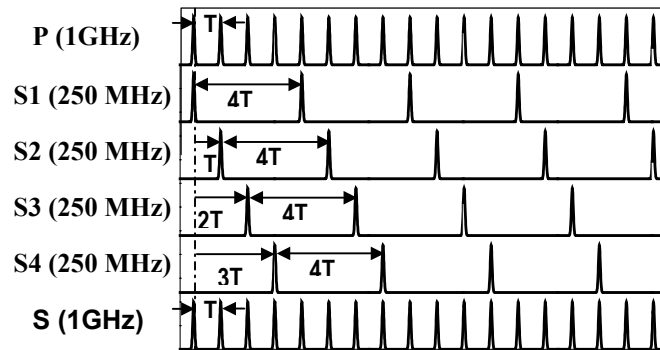


Fig. 3.5.4 The 4th order synchronous pumping, generating 1GHz signal pulses. P, pump pulse train; S1 - S4, four generated signal pulse trains; S, output signal pulse train; T, period of the pump pulses.

3.5.4 1-GHz-repetition-rate operation of the PPLN OPO

We define Rr as the repetition rate and SP as the order of synchronous pumping.

For 1 GHz operation ($Rr=1\text{GHz}$) of the OPO, we employed 4th order ($SP=4$) synchronous pumping with $L_P=30.2$ cm and $L_{OPO}=120.8$ cm.

To confirm our theory about the higher-order synchronous pumping, we first measured the repetition rate of the OPO using a fast *Si* photodiode connected to a spectrum analyzer. However, the *Si* photodiode is not sensitive to the signal wavelength above 1160 nm, so we had to make use of the visible light generated through SHG (red light) of the signal and SFG (blue light) between the signal and the pump. To filter out the residual pump and the signal, we placed two SCHOTT glass filters BG 39 and RG 1000 before the photodiode. Fig. 3.5.5 presents the measurement results of the repetition rate of the signal pulses. The exact repetition rate is 991.0135 MHz, which is exactly the same as that of the pump laser. We also scanned the measurement range of the spectrum analyzer from 100 MHz to 1.5 GHz to make sure that our measurement was not the harmonic of low frequencies. We observed no other peaks in the measured spectrum.

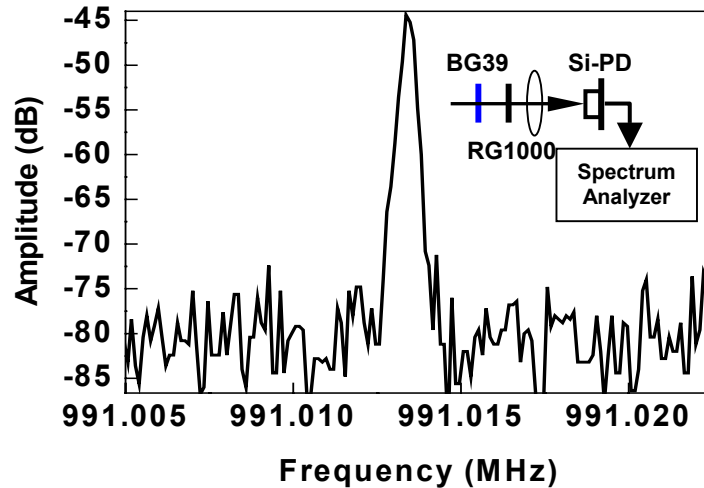


Fig. 3.5.5 Repetition rate measurement of the PPLN OPO pumped by a Ti:sapphire laser operating at $\sim 1\text{GHz}$ repetition rate. Inset: setup for the measurement.

Because the Ti:sapphire laser operates at a fixed center wavelength, the signal wavelength of the OPO cannot be tuned by changing the pump wavelength. Due to photorefractive effects and the upper limit of the heater, the temperature of the crystal can only be changed from about 95 °C to 125 °C, thus the tuning range of the signal wavelength by changing the temperature is very limited. Therefore, we used cavity length tuning in combination with tuning the grating period (20.5~21.5 μm) of PPLN as the main method to tune this 1 GHz OPO. Fig. 3.5.6 demonstrates the tuning characteristics of the 1 GHz PPLN OPO. The center wavelength of signal wave is tunable from 1170 nm to 1235 nm. Smooth signal spectra were mostly observed with nearly Gaussian distribution. Fig. 3.5.7 shows the signal output power versus the cavity length detuning. The OPO maintained oscillation within a cavity length mismatch range of about 1.25 μm . Generally speaking, the signal power varied smoothly and continuously with changing the cavity length. The highest output power was 18 mW and the pump power threshold was measured to be 790 mW.

Because of high pump threshold at high repetition rate operation, very small pump depletion was observed, as shown by the comparison between the depleted and undepleted pump spectrum in Fig. 3.5.8.

Another reason for the small pump depletion is that the pump wavelength cannot be tuned to optimize the phase matching conditions. Increasing the temperature and tuning the grating period of PPLN proved to be very effective to improve the efficiency of the OPO, so that the pump will be more deeply depleted.

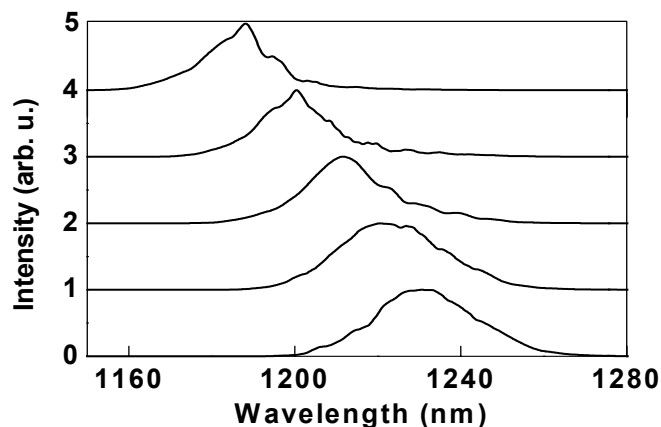


Fig. 3.5.6 *Tuning of the signal spectra by changing the cavity length of the PPLN OPO at 1 GHz operation.*

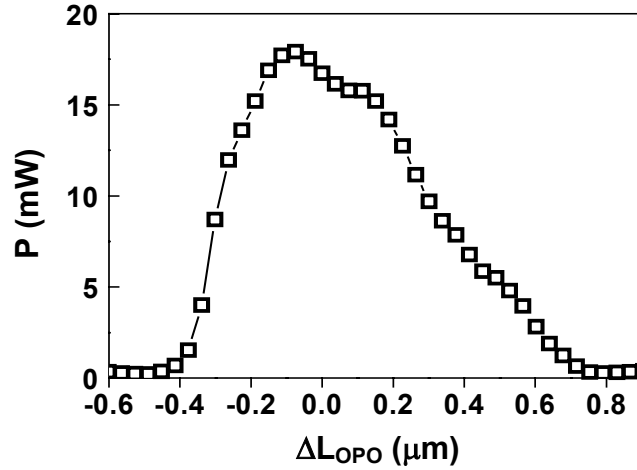


Fig. 3.5.7 Signal output power (P) versus cavity length detuning (ΔL_{OPO}).

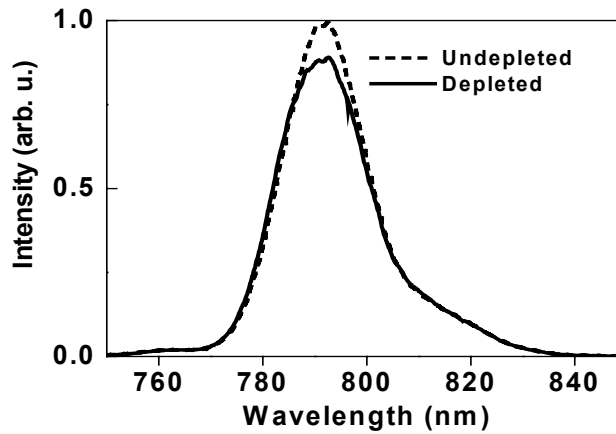


Fig. 3.5.8 Depletion of the pump spectra at 1 GHz repetition rate operation.

Because of low output power, it was difficult to measure the interferometric autocorrelation of the signal pulses. We used an NT & C autocorrelator to measure the intensity autocorrelation. The autocorrelation measurements showed that the signal pulse duration ranges from 60 to 65 fs. Without intracavity compensation for the GVD, the signal pulses were measured to be nearly transform-limited. Fig. 3.5.9 shows the autocorrelation trace and corresponding spectrum (in the inset) of the signal pulses at 1 GHz operation. The signal pulses are almost exactly Gaussian-shaped according to the fit by the Gaussian function to the measurement data. At FWHM, the pulse duration is about 60 fs and the bandwidth is about 36 nm, resulting in a time-bandwidth product of 0.456.

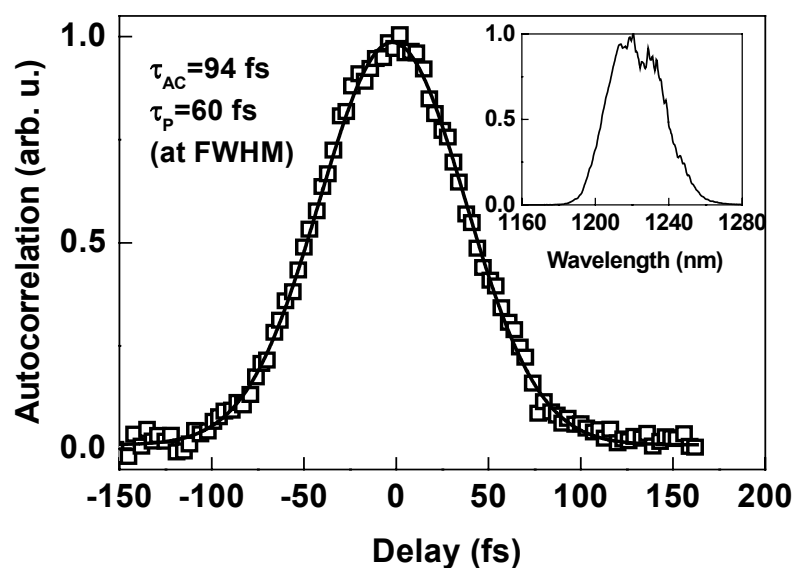


Fig. 3.5.9 Intensity autocorrelation measurement (opened squares) of the signal pulses, pulse duration is denoted by τ_p . The solid line is the Gaussian fit to the measurement data. Inset: corresponding spectrum.

3.5.5 Intracavity GDD compensation by a chirped mirror

We tried to shorten the signal pulses by replacing M2 by a chirped mirror (CM). The reflection and GDD characteristics of the chirped mirror are shown in Fig. 3.5.10.

Because of higher reflection of the chirped mirror than of the normal high reflector, the pump threshold was reduced to about 690 mW. The highest output power at 1 GHz repetition rate was 20 mW when pumping with 910 mW. The tuning range was shifted to longer wavelengths from 1200 nm to 1266 nm. Even with a single chirped mirror, the GDD of the 0.5 mm PPLN crystal was already overcompensated, meaning net negative intracavity GDD, as shown in Fig. 3.5.10. Net negative GDD in the OPO oscillation range resulted in negative cavity length detuning effect, meaning that a shorter signal wavelength oscillated at a longer cavity length. The permitted cavity length mismatched range with the OPO maintaining oscillation was about 1.0 μm , which agreed well with the calculation result demonstrated in Fig. 3.5.11. However, we did not observe apparently shortened signal pulses and broadened signal spectrum.

Since our PPLN has a poling duty cycle of $\sim 56\%$ which enhanced the SFG between the signal and the pump and doubling of the signal frequency [94], we observed very efficient generation of visible light that was coupled out through the curved mirror C2. The highest output power of the visible light was measured when the signal wavelength was tuned to about 1240 nm and the pump wavelength was fixed at about

800 nm, so that we measured 15 mW at about 620 nm and more than 10 mW at about 486 nm.

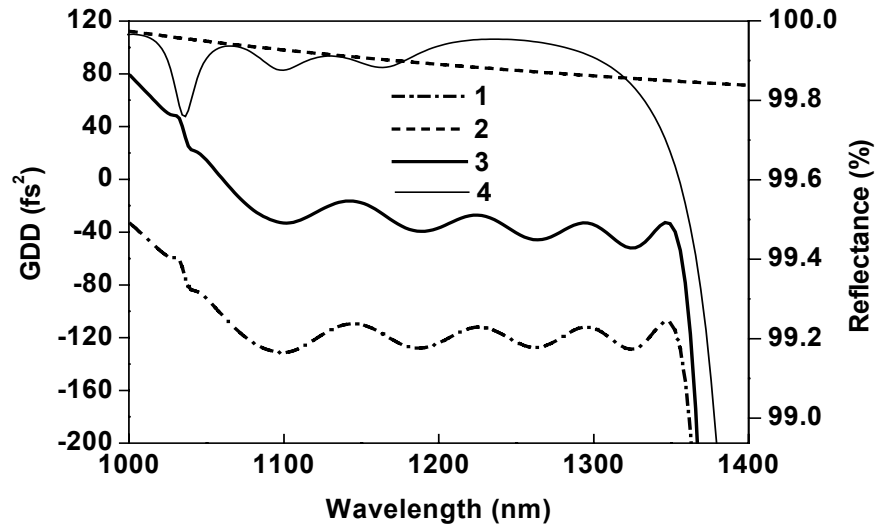


Fig. 3.5.10 1. Group delay dispersion (GDD) characteristics of a single chirped mirror.
 2. GDD of 0.5 mm PPLN.
 3. Intracavity GDD after compensation.
 4. Reflectivity of the chirped mirror.

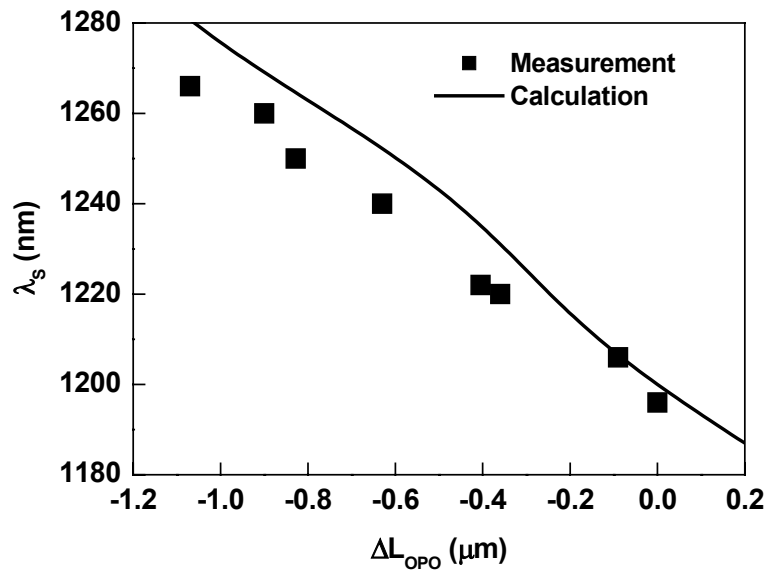


Fig. 3.5.11 Calculated cavity length detuning characteristics of the PPLN OPO and comparison with measurement data.

3.5.6 Optimization of the output coupling rate

Above discussions imply low conversion efficiency ($\sim 2\%$) of the 1 GHz operation of the PPLN OPO. To improve this situation and to find out the optimal output coupling rate, we employed the following cavity configuration for the OPO: replacing the focusing lens with a 50-mm-focal-length achromat, inserting a 2-mm quartz plate (QP) near the middle of the OPO ring cavity for output coupling, and applying 4th order synchronous pumping ($SP=4$) at a lower pump repetition rate (~ 666 MHz). Using tighter focusing of the pump beam, we were able to increase the pump intensity at the focus in the PPLN crystal. Owing to the longer cavity ($L_P \approx 43.7$ cm, $L_{OPO} \approx 175$ cm) and smaller pump focus in the PPLN crystal, mode matching between the signal and the pump beams was largely improved with increased interaction intensities. The QP was initially inserted near the Brewster angle. Then we rotated the incidence angle of the signal beam on QP slowly (from about 50° to 17°), so that we could change the output coupling rate continuously and find out the optimal value.

Figure 3.5.12 shows the calculated reflectivity of the quartz plate at different incidence angles and the corresponding measurement of the output signal power of the PPLN OPO. In the calculation, the wavelength of incidence beam was fixed at about 1280 nm. The tuning range of the OPO signal shifted to 1238 nm \sim 1325 nm. At 666 MHz repetition rate, the highest output power is about 66 mW with a pump power of 950 mW, corresponding to a conversion efficiency of about 7%. The pump threshold was lowered to about 510 mW. Therefore we can conclude that the optimal output coupling for the PPLN OPO is about 2%, as illustrated by the dashed lines in Fig. 3.5.12.

Then we increased the pump repetition rate to 1 GHz while keeping the long OPO cavity (~ 180 cm). The OPO was pumped at 6th-order synchronous pumping.

Pumping with 950 mW, we measured more than 43 mW OPO signal power. Thus, the power conversion efficiency was increased to 4.5% and the pump threshold was measured to be lower than 580 mW.

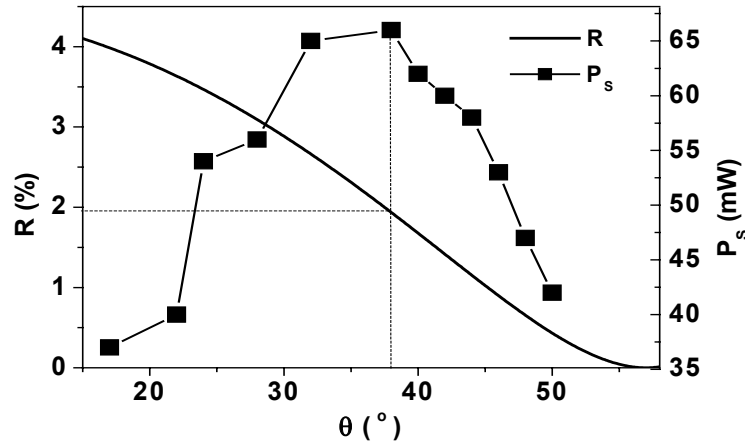


Fig. 3.5.12 Calculated reflectivity (R , solid curve) of a 2-mm quartz plate versus the incidence angle (θ) and the correspondingly measured signal power (P_s , solid square) of the PPLN OPO.

3.5.7 Summary

We have demonstrated 1 GHz operation of a femtosecond PPLN OPO. Higher-order synchronous pumping has been used to increase the interaction efficiency between the signal and pump beams. Transform-limited 65 fs signal pulses tunable from 1160 nm to 1325 nm (using different mirror sets) were obtained with a conversion efficiency of about 4.5% when pumping with 950 mW at 800 nm. The OPO has a pump threshold as low as 580 mW at 1 GHz. In our present setup we utilized standard components designed for an 80 MHz OPO. Substantial improvement of the conversion efficiency seems feasible, e.g., by use of a smaller radius for the curved mirrors, more compact mirror holders, and reducing the disturbing photo-refractive effects by higher heating or Mg-doping of the LiNbO_3 . The low threshold of the present setup enables the use of additional folding mirrors, leading to a very compact OPO which can be easily integrated with the pump laser into one device. Inserting appropriate mirror sets into the OPO cavity, generation of 1.55 μm signal pulses at 1 GHz should also be possible.

Table 3.5.1 summarizes the operation characteristics of the PPLN OPO at different cavity configurations as we discussed above. Fig. 3.5.13 gives a summary of the pump threshold of the PPLN OPO versus repetition rate.

Table 3.5.1 Operation characteristics of the PPLN at different cavity configurations

Cavity configuration						Operation characteristics		
f (mm)	M1	M2	C1&C2 (r)	SP (Rr)	T (°C)	Tuning range	Pump Threshold	Output ^a (Pump)
60	1% OC	HR 99.8%	UCM (100mm)	2 (500MHz)	100	1160nm~ 1235nm	500 mW	28 mW (900mW)
60	1% OC	HR 99.8%	UCM (100mm)	4 (1 GHz)	100	1180nm~ 1240nm	790 mW	18 mW (900mW)
60	1% OC	CM	UCM (100mm)	4 (1 GHz)	100	1200nm~ 1266nm	700 mW	18 mW (910mW)
60	CM 99.8%	CM 99.8%	CM 99.8%	4 (1 GHz)	100	1240nm~ 1325nm	600 mW	8 mW ^b (640 mW)
50	2% OC	CM 99.8%	UCM (100mm)	4 (666MHz)	100	1250nm~ 1320nm	<600 mW	68 mW (~1 W)
50	2% OC	CM 99.8%	UCM (100mm)	5 (825MHz)	100	1240nm~ 1320nm	620 mW	40 mW (860 mW)
50	2% OC	CM 99.8%	UCM (100mm)	5 (825MHz)	125	1240nm~ 1325nm	600 mW	60 mW (860 mW)
50	2% OC	CM 99.8%	UCM (100mm)	6 (1 GHz)	125	1250nm~ 1320nm	580 mW	43 mW (950 mW)

^a The output of the OPO refers to as the highest average power. The pump means the average pump power measured before the focusing lens FL (see Fig. 3.5.1).

^b The output power measured behind each flat mirror was 2 mW.

f : focal length of the focusing lens FL (Fig. 3.5.1)

OC: output coupler

CM: chirped mirror

UCM: unchirped mirror

HR: unchirped high reflector

SP : order of synchronous pumping

Rr : repetition rate

T: temperature of PPLN

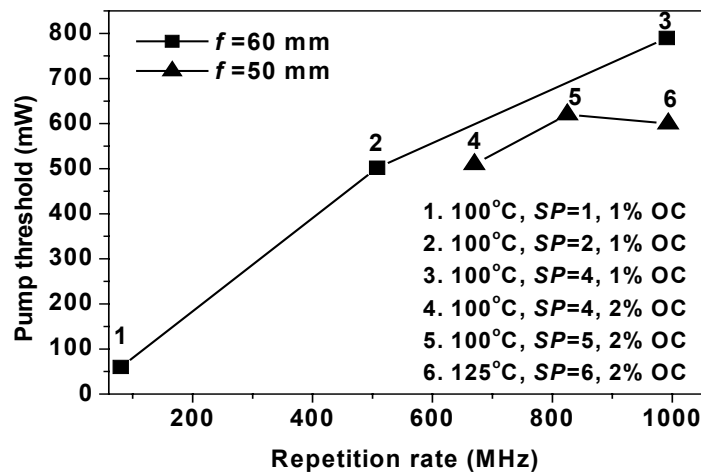


Fig. 3.5.13 Pump threshold of the PPLN OPO at different repetition rates and cavity configurations. f , focal length of the focusing lens; SP , the order of synchronous pumping.

Section IV Summary and outlook

4.1 Summary

High-repetition-rate femtosecond optical parametric oscillators based on KTP and PPLN are described comprehensively in this dissertation work.

The goal of our research work was to construct OPO devices operating at high repetition rate, large tuning range, and ultrashort pulse duration (large spectral bandwidth), which can be applied directly in spectroscopy research or will be especially important for telecommunication applications.

First, in the theory part we studied systematically the basic principles of OPOs and related devices, phase-matching methods and tunability of OPOs, dispersion characteristics of nonlinear crystals and optical glasses, and correspondingly the methods for intracavity dispersion compensation and extracavity pulse compression.

Then the experimental work and related theoretical analysis are described. We demonstrated our results as new achievements in the research field of femtosecond optical parametric processes, which are summarized as follows:

(1) Up to 1-GHz repetition-rate operation of a PPLN OPO

We achieved up to 560-MHz-repetition-rate operation of a 65-fs PPLN OPO when pumping at 80 MHz and using 3/7 (4/7) order synchronous pumping. This is the highest repetition rate of a femtosecond OPO reported so far using lower-order methods. Due to the large cavity loss, the OPO operated at low efficiency and small tuning range for this configuration.

We achieved 1 GHz operation of a 60-fs PPLN OPO making use of 4th- and 6th-order synchronous pumping, which is the highest repetition rate of any femtosecond OPOs reported so far. The conversion efficiency defined by the ratio between the signal and pump average power reaches 4.5%.

(2) 32-fs KTP OPO

We achieved 32-fs operation of a KTP OPO using chirped mirrors for intracavity GVD compensation, which is presently the shortest pulse duration in the world for the signal pulses generated directly from an OPO.

The signal pulses are tunable from 1140 nm to 1210 nm. More than 40 mW signal power was measured when using 900 mW pump power and synchronously pumping at 80 MHz.

(3) Intracavity doubling KTP OPO

We achieved intracavity doubling of the signal wave using a BBO crystal in a femtosecond KTP OPO. Up to 106 mW visible power tunable from 540 nm to 630 nm was obtained using 800 mW pump power of a Ti:sapphire laser operating at 80 MHz, providing an effective laser source for spectroscopy research.

(4) An uneven poling duty cycle enhanced efficient visible light generation in a femtosecond PPLN OPO

We discovered for the first time that a non-50% poling duty cycle enables efficient even-order QPM SHG and SFG processes simultaneously in a first-order QPM PPLN OPO.

As a result, multiples higher-order QPM processes (odd- and even-order) can operate simultaneously and efficiently in the same OPO device with small reduction in the first-order QPM OPO process. The tuning range of the PPLN OPO covers the visible range from 460 nm to 660 nm and the near infrared range from 1020 nm to 1340 nm. Optimization of the poling duty cycle for a specific higher-order QPM process can improve the efficiency significantly, providing a promising method to generate visible pulses from an OPO. This method is advantageous over the classical intracavity and extracavity methods. Precise control of the duty cycle does not only allow flexible applications of the periodically poled crystals, but also improve the production technology of these crystals.

(5) Theoretical modelling of the coupling among multiple higher-order QPM processes in a PPLN OPO

We developed a theoretical model to simulate the behaviour of all of the interacting waves in a PPLN OPO, involving the first-order QPM OPO process and multiple higher-order QPM frequency conversion processes (SHG and SFG). This theoretical model included a variable poling duty cycle of PPLN to investigate in a sophisticated manner the influence of the poling duty cycle on the even- and odd-order QPM processes, and it can be applied to any studies with multiple frequency processes coupled with one another simultaneously.

(6) GVD compensation using an intracavity fused silica glass plate

We put forth the method to achieve GVD compensation for femtosecond OPOs that oscillate at wavelengths longer than 1320 nm using an intracavity fused silica (or BK7) glass plate.

Low insertion loss at Brewster angle, extremely low costs, relatively flat and smooth compensation curves, simplification of the construction and alignment of the cavity make this method advantageous over others. Feasibility of this technique has been proved in theory and by some initial experiments. A disadvantage of this method is that it can only be applied to OPOs operating at wavelengths larger than 1.32 μm .

4.2 Outlook

Based on our achievements, the requirements from spectroscopy research, and the direction of development in the research field of ultrashort phenomena and nonlinear optics, we plan to make progress in the following aspects:

(1) Chirped pump and chirped grating period of PPLN or PPKTP

GVM is an important factor limiting further shortening of the signal pulses from a femtosecond PPLN or PPKTP OPO. Intracavity GVD compensation cannot solve this problem. Using positive chirped pump pulses and negatively chirped grating periods, or vice versa, can possibly lead to oscillation of transform-limited femtosecond signal pulses. However, this technique has been proved feasible only for the single-pass idler wave and the SHG process. We will firstly perform theoretical simulations to find technical solutions and then have this technique realized in the oscillating signal pulses experimentally.

(2) Femtosecond PPLN OPO operating at repetition rate >3 GHz

Based on the considerably low pump threshold of the femtosecond PPLN OPO operating at 1 GHz, we will explore >3 GHz operation of the PPLN OPO using tighter focusing, higher heating temperature of the crystal, and higher-order synchronous pumping.

(3) Largely extended tuning range of femtosecond PPLN or PPKTP OPO: new poling technology and large coverage of duty cycle

New poling technology is expected to be able to control the grating period and duty cycle more precisely. We will have PPLN or PPKTP crystals manufactured with a series of exactly designed values of grating periods and duty cycles, so that we could explore the most efficient higher-order (even- and odd-order) QPM SHG and SFG processes and be able to extend the tuning range of the PPLN or PPKTP OPO to cover the whole range from the visible to the near infrared. Furthermore, one might think of other poling patterns such as Fibonacci series [90].

(4) Experimental studies of intracavity GVD compensation by a glass plate for a femtosecond PPKTP OPO operating at 1.55 μm

This experimental work was supposed to be included in this thesis. Due to the delay of the arrival of the PPKTP crystal, it had to be postponed.

Inserting a fused silica plate with a designed thickness into the cavity of a PPKTP OPO at the Brewster angle, we expect sub-40 fs operation of the PPKTP OPO for the signal wave at $\sim 1.55 \mu\text{m}$. We will optimize the compensation by trying a series of fused silica plates with different thicknesses.

Appendix A

Sellmeier equations for optical crystals and glasses

In the following, we present the Sellmeier equations for some typical OPO and laser crystals and some commonly used glasses. In the equations, n denotes the refractive index; λ is the wavelength of incident light in μm ; $A, B, C, D, A1, A2, A3, A4, A5, A6, B1, B2, B3, B4, \dots$, are the Sellmeier coefficients; the footnotes X, Y, Z , stand for the directions of the principal axes of the biaxial crystals.

1. KTP[38]:

$$n^2 = A + \frac{B}{1 - \left(\frac{C}{\lambda}\right)^2} - D\lambda^2$$

	A	B	C	D
n_X	2.1146	0.89188	0.20861	0.01320
n_Y	2.1518	0.87862	0.21801	0.01327
n_Z	2.3136	1.00012	0.23831	0.01679

2. KTA[107]:

$$n^2 = A + \frac{B}{\lambda^2 - C} - D\lambda^2$$

	A	B	C	D
n_X	3.1413	0.04683	0.04055	0.01023
n_Y	3.1593	0.04828	0.04710	0.01049
n_Z	3.4435	0.06571	0.05435	0.01460

3. RTA[108]:

$$n^2 = A + \frac{B}{1 - \left(\frac{C}{\lambda}\right)^2} - D\lambda^2$$

	A	B	C	D
n_X	2.04207	1.17785	0.20157	0.01035
n_Y	2.14941	1.09267	0.21462	0.01067
n_Z	2.18962	1.30103	0.22809	0.01390

4. CTA[109]:

$$n^2 = A + \frac{B}{1 - \left(\frac{c}{\lambda}\right)^2} - D\lambda^2$$

	A	B	C	D
n_X	2.34498	1.04863	0.22044	0.01483
n_Y	2.74440	0.70733	0.26033	0.01526
n_Z	2.53666	1.10600	0.24988	0.01711

5. LiNbO₃[56]:

$$n_e^2 = A_1 + B_1 f + \frac{A_2 + B_2 f}{\lambda^2 - (A_3 + B_3 f)^2} + \frac{A_4 + B_4 f}{\lambda^2 - A_5^2} - A_6 \lambda^2$$

$$f = (T - T_0)(T + T_0 + 546) \text{ and } T_0 = 24.5 \text{ }^\circ\text{C}$$

Coefficients	Values
A_1	5.35583
A_2	0.100473
A_3	0.20692
A_4	100
A_5	11.34927
A_6	1.5334×10^{-2}
B_1	4.629×10^{-7}
B_2	3.862×10^{-8}
B_3	-0.89×10^{-8}
B_4	2.657×10^{-5}

6. LBO[43, 44]:

$$n^2 = A + \frac{B}{\lambda^2 + C} + D\lambda^2$$

	A	B	C	D
n_X	2.4543	1.1413×10^{-2}	-9.4981×10^{-3}	-1.3900×10^{-2}
N_Y	2.5382	1.2830×10^{-2}	-1.1387×10^{-2}	-1.7034×10^{-2}
N_Z	2.5854	1.3065×10^{-2}	-1.1617×10^{-2}	-1.8146×10^{-2}

$$\frac{dn_X}{dT} = 2.0342 \times 10^{-7} - 1.9697 \times 10^{-8} T - 1.4415 \times 10^{-11} T^2$$

$$\frac{dn_Y}{dT} = -1.0748 \times 10^{-5} - 7.1034 \times 10^{-8} T - 5.7387 \times 10^{-11} T^2$$

$$\frac{dn_Z}{dT} = -8.5998 \times 10^{-7} - 1.5476 \times 10^{-7} T + 9.4675 \times 10^{-10} T^2 - 2.2375 \times 10^{-12} T^3$$

7. BBO[110]:

$$n_o^2 = 1.7018379 + \frac{1.0357554\lambda^2}{\lambda^2 - 0.01800344} + \frac{1.2479989\lambda^2}{\lambda^2 - 91}$$

$$n_e^2 = 1.5920433 + \frac{0.7816893\lambda^2}{\lambda^2 - 0.016067891} + \frac{0.8403893\lambda^2}{\lambda^2 - 91}$$

8. Sapphire:

$$n^2 = 1 + \frac{A_1 \lambda^2}{\lambda^2 - B_1} + \frac{A_2 \lambda^2}{\lambda^2 - B_2} + \frac{A_3 \lambda^2}{\lambda^2 - B_3}$$

A_1	A_2	A_3	B_1	B_2	B_3
1.023798	1.058264	5.280792	0.00377588	0.0122544	321.3616

9. Fused Silica:

$$n^2 = 1 + \frac{A_1 \lambda^2}{\lambda^2 - B_1} + \frac{A_2 \lambda^2}{\lambda^2 - B_2} + \frac{A_3 \lambda^2}{\lambda^2 - B_3}$$

A_1	A_2	A_3	B_1	B_2	B_3
0.6961663	0.4079426	0.8974794	0.0684043	0.1162414	9.896161

10. Quartz [111]:

$$n_{o,e}^2 = A + \frac{B \lambda^2}{\lambda^2 - C} + \frac{D \lambda^2}{\lambda^2 - E}$$

	A	B	C	D	E
n_o	1.28604141	1.07044083	0.0100585997	1.10202242	100
n_e	1.28851804	1.09509924	0.0102101864	1.15662475	100

11. BK7:

$$n^2 = 1 + \frac{A_1 \lambda^2}{\lambda^2 - B_1} + \frac{A_2 \lambda^2}{\lambda^2 - B_2} + \frac{A_3 \lambda^2}{\lambda^2 - B_3}$$

A_1	A_2	A_3	B_1	B_2	B_3
1.03961212	0.231792344	1.01046945	0.0060007	0.0200179	103.560653

12. SF2, SF5, SF10, SF11, SF 18:

$$n^2 = 1 + \frac{A_1 \lambda^2}{\lambda^2 - B_1} + \frac{A_2 \lambda^2}{\lambda^2 - B_2} + \frac{A_3 \lambda^2}{\lambda^2 - B_3}$$

	A_1	A_2	A_3	B_1	B_2	B_3
SF2	1.40301821	0.23176750	0.93905659	0.0105796	0.04932270	112.405955
SF5	1.46141885	0.24771302	0.94999583	0.0118261	0.05085946	112.041888
SF10	1.61625977	0.25922933	1.07762317	0.0127535	0.05819840	116.607680
SF11	1.73848403	0.31116897	1.17490871	0.0136069	0.06159605	121.922711
SF18	1.56441436	0.29141358	0.96030788	0.0121864	0.05355680	111.451201

Appendix B Abbreviations

BPM	Birefringent Phase Matching (Matched)
CPM	Critical Phase Matching
Dc	Duty cycle
DFG	Difference-Frequency-Generation
GDD	Group Delay Dispersion
GVD	Group Velocity Dispersion
GVM	Group Velocity Mismatch
NCPM	Non-Critical Phase Matching (Matched)
OPA	Optical Parametric Amplifier
OPG	Optical Parametric Generation
OPO	Optical Parametric Oscillator
PM	Phase Matching
PPKTP	Periodically Poled KTP
PPLN	Periodically Poled LiNbO ₃
QPM	Quasi-Phase-Matching (Matched)
SFG	Sum-Frequency-Generation
SHG	Second-Harmonic-Generation
SNR	Signal-to-Noise Ratio
SP	the order of Synchronous Pumping
SPM	Self-Phase-Modulation
SPOPO	Synchronously Pumped OPO
TFWM	Transient Four-Wave Mixing

Literature:

- [1] Richard. L. Sutherland, “*Handbook of Nonlinear Optics*”, MARCEL DEKKER, INC., New York, 1996.
- [2] T. F. Albrecht, J. H. H. Sandmann, J. Feldmann, W. Stolz, E. O. Göbel, H. Hillmer, R. Lösch, W. Schlapp, Appl. Phys. B, **60**, 459 (1995).
- [3] N. Peyghambarian, S. W. Koch, A. Mysyrowicz, “*Introduction to Semiconductor Optics*”, Prentice-Hall, Inc., Englewood Cliffs, New Jersey 07632, 1993.
- [4] A. Bartels, T. Dekorsy, and H. Kurz, Opt. Lett. **24**, 996 (1999).
- [5] J. A. Giordmaine and R. C. Miller, Phys. Rev. Lett., **14**, 973 (1965)
- [6] L. E. Myers, R. C. Eckardt, M. M. Fejer, R. L. Byer, W. R. Bosenberg, J. W. Pierce, J. Opt. Soc. Am. B, **12**, 2102 (1995).
- [7] J. A. Armstrong, N. Bloembergen, J. Ducuing, P. S. Pershan, Phys. Rev. **127**, 1918 (1962).
- [8] Kent C. Burr, C. L. Tang, Mark A. Arbore, Martin M. Fejer, Appl. Phys. Lett., **70**, 3341 (1997).
- [9] Kent C. Burr, C. L. Tang, Mark A. Arbore, Martin M. Fejer, Opt. Lett. **22**, 1458 (1997)
- [10] P. Loza-Alvarez, C. T. A. Brown, D. T. Reid, W. Sibbett, Opt. Lett. **24**, 1523 (1999)
- [11] P. J. Phillips, S. Das, M. Ebrahimzadeh, Appl. Phys. Lett. **77**, 469 (2000).
- [12] G. Zhong, J. Jian, Z. Wu, IEEE Catalog No. 80CH 1561-0, p.631 (1980).
- [13] Tolga Kartaloglu, Kahraman G. Köprülü, Orhan Aytür, Opt. Lett. **23**, 61 (1998)
- [14] D. T. Reid, Z. Penman, M. Ebrahimzadeh, W. Sibbett, H. Karlsson, F. Laurell, Opt. Lett. **22**, 1397 (1997)
- [15] A. Robertson, M. E. Klein, M. A. Tremont, K.-J. Boller, and R. Wallenstein, Opt. Lett. **25**, 657 (1999).
- [16] B. Ruffing, A. Nebel, R. Wallenstein, Appl. Phys. B **67**, 537 (1998).
- [17] J. Hebling, H. Giessen, S. Linden, J. Kuhl, Opt. Commun. **141**, 229 (1997).
- [18] Kent C. Burr, C. L. Tang, Mark A. Arbore, Martin M. Fejer, Appl. Phys. Lett. **70**, 3341 (1997).
- [19] M. Nisoli, S. Stagira, S. De Silvestri, O. Svelto, G. Valiulis, A. Varanavicius, Opt. Lett. **23**, 630 (1998)

- [20] T. Beddard, M. Ebrahimzadeh, T. D. Reid, W. Sibbett, *Opt. Lett.* **25**, 1052 (2000)
- [21] G. Gerullo, M. Nisoli, S. Stagira, S. De Silvestri, *Opt. Lett.* **23**, 1283 (1998).
- [22] M. Nisoli, S. Stagira, S. De Silvestri, O. Svelto, G. Valiulis, and A. Varanavicius, *Opt. Lett.* **23**, 630 (1998).
- [23] M. A. Arbore, A. Galvanauskas, D. Harter, M. H. Chou, M. M. Fejer, *Opt. Lett.* **22**, 1341 (1997)
- [24] P. Loza-Alvarez, D. T. Reid, P. Faller, M. Ebrahimzadeh, W. Sibbett, *J. Opt. Soc. Am. B* **16**, 1553 (1999)
- [25] Robert W. Boyd, “*Nonlinear Optics*”, the Institute of Optics, University of Rochester, New York, ACADEMIC PRESS, INC. (1992).
- [26] R. Danielius, A. Piskarskas, A. Persson, and S. Svanberg, *Lithuanian J. Phys.* **33**, 305 (1994).
- [27] K. Finsterbusch, R. Urschel, H. Zacharias, *Appl. Phys. B* **74**, 319 (2002).
- [28] G. W. Baxter, Y. He, B. J. Orr, *Appl. Phys. B* **67**, 753 (1998).
- [29] J. D. McMullen, *J. Appl. Phys.* **46**, 3076 (1975).
- [30] P. D. Maker, R. W. Terhune, M. Nisenoff, and C. M. Savage, *Phys. Rev. Lett.*, **8**, 21 (1962).
- [31] H. J. Bakker, P. C. M. Planken, and H. G. Muller, *J. Opt. Soc. Am. B* **6**, 1665 (1989).
- [32] E. C. Cheung and J. M. Liu, *J. Opt. Soc. Am. B* **7**, 1385 (1990).
- [33] T. Nishikawa and N. Uesugi, *J. Appl. Phys.* **77**, 4941 (1995).
- [33] X. Liu, L. Qian, F. Wise, *Opt. Commun.* **164**, 69 (1999).
- [35] D. C. Hanna, M. V. O’Connor, M. A. Watson, and D. P. Shepherd, *J. Phys. D: Appl. Phys.* **34**, 2440 (2001).
- [36] A. Agnesi, G. C. Reali, V. Kubecek, S. Kumazaki, Y. Takagi, and K. Yoshihara, *J. Opt. Soc. Am. B* **10**, 2211 (1993).
- [37] J. Q. Yao and Theodore S. Fahlen, *J. Appl. Phys.* **55**, 65 (1984).
- [38] John D. Bierlein and Herman Vanherzeele, *J. Opt. Soc. Am. B* **6**, 622 (1989).
- [39] F. C. Zumsteg, J. D. Bierlein, and T. E. Gier, *J. Appl. Phys.* **47**, 4980 (1976).
- [40] C. Chen, B. Wu, A. Jiang, G. You, R. Li, S. Lin, *J. Opt. Soc. Am. B* **6**, 235 (1989).
- [41] C. Chen, B. Wu, A. Jiang, G. You, *Sci. Sin. B* **28**, 235 (1985).

- [42] T. Schröder, K. –J. Boller, A. Fix, R. Wallenstein, Appl. Phys. B **58**, 425 (1994).
- [43] S. P. Velsko, M. Webb, L. Davis, and C. Huang, IEEE J. Quantum Electron. **27**, 2182 (1991).
- [44] Y. Tang, Y. Cui, and M. H. Dunn, J. Opt. Soc. Am. B **12**, 638 (1995).
- [45] B. ruffing, A. Nebel, R. Wallenstein, Appl. Phys. B **72**, 137 (2001).
- [46] J. D. Kafka, M. L. Watts, and J. W. Pieterse, J. Opt. Soc. Am. B **12**, 2147 (1995).
- [47] R. L. Byer, “*Optical parametric oscillators*”, in Quantum Electronics: A Treatise, H. Rabin and C. L. Tang, eds. (Academic, New York, 1975), pp. 587.
- [48] <http://www.impex-hightech.de/NLO-LN.html>
- [49] <http://www.casix.com/products/crystals/linbo3.htm>
- [50] Charles Kittel, “*Introduction to Solid State Physics*”, John Wiley & Sons, Inc., New York, 1996, pp381.
- [51] M. Yamada, N. Nada, M. Saitoh, and K. Wantanabe, Appl. Phys. Lett. **62**, 435 (1993).
- [52] W. K. Burns, W. McElhanon, and L. Goldberg, IEEE Photon. Technol. Lett. **6**, 252 (1994).
- [53] J. Webjörn, V. Pruneri, P. St. J. Russell, J. R. M. Barr, and D. C. Hanna, Electron. Lett. **30**, 894 (1994).
- [54] S. N. Zhu, Y. Y. Zhu, Z. Y. Zhang, H. Shu, H. F. Wang, J. F. Hong, C. Z. Ge, and N. B. Ming, Opt. Lett. **20**, 52 (1995).
- [55] Q. Chen and W. P. Risk, Electron. Lett. **30**, 1516 (1994).
- [56] Dieter H. Jundt, Opt. Lett. **22**, 1553 (1997).
- [57] A. Nebel, C. Fallnich, R. Beigang, and R. Wallenstein, J. Opt. Soc. Am. B **10**, 2195 (1993).
- [58] A. Mokhtari, L. Fini, and J. Chesony, Opt. Commun. **61**, 421 (1987).
- [59] H. J. Bakker, P. C. M. Planken, and H. G. Muller, J. Opt. Soc. Am. B **6**, 1665 (1989).
- [60] R. Laenen, K. Wolfrum, A. Seilmeier, and A. Laubereau, J. Opt. Soc. Am. B **10**, 2151 (1993).
- [61] Jean-Claude Diels, Wolfgang Rudolph, “*Ultrashort Laser Pulse Phenomena*”, Academic Press, Inc., San Diego, California (1996).
- [62] J. Kuhl, J. Heppner, IEEE J. Quantum Electron. **22**, 182 (1986).

- [63] R. Szipöcs, K. Ferencz, Ch. Spielmann, F. Krausz, *Opt. Lett.* **19**, 201 (1994).
- [64] R. Szipöcs, A. Köházi-Kis, *Appl. Phys. B* **65**, 115 (1997).
- [65] F. X. Kärtner, N. Matuschek, T. Schibli, U. Keller, H. A. Haus, C- Heine, R. Morf, V. Scheuer, M. Tilsch, T. Tschudi, *Opt. Lett.* **22**, 831 (1997).
- [66] N. Matuschek, L. Gallmann, D. H. Sutter, G. Steinmeyer, U. Keller, *Appl. Phys. B-Lasers O* **71**, 509 (2000).
- [67] T. Tomaru, H. Petek, *Opt. Lett.* **25**, 584 (2000).
- [68] T. Tomaru, H. Petek, *J. Opt. Soc. Am. B* **18**, 388 (2000).
- [69] J. Hebling, X. P. Zhang, H. Giessen, J. Kuhl, and J. Seres, *Opt. Lett.* **25**, 1055 (2000).
- [70] X. P. Zhang, H. Giessen, J. Hebling, W. W. Rühle, and J. Kuhl, Topical Meeting on Advanced Solid-State Lasers, Postdeadline Papers PD7, 14-16 February 2000, Davos, Switzerland.
- [71] H. Giessen, X. P. Zhang, J. Hebling, W. Rühle, J. Kuhl, CWH6, CLEO 2000, May 7-12, 2000, Sanfrancisco, California.
- [72] K. Kato and M. Masutani, *Opt. Lett.* **17**, 178 (1992).
- [73] D. C. Edelstein, E. S. Wachman, and C. L. Tang, *Appl. Phys. Lett.* **54**, 1728 (1989).
- [74] E. S. Wachman, D. C. Edelstein, and C. L. Tang, *Opt. Lett.* **15**, 136 (1990).
- [75] G. Mak, Q. Fu, and H. M. van Driel, *Appl. Phys. Lett.* **60**, 542 (1992).
- [76] Q. Fu, G. Mak, and H. M. van Driel, *Opt. Lett.* **17**, 1006 (1992).
- [77] W. S. Pelouch, P. E. Powers, and C. L. Tang, *Opt. Lett.* **17**, 1070 (1992).
- [78] R. J. Ellingson, C. L. Tang, *Opt. Lett.* **18**, 438 (1993).
- [79] J. M. Dudley, D. T. Reid, M. Ebrahimzadeh and W. Sibbett, *Opt. Commun.* **104**, 419 (1994).
- [80] A. Nebel, H. Frost, R. Beigang, R. Wallenstein, *Appl. Phys. B* **60**, 453 (1995).
- [81] J. Seres, J. Hebling, *J. Opt. Soc. Am. B* **17**, 741 (2000).
- [82] A. Shirakawa, H. W. Mao, T. Kobayashi, *Opt. Commun.* **123**, 121 (1996).
- [83] E. C. Cheung, K. Koch, and G. T. Moore, *Opt. Lett.* **19**, 1967 (1994).
- [84] T. J. Driscoll, G. M. Gale, F. Hache, *Opt. Commun.* **110**, 638 (1994).
- [85] J. Hebling, E.J. Mayer, J. Kuhl and R. Szipöcs, *Opt. Lett.* **20**, 919 (1995)
- [86] T. Kartaloglu, K. G. Köprülü, and O. Aytür, *Opt. Lett.* **22**, 280 (1997).
- [87] K. G. Köprülü, T. Kartaloglu, Y. Dikmelik, and O. Aytür, *J. Opt. Soc. Am. B* **16**, 1546 (1999).

- [88] C. McGowan, D. T. Reid, Z. E. Penman, M. Ebrahimzadeh, and W. Sibbett, *J. Opt. Soc. Am. B* **15**, 694 (1998).
- [89] S. D. Butterworth, P. G. R. Smith, and D. C. Hanna, *Opt. Lett.* **22**, 618 (1997).
- [90] Y. Q. Lu, J. J. Zheng, Y. L. Lu, N. B. Ming, *Appl. Phys. B* **67**, 29 (1998).
- [91] Y. Qin, Y. Zhu, S. Zhu, and N. Ming, *J. Appl. Phys.* **84**, 6911 (1998).
- [92] M. A. Arbore, O. Marco, and M. M. Fejer, *Opt. Lett.* **22**, 865 (1997).
- [93] K. Mizuuchi and K. Yamamoto, *Opt. Lett.* **21**, 107 (1996).
- [94] X. P. Zhang, J. Hebling, J. Kuhl, W.W.Rühle, and H. Giessen, *Opt. Lett.*, **26**, 2005 (2001).
- [95] M. M. Fejer, G. A. Magel, D. H. Jundt, and R. L. Byer, *IEEE J. Quantum Electron.* **28**, 2631 (1992).
- [96] WWW.ntandc.de.
- [97] R. C. Miller, *Appl. Phys. Lett.* **5**, 17 (1964).
- [98] I. Shoji, T. Kondo, A. Kitamoto, M. Shirane, and R. Ito, *J. Opt. Soc. Am. B* **14**, 2268 (1997).
- [99] W. J. Alford and A. V. Smith, *J. Opt. Soc. Am. B* **14**, 524 (2001).
- [100] D. H. Kim, S. H. Kim, J. C. Jo, S. S. Choi, *Opt. Commun.* **182**, 329 (2000).
- [101] T. Papakyriakopoulos, K. Vlachos, A. Hatziefremidis, and H. Avramopoulos, *Opt. Lett.* **24**, 717 (1999).
- [102] D. J. Jones, S. A. Diddams, M. S. Taubman, S. T. Cundiff, L. S. Ma, and J. L. Hall, *Opt. Lett.* **25**, 308 (2000).
- [103] Th. Udem, S. A. Diddams, K. R. Vogel, C. W. Oates, E. A. Curtis, W. D. Lee, W. M. Itano, R. E. Drullinger, J. C. Bergquist, and L. Hollberg, *Phys. Rev. Lett.* **86**, 4996 (2001).
- [104] R. Holzwarth, Th. Udem, T. Hänsch, J.C. Knight, W.J. Wadsworth, and P.S.J. Russell, *Phys. Rev. Lett.* **85**, 2264 (2000).
- [105] A. Robertson, M. E. Klein, M. A. Tremont, K.-J. Boller and R. Wallenstein, *Opt. Lett.* **25**, 657 (2000).
- [106] X. P. Zhang, J. Hebling, *Appl. Phys. Lett.* **80**, 1873 (2002).
- [107] K. Kato, N. Umemura, and E. Tanaka, *Jpn. J. Appl. Phys.* **2**, **36(4A)**, L 403 (1997).
- [108] D. L. Fenimore, K. L. Schepler, D. Zelmon, S. Kuck, U. Ramabadran, P. Von Richter, and D. Small, *J. Opt. Soc. Am. B* **13**, 1935 (1996)

- [109] L. T. Cheng, L. K. Cheng, and J. D. Bierlein, SPIE Proceedings, OE LASE
Los Angeles FEB 1993.
- [110] G. Ghosh, J. Appl. Phys. **78**, 6752 (1995).
- [111] G. Ghosh, Opt. Commun. **163**, 95 (1999).

Acknowledgement

I gratefully acknowledge all the people who gave me supports and helps to my Ph. D. program and my life during the past years of my stay in Germany, although the words here are too limited to express my sincere thanks. I also acknowledge the Graduate College (Optoelektronik Mesoskopischer Halbleiter) for the funding.

- I would deeply thank Prof. Dr. Harald Giessen who led me to the research field of ultrafast lasers and nonlinear optics. With his constant guidance and encouragement, I was more confident in the work of this dissertation. Many opportunities he gave me to practice have stimulated many of my interests and enabled me to gain more experiences in my research field. I have learned quite a lot from his extensive knowledge in physics and many brilliant and creative ideas. His kind and all-aspect help has made the past years an ever-good memory in my life.
- I am especially grateful to Prof. Dr. Wolfgang W. Rühle for hosting me in his group as a Ph. D. student. His supervision and continuous supports laid a smooth way for my studies and research work. Through rewarding discussions with Prof. Rühle, I have gained much more knowledge in experimental techniques. Many thanks to Prof. Rühle also for his kind help in other aspects.
- I am greatly thankful to Prof. Dr. Peter Thomas for accepting me as a fellow of the Grauertkolleg "Optoelektronik mesoskopischer Halbleiter" and for his kind supports to my work.
- I am deeply grateful to Dr. Jürgen Kuhl for much valuable advice on writing the papers and the strict corrections to them, and especially for providing the PPLN crystal that is of key importance for my experimental work.
- I like to express my sincere appreciation to Dr. Janos Hebling for the nice collaborations on the experimental work and on the co-authored papers.
- I wish to say many thanks to Dr. Rainer F. Mahrt for providing the full opportunity to use the Ti:sapphire laser and the optical spectrum analyzer that are indispensable for my experiments.
- Dipl.-Phys. Makus Bender helped me to the largest extent in the first days when I came to Germany and met with many difficulties as a foreigner. I will never forget his kindness.
- It has been a very nice time and a good memory for me to share the office with Dr. Gunter Urbasch and Dr. Christian Bauer. Dr. Urbasch gave me much important advice to my work. Dr. Bauer was always giving me instant help. The pleasant atmosphere in our office has made my work efficient and enjoyable.
- I would like to show my sincere gratitude to Dipl.-Phys. Mirko Leuschner and Dr. Martin Schüttler for their helps in the lab. Mirko is so kind that he is always willing to help me whenever being asked and he is always capable of solving problems.
- I wish to express my great appreciation to Dr. Limei Klar and Dr. Peter Klar for their kind considerations for my work and their warm help with my family. My wife and I will never forget their kindness.

- I would say many thanks to Dipl.-Phys. Dietmar Nau for his help with my experimental work in Bonn.
- I thank Dr. Albrecht Bartels for his excellent work with the stable operation of the Ti:sapphire laser, ensuring our successful work of the 1 GHz OPO.
- I thank Dr. Arno Euteneuer and Dipl.-Phys. Eckhard Finger for their important suggestions when I built up the 10-fs Ti:sapphire laser.
- My sincere thanks should also go to Dipl.-Phys. Jens Hübner, Dipl.-Phys. Thosten Hartman, Dipl.-Phys. Heiko Grüning, Dipl.-Phys. Shuangli Ye, and Dr. Horst Falk for their kind help and for the pleasant working atmosphere in the lab building II.
- I am sincerely grateful to Mr. Fries for his kindness and his technical suggestions on the making of mechanical parts, and the machining group for their perfect work.
- I thank Ms. Anja Ehlers for her kind help with frequent office affairs and Ms. Sabine Johanna Klapper for her much help with the troublesome orderings.
- I would also say many thanks to my good friends Dr. Yuping Wu and Ms. Rong Xu for their help in the past years.
- At last, I thank my family: my wife, Xiaoyan Song, for giving me the most patient and loving supports and encouragement to my work, and for her many good suggestions to my dissertation; My parents, for their ever-loving supports and understanding during the years of my studies and work. The success of finishing this dissertation is my first present to my son.

Curriculum Vitae

12. 09. 1968 born in Laoting County, Hebei Province, P. R. China
- 02.1976 – 07.1981 elementary school, Laoting, Hebei, P. R. China
- 08.1981 – 07.1987 middle school and high school, the First Middle School
of Laoting County, Hebei Province, P. R. China
- 09.1987 – 07.1991 study in the Department of Precision Instrument, Tianjin
University, 300072 Tianjin, P. R. China.
- 07.1991 BACHELOR's degree of Engineering in Photo-
electronics
- 09.1991 – 08.1994 postgraduate study in the Department of Laser
Application, the Institute of Physical and Chemical
Engineering, 300180 Tianjin, P. R. China
- 08.1994 MASTER's degree of Engineering in Laser Physics
- 09.1994 – 09.1998 engineer with the Institute of Physical and Chemical
Engineering, 300180 Tianjin, P. R. China
- 10.1998 – 10.1999 visiting scholar in the research group of Prof. Dr. W. W.
Rühle, the Department of Physics, Philipps-University
of Marburg, 35032 Marburg, Germany
- from 01.2000 Ph. D. student in the research group of Prof. Dr. W. W.
Rühle, the Department of Physics, Philipps-University
of Marburg, 35032 Marburg, Germany.
- from 01.2000 fellow of the Graduiertenkolleg “Optoelektronik
mesoskopischer Halbleiter”, Philipps-University of
Marburg, 35032 Marburg, Germany.